UNIVERSITÀ DEGLI STUDI DI MILANO

Scuola di Dottorato in Fisica, Astrofisica e Fisica Applicata

Dipartimento di Fisica

Ciclo XXXIV

Measurement of the SM Higgs boson properties in the diphoton decay channel with the ATLAS Run 2 dataset

CERN-THESIS-2022-193
11/03/2022

Supervisori: Prof. Leonardo Carminati
Dott. Ruggero Turra

Coordinatore: Prof. Matteo Paris

Tesi di Dottorato di:
Davide Pietro Mungo

Anno Accademico 2020/2021

Commission of the final examination:

Prof. Mauro Donegà
Prof. Marumi Kado
Prof. Alexander Lincoln Read (*Chair*)

Referees:

Prof. Fabio Cerutti
Prof. Paolo Meridiani

Final examination:

11 March 2022
Università degli Studi di Milano, Dipartimento di Fisica, Milano, Italy

Settore Scientifico Disciplinare:
FIS/04 FIS/01

PACS:
07.05.Mh, 14.80.Bn, 14.80.Da, 07.05.Dz

Cover illustration:
Artwork by C. Merlassino

Ai miei Nonni

Contents

Introduction

This manuscript presents the work I carried out during my PhD in particle physics at the Milano university and CERN from Autumn 2018 to March 2021. The work presented here is based on proton-proton collision data at a center-of-mass energy $\sqrt{s} = 13\,\text{TeV}$ collected by the ATLAS experiment [1] and produced during the Run 2 period of the LHC [2], corresponding to $139\,\text{fb}^{-1}$ of data. The ATLAS detector is one of the four main experiments placed on the LHC interaction points. It is built to register the outcome of the collisions occurring every 25 ns by reconstructing and measuring the properties of the elementary particles produced during the interactions. Its research program ranges from the precise measurement of the parameters of the Standard Model (SM) of particle physics to the testing of the plethora of Beyond Standard Model (BSM) theories.

On the 4th July 2012, the ATLAS and CMS [3] collaborations announced the discovery of a particle compatible with the Higgs boson predicted by the Standard Model, with a mass around 125 GeV [4, 5]. The Higgs boson is a fundamental scalar field predicted in the sixties which spontaneously breaks the electroweak symmetry, generating the required mass term in the Standard Model lagrangian. The long sought Higgs boson was observed combining the three most sensitive decay channels in a hadron collider, the $H \to \gamma\gamma$, the $H \to ZZ \to 4\ell$ and the $H \to \ell\nu\ell\nu$ channels. The collaborations have then started a huge effort in assessing its properties like the mass, charge, spin and the couplings to other SM particles with the highest possible precision and found them to be in agreement with the ones predicted for the SM Higgs boson within the statistical precision. Nowadays, this program is not settled yet: the Higgs boson still attracts our interest because it interacts with almost all the Standard Model particles and it is considered a portal towards new physics beyond the SM.

The work reported in this manuscript is fully part of this physic program, focusing on the measurement of the Higgs boson mass and production cross sections in the $H \to \gamma\gamma$ channel. The diphoton decay represents one of the best channel to access the fundamental properties of the Higgs boson: this is due to the excellent photon reconstruction performance, to the clear final state signature and to the robust background description and subtraction. In fact, the Higgs boson manifests itself as a narrow peak over a smoothly falling background in the diphoton invariant mass distribution, which can be

both modeled with analytical functions. In this manuscript, the full $H \to \gamma\gamma$ analysis chain is described. Particular emphasis is placed in the description of the innovative event categorization procedures I have designed for the coupling and mass measurements. The production cross sections measurement is presented in a number of different parameterizations which explore the full Higgs production phase space and represents the final Run 2 results for this decay channel. The expected result for the Higgs mass measurement is presented as well.

Summary of the manuscript and personal contributions

This manuscript is composed by six chapters, articulated as follows.

- Chapter 1 summarizes the formulation of the Standard Model, focusing on the electroweak symmetry breaking and the Higgs mechanism. This chapter includes also a review of the main measurements of the Higgs boson properties performed by the ATLAS and CMS collaborations with the data collected at $\sqrt{s} = 7$ and 8 TeV.

- Chapter 2 presents the LHC accelerator and the ATLAS detector, emphasizing in particular the data taking conditions and the main sub-detectors exploited for the photon detection and reconstruction. During my doctorate, I have actively participated in the operation and the upgrade of the Liquid Argon (LAr) calorimeter of the ATLAS detector. During data-taking year (2018) I have served as hardware on-call expert, while during Long Shutdown 2 (2019-2021) I was in charge of upgrading the system, both in its software and hardware components, that delivers the high-voltage to the calorimeter cells.

- Chapter 3 describes the details of the reconstruction of physics objects for the events collected by ATLAS. Special attention is given to photon reconstruction, calibration and performance, since these are of paramount importance for the analyses described in the following chapters. It includes also a brief description of the reconstruction and performance of all other physics objects employed in the Higgs production cross section analysis. In addition, this chapter includes Section 3.3 concerning a multivariate analysis I have developed for e/γ ambiguous object classification.

- Chapter 4 details the full $H \to \gamma\gamma$ analysis strategy, used to extract the results reported in Chapter 5 and 6, covering the common aspects of the mass and coupling analyses. I have actively contributed to the service tasks of the physic group these analyses belong to, by maintaining and updating the software infrastructure, by managing and storing the common dataset produced and by acting as a liason between this group and the Higgs combination one. Moreover, this chapters describes a re-optimization of the diphoton primary vertex I have performed, reported in Section 4.3.2.

- Chapter 5 reports the details of the Higgs production cross section measurements, which has been the main topic of my doctorate program throughout the three years

of the school. The chapter describes the theoretical framework in which the measurement is carried out and the additional physics object selections needed to perform the measurement. A major emphasis is then given to a detailed description of the innovative categorization procedure employed for these results: this is, by far, my major contribution to this analysis. The signal and background modeling are described in details as well, along with the various peculiarities of the systematic uncertainties included. The Higgs production cross sections measurements are presented in a number of different parametrizations in order to test the details of the Higgs production phase space and hence of the Higgs boson couplings. My involvement in this analysis was thorough and I have participated in the production and validation of almost all the topics presented in the chapter. The legacy Run 2 results [6] are presented here, which supersede the preliminary full Run 2 $H \to \gamma\gamma$ results published during 2020 [7], with a slightly improved analysis. I have taken part in other $H \to \gamma\gamma$ coupling analyses [8–10] which are superseded as well and not covered in this manuscript. The final section of this chapter provides a brief overview of the latest Higgs combination results [11]: I have participated to this effort throughout the years [12–14] as contact person for the $H \to \gamma\gamma$ statistical workspace, by maintaining common statistical tools and ensuring technical compatibilities among the input analyses.

- Chapter 6 focuses on the Higgs mass measurement in the $H \to \gamma\gamma$ decay channel, for which I am acting as collaboration contact for this analysis. Emphasis is given to the categorization part, which was one of the main development points during my doctorate. The signal and background models and the systematic uncertainties are described as well, which I have thoughtfully supervised. Expected results are reported, since this measurement is still in the collaboration approval stage and the signal region is still blinded.

CHAPTER 1

The Standard Model and Higgs Boson physics

The *Standard Model* (SM) of particle physics is the theoretical framework in which the work presented in this manuscript has been carried out. The model has been developed during the sixties and seventies of 1900. From then on, it has been proven to describe Nature with unprecedented precision by a large number of experimental measurements, a physics programme that nowadays is still exciting and ongoing. The Higgs boson discovery in 2012 [4, 5] has finally completed the model, opening a new era of precision measurements of the properties of the newly discovered particle.

In this chapter I will briefly describe the Standard Model from a basic theory point of view in Section 1.1. The Higgs mechanism will be outlined in the Section 1.2. A description of the Higgs boson phenomenology at hadron colliders and its discovery will be given in Section 1.3 and Section 1.4 respectively.

1.1 The Standard Model

The Standard Model is a quantum field theory that describes and predicts the phenomenology of high energy elementary particles interactions with very high accuracy. In its description, matter particles are represented by fermion fields of spin $1/2$ and the interactions among them by boson fields of spin 1. The SM describes three out of four known interactions of Nature using the Lie groups $SU(3)_C \times SU(2)_L \times U(1)_Y$ which are associated to the *Quantum Chromodynamics* ($SU(3)_C$) and the *Electro-weak interaction* ($SU(2)_L \times U(1)_Y$). In fact, in the SM the $SU(2)_L \times U(1)_Y$ allows a unified description of the *Quantum Electrodynamics* and *Weak force*. The SM gauge symmetry is spontaneously broken to $SU(3)_C \times U(1)_{EM}$ where $U(1)_{EM}$ couples to the electromagnetic charge Q_{EM}. The model describes all the interactions of the known fermions once they are assigned to well defined representation of the gauge group. The *Gravity* is not included in the Standard Model but it is the weakest among all the forces and can be safely neglected in the description of high energy interaction processes. An overview of SM particles and their properties is shown in Figure 1.1.

1.1.1 The matter

Matter is described with Dirac fermion fields, divided in two groups called *quarks* and *leptons*, both in three families (or generations) and organized in doublets. They are all

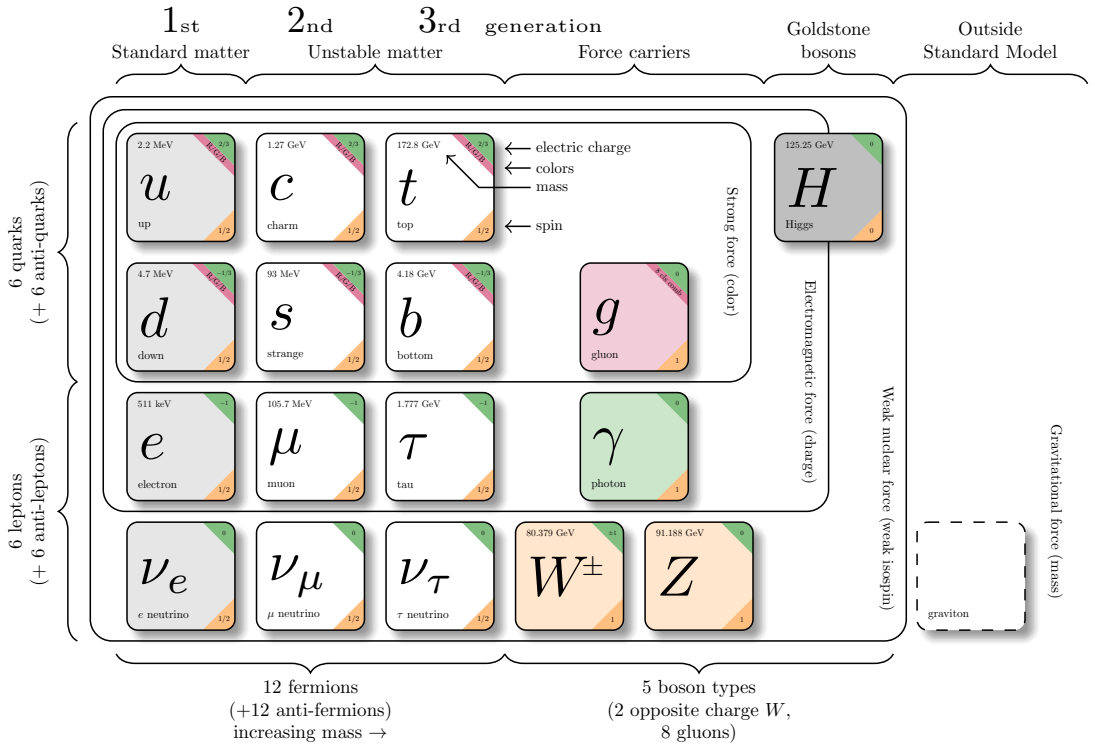

Figure 1.1 – The Standard Model of particle physics. Matter fields are reported on the left, while boson responsible for particle interactions on the right. Each field is represented with its quantum numbers (the weak isospin is not shown). Masses are taken from [15]: the u-, d-, and s-quark masses are estimates of the so-called "current-quark masses", in a mass-independent subtraction scheme such as $\overline{\text{MS}}$ at a scale $\mu \sim 2\,\text{GeV}$. The c- and b-quark masses are the "running" masses in the $\overline{\text{MS}}$ scheme, while the t-quark mass is a combination of direct measurements from Tevatron and LHC $\sqrt{s} = 7\,\text{TeV}$ results. Neutrinos are considered massless in this overview. Adapted and updated from [16].

charged with respect to electromagnetic force but behave in different ways under the other two forces. In particular, leptons can only interact via electro-weak force, because they are neutral with respect to the strong force; quarks additionally present strong charge, therefore interact with all the forces described in the Standard Model.

All the matter fields have mass with the exception of neutrinos. In fact, these are considered massless in the SM and throughout this manuscript. Nevertheless, it has been experimentally proven via neutrino oscillations that they have mass: their mass differences are known and the upper limit on m_{ν_e} is very tiny (< 1.1 eV at 90% CL) [15].

1.1.2 The forces

As already stated, the forces described in the Standard Model are the Strong, Weak and the Electromagnetic one. A mediator, called *gauge boson*, is associated to each of them and is exchanged between particles when they interact. The properties of the interaction are specified by the Lie group on which the gauge theories are based on.

Quantum Chromodynamics

The *Quantum Chromodynamics* (QCD) is the theory which describes the Strong force. This interaction is the strongest among the forces and it is responsible for gluing the quarks together in the hadrons.

The QCD was theoretically developed during the late sixties and first seventies, when the static quark models by Gell-Man [17] and Zweig [18] showed their limits in describing the Δ^{++} state. After its formulation, QCD was experimentally proven during the eighties through the di-jet and tri-jet observations at the JADE experiment [19], placed on the PETRA e^+e^- collider at DESY.

The QCD is a Yang-Mills non-Abelian gauge theory based on the $SU(3)_C$ Lie group, where the subscript C stands for "Colour", the charge of the group. Quarks carry a colour charge ("red", "green" or "blue") and are represented with an isospin triplet of fields. They interact through force carriers called *gluons* which are eight massless bosons, as 8 is the dimension of the adjoint representation of $SU(3)$. Since the QCD is a non-Abelian theory, gluons are coloured and therefore they are subjected to trilinear and quartic auto-interactions.

Indicating with g_s (or $\alpha_s = g_s^2/(4\pi)$) the strong coupling constant and with a the color-index of $SU(3)$ parameters which runs from 1 to 8, the Lagrangian for the QCD could be written as:

$$\mathcal{L} = \sum_f \bar{\psi}_f \left(i\gamma^\mu \mathcal{D}_\mu - m_f \right) \psi_f - \frac{1}{4} G_a^{\mu\nu} G_{a\mu\nu} \tag{1.1}$$

where

- the sum on f runs over quark flavour: *up* (u), *down* (d), *charm* (c), *strange* (s), *top* (t), *bottom* (b), grouped in three generations as shown in Figure 1.1

- ψ_f indicates the matter fields, i.e. quarks, grouped in a colour isospin triplet $\psi_f = (\psi_f^r, \psi_f^g, \psi_f^b)$;
- $G_a^{\mu\nu}$ is the field strength of the gluon field G_a^μ and is defined as

$$G_a^{\mu\nu} = \partial^\mu G_a^\nu - \partial^\nu G_a^\mu - g_s \lambda_{abc} G^{b\mu} G^{c\nu}$$

  with λ_{abc} being the structure constants of $SU(3)$;
- $\mathcal{D}_\mu$ indicates covariant derivative, which is flavour blind and is defined as

$$\mathcal{D}_\mu = \partial_\mu + i g_s \mathbf{T}_a G_{a\mu}$$

  where a is the index of $SU(3)$ parameters and $\mathbf{T_a}$ are matrices representing the gauge group generators in the quark representation, which has dimension eight.

The theory is invariant both globally and locally under $SU(3)$ group transformation

$$\mathbf{U}\left(\vec{\theta}(x)\right) = e^{i g_s \sum_a \theta_a(x) \mathbf{T}_a} \tag{1.2}$$

and therefore it is renormalizable, introducing appropriate counterterms in Eq. (1.1).

Due to the renormalization, the coupling constant g_s is a function of an (unphysical) renormalization scale μ_R. When one takes μ_R close to the scale of the momentum transfer Q^2 in a given process, then $\alpha_S(\mu_R \simeq Q^2)$ is indicative of the effective strength of the strong interaction in that process. At the first perturbative order, the running of α_S is expressed by

$$\alpha_S(\mu_R) = \frac{1}{\frac{11N_C - 2n_f}{12\pi} \log \frac{\mu^2}{\Lambda^2}}$$

where N_C is the number of colors, n_f the number of flavours and Λ is the typical hadronic scale ($\sim$300 MeV). It can be seen that for higher and higher momenta the constant acquires lower and lower values: this is called *asymptotic freedom*. For this reason, perturbative QCD calculations are reliable only in the high energy regime, like the one of the LHC. For momentum transfers in the 0.1–1 TeV range, $\alpha_S \sim 0.1$, while the theory is strongly interacting for scales around and below 1 GeV

The second important property of Quantum Chromodynamics is the *colour confinement*. It has not been proven mathematically yet but it shows itself experimentally. The colour charge of a particle is confined inside a colour-singlet hadron so no colourful particles exist free. Indeed, the quarks have not been observed as isolated particles and they always group together to form bound states. Experimentally, groups of two or three quarks can be observed, called respectively *mesons* and *barions*, or even more exotic particles like tetraquark, pentaquark and glueball, which are predicted by the QCD. At high energy, when a quark or a gluon is produced in the final state of a physical process, it *hadronizes*, namely it creates a bunch of hadrons around it called *hadronic jet*. There is a relevant exception to this fact provided by the most massive quark: indeed top quark decays through a weak process before hadronizing.

Electro-Weak interaction

The *Quantum Electrodynamics* (QED) [20] is the theory which describes the electromagnetic force at the quantum level, where the interaction is represented by the exchange of photons, the vector boson of QED indicated with γ. Historically, it was the first relativistic quantum field theory, developed before the middle of the previous century, and it was able to describe experimental measurements with high precision. It has played a special role in posing the questions towards the renormalization formulation.

The QED is an Abelian quantum field theory based on the $U(1)$ Lie group. The charge of the group is the electric charge of a particle and photons interacts with charged particles. Photons are massless and neutral, therefore they don't interact among themselves (Abelian theory).

The weak force was firstly theorized by Fermi as a four fermions contact interaction, while trying to explain the β decay. From the experimental measurements of the emitted energy spectrum of the electron, their angular correlations and parity violation, it was understood that the weak interaction through charged currents has a V–A structure and maximally violates parity; in a more modern language, weak charged force interacts only with the left-handed chiral part of fermions. Further studies made on neutrinos interactions showed that also neutral currents interactions could take place but without being maximally parity violating. The very weak cross sections measured in the experiments was interpreted with a short-range force, carried by massive bosons: in the case of charged currents the bosons exchanged were called W^+ and W^-, while Z^0 for neutral currents.

The experimental observations were theoretically accommodated by Glashow [21] in 1961: he proposed to describe the weak and electromagnetic interactions together as one Yang-Mills theory based on a $SU(2)_L \times U(1)_Y$ Lie group. This is what is called the *Electro-Weak interaction*. The group has four generators and therefore could accommodate four different interactions. The implementation is not straightforward: weak charged current couples to left-handed component of fermions, weak neutral current couples to both left and right components with different strengths and electromagnetism is completely symmetric to the two. To overcome the problem, Glashow did not use the electric charge as a charge for the $U(1)$ group, but defined the *hypercharge* Y. Then he grouped left-handed states in isoposin doublets, $\psi_L = (u_L, d_L)$ with the same hypercharge, letting right-handed state to be isospin singlet. The doublets carry $T = \frac{1}{2}$ and $T_3 = \pm\frac{1}{2}$ weak isospin quantum numbers, instead isospin singlet are represented by $T = 0$. Since T_3 eigenvalues are quantized, as from a $SU(2)$ algebra, and Y eigenvalues are real numbers, one could choose a relation between weak isospin, hyperchage and electric charge generators like[1]

$$Q = \frac{Y}{2} + T_3 \tag{1.3}$$

where T_3 is the eigenvalue of the third component of isospin generators vector $\mathbf{T} = \frac{\sigma}{2}$, with σ being the Pauli matrices. The four generators of the group are associated to four

[1] This equation holds both for generators ($\mathbf{T}$) and for their eigenvalues (T) since we are working always with eigenstates of the these operators.

gauge bosons: W_1, W_2, W_3 for the $SU(2)_L$ part, B for $U(1)_Y$. The local gauge invariance is obtained by defining the covariant derivative as

$$\mathcal{D}_\mu = \partial_\mu + i\frac{g'}{2} Y B_\mu + i g T_i W_\mu^i \tag{1.4}$$

with g and g' being the coupling constants associated to the $SU(2)_L$ and $U(1)_Y$ groups respectively. Therefore, the interaction part of the Lagrangian will result in

$$\mathcal{L}_{int}^{\text{EW}} = -\frac{g'}{2}\left(\bar{\psi}\gamma^\mu Y \psi\right) B_\mu - g\left(\bar{\psi}\gamma^\mu T_k \psi\right) W_\mu^k \tag{1.5}$$

$$\begin{aligned} = &-\frac{g'}{2}\bar{u}_R Y_R^u \not{B} u_R - \frac{g'}{2}\bar{d}_R Y_R^d \not{B} d_R \\ &-\frac{1}{2}\left(\bar{u}_L \bar{d}_L\right)\begin{pmatrix} g' Y_L \not{B} + g\not{W}^3 & g\left(\not{W}^1 - i\not{W}^2\right) \\ g\left(\not{W}^1 + i\not{W}^2\right) & g' Y_L \not{B} - g\not{W}^3 \end{pmatrix}\begin{pmatrix} u_L \\ d_L \end{pmatrix}. \end{aligned} \tag{1.6}$$

To obtain the weak charged currents, one needs to define the $W^\pm$ bosons as a linear combination of W^1 and W^2

$$W^\pm = \frac{1}{\sqrt{2}}\left(W^1 \pm i W^2\right). \tag{1.7}$$

The Z^0 and A fields of the photons are obtained with a rotation $\left(B, W^3\right) \to (A, Z)$ by an angle θ_W, called the *Weinberg angle*:

$$\begin{pmatrix} B \\ W^3 \end{pmatrix} = \begin{pmatrix} \cos\theta_W & -\sin\theta_W \\ \sin\theta_W & \cos\theta_W \end{pmatrix}\begin{pmatrix} A \\ Z \end{pmatrix}. \tag{1.8}$$

In order to obtain the electromagnetic coupling, a relation between group constants and electric charge is imposed

$$g \sin\theta_W = g' \cos\theta_W = e. \tag{1.9}$$

Applying these rotations to the Lagrangian terms in Eq. (1.6) and defining $J_\mu^+ = \bar{u}_L \gamma_\mu d_L$, $J_\mu^- = \bar{d}_L \gamma_\mu u_L$ and $J_\mu^{\text{em}} = \bar{\psi}\gamma_\mu Q \psi$, one would obtain:

$$\begin{aligned} \mathcal{L}_{int}^{\text{EW}} = &-eA^\mu J_\mu^{\text{em}} \\ &-\frac{g}{\sqrt{2}}\left(W^{+\mu} J_\mu^- + W^{-\mu} J_\mu^+\right) \\ &+\frac{e}{2\sin\theta_W \cos\theta_W}\bar{\psi}\not{Z}\left[\left(T^3 - 2Q\sin^2\theta_W\right) - T^3\gamma^5\right]\psi \end{aligned} \tag{1.10}$$

where the three lines represent the electromagnetic, the weak charged and weak neutral interactions, respectively.

1.2 The Standard Model Higgs boson

The Standard Model presented in the previous section foresees that all the described particles are massless. Indeed, vector bosons must be massless not to break the proper local gauge symmetry in the model: photons and gluons are effectively massless in Nature but a problem arises for $W^{\pm}$ and Z^0 bosons. Fermions must be massless too, because their mass terms would break the global invariance of a $SU(2)_L$ group, but again it is not the case in Nature.

To give mass to weak gauge bosons without spoiling the local gauge invariance, the particles must acquire their masses *dynamically*. The mechanism was established in the independent works of Higgs [22–24], Englert-Brout [25] and Guralnik-Hagen-Kibble [26] in 1964: they showed that the combination of a gauge theory with an additional field which *spontaneously breaks* the gauge symmetry can consistently produce mass terms for the gauge bosons. The mechanism was later introduced by Weinberg and Salam in a model with Chiral symmetry [27] in 1967, therefore applicable to the $SU(2)_L \times U(1)_Y$ group. The EW theory spontaneously broken with the Higgs mechanism has been shown being renormalizable by 't Hooft in 1971 [28, 29].

1.2.1 Higgs Mechanism in QED

In this section I will introduce the Higgs mechanism with a simple although unphysical example, trying to give mass to the QED photon.

Starting from the QED lagrangian

$$\mathcal{L}_{QED} = \bar{\psi}\left(i\gamma_\mu \mathcal{D}_\mu - m\right)\psi - \frac{1}{4}F^{\mu\nu}F_{\mu\nu} \tag{1.11}$$

$$\mathcal{D}_\mu = \partial_\mu + ieA_\mu \tag{1.12}$$

we introduce a massless non-free complex scalar field $\boldsymbol{\phi} = \frac{1}{\sqrt{2}}(\phi_1 + i\phi_2)$, which has a particular potential $U(\boldsymbol{\phi}) = \lambda\left(\boldsymbol{\phi}^*\boldsymbol{\phi}\right)^2 - \mu^2\boldsymbol{\phi}^*\boldsymbol{\phi}$, shown in Figure 1.2. In this case, the Lagrangian for this field would be:

$$\mathcal{L}_{\text{Higgs}} = K(\boldsymbol{\phi}) - U(\boldsymbol{\phi}) = \left(\mathcal{D}^\mu\boldsymbol{\phi}\right)^*\left(\mathcal{D}_\mu\boldsymbol{\phi}\right) - \left[\lambda\left(\boldsymbol{\phi}^*\boldsymbol{\phi}\right)^2 - \mu^2\boldsymbol{\phi}^*\boldsymbol{\phi}\right] \tag{1.13}$$

where λ and μ are two real parameters and $\lambda > 0$.

The Lagrangians of Eq. (1.11) and Eq. (1.13) are both invariant under local gauge transformation of the $U(1)$ group, where the fields transform as

$$\boldsymbol{\phi} \to e^{ie\alpha(x)}\boldsymbol{\phi}, \qquad \psi \to e^{ie\alpha(x)}\psi, \qquad A_\mu \to A_\mu - \partial_\mu\alpha(x). \tag{1.14}$$

After imposing $\lambda > 0$, the potential $U(\boldsymbol{\phi})$ has a minimum for an infinite set of field configurations $\boldsymbol{\phi}_0$ such that

$$|\boldsymbol{\phi}_0|^2 = \frac{\mu^2}{2\lambda} \stackrel{\text{def}}{=} \frac{1}{2}v^2. \tag{1.15}$$

where v is the so called *Vacuum Expectation Value* (VEV). Therefore the Higgs field will

acquire one of this configurations as ground state. This choice *spontaneously* breaks the invariance of the theory, namely the symmetry is not manifested in the ground state chosen, and so the Lagrangian will now change under a gauge transformation. For the sake of simplicity, we choose the minimum as completely real $\boldsymbol{\phi}_0 \stackrel{\text{def}}{=} \frac{v}{\sqrt{2}}$ and rewrite the field as variations around the vacuum:

$$\boldsymbol{\phi} = \boldsymbol{\phi}_0 + \frac{\phi + i\chi}{\sqrt{2}} = \frac{v + \phi + i\chi}{\sqrt{2}} \qquad (\phi, \chi \text{ real fields}) \tag{1.16}$$

In this way, translations perpendicular and tangential to the circle of minimum are parametrized by ϕ and χ respectively. Substituting this equation in Eq. (1.13), a bunch of interesting term appears:

- a photons mass term

$$\frac{(ev)^2}{2} A_\mu A^\mu \qquad \text{and so} \qquad m_\gamma \stackrel{\text{def}}{=} ev \tag{1.17}$$

- a massive scalar field with mass $m_\phi = \sqrt{2}\mu = v\sqrt{2\lambda}$ and its auto-interactions terms

$$\frac{1}{2}\left(\partial_\mu \phi \partial^\mu \phi - 2\mu^2 \phi^2\right) - \left(\frac{\mu^2}{v}\phi^3 + \frac{\mu^2}{4v^2}\phi^4\right) \tag{1.18}$$

- ϕ-γ interactions, where the coupling constant is proportional to the gauge boson mass

$$evA_\mu A^\mu \phi + \frac{e^2}{v} A_\mu A^\mu \phi^2 \stackrel{(1.17)}{\rightarrow} m_\gamma A_\mu A^\mu \phi + \frac{m_\gamma^2}{v^3} A_\mu A^\mu \phi^2 \tag{1.19}$$

- a massless scalar boson (*Goldstone boson*) with its interaction terms

$$\frac{1}{2}\left(\partial_\mu \chi \partial^\mu \chi\right) + evA_\mu \partial^\mu \chi + (\text{others}). \tag{1.20}$$

The last terms in the list are expected to come out whenever a continuous symmetry, under which the Lagrangian is invariant, is spontaneously broken. This is stated in the *Goldstone theorem* [30]: if M generators are spontaneously broken out of N symmetry generators, M spin-0 massless particles are generated. Intuitively, they are massless because represent variations in the infinite set of minima configurations (translations along χ are free to occur since the circle of minimum is a flat, isopotential line).

In this case, the further apparent degree of freedom χ is not an independent physical particle: when the photon acquires mass, it acquires one more degree of freedom too, namely the longitudinal polarization (along with two transversal polarization state already present in the massless case). Translating a field like in Eq. (1.16) could not create a new degree of freedom though. Instead of Eq. (1.16), one can parametrize the field like

$$\boldsymbol{\phi} = \frac{(v + \phi)e^{i\frac{\chi}{v}}}{\sqrt{2}}. \tag{1.21}$$

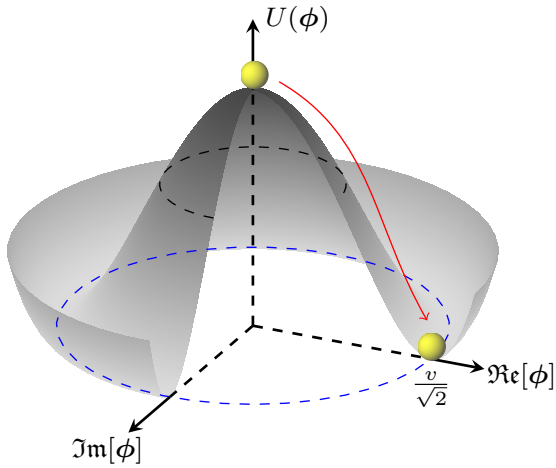

Figure 1.2 – The so called "mexican hat" potential $U(\boldsymbol{\phi})$ of Eq. (1.13). The dashed blue line corresponds to the potential minimum, described by Eq. (1.15). The Higgs boson acquires a vacuum expectation value different from zero in one of the infinite possible positions on this minimum. For simplicity, the vacuum chosen is $\boldsymbol{\phi}_0 \overset{\text{def}}{=} \frac{v}{\sqrt{2}}$.

Since we have the freedom of performing gauge transformations like in Eq. (1.14), it is possible to choose the one which eliminates the field χ

$$\boldsymbol{\phi} \to e^{-i\frac{\chi}{v}}\boldsymbol{\phi} = \frac{v+\phi}{\sqrt{2}} \qquad A_\mu \to A_\mu - \partial_\mu \frac{\chi}{v} \tag{1.22}$$

This is a particular choice of gauge called *unitary gauge*, where all the degrees of freedom of the theory are manifest and the resultant Lagrangian will be independent of χ. Since Eq. (1.16) is the lowest order expansion of Eq. (1.21), the terms from Eq. (1.17) to (1.19) remain the same, while the Goldstone boson terms will disappear. The apparent degree of freedom is therefore spurious, it represents the possibility to make a gauge transformation.

1.2.2 Higgs mechanism in the Standard Model

In the Standard Model, we need to give mass to all the fermions and to the gauge bosons of the weak interaction, $W^\pm$ and Z^0. The Higgs mechanism explained in the previous paragraph should be applied to the $SU(2)_L \times U(1)_Y$ local gauge group, while the $SU(3)_C$ part of the SM is left unchanged.

To give mass to $W^\pm$, the Higgs boson must couple to them. In order to generate this coupling, Higgs boson should be a weak isospin multiplet. The minimal model

introduces a doublet $\left(T_3 = \pm\frac{1}{2}\right)$ of complex scalar fields

$$\mathbf{\Phi} = \begin{pmatrix} \boldsymbol{\phi}^+ \\ \boldsymbol{\phi}^0 \end{pmatrix}. \tag{1.23}$$

Concerning the photon instead, since it should remain massless, the mechanism should not break the $U(1)_Q$ symmetry of the QED. Therefore, the Higgs should be a neutral particle. We must have $\mathbf{Q}\Phi = 0$, which implies $\mathbf{Y} = \pm\mathbf{1}$, recalling Eq. (1.3). We are free therefore to choose $\mathbf{Y} = \mathbf{1}$. This choice leads to

$$\mathbf{Q} = \begin{pmatrix} 1 & 0 \\ 0 & 0 \end{pmatrix} \quad \Rightarrow \quad \mathbf{\Phi} = \begin{pmatrix} 0 \\ \boldsymbol{\phi}^0 \end{pmatrix}. \tag{1.24}$$

The field $\mathbf{\Phi}$ has a Lagrangian similar to the one in Eq. (1.13)

$$\mathcal{L}_{\text{Higgs}} = \left(\mathcal{D}^\mu \mathbf{\Phi}\right)^\dagger \left(\mathcal{D}_\mu \mathbf{\Phi}\right) - \left[\lambda\left(\mathbf{\Phi}^\dagger \mathbf{\Phi}\right) - \mu^2 \mathbf{\Phi}^\dagger \mathbf{\Phi}\right] \tag{1.25}$$

where now the $\mathcal{D}_\mu$ is the one in Eq. (1.4), and the minimum of the potential is given by

$$|\mathbf{\Phi}_0|^2 = \frac{\mu^2}{2\lambda} \stackrel{\text{def}}{=} \frac{1}{2}v^2. \tag{1.26}$$

One could then choose the vacuum state in the unitary gauge to be like

$$\mathbf{\Phi} = \frac{1}{\sqrt{2}} \begin{pmatrix} 0 \\ v + \phi \end{pmatrix} \tag{1.27}$$

with the Higgs boson field ϕ being completely real. Now, substituting this parametrization on the field into Eq. (1.25) as was done in the previous section, it will create the mass and interaction terms for the weak gauge bosons. In particular, from the kinetic term in Eq. (1.25) and making use of relations from Eqs. (1.7) to (1.9), one will obtain

$$\begin{aligned} \left(\mathcal{D}^\mu \mathbf{\Phi}\right)^\dagger \left(\mathcal{D}_\mu \mathbf{\Phi}\right) = \frac{1}{2}\left(\partial_\mu \phi \partial^\mu \phi\right) + \\ + \left(\frac{gv}{2}\right)^2 W^+ W^- + \frac{1}{2}\left(\frac{gv}{2\cos\theta_W}\right)^2 Z^2 + \\ + \frac{g^2 v}{2}\phi W^+ W^- + \left(\frac{g}{2}\right)^2 \phi^2 W^+ W^- + \\ + \frac{1}{4}\frac{g^2 v}{\cos^2\theta_W}\phi Z^2 + \frac{1}{2}\left(\frac{g}{2\cos\theta_W}\right)^2 \phi^2 Z^2. \end{aligned} \tag{1.28}$$

The first term is the kinetic part of the Higgs boson Lagrangian, like in Eq. (1.18).

The second two are clearly the mass terms for $W^\pm$ and Z^0 bosons. The values of the masses are related to the weak coupling constant and the vacuum expectation value

with the relations

$$m_W = \frac{gv}{2} \qquad m_Z = \frac{gv}{2\cos\theta_W} = \frac{m_W}{\cos\theta_W}. \tag{1.29}$$

The last two couples of terms in Eq. (1.28) are instead the triple and quartic interactions of Higgs field with W and Z respectively. Rewriting them with the help of Eq. (1.29) makes clear that the couplings between the Higgs and the gauge bosons scales with the squared mass of the gauge boson:

$$\frac{m_W^2}{v^2}\left(2v\phi W^+W^- + \phi^2 W^+W^-\right) + \frac{1}{2}\frac{m_Z^2}{v^2}\left(2v\phi Z^2 + \phi^2 Z^2\right). \tag{1.30}$$

The potential in Eq. (1.25) brings instead to the very same mass and interaction terms that have been found in Eq. (1.18). So, a Higgs boson with mass $m_H = \sqrt{2}\mu = \sqrt{2\lambda}v$ is obtained along with triple and quartic self-interactions.

The Higgs boson field is able to provide mass for fermions too. Masses for fermions are forbidden in the theory because they mix left- and right-handed component, which behaves differently under weak interaction thus breaking the global gauge invariance. Making use of the Eq. (1.27) and his charge coniugate

$$\mathbf{\Phi}_C \overset{\text{def}}{=} -i\sigma_2\mathbf{\Phi}^* = \frac{1}{\sqrt{2}}\begin{pmatrix} v+\phi \\ 0 \end{pmatrix} \tag{1.31}$$

is it possible to introduce mass terms in the SM Lagrangian in a gauge invariant way thanks to a specific coupling (*Yukawa coupling*) between fermions and Higgs field. Indicating with u_L and d_L the up and down components of the isospin doublet and u_R, d_R their singlets,

$$\mathcal{L}_{Yukawa} = -g_u\begin{pmatrix} u_L^\dagger & d_L^\dagger \end{pmatrix}\mathbf{\Phi}_C u_R - g_d\begin{pmatrix} u_L^\dagger & d_L^\dagger \end{pmatrix}\mathbf{\Phi} d_R + h.c. \tag{1.32}$$

provides the fermion mass terms. Indeed, expanding with $\mathbf{\Phi}_{(C)}$, it is possible to generate the mass terms of the fermions $m_u u\bar{u}$ and $m_d d\bar{d}$ where:

$$m_{u,d} = \frac{v}{\sqrt{2}}g_{u,d} \tag{1.33}$$

and the Higgs-fermion interaction

$$\frac{m}{v}\phi\psi_L^\dagger\psi_R + h.c. \tag{1.34}$$

which scales linearly with the mass of the fermion. Therefore the Higgs boson couples the most with third generation fermions, namely top and bottom quarks and τ lepton.

1.3 Higgs boson phenomenology at hadron colliders

As shown in the previous section, the mass terms for fermions are generated "dynamically" through the interaction with the Higgs boson field. Moreover, the more a particle

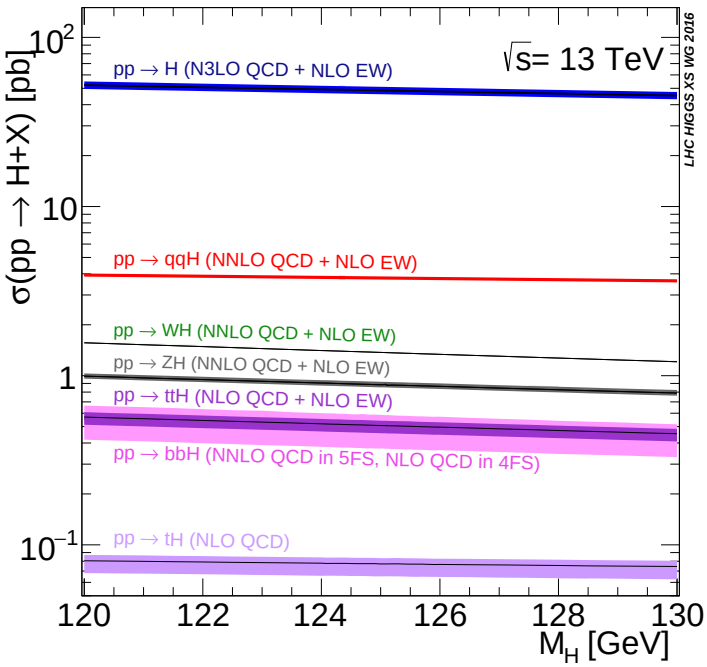

Figure 1.3 – Standard Model Higgs boson production cross sections in pp collisions at 13 TeV as a function of m_H. The line width represents the theoretical uncertainty [31].

is massive and the more the strength of the coupling to the Higgs boson is large: for bosons and fermions with mass m the coupling is proportional to m^2 and m respectively. For this reason, the Higgs boson production and decay processes are led by the couplings to the most massive particles in the Standard Model, namely weak gauge bosons and top quark; however, since most of the SM particles have mass, the Higgs boson phenomenology is very rich and complex. The production cross sections and decay branching ratios are computed as a function of the Higgs boson mass which is a free parameter in the SM and has to be experimentally determined.

1.3.1 Production processes

At the LHC, the proton proton collision could create Higgs bosons in a large variety of ways. The most common production mode is the gluon-gluon fusion process (ggF), followed by the vector boson fusion (VBF), the vector boson associated production (VH, hence WH and ZH), top pair associated production ($t\bar{t}H$), bottom pair associated production ($b\bar{b}H$) and single top associated production (tHW and tHq). The production cross sections of the Higgs boson vary with m_H and $\sqrt{s}$ and are shown in Figure 1.3, while the values for the Standard Model Higgs boson with $m_H = 125\,\text{GeV}$ and $\sqrt{s} = 13\,\text{TeV}$ are reported in Table 1.1.

In the ggF, two gluons are extracted from the two colliding protons and the coupling to the Higgs is provided by a quark loop, involving mainly top quarks due to

their high masses, while other light quarks q contributions are suppressed proportionally to $\left(m_q/m_t\right)^2$. The leading order Feynman diagram is reported in Figure 1.4a. At $\sqrt{s} = 13\,\text{TeV}$, this process accounts for about the 81% of the total Higgs boson production cross section for $m_H = 125\,\text{GeV}$. Precise theoretical QCD calculation of the production cross section at next-to-next-to-next-to-leading order (N^3LO) and EW at next-to-leading (NLO) performed in the limit $m_t \to \infty$ are available and the prediction [32] is

$$\sigma_{\text{ggF}}\left(m_H = 125\,\text{GeV}\right) = 48.58^{+2.22}_{-3.27}\,\text{pb (theo)} \pm 1.56\,\text{pb (PDF + } \alpha_S\text{)} \tag{1.35}$$

As shown in Figure 1.3, below 1 TeV the VBF is the second largest contribution to the total Higgs production at LHC ($\sim$ 10% at $m_H = 125\,\text{GeV}$). This process proceeds through the fusion of W or Z bosons emitted by two interacting quarks. The gauge bosons then fuse together to give a Higgs boson. The VBF has a clear signature since the quarks which emitted the bosons hadronize in two jets in the forward region of the detector, without other activity in between. The VBF diagram is reported in Figure 1.4b.

The next most relevant Higgs boson production mode at the LHC is the associated production with a gauge boson. This process is often called "Higgsstrahlung": an off-shell W or Z produced by quarks annihilation radiates a Higgs boson. The tree level Feynman diagram is shown in Figure 1.4c. ZH associated production is possible in an additional way, called ggZH: it starts from a pair of gluons which fuse together through a quark loop, which radiates a Z boson. This process could be considered separated by the main VH process since it has a smaller contribution and a different coupling order. The ggZH process is reported in Figure 1.4d and 1.4e. The VH processes are tagged by the final state particles produced by the W/Z bosons decay.

Finally, the $\text{b}\bar{\text{b}}\text{H}$, $\text{t}\bar{\text{t}}\text{H}$ and tH production modes are the ones with the lowest cross sections. These processes are of great interest because they provide direct information on the Yukawa coupling between fermions and Higgs although they are experimentally challenging due to the very small cross section. The leading order Feynman diagrams are shown from Figure 1.4f to 1.4l.

1.3.2 Decay processes

As outlined above, the Higgs boson decay features a very rich phenomenology. The Higgs boson could decay in many different fermionic and bosonic final states, therefore its phase space is wide and the expected lifetime is small.

The branching ratio of any single possible final state i is defined as the ratio between the relative partial decay width for that final state over the total width, which is defined as the sum of the relative widths of all the possible Higgs boson decay modes:

$$BR\left(H \to X_i\right) = \frac{\Gamma\left(H \to X_i\right)}{\sum_j \Gamma\left(H \to X_j\right)}$$

The branching ratio and the total decay width for a Standard Model Higgs boson are shown in Figure 1.5 while Table 1.2 shows the branching ratios for the various decay

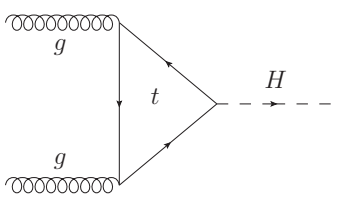

(a) Gluon-Gluon fusion, ggF

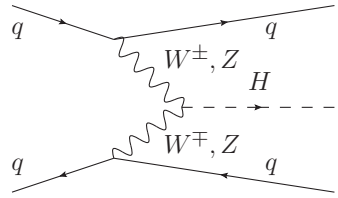

(b) Vector Boson Fusion, VBF

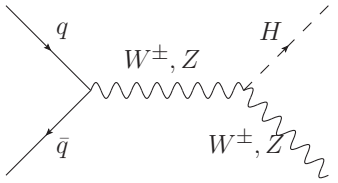

(c) W or Z boson associate production, WH ZH

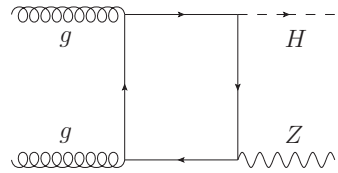

(d) Gluon iniziated ZH, ggZH

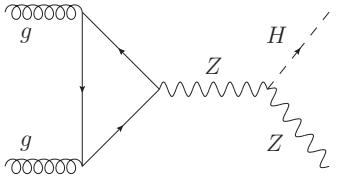

(e) Gluon iniziated ZH, ggZH

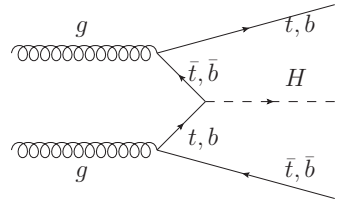

(f) Top and bottom pair associated production, $t\bar{t}H$ $b\bar{b}H$

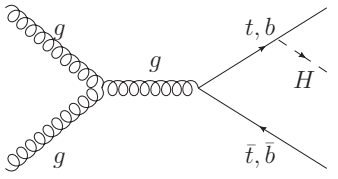

(g) Top and bottom pair associated production, $t\bar{t}H$ $b\bar{b}H$

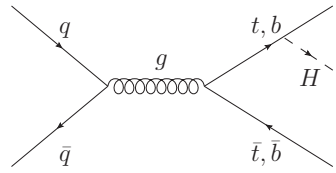

(h) Top and bottom pair associated production, $t\bar{t}H$ $b\bar{b}H$

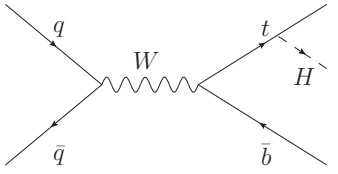

(i) Top associated production, tHq (s-channel)

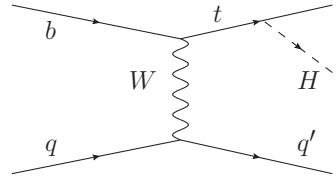

(j) Top associated production, tHq (t-channel)

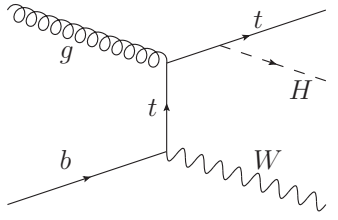

(k) W boson associated production, tHW

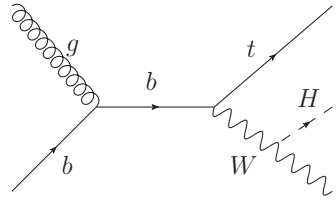

(l) W boson associated production, tHW

Figure 1.4 – Leading order Feynman diagrams for Higgs boson production at LHC.

Production mode	Cross section [pb]	Scale [%]	PDF + α_S [%]
ggF	48.58	$^{+4.56}_{-6.72}$	3.19
VBF	3.797	$^{+0.4}_{-0.3}$	2.1
WH	1.3728	$^{+0.5}_{-0.7}$	1.1
ZH	0.7612	$^{+3.9}_{-3.0}$	1.6
ggZH	0.1226	$^{+3.9}_{-3.0}$	1.6
$t\bar{t}H$	0.5071	$^{+5.8}_{-9.2}$	3.6
$b\bar{b}H$	0.4880		$^{+20.2}_{-23.9}$
tHq (t-chan)	7.425×10^{-2}	$^{+6.5}_{-14.9}$	3.7
tHq (s-chan)	2.879×10^{-3}	$^{+2.4}_{-1.8}$	2.2
tHW	1.517×10^{-2}	$^{+4.9}_{-6.7}$	6.3

Table 1.1 – Standard Model production cross sections [31] for a Higgs boson of $m_H = 125\,\text{GeV}$ in pp collision at $\sqrt{s} = 13\,\text{TeV}$. Their relative theoretical uncertainties on QCD scale and PDF + α_S are reported. For $b\bar{b}H$, only the total uncertainty is provided.

channels for a Higgs boson with $m_H = 125\,\text{GeV}$. As it can be observed, the decay phenomenology highly depends on the Higgs boson mass.

For a light Higgs boson, with mass $m_H < 160\,\text{GeV}$, the Higgs boson decays mostly into $b\bar{b}$ pairs. Unfortunately, at a hadron collider, the high rate of jets production from QCD dominates this kind of signature, hence lowering the experimental sensitivity of this channel. Indeed this decay mode is typically used to target particular production modes like VH and $t\bar{t}H$ where additional final state particles that can be used to identify the events are produced. In this m_H range, two "golden channels" are present.

The first is represented by the $H \to ZZ^* \to 4\ell$ decay process, with ℓ being electrons or muons: this channel has a very clear signature, excellent mass resolution and it features almost no background. Asking a full leptonic decay in the ZZ^* and WW^* channels lowers their branching ratio by a factor of ~ 100, thus limiting the statistical power of these channels.

The second golden channel for Higgs studies in the low mass range is the $H \to \gamma\gamma$. The branching ratio (see Table 1.2) is very small because photons, being massless, couple to the Higgs boson only through a loop involving either W bosons or top quarks, as shown in the leading order Feynman diagrams in Figure 1.6, and the two diagrams are even in destructive interference among themselves. However, this decay is extremely interesting because its strength is sensitive to scales far beyond the Higgs boson mass: indeed, new and unknown massive particles could take part in the loop, therefore changing the rate of expected events. Moreover this channel has a very good mass resolution but an excellent detector performance is needed to reduce the rate of background events coming from $j \to \gamma$ fakes.

For m_H above 160 GeV, decays to weak vector boson open up because both boson can be produced on-shell. The WW decay mode start dominating over $b\bar{b}$ while the $H \to ZZ \to 4\ell$ become the only golden channel, with high BR in particular above 190 GeV.

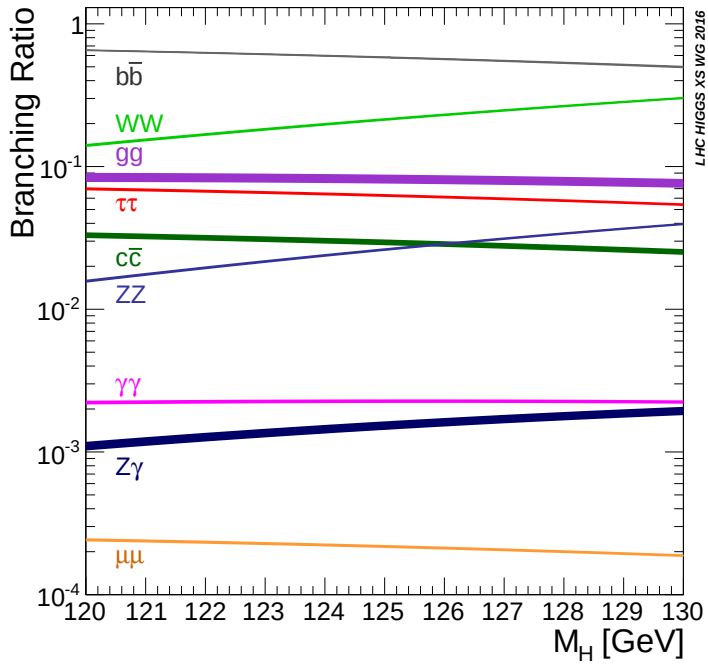

(a)

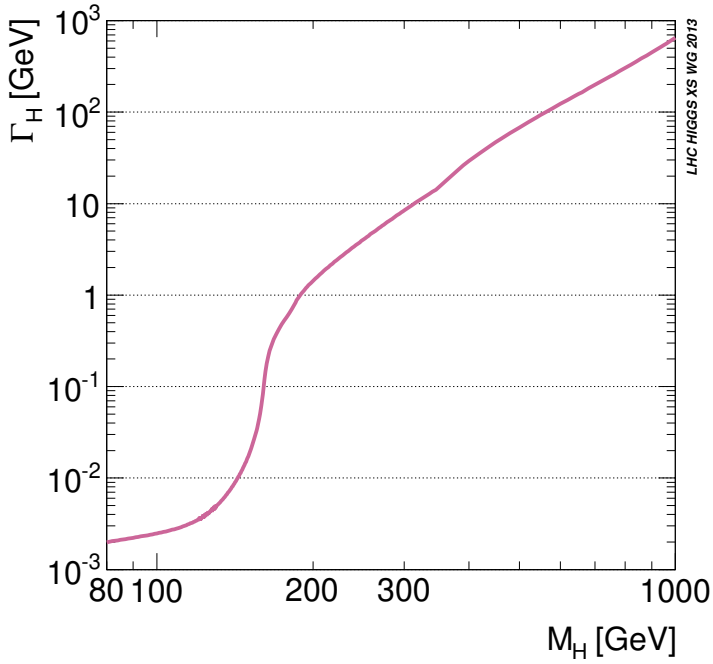

(b)

Figure 1.5 – Standard Model Higgs boson branching ratios (a) and total decay width (b) as a function of m_H for different decay processes [31]. The line width represents the theoretical uncertainty.

Decay Channel	Branching ratio	Rel. Uncert [%]
$H \to b\bar{b}$	0.5824	$^{+1.7}_{-1.7}$
$H \to WW^*$	0.2137	$^{+2.2}_{-2.2}$
$H \to \tau\bar{\tau}$	0.062 72	$^{+2.3}_{-2.3}$
$H \to c\bar{c}$	0.028 91	$^{+6.6}_{-2.8}$
$H \to ZZ^*$	0.026 19	$^{+2.2}_{-2.2}$
$H \to \gamma\gamma$	2.273×10^{-3}	$^{+2.8}_{-2.9}$
$H \to Z\gamma$	1.533×10^{-3}	$^{+6.8}_{-6.9}$
$H \to \mu\bar{\mu}$	2.176×10^{-4}	$^{+2.4}_{-2.4}$

Table 1.2 – Higgs decay branching ratios with their relative theoretical uncertainty for $m_H = 125\,\text{GeV}$ [31]

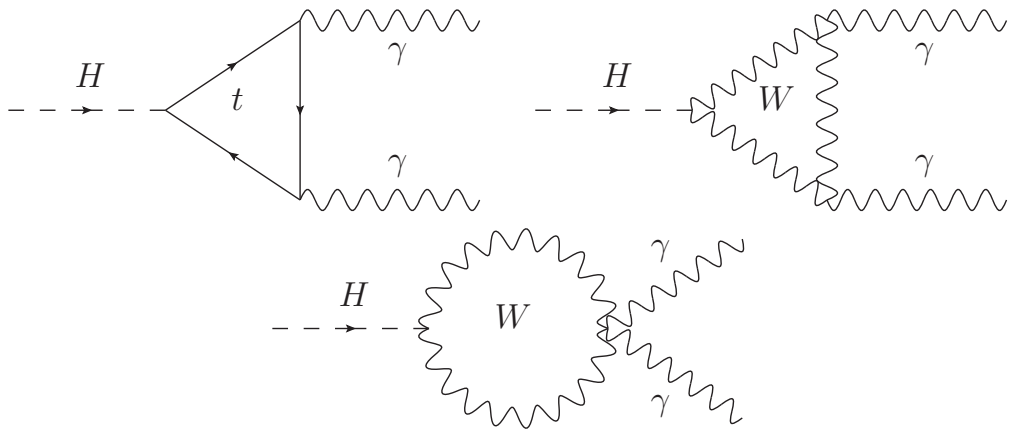

Figure 1.6 – Leading order Feynman diagrams for $H \to \gamma\gamma$ decay. The top mediated and W mediated graphs interfere destructively, therefore lowering the branching ratio of this channel. For $m_H = 650\,\text{GeV}$ the cancellation is total.

1.4 Higgs Boson discovery and property measurements at LHC

During 2012, on the 4th of July, ATLAS and CMS experiments in a joint press conference claimed the discovery of a new particle, compatible with the Standard Model Higgs boson, with a mass around 125 GeV. The two collaborations made use of the partial Run 1 dataset, produced by the LHC during 2010-2012 and corresponding to $\sim$5 fb^{-1} at $\sqrt{s} = 7$ TeV plus $\sim$6 fb^{-1} at $\sqrt{s} = 8$ TeV. The results were obtained combining different decay channels, where the largest contribution to the discovery was given by the $H \to \gamma\gamma$ and $H \to ZZ$ processes. The plots in Figure 1.7 shows the local significance for the background only hypothesis as a function of the Higgs mass for the ATLAS [4] and CMS [5] experiments. Furthermore, the collaborations excluded any other possible Higgs boson with mass up to 600 GeV. The collaborations started then to analyse the data trying to establish the properties and quantum numbers of this new particle, such as the precise mass, the production cross section and the spin/parity. The results presented in the following paragraphs are extracted with the full statistic of the Run 1 data taking, amounting to 4.5 fb^{-1} at $\sqrt{s} = 7$ TeV plus 20.3 fb^{-1} at $\sqrt{s} = 8$ TeV.

1.4.1 Higgs boson mass

The Higgs boson mass was one of the first property to be addressed. The measurements is mainly based on the $H \to \gamma\gamma$ and $H \to ZZ$ channel, as the energy and direction of photons, electrons and muons are measured very precisely by ATLAS and CMS, leading to a 1-2% resolution on the Higgs signal. With this excellent resolution, the Higgs boson manifests itself as a narrow peak on top of a continuous non-resonant background, composed mainly by the QCD production of $\gamma\gamma$ or ZZ pairs respectively for the two channels, as shown in Figure 1.8. Higgs boson in other decay channels reported in Table 1.2 can be reconstructed with a much worse mass resolution, ranging between 15% and 20%, therefore are not so sensitive to the peak position. The Higgs boson width instead is not directly accessible, since the detector resolution is much larger than the intrinsic Higgs width.

To improve the accuracy of the mass measurement, the selected events are separated in mutually exclusive categories that have different Higgs signal purities, different invariant mass resolutions and different source of systematic uncertainties. The combined Higgs mass value based on ATLAS and CMS results [33] is

$$m_H = 125.09 \pm 0.21\ (\text{stat}) \pm 0.11\ (\text{syst})\ \text{GeV} \tag{1.36}$$

with the full breakdown of the various analyses and combinations reported in Figure 1.9.

1.4.2 Higgs boson production cross sections and decay rates

Other important quantities to be measured are the production cross sections and the decay rates of the new particles. Given a measured mass of the Higgs, no more free parameters are present in the Standard Model and therefore the couplings are fixed. The

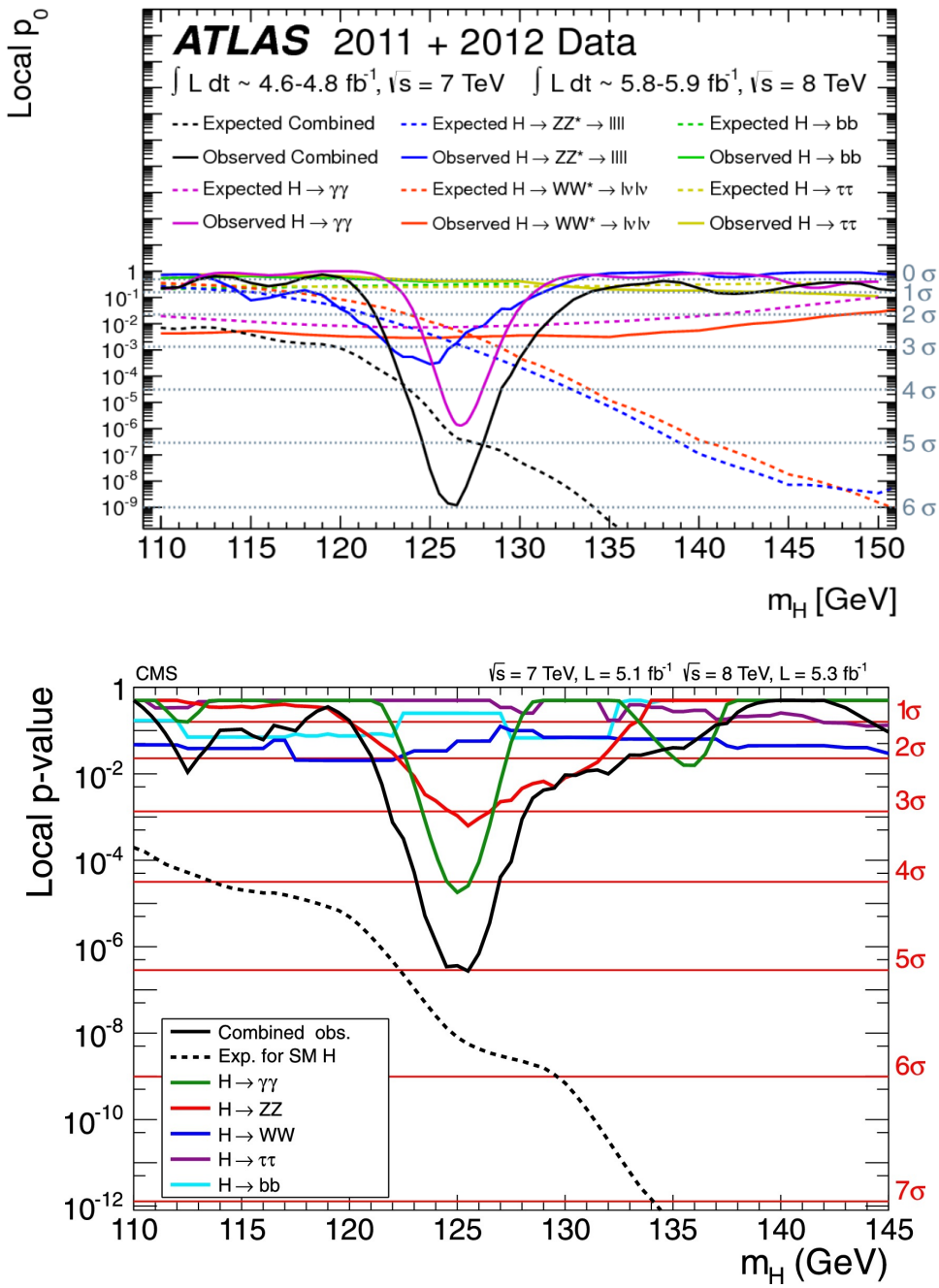

Figure 1.7 – The expected and observed local p-value p_0 measured by ATLAS (upper plot) and CMS (lower plot) experiments for the background only hypothesis, for each individual channels present in the combination. The solid black lines represent the combined result. Horizontal lines link p_0 values to the corresponding significance.

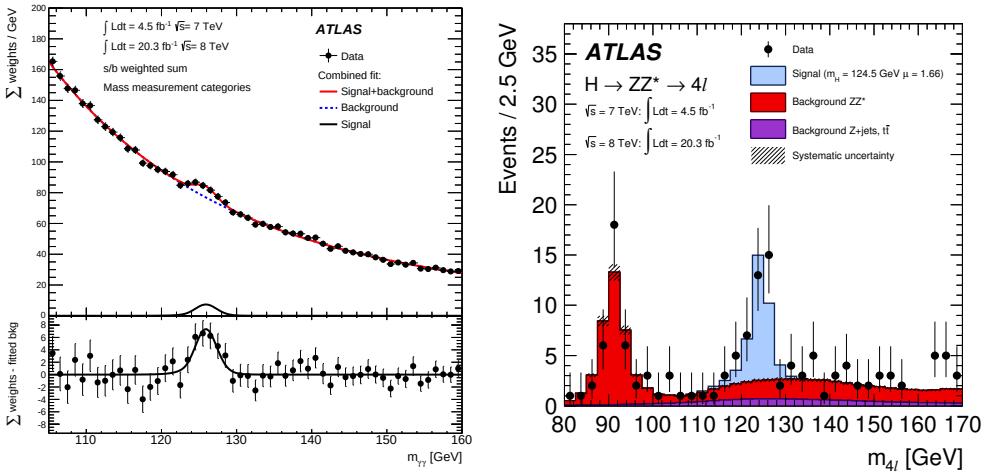

(a) $H \to \gamma\gamma$ **(b)** $H \to ZZ^* \to 4\ell$

Figure 1.8 – Invariant mass spectra for the diphoton (a) and four leptons (b) channels for the full Run 1 dataset collected by the ATLAS experiment [34], with the result of the simultaneous fit over analysis categories. On (a), data are weighted by the signal over background ratio of the category they fall into. The narrow Higgs mass peak is easily visible over the non resonant background.

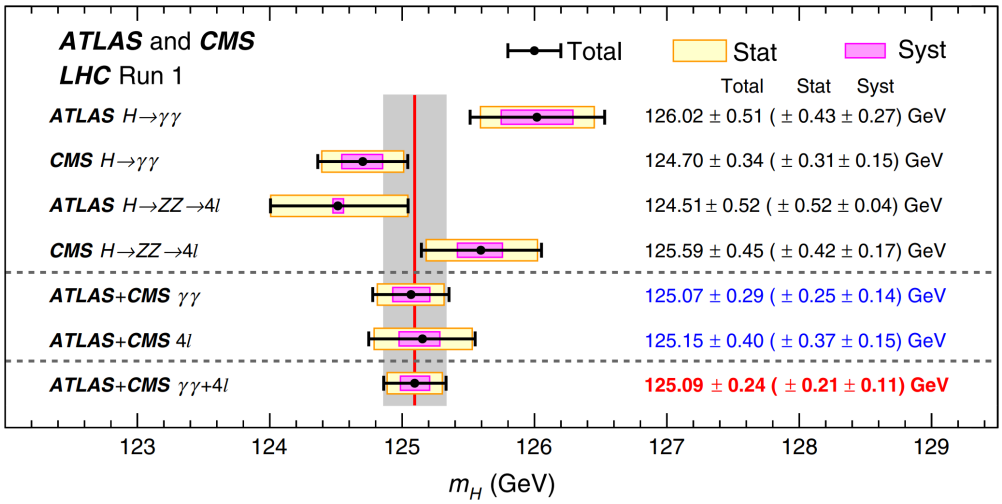

Figure 1.9 – Summary of Higgs boson mass measurements from the individual analyses of ATLAS and CMS and from the combined analysis. The systematic (narrower, magenta-shaded bands), statistical (wider, yellow-shaded bands), and total (black error bars) uncertainties are indicated. The (red) vertical line and corresponding (gray) shaded column indicate the central value and the total uncertainty of the combined measurement, respectively [33].

ATLAS and CMS collaborations measured the production and decay rates using the full Run 1 dataset [35].

The main production channels used for the measurement are ggF, VBF, VH and $t\bar{t}H$. They were studied with different analyses, each one dedicated to a certain final state: in particular $H \to \gamma\gamma$, $H \to ZZ$, $H \to WW$, $H \to \tau\bar{\tau}$ and $H \to b\bar{b}$ were considered in the combination. Each of these analyses performed an event categorization, optimized to increase the signal over background ratio for a particular production mode. Indeed, the Higgs boson production could be tagged by the specific final states, each with their particles and kinematics.

The combination of the ATLAS and CMS results is performed through a global fit to over 600 categories, that are used in the individual analyses to improve the sensitivity and to discriminate among different production process.

The parameter to be measured is the *signal strength* indicated by μ. It is a cross section or branching ratio modifier, defined as

$$\sigma_{\text{meas}} = \mu_p \cdot \sigma_{\text{SM}} \qquad \text{BR}_{\text{meas}} = \mu_d \cdot \text{BR}_{\text{SM}} \tag{1.37}$$

which is by definition equal to one in the Standard Model hypothesis.

The number of signal events for a given analysis category c which targets a process p with decay d is given by

$$s^c_{pd} = L \cdot \mu_p \sigma_{SM} \cdot \mu_d \text{BR}_{\text{SM}} \cdot \mathcal{A}_{pd} \cdot \epsilon^c_{pd} \tag{1.38}$$

where L is the integrated luminosity (see Section 2.1.3), p and d span all the possible Higgs production and decay processes, $\mathcal{A}_{pd}$ is the detector acceptance and ϵ^c_{pd} the selection efficiency.

From the above equation, it is clear that only the product $\mu_{pd} \overset{\text{def}}{=} \mu_p \cdot \mu_d$ could be measured with data if no assumptions are made on their ratio. The simplest hypothesis ATLAS and CMS tested is to assume that all the modifiers are equal, $\mu_{pd} \equiv \mu$, providing a global data normalization to be compared to the Standard Model prediction. The best fit value obtained combining ATLAS and CMS for $m_H = 125.09\,\text{GeV}$ was

$$\mu = 1.09^{+0.11}_{-0.10} = 1.09^{+0.07}_{-0.07}\,(\text{stat})^{+0.04}_{-0.04}\,(\text{syst})^{+0.03}_{-0.03}\,(\text{thbgd})^{+0.07}_{-0.06}\,(\text{thsig}) \tag{1.39}$$

where thbgd and thsig indicate the theory uncertainties on background and signal, stat indicates the statistic uncertainty and syst collects the contributions of all the experimental systematic uncertainties. The result was consistent with the SM hypothesis $\mu = 1$ within 1σ and the p-value of the compatibility between data and SM was 40%. A global measurement is constrained by the ratios among production and decay processes in the sense that an internal compensation among different parameters could not be visible. A less constrained test is assuming the SM ratios for the decay process and simultaneously fit the production mode, or vice-versa. The results of these two tests are shown in Figure 1.10.

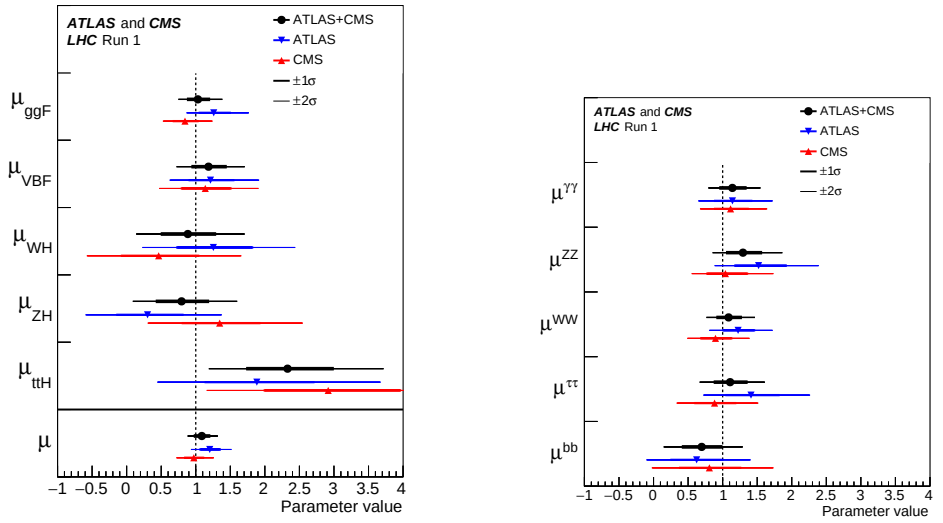

Figure 1.10 – On the left, best fit signal strength values with 1 and 2σ error bands for global and five production modes once Standard Model branching ratios are assumed. On the right, the same plot for modifiers on the branching ratios are shown, assuming Standard Model production cross sections [35].

1.4.3 Higgs boson spin, parity and charge conjugation measurements

The Standard Model Higgs boson in the minimal model described in Section 1.2.2 is a neutral scalar particle and it is predicted to have spin (J), parity (P) and charge conjugation (C) of the form $J^{CP} = 0^{++}$.

The charge conjugation is easily addressed: since the photons are C-odd eigenstates ($C = -1$) and the charge conjugation is multiplicative, a particle decaying in a pair of γ must have $C = 1$. As the $H \to \gamma\gamma$ decay was observed, the Higgs boson is a $C = 1$ particle.

Spin and parity measurements are more demanding. Starting from the spin, the Landau-Yang theorem [36, 37] states that a massive spin-1 particles could not decay into a pair of photons. Therefore, following the spin composition rules, a particles decaying in two photons must be only a spin 0 or spin 2 boson. To discriminate between the two hypotheses, mainly the $H \to \gamma\gamma$ decay process is exploited, along with the $H \to ZZ^* \to 4\ell$ and the $H \to WW^* \to e\nu\mu\nu$. A spin 0 particle decays isotropically while spin a 2 doesn't, therefore an inference could be made testing the angular distribution of the final states particles. For example the angle between the two photons in the Collins–Soper frame [38] is sensitive to the spin of the decaying particle as shown in Figure 1.11a. The $H \to 4\ell$ analysis is instead more powerful in discerning the parity of the decaying boson. Indeed, the precise reconstruction of the full final state topology for each event, sketched on Figure 1.11b, gives access to the polarization of the decaying boson and of the Z bosons. Five angles are used to discriminate between different J^P hypothesis. The results of these studies for both ATLAS [39] and CMS [40] showed that data favours the $J^P = 0^+$ hypothesis and rejects all alternative hypotheses at more than

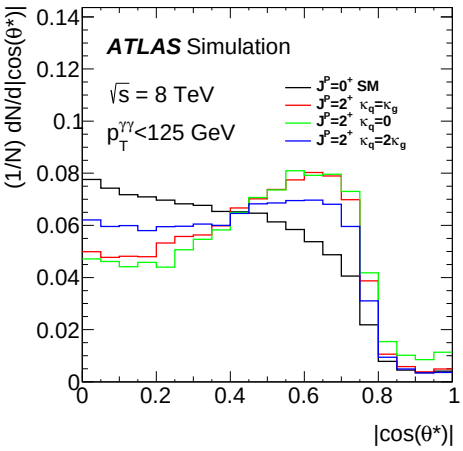

(a)

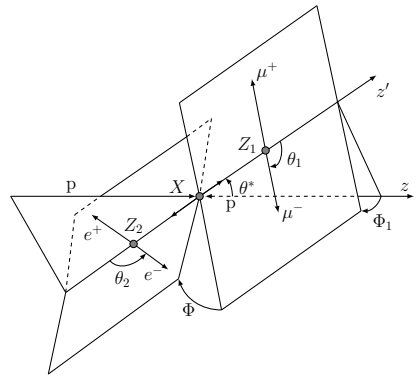

(b)

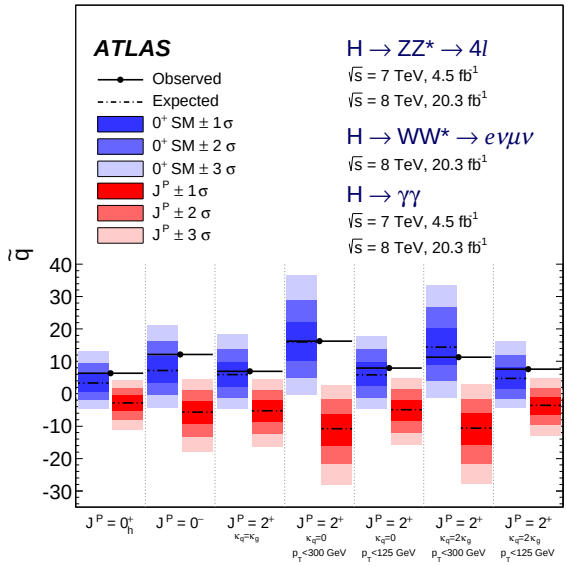

(c)

Figure 1.11 – (a) Production angle of the two photons in the Collins–Soper frame $|\cos\theta^*|$, for a SM Higgs boson and for spin-2 particles with three different choices of the QCD couplings to quark and gluon. (b) Full decay topology of a $H \to ZZ^* \to 2e2\mu$ event and definitions of the five angles. (c) Test statistics distribution and observed value (solid black line) for the Standard Model (blue) and alternate J^P hypothesis (red), combining three decay channels.

99.9% confidence level. The test statistic results of ATLAS are reported in Figure 1.11c and they show a good agreement with the Standard Model hypothesis.

CHAPTER 2

The Large Hadron Collider and the ATLAS experiment

The analyses presented in this manuscript are based on the data collected during the Run 2 of *Large Hadron Collider* (LHC) and recorded by the ATLAS experiment. In this chapter I will describe the experimental setup and the data taking conditions, starting from the LHC machine main features and concluding with the ATLAS detector details.

2.1 The Large Hadron Collider

The Large Hadron Collider [2] is the largest and most powerful particle accelerator ever built. It is a circular ring which spans a 27 km circumference, located underground between 50 m and 175 m and straddling Swiss and French borders. The LHC is designed to collide two counter-rotating beams of protons or heavy ions at high energy and high luminosity, producing particles interactions of physical interest.

2.1.1 Interactions in hadron collisions

The LHC was conceived as the natural step forward of the *Large Electron Positron* collider (LEP), built in the same 27 km tunnel and operating from 1989 to 2000. The LEP collider was designed to be a W and Z bosons factory, used to measure with high precisions the details of the electroweak interaction: collisions of electrons and positrons were produced with a center-of-mass energy around m_Z value and then around $2m_W$, therefore producing resonantly weak gauge bosons with almost no remaining activity.

In contrast, LHC is a discovery machine, since the hadron collisions permit to explore interactions in a wide range of transferred momentum between the colliding partons and overcome the high energy loss experienced by accelerated leptons, a major problem of a circular lepton collider like LEP. Indeed, the rate of synchrotron radiation emitted by an accelerated charged particle to the beam energy E of mass m scales as $\gamma^4 = (E/m)^4$, therefore lighter particles suffer from higher energy loss: in particular, for the same beam energy the energy loss is a factor $\left(m_p/m_e\right)^4 \sim 10^{13}$ larger for e than for p, restricting the center-of-mass energy that can be reached.

The LHC overcomes the problem accelerating protons and therefore the main limiting factor becomes the magnetic field used to bend the beams. On the other hand, the principal drawback of colliding protons is their compositeness. The quark and gluons composing the proton carry only a fraction of the total proton momentum and can

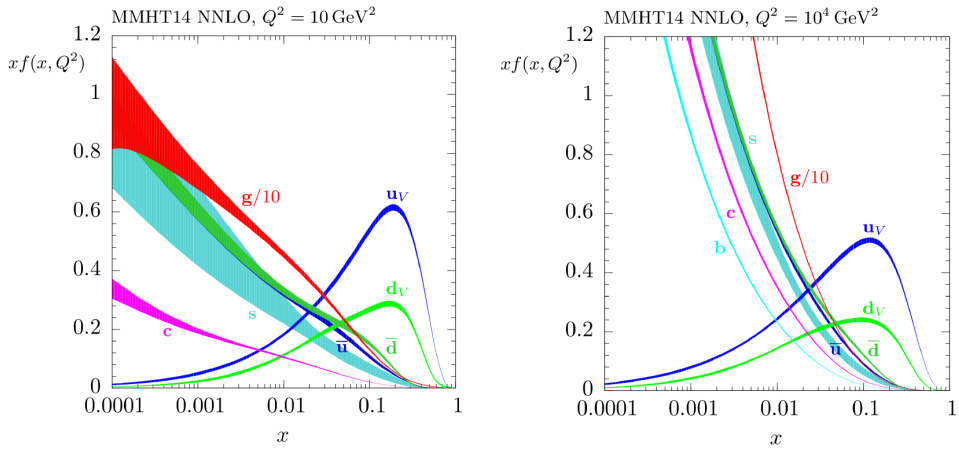

Figure 2.1 – Parton distribution functions from MMHT14 PDF set [41], at values two different values of the evolution scale $Q^2 = 10\,\mathrm{GeV}^2$ and $Q^2 = 10^4\,\mathrm{GeV}^2$. The gluon PDF is dominating at low value of x.

produce two different types of collisions, called hard and soft collisions depending on the momentum transferred: the first contain the processes of physical interest while the second is usually considered as the main background in a hadronic collider.

Hard collisions are rare events in which high momentum is transferred between two partons of the incoming protons. The real center-of-mass energy depends on the fraction of the momentum carried by the two partons, which is lower than the pp center-of-mass energy. In particular, proton constituents and their momenta are described by Parton Distribution Functions (PDFs), with an example shown in Figure 2.1. The x value represents the fraction of the proton momentum carried by the colliding parton, and it is called Björken variable. The partonic center-of-mass energy $\sqrt{\hat{s}}$ is given therefore by

$$\sqrt{\hat{s}} = \sqrt{x_a x_b s}$$

where x_i are the fraction of the momentum carried by the parton i with respect to the proton, while the cross section for a $pp \to X$ process is given by

$$\sigma_{pp\to X} = \sum_{a,b} \int dx_a dx_b f_a\left(x_a, Q^2\right) f_b\left(x_b, Q^2\right) \hat{\sigma}_{ab\to X}\left(x_a, x_b\right)$$

where $\hat{\sigma}_{ab\to X}$ represents the partonic cross section, while $f_i\left(x_i, Q^2\right)$ the probability to extract a parton i from the proton with a x_i momentum fraction at the scale Q^2. Since the two x_i are usually different, one of the main drawback of the hadron collider is that the partonic center-of-mass is boosted in an unknown direction. The second main draw back is that the proton remnants after parton extraction are responsible for the so called underlying events (UE), which is dominated by soft interactions where the perturbative QCD is not applicable. These UEs belong to the realm of soft collisions along side long

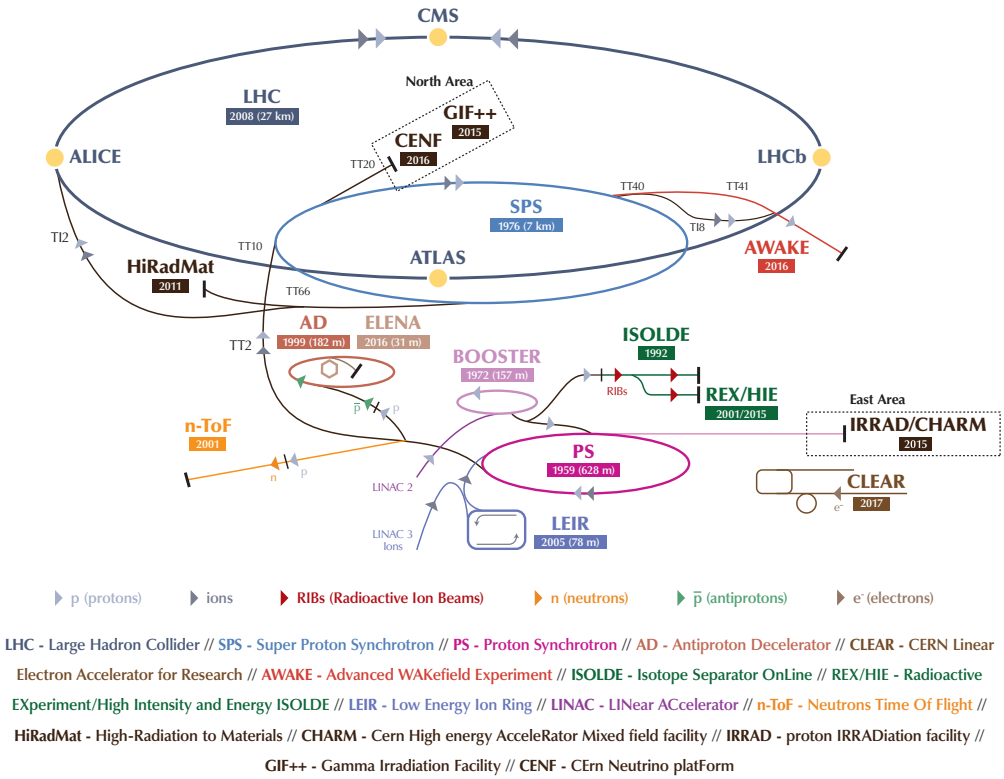

Figure 2.2 – CERN accelerators complex [42]. The LHC is the last ring (dark blue line) in a complex chain of particle accelerators. The smaller machines are used in a chain to help boost the particles to their final energies and provide beams to a whole set of smaller experiments. The Linac3 and LEIR facilities are employed to accelerate lead ions.

range interactions among protons with low momentum transferred. Soft collisions are the main source of background in a hadron collider, creating a busy and dense environment where distinguish and accurately reconstruct the interesting hard interaction becomes a challenge.

2.1.2 Design and experimental conditions

The LHC is the last of a series of accelerators built over the time at CERN. Each machine injects the beam into the next one, which takes over to bring the beam to an increasingly higher energy. Each of them has a role in tuning the beams parameters too. An overview of the CERN accelerator complex is shown in Figure 2.2 where it is shown that the main LHC chain is composed by five accelerators. The Linac2, which speeds up protons up to 50 MeV, the Booster, which brings beams energy to 1.4 GeV, and the Proton Synchrotron (PS), which brings protons to 25 GeV, form all together the so-called PS complex [45]. This chain supplies the Super Proton Synchrotron (SPS) [46] with protons, allowing them to reach 450 GeV energy before being injected in the LHC, where final acceleration to

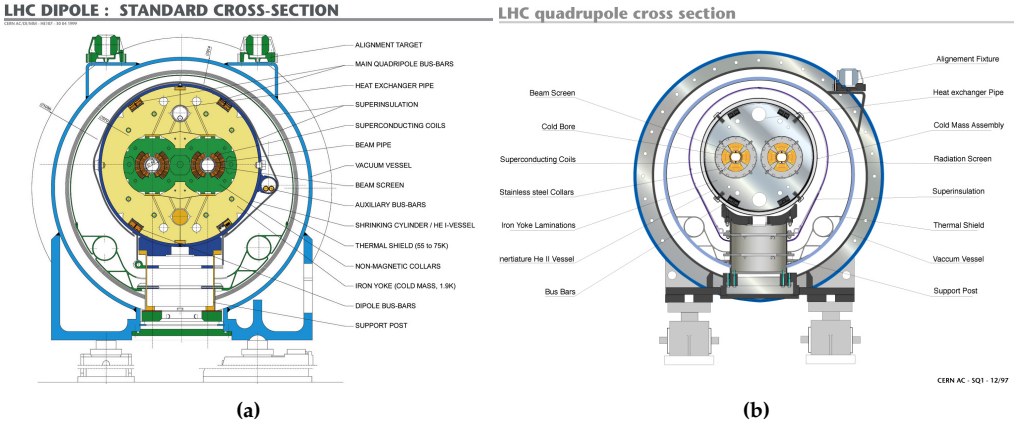

(a) (b)

Figure 2.3 – Cross sections of a LHC dipole (a) [43] and quadrupole (b) [44] showing the twin-bore magnet design with all the support elements.

6.5 TeV per beam and collisions are carried out.

Contrary to $p\bar{p}$ interactions, two separated beam rings are needed in order to produce pp interactions. The hard limit on the space of the existing LEP cavern led to the adoption of the twin-bore magnet design, where the two beam pipes permeated with opposite magnetic dipole fields are contained within the same mechanical structure and cryostat, as shown in Figure 2.3. The main disadvantages of this choice are that the rings are magnetically coupled, which adversely affects flexibility, and that two different vacua are needed. The two beams share an approximately 130 m long common beam pipe along the interaction regions.

The LHC has eight arcs and eight straight sections. Each straight section is approximately 528 m long and can serve as an experimental or utility insertion. The injection kick occurs in the vertical plane with the two beams arriving at the LHC from below the LHC reference plane. The beams cross from one magnet bore to the other at the four interaction regions.

The collider is composed mainly from 1232 superconducting Niobium - Titanium dipoles magnets, each of them producing an 8.33 T magnetic field used to bend the particles. To obtain their superconducting state, dipoles are cooled down to 1.9 K, a temperature colder than outer space, by means of a constant liquid Helium flow. Beams optic is further corrected by several types of magnets installed on the LHC ring: quadrupoles, sextupoles, octapoles and decapoles are used to focus the beams, to correct for non linear and chromatic effects, and to counteract other interactions which each beam suffers such as gravitational interactions over protons, electromagnetic interactions among bunches, electron clouds from the pipe wall among others. These corrections are needed to maintain beams stability over the time. There are, in addition, eight sets of so called "inner triplet" magnets in the LHC: their role is to focus the particle beams into the four areas where particles collide and detectors like ATLAS observe the products of these collisions. The nominal transverse size of the bunches is 0.2 mm and is squeezed down to 16 µm by the triplets at the interaction points.

The acceleration is performed through the passage of particles in *Radio Frequency* (RF) cavities: they generate a longitudinal oscillating voltage, which is applied across an isolated gap in the vacuum chamber, so that the particle sees an accelerating voltage at the gap. If the proton is synchronized with the RF frequency it will be accelerated, otherwise decelerated. Therefore, particles are grouped in structures called "bunches".

The LHC is designed to collide two beams made of up to 2808 bunches, each of them composed of $\sim 10^{11}$ protons and colliding with another every 25 ns. The designed center-of-mass energy of LHC for each pp collision is 14 TeV, although the energy set for the Run 2 data taking period, referring to the years from 2015 to 2018, was 13 TeV. The beam energy will be further increased to 13.6 TeV during the Run 3 period, from 2022 to 2025. A summary of beam and LHC parameters during the Run 2 is given in Table 2.1.

Parameter	Design	2015	2016	2017	2018
Energy [TeV]	7.0	6.5	6.5	6.5	6.5
Revolution frequency ν [kHz]	11.2	11.2	11.2	11.2	11.2
Number of bunches	2808	2244	2220	2556 - 1868	2556
Bunch population, N_b [10^{11} p]	1.15	1.2	1.25	1.25	1.1
β^* [cm]	55	80	40	$40 \rightarrow 30$	$30 \rightarrow 27 \rightarrow 25$
Normalized emittance [µm rad]	3.75	2.6 - 3.5	1.8 - 2	1.8 - 2.2	1.8 - 2.2
Crossing angle θ_c [µrad]	285	370	$370 \rightarrow 280$	$300 \rightarrow 240$	$320 \rightarrow 260$
RMS bunch length σ_z [cm]	7.55	9	9	8	8
Relativistic γ_r for the proton	7462	6929	6929	6929	6929
Geometric luminosity loss F [%]	84	84	65	72	61
Peak luminosity [10^{34} cm^{-2} s^{-1}]	1.0	< 0.6	1.5	2.0	2.1
Max. stored energy [MJ]	362	280	280	315	312

Table 2.1 – Summary of beam and machine parameters during the four years of Run 2, compared to the design values [47–49].

2.1.3 Luminosity and pileup

The numbers reported in Table 2.1 are of great interest from the physics point of view because they concur to define an important quantity called luminosity. Indeed, for a certain process with cross section σ_p, the number of events, N_p, produced by the colliding machine in the time unit is given by

$$\frac{dN_p}{dt} = \mathcal{L} \cdot \sigma_p \tag{2.1}$$

where $\mathcal{L}$ is what is called *instantaneous luminosity* and it is a quantity that can be described in terms of machine parameters:

$$\mathcal{L} = \frac{N_b^2 \, n_b \, \nu \, \gamma_r \, F}{4\pi \, \epsilon_n \, \beta^*} \tag{2.2}$$

where N_b is the number of protons per bunch, n_b the number of bunches per beam, ν the revolution frequency, γ_r the relativistic gamma factor of the proton, ϵ_n the transverse

normalized beam emittance, β^* is the focusing function at the collision point and F a geometric luminosity reduction factor due to the crossing angle at the interaction point (always lower than 1). This reduction factor can be computed as

$$F \simeq \left(\sqrt{1 + \left(\frac{\theta_c \cdot \sigma_z}{2\sigma} \right)^2} \right)^{-1} \tag{2.3}$$

where $\sigma = \sqrt{\epsilon_n \beta^* / \gamma_r}$ is the RMS transverse beam size, in case of rounded beam.

During Run 2, the LHC was capable of operating at at an instantaneous luminosity of $2.1 \times 10^{34}\,\mathrm{cm}^{-2}\,\mathrm{s}^{-1}$, a factor of two higher than the designed value.

The instantaneous luminosity could be integrated in the time, resulting in the *integrated luminosity* (L) which is measured using the inverse "barn"[1], b^{-1}. This quantity defines the size of a dataset and is needed to calculate the number of expected events from a given process with a cross section value σ_p; just integrating the Eq. (2.1)

$$N_p = L \cdot \sigma_p \tag{2.4}$$

The luminosity in the LHC is not constant but decreases with time due to the degradation of the intensity and of the emittance of the circulating beams. The time available for data taking with stable beams in the LHC is optimized considering the beam luminosity degradation and the amount of time taken by the accelerator chain to provide a new beam for data taking. The main cause of the luminosity decay at the LHC are the pp collision themselves in the LHC interaction points. The behaviour of the luminosity as a function of time is given by

$$\mathcal{L}(t) = \frac{\mathcal{L}_i}{(1 + t/\tau)^2} \quad \text{with} \quad \tau = \frac{N_{tot,0}}{k \cdot \sigma_{pp} \cdot \mathcal{L}_i} \tag{2.5}$$

where $\mathcal{L}_i$ is the initial luminosity, $N_{tot,0}$ the initial beam intensity, σ_{pp} the inclusive pp cross section and k the number of interaction points, which is 4 at the LHC.

2.2 The ATLAS detector

The ATLAS detector (*A Toroidal LHC ApparatuS*) [1] is one of the two general purpose experiments built on the interaction points of the LHC. Its physics programme is very broad: the detector was designed to precisely measure the fundamental parameters of the Standard Model, disclose the Higgs sector and test Beyond SM theories, like SuperSymmetry and Extra Dimensions models. Almost 6000 people, half of which are collaboration authors, work together to accomplish this programme.

ATLAS weights nearly 7000 t and is enclosed in a cylindrical 44 m-long shape with a radius of 12 m. It has an onion-like structure where multiple and different sub-detectors

[1] The barn (b) is a derived unit of measurement widely used in nuclear and particle physics to quote cross sections. One barn is equal to $10^{-24}\,\mathrm{cm}^{-2}$.

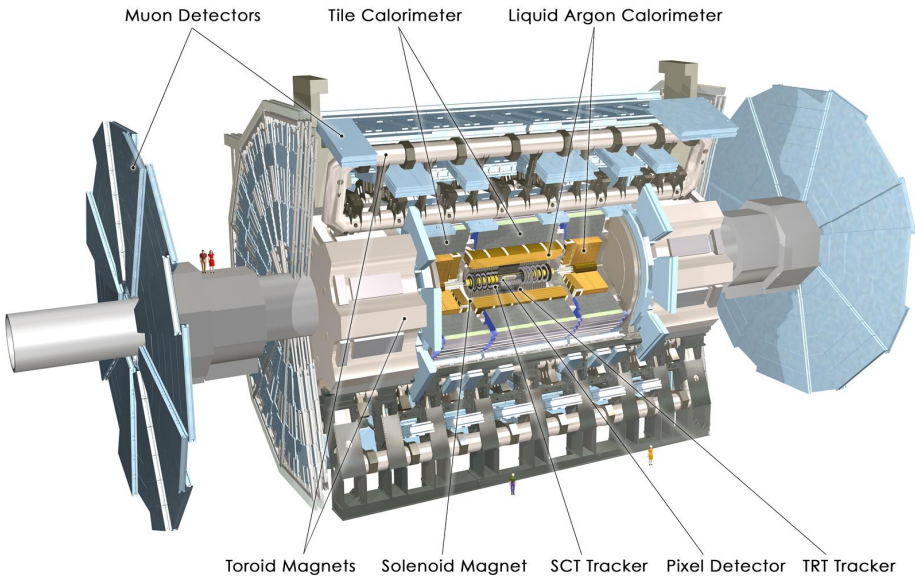

Figure 2.4 – A full view of the ATLAS detector where all the sub-detectors are pointed out [1, 50].

are stacked on top of each other. Moving from the interaction point outwardly in the radial direction, particles will encounter:

- the Inner Detector, capable of reconstructing tracks of charged particles together with primary and secondary vertices;
- the Electromagnetic Calorimeter, which measure the energy and direction of electrons and photons;
- the Hadronic Calorimeter, devoted instead to neutral and charged hadrons measurements;
- the Muon Spectrometer, used to reconstruct and identify muons tracks.

An overview of the ATLAS detector is shown in Figure 2.4.

In this chapter I will describe the sub-detectors specifications and how they work together to reconstruct physics objects created in the hard scattering processes.

2.2.1 ATLAS frame of reference

The ATLAS coordinate system is shown in Figure 2.5. The LHC ring lies on the x-z plane, with the x axis point towards the centre of it and the z along the beams. The y axis points upwards, so defining the versus of the z axis. However, since at a hadron collider the interaction reference frame is boosted along the beam axis differently on an event by event basis, a more convenient reference frame is defined using angular (ϕ,

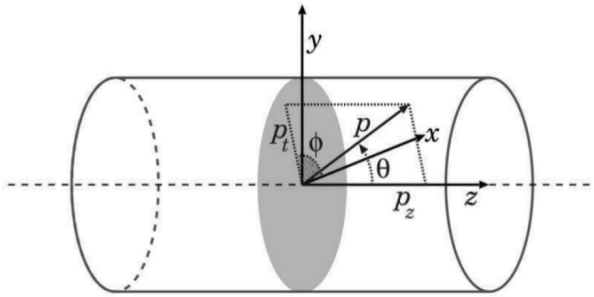

Figure 2.5 – Coordinate system in the ATLAS detector.

η) and transverse variables (p_T, E_T, etc). The latter are quantities projected in the x-y plane and they are useful because energy and momentum conservation can be only imposed in the transverse plane. The azimuthal angle ϕ is measured around the beam direction. With the use of the polar angle θ, a more useful quantity could be defined, called *pseudorapidity*:

$$\eta = -\ln\left[\tan\left(\frac{\theta}{2}\right)\right]. \tag{2.6}$$

which is obtained as the massless limit of the *rapidity*: $Y = \frac{1}{2}\ln\left(\frac{E+p_{||}}{E-p_{||}}\right)$. Rapidity and pseudorapidity have the nice feature that ΔY and $\Delta\eta$ are z-boost invariant and therefore provide a compromise-free measurement of an angle. With the two angular measurements one could compute the angular distance as:

$$\Delta R = \sqrt{(\Delta\phi)^2 + (\Delta\eta)^2}. \tag{2.7}$$

2.2.2 Magnet system

In detecting particles, the various sub-detector composing ATLAS are assisted by two magnetic fields produced by an inner solenoid and an outer toroid magnet, covering approximately 12 000 m^3, which are sketched in Figure 2.6. The barrel part of the toroid and the central solenoid are magnetically decoupled by a iron shield.

The central solenoid [51] is located between the Inner Detector and the calorimetric system and provides a axial magnetic field inside the Inner Detector. The magnet is composed by a coil of superconducting material, cooled to 4.5 K, which produces a 2 T magnetic field, generated by a 7.7 kA current. It is 5.8 m long and with a diameter of 2.56 m, for a total weight of 5.7 t. Since the location of the solenoid is chosen to be in front of the Electromagnetic Calorimeter, the material budget has been kept at the minimum, amounting to 0.66 radiation lengths only: the coil has been design to be as thin as possible, corresponding to a thickness of only 4.5 cm, without sacrificing safety and reliability

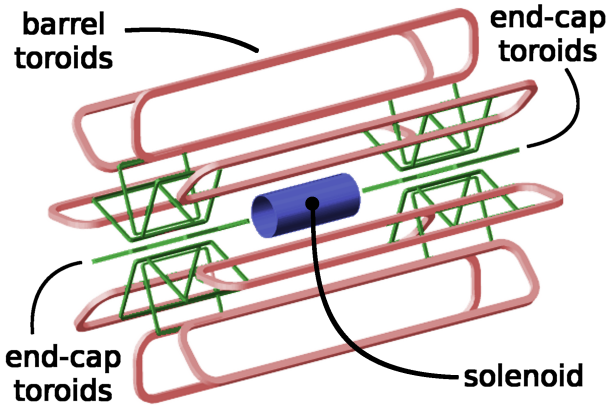

Figure 2.6 – Sketch of the ATLAS magnet systems [54].

and it is placed in the same cryostat as the Liquid Argon calorimeter (see Section 2.12).

The toroidal system is composed by two sub-systems, an air-core barrel toroid [52] and two endcap toroids [53].The barrel toroid consists of 8 superconductive coils, which provides a toroidal field from 0.5 T up to 1 T outside of the calorimeters, thanks to 20.5 kA passing through all the coils. Each coil is arranged in a "racetrack" configuration, assembled radially and symmetrically around the beam axis, and it is contained in an independent cryostat. The barrel toroid has an inner diameter of 9.4 m, an outer diameter of 20.1 m and it is 25.3 m long. Two endcap toroids provide instead the toroidal field in the forward regions to ensure an almost complete coverage of the magnetic field. Each endcap toroid is composed of 8 superconducting coils, each 5 m long and from 1.65 m to 10.7 m radially wide, housed in a cryostat which provide a peak field in the bore of 3.5 T in the $1.6 < |\eta| < 2.7$ region.

2.2.3 Inner Detector

The ATLAS *Inner Detector* (ID) is the closest system to the interaction point. It is a composite tracking detector consisting of silicon pixels, silicon strips and straw tubes, immersed in the axial field created by the solenoid magnet. The ID is able to provide track information for each charged particle produced during interaction, reconstruct primary and secondary vertices and it could provide identification information. It is a very high granular detector, especially closer to the beam axis, to cope with the huge number of tracks generated at each bunch crossing and it is requested to be radiation resistant. The ID is composed of a barrel and two end-cap regions, covering a region up to $|\eta| < 2.5$. An overview of the system is shown in Figure 2.7 and Figure 2.8. Overall, the ID has a diameter of 2.1 m and is 6.2 m long and its material budget is shown in Figure 2.9. It is composed by three sub-systems with different technologies, from the innermost: the Pixel Detector, the Semi-Conductor Tracker and the Transition Radiation Tracker.

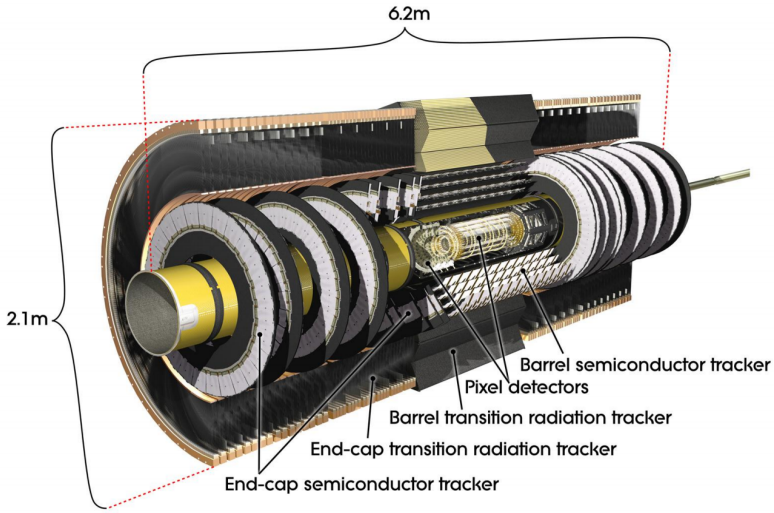

Figure 2.7 – Schematic view of the ATLAS Inner Detector [1, 55].

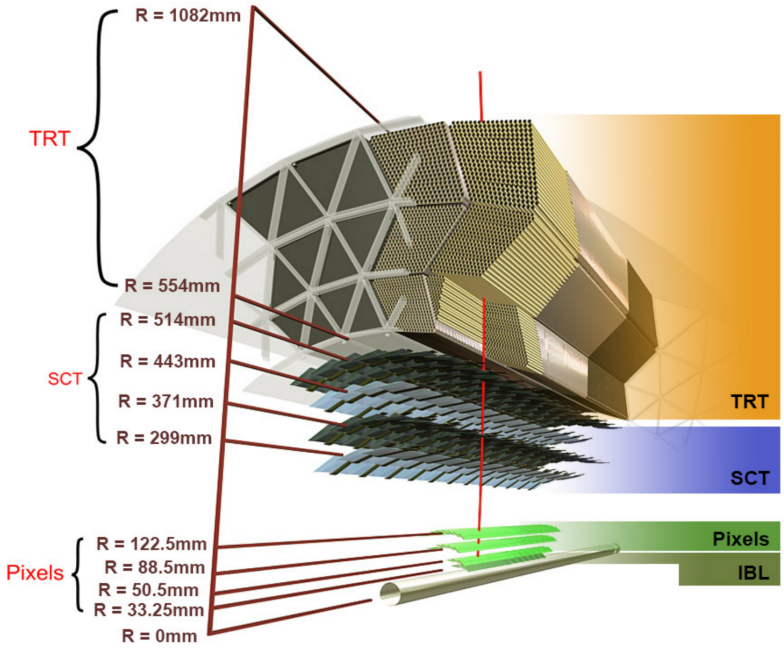

Figure 2.8 – Cut view of the barrel Inner Detector [56].

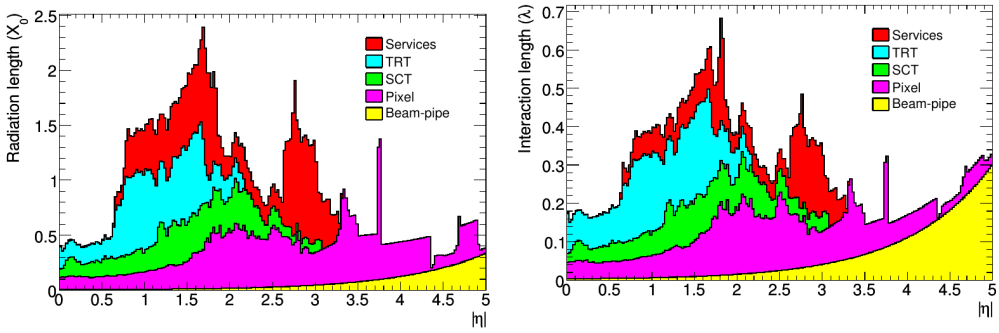

(a) X_0 **(b)** λ

Figure 2.9 – Radiation length X_0 (see Eq. (2.10)) and interaction length λ (see Eq. (2.12)) after the various ID components, including the services and thermal enclosures. The distributions are shown as a function of $|\eta|$ and averaged over ϕ [1].

Pixel Detector

The Pixel Detector [57] is the closest system to the beam pipe and the one with the highest granularity. It is made of pixels silicon sensors since they provide the highest spatial resolution. The detector is arranged in four concentric barrel layers and two end-caps of three disks each. The first of these layers is the *Insertable B-Layer* (IBL) [58], the newest part of the ID which has been installed during the LHC shutdown in 2014, between Run 1 and Run 2 and it is placed at a radii of 3.3 cm. In the barrel section, three more pixel layers are positioned between a radii of 3.3 cm and 12.3 cm, while in the end-cap the disks stand between 49.5 cm and 65 cm. The typical pixel size is $50 \times 400\,\mu m^2$, which leads to a single hit resolution of $\sim$12 µm in the $(R-\phi)$ plane and from $\sim$72 µm for the IBL and $\sim$115 µm for other layers in the z direction. The number of readout channels is around 80 millions.

Semi-Conductor Tracker

The *Semi-Conductor Tracker* (SCT) stands behind the Pixel detector. The detector has a radial extension from 30 cm and 51 cm and is arranged in eight concentric barrel layers [59], covering the pseudorapidity range $|\eta| < 1.4$ and two end-caps of nine disks each [60], completing the coverage up to $|\eta| = 2.5$. The strip silicon sensors technology is employed, with typical pitch size of 80 µm in the barrel, and from 56.9 µm to 90.4 µm for the endcaps. In the barrel region, the sensors are organized in four cylinders where two layers of strips are glued with 40 mrad stereo-angle, therefore providing 3D information. They record four more hits to be added to the ones obtained from the Pixel Detector. The intrinsic single hit resolution is $\sim$16 µm in the $(R-\phi)$ plane and $\sim$580 µm along z axis.

Transition Radiation Tracker

The outermost part of the ID is the *Transition Radiation Tracker* (TRT) [61, 62], radially placed from 56 cm to 108 cm. It is a tracking detector based on 370 000 drift tubes (called *straw*), filled with Xenon or Argon gas mixture.

Straw are place parallel to the beam axis in the barrel region, while perpendicular to it in the endcaps, covering a region up to $|\eta| < 2.5$.In the centre of each tube a gold-plated tungsten wire is kept at ground potential while the wall are biased at a voltage of $-1.5\,\text{kV}$, therefore each tube acts as a small proportional counter. In addition, the spaces between the straws are filled with polymer fibers in the barrel and foils in the endcap, therefore transition radiation is emitted by charged particles passing through material boundaries. The TRT provides a combination of continuous tracking, with many drift time measurements in individual tubes, and particle identification information from transition radiation. The spectrum of the emitted photons depends on the γ factor of the particles, thus allowing discrimination power between electrons and pions up to 200 GeV: the additional energy deposited in the gas leads to significantly higher readout signals with an amplitude that can exceed the 6 keV high threshold (HT).

The TRT system provides $\sim$ 30 space points with 130 µm resolution in the $R - \phi$ plane for charged tracks with $|\eta| < 2$ and $p_{\text{T}} > 0.5\,\text{GeV}$.

Inner Detector performance

Once the magnetic field generated by the central solenoid is known (see Section 2.2.2), the determination of the momentum a particle follows from the measured radius of the track curvatures and from the particle charge. The momentum resolution for a tracking device is given by

$$\frac{\sigma_{p_{\text{T}}}}{p_{\text{T}}} = a \cdot p_{\text{T}} \oplus b \tag{2.8}$$

where the first term derives from the resolution of the curvature measurement and increases for high-momentum particles, while the constant term b accounts for the impact of multiple Coulomb scattering, while $\oplus$ indicates the quadrature sum. The overall ID momentum resolution achieved in Run 1, so before the IBL insertion, was $0.05\% \cdot p_{\text{T}} \oplus 1\%$. The impact of the additional inclusion of the Insertable B-Layer is visualized in Figure 2.10a which shown the improvement in transverse impact resolution. The probability for electrons and pions to exceed the HT as a function of the Lorentz γ-factor is shown in instead in Figure 2.10b, where it can be observed that only the most energetic pions have large enough γ-factor to emit transition radiation.

2.2.4 Calorimeters

Proceeding outward, particles created in the interaction point encounter the calorimetric system. It is devoted to measure the energy and direction of charge and neutral particles, with a fundamental role in reconstructing the missing transverse momentum. It has a hermetic coverage on the azimuthal solid angle up to $|\eta| < 4.9$ and consists of three different sub-systems, built with different technologies: the Electromagnetic Calo-

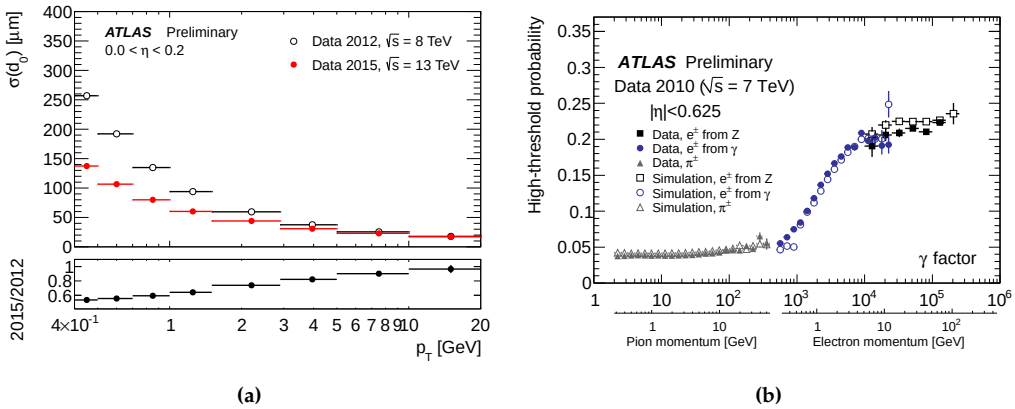

(a) **(b)**

Figure 2.10 – (a) Transverse impact parameter resolution as a function of p_{T}, measured from minimum bias trigger data in 2015, where Inner Detector includes the IBL, compared to 2012 data [63]. (b) Probability of a TRT high-threshold (HT) hit as a function of the Lorentz factor γ for the TRT ($|\eta| < 0.625$) [64].

rimeter, the Hadronic Calorimeter and the Forward Calorimeter, which are sketched in Figure 2.11.

Because the calorimeters play a key role in the results presented in this manuscript, I will briefly discuss their basic operation principles. A calorimeter measures the energy of a particle by collecting the energy deposits created by the interactions of that particle with the detector material. When the particle interacts, it creates secondary particles which in turn interact with the detector again. It is a cascade process in which the initial incident particle generates less energetic secondary particles which leave their energy in the material. This cascade is called *shower* and it keeps growing until the particles produced have low enough energy to be absorbed by the detector. To create the shower and measure the energy of incident particle two main designs are generally feasible:

- using one single dense material absorbing completely an electron or a photon while providing a signal at the same time, therefore building a *homogeneous calorimeter*. The CMS [65] electromagnetic calorimeter is made of $PbWO_4$ crystals, a very dense scintillator;

- using alternate active and passive materials. In this case only the energy deposited by secondary particles in the active material (typically a gas or a liquid gas) is measured. This is what is called a *sampling calorimeter* and is the way in which ATLAS calorimeters are built.

Both the approaches have their advantages and disadvantages. A homogeneous calorimeter could collect the whole energy deposit and therefore has a typically better energy resolution; in contrast a sampling calorimeter can be radiation harder and cheaper and can be segmented longitudinally making possible particle direction measurements.

When the incident particle is an electron or a photon, electromagnetic showers are produced recursively via photon pair production and via electron bremsstrahlung, supplying each other. These two processes continue until the secondary photon energy falls

below the pair production threshold or when the energy of the secondary electrons falls below the the critical energy. The critical energy E_C is the energy at which the loss by ionization and by bremsstrahlung are equivalent and can be parametrized as

$$E_C = \frac{610\,\text{MeV}}{Z + 1.24}$$

where Z is the material atomic number. This threshold is connected to the shower depth since it can be parametrized as

$$L_{EM}(95\%) \sim \ln\left(\frac{E_0}{E_C}\right) + C_j + 0.08Z + 9.6 \tag{2.9}$$

where E_0 is the energy of the incident particle, C_j takes $+0.5$ or -0.5 value for photon or electron respectively, and $L_{EM}(95\%)$ quantifies the material thickness needed to contain 95% of a electromagnetic shower in unit of X_0. The radiation length X_0 can be defined as

$$X_0 = \frac{716.4\,\text{g}\,\text{cm}^{-2} \cdot A}{Z\,(Z+1)\ln\left(287/\sqrt{Z}\right)} \tag{2.10}$$

and represents the amount of material which causes an electron beam reduce its energy by a factor of e. The second important parameter for electron and photon showers is the Molière radius R_M since the 95% of an electromagnetic shower is enclosed in $2R_M$. It is defined as

$$R_M = \frac{21\,\text{MeV}}{E_C} X_0 \tag{2.11}$$

and it is important to notice that it does not depend on the incoming particle energy, but only on the material properties.

Hadronic shower are considerably different from electromagnetic ones due to the physics processes leading to the shower development. Two main components can be identified, one electromagnetic and one hadronic. The first is very similar to the electromagnetic shower and it is produced by the decay into photons of π^0 and η generated in a hadronic interaction. This component can take up from 30% up to 60% of the total hadronic shower energy. The second component instead is fully hadronic and is generated by many different strong processes like slow neutron emission or proton spallation. It is important to notice that some of these processes produce *invisible* energy, mainly due to the binding energy of nucleons released in the nuclear reactions, which can represent up to 40% of the total non-EM energy.

Hadronic shower length can be described by the interaction length λ

$$\lambda \sim 35A^{1/3}\text{g}\,\text{cm}^{-2} \tag{2.12}$$

since $L_{Had}(95\%)$ can be parametrized in unit of λ as

$$L_{Had}(95\%) = 0.2\ln\left(E/1\,\text{GeV}\right) + 0.7 + 2E^{0.13}. \tag{2.13}$$

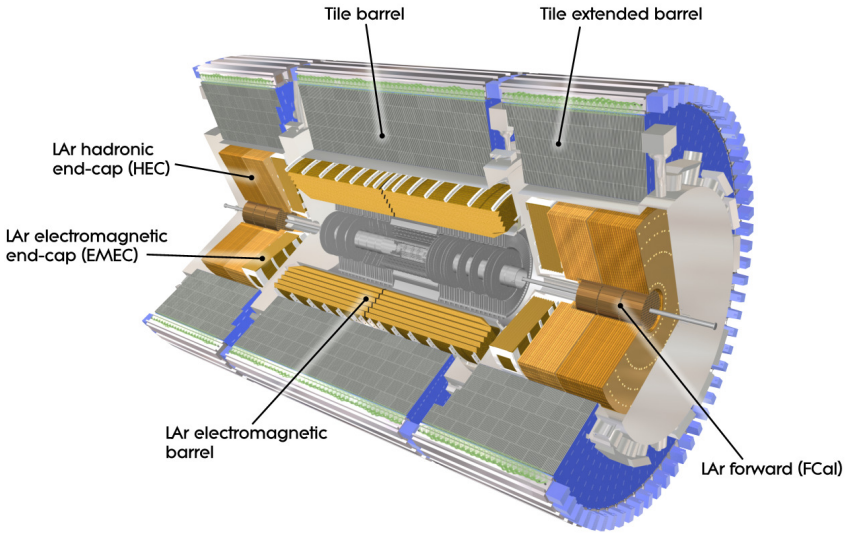

Figure 2.11 – The calorimeter systems in ATLAS. Gold/yellow parts employ liquid Argon as active medium [1, 66].

The interaction length λ is usually much larger than the radiation length X_0, therefore the electromagnetic calorimeter is always placed in front of the hadronic one and considered from the hadronic calorimeter perspective.

For both electromagnetic and hadronic showers described above, the energy resolution of a calorimeter is given by

$$\frac{\sigma_E}{E} = \frac{a}{\sqrt{E}} \oplus \frac{b}{E} \oplus c, \tag{2.14}$$

where E is the energy of the incident particle and $\oplus$ indicates the quadrature sum. The three term in the equation are called *stochastic*, *noise* and *constant* terms. The first term a represents the contributions to the resolution given by the statistical fluctuations of the shower development: in a ideal, uniform and homogenous calorimeter, the sum of all ionization tracks is directly proportional to the number of charged secondary particles, which in turn depends directly from the E/E_C ratio. Therefore, from purely statistical arguments, the intrinsic energy resolution is given $\sigma_E \propto \sqrt{E}$. Moreover, in case of a sampling calorimeter, the energy deposited in the active medium fluctuates event by event because the active layers are interleaved with absorber layers. This is caused by the variation in the number of charged particles crossing the active layers, which is proportional to E/t, with t being the thickness of the absorber material in unit of X_0. Therefore in a sampling calorimeter the resolution is worse by a factor of $\sqrt{t}$ with respect to a homogeneous one.

The noise and constant terms instead represent a further modelling of real calorimeters. The noise term b represents the contributions of the electronic noise of the readout

chain and therefore increases with decreasing energy of the incident particle. The constant term c includes instead all the sources of possible response non-uniformities, like imperfection in detector geometry or mechanical structure, detector ageing or temperature gradients. In a detector for high-energy physics like ATLAS, the noise term is usually negligible while the stochastic and constant terms are limiting the resolution at low and high energies respectively.

Electromagnetic Calorimeter

The ATLAS *Electromagnetic Calorimeter* (EM) [67, 68] surrounds the ID. It is a sampling calorimeter of cylindrical shape, 6.65 m long and with 4.5 m radius, divided in a barrel and two endcaps regions, which cover the ranges $|\eta| < 1.475$ and $1.375 < |\eta| < 3.2$ respectively. The barrel and the two endcaps are housed in three different cryostats. The EM basic structure is a 2 mm liquid Argon (LAr) gap between copper electrodes and lead layers of different thickness in a folded "accordion-shape" geometry as shown in Figure 2.12a, to provide a full ϕ coverage and avoid cracks due to the readout system. The lead layers have different thickness, 1.5 mm for $|\eta| < 0.8$ and 1.1 mm for $0.8 < |\eta| < 1.475$ for the barrel region, while in the end-cap 1.7 mm for $1.375 < |\eta| < 2.5$ and 2.2 mm for $2.5 < |\eta| < 3.2$): in this way, EM provides $22\,X_0$ in the barrel and $24\,X_0$ in the end-cap, guaranteeing a full containment of electromagnetic showers.

The calorimeter is segmented in around 180 000 cells along η and ϕ and it is composed of four layers with different granularities as shown in Figure 2.12:

- *Presampler*: a thin layer (1.1 cm) of LAr placed before the calorimeter covering the $|\eta| < 1.8$ region, used to corrected for energy losses in the material upstream of the calorimeter ($1.7\,X_0$ at $\eta = 0$ and $2.2\,X_0$ at $\eta = 1.4$). It is segmented in cells of 0.025×0.1 in $\Delta\eta \times \Delta\phi$.
- *Strips* or *Layer1*: it is the first layer of the accordion structure, shown in Figure 2.12, and it is finely segmented in $\Delta\eta$ in order to allow the separation of prompt photon from a $\pi^0 \to \gamma\gamma$ decay. The strips present cells of different $\Delta\eta \times \Delta\phi$ dimension moving to higher and higher $|\eta|$: 0.003×0.1 for cells in the region $|\eta| < 1.8$, 0.004×0.1 for $1.8 < |\eta| < 2.0$, 0.006×0.1 for $2.0 < |\eta| < 2.5$ and 0.1×0.1 for the region $2.5 < |\eta| < 3.2$.
- *Middle* or *Layer2*: this is the layer where the shower will develop the most ($16\,X_0$) and so it performs the measurement of the bulk of the energy deposited by electrons and photons. It is segmented in $\Delta\eta \times \Delta\phi$ in squared cells of 0.025×0.025 size.
- *Back* or *Layer3*: the last layer of the calorimeter is rather thin ($2\,X_0$), and it permits to estimate the shower fraction leaked in the hadronic calorimeter. It is segmented with 0.050×0.025 cells size in $\Delta\eta \times \Delta\phi$.

The nominal EM calorimeter resolution is

$$\frac{\sigma_E}{E} = \frac{10\% \div 19\%}{\sqrt{E}} \oplus 0.7\% \tag{2.15}$$

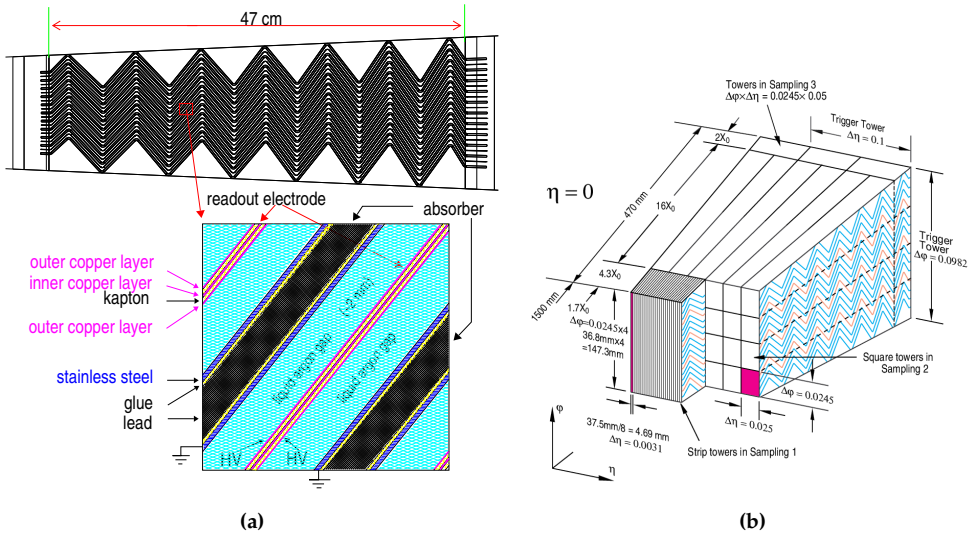

Figure 2.12 – (a) Accordion geometry of the electromagnetic calorimeter, with a close detail of the LAr gap, showing electrods composition too [67]. (b) Sketch of the EM barrel structure [1, 67]. The size of the cells at $\eta = 0$ for each longitudinal compartment is reported. The Presampler is not shown here and it is placed in front of the Layer1.

with the sampling term depending on $|\eta|$ and a noise term which is negligible and account for 500 MeV.

Hadronic Calorimeter

The ATLAS *Hadronic Calorimeter* (HAD) [67, 69, 70] is placed after the EM one in the radial direction. It is designed to contain the showers created by hadrons and to measure their energies. It has cylindrical shape with 4.2 m external radius and it is 11.5 m long, covering a range in pseudorapidity of $|\eta| < 3.9$. The HAD calorimeter is mainly composed of two sub-systems, which use different technologies. In the central region $|\eta| < 1.7$, the *Tile barrel* and *extended barrel* calorimeters encircle the EM one and make use of steel as absorber material and scintillating plates (tiles) read out by wavelength shifting fibres as the active medium. The tiles are placed in planes perpendicular to the colliding beams as shown in Figure 2.13a. It is radially segmented in three regions while the segmentation in $\Delta\eta \times \Delta\phi$ is 0.1×0.1. In the end-cap region the *Hadronic End-Cap* (HEC) calorimeter, covering the the range $1.5 < |\eta| < 3.2$, is placed longitudinally after the EM end-cap. It uses LAr as active medium and it is composed by two, equal diameter, independent wheels, one with 25 mm copper plain plates of passive absorber and the second with 50 mm plates (Figure 2.13b). The overall thickness of the hadronic calorimeter is 11λ for $\eta = 0$. The typical energy resolution for hadronic jets (combined with the EM calorimeter) is

$$\frac{\sigma_E}{E} = \frac{50\%}{\sqrt{E}} \oplus 3\% \tag{2.16}$$

with a negligible noise term.

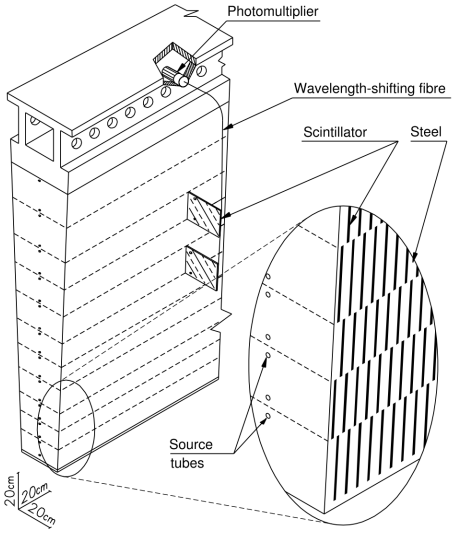

(a) Tile barrel and extended barrel design

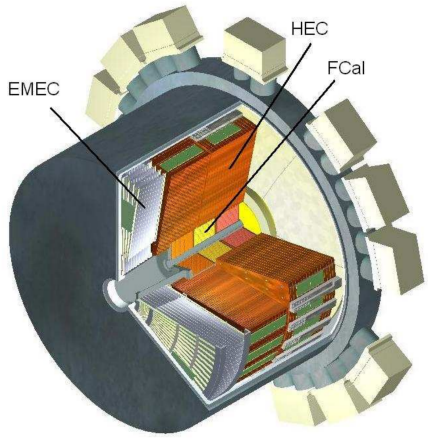

(b) EM and HAD end-caps enclosing the forward calorimeter

Figure 2.13 – (a) Tile calorimeter [67] and (b) LAr calorimeters in the end-cap regions [67].

Forward Calorimeter

The ATLAS *Forward Calorimeter* (FCal) [67, 71] completes the full solid angle coverage, measuring energy of particles in the $3.1 < |\eta| < 4.9$ region. It plays an important role for forward jet physics and $E_{\mathrm{T}}^{\mathrm{miss}}$ measurements. As shown in Figure 2.13b, it is housed inside the two HEC wheels at 4.7 m from the interaction point. To cope with the very harsh environment it is exposed to, the FCal makes use of LAr as active medium. It consists of three longitudinal sections with copper (in the first section) and tungsten (in the others two) as absorber materials, as shown in Figure 2.14. Each of them is a metal matrix filled with longitudinal rods, and gaps between the matrix and the rods are filled with Liquid Argon. The typical energy resolution of this calorimeter is

$$\frac{\sigma_E}{E} = \frac{100\%}{\sqrt{E}} \oplus 10\% \tag{2.17}$$

with a negligible noise term.

2.2.5 Muon Spectrometer

The outermost system of the ATLAS detector is the *Muon Spectrometer* (MS) [72]. Among all the particles produced in the interaction vertex only muons, neutrinos and possibly beyond Standard Model particles will escape the calorimeters. The aim of the MS is to measure with high accuracy the momentum of charged particles exiting from calorimeters in the $|\eta| < 2.7$ range and to trigger on them in the region $|\eta| < 2.4$. A full view of the MS is shown in Figure 2.15. In the barrel region, tracks are measured in chambers arranged in three cylindrical layers located inside and outside the air-core toroid. In the

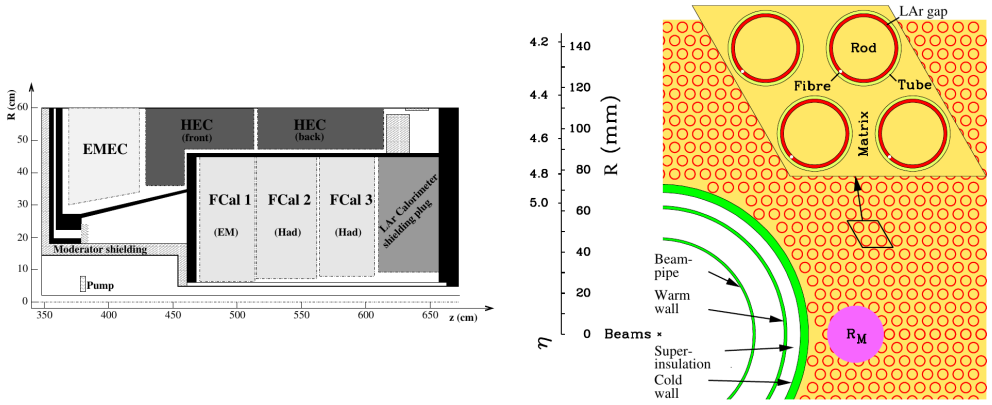

Figure 2.14 – (Left) Schematic diagram showing the three FCal modules located in the end-cap cryostat. The black regions are structural parts of the cryostat. (Right) Electrode structure of FCal1 with the matrix of copper plates and the copper tubes and rods with the LAr gap for the electrodes. The Molière radius, R_M, is represented by the solid disk [1].

end-cap region, instead, they are placed in three planes perpendicular to beams axis, in front and behind the two end-cap toroid magnets.

The measurements are provided by *Monitored Drift Tubes* (MDT) over the $|\eta| < 2.7$ range. They are built from 3-8 layers of 3 cm tubes, filled with high pressure Ar/CO_2 gas and a central 50 µm wire. In the $2.0 < |\eta| < 2.7$ range where high rate capability and time resolution is needed, *Cathode Strip Chambers* (CSC) replace MDTs in the innermost layer. They are multiwire proportional chambers filled with Ar/CO_2 gas and with wires oriented in the radial direction and cathode planes segmented into strips in orthogonal directions, allowing both coordinates to be measured.

These chambers are equipped with a fast trigger system composed by *Resistive Plate Chambers* (RPC) for $|\eta| < 1.05$ and *Thin Gap Chambers* for $1.05 < |\eta| < 2.4$ [72]. The ATLAS muon system is able to provide with the MDTs a momentum resolution between 2-3% and $\sim 10\%$ in a p_T range between 10 GeV and 1 TeV.

2.2.6 Trigger and data acquisition system

The trigger system [73, 74] is an essential and critical component of a collider experiment, since it is responsible for online processing and selection of interesting events for offline analysis. This is shown diagrammatically in Figure 2.16. Given that collisions occur in ATLAS at a rate of 40 MHz and the fact that the average event size is $O(1\,\text{MB})$, the resulting data rate would be around 1 TB/s. This is far too much data to store and process economically, therefore the trigger system is in charge of reducing the data rate to around 1 kHz. The trigger is arranged in two sub-systems, the *Level 1* trigger (L1) and the *High Level Trigger* (HLT), shown on the left part of Figure 2.16.

The L1 trigger is a hardware-based system that uses custom on-detector electronics to trigger on reduced granularity information from the calorimeter and muon detectors.

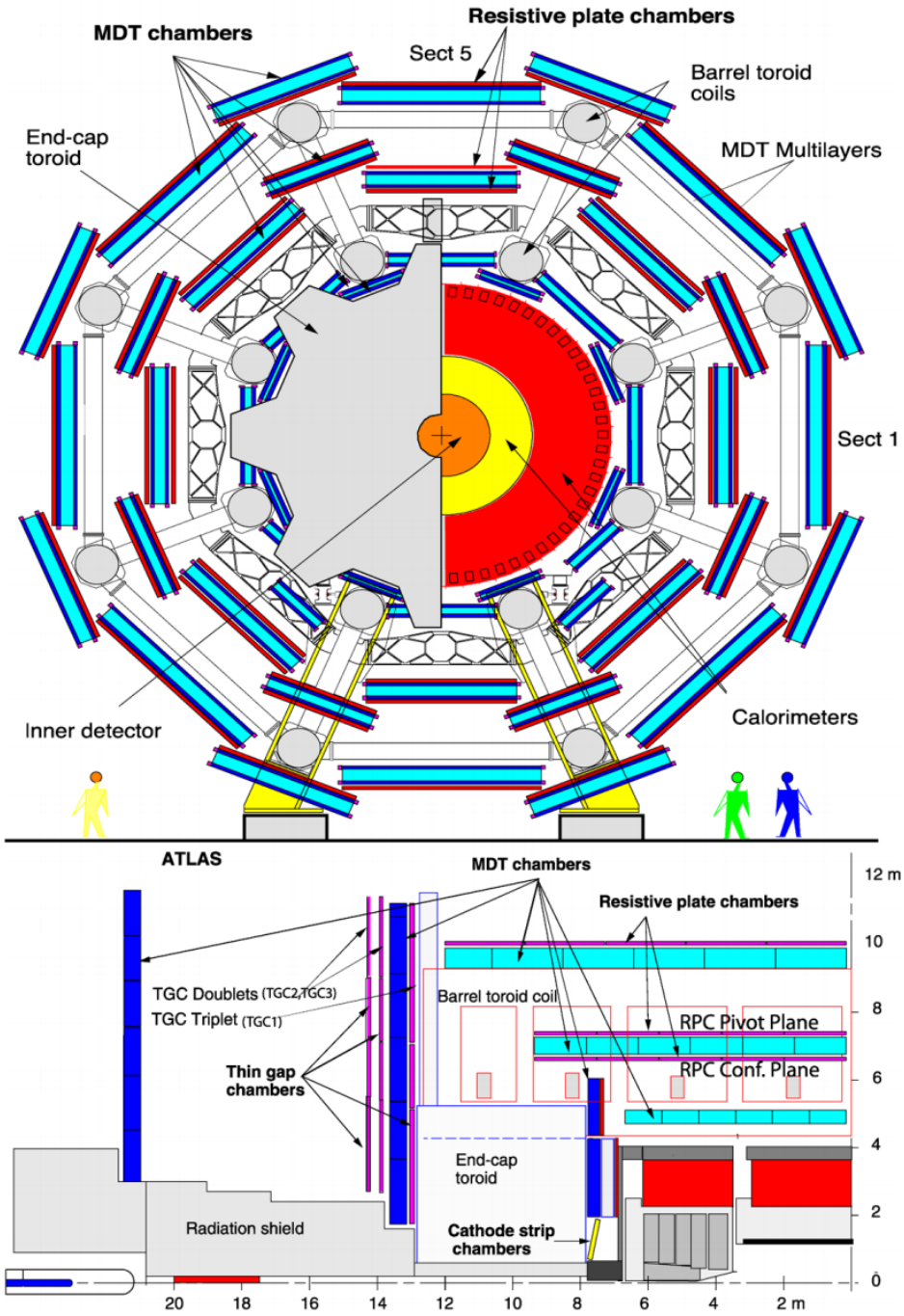

Figure 2.15 – Cut-away views of ATLAS Muon Spectrometer. The upper figure displays ATLAS in the x-y plane and the bottom in the z-y [72].

It can select events by considering event-level quantities (e.g. the total energy in the calorimeter), the multiplicity of objects above thresholds (e.g. the transverse momentum of a muon, etc.), or by considering topological requirements (such as invariant masses or angular distances). The L1 trigger accepts events at a rate up to the maximum detector read-out rate of 100 kHz within a latency of 2.5 µs.

Once identified an interesting event, the L1 system sends a L1-accept signal to the front end electronic to read out the event data from all the detectors. The data are sent first to ReadOut Drivers (RODs), performing the initial processing and formatting, and then to the ReadOut System (ROS) to buffer the data, as sketched on the right side of Figure 2.16. The data from the different sub-detectors are sent from the ROS to the HLT, only when requested by it. In addition to performing the first selection step, the L1 triggers identify Regions-of-Interest (RoIs) in η and ϕ within the detector to be investigated by the second trigger stage.

The HLT trigger is a software-based system, which makes use of dedicated trigger algorithms to perform the final event selection. These algorithms are executed on a dedicated computing farm of approximately 40 000 selection applications known as Processing Units (PUs), which are designed to make decisions within a few hundred milliseconds. The physics output rate of the HLT during an ATLAS data-taking run is on average 1.2 kHz with an average physics throughput to permanent storage of 1.2 GB/s. The HLT then sends a final accept signal in order to store the event for offline reconstruction.

L1 and HLT triggers are activated based on the requirements of the measured quantities in an event. The total L1 trigger rate for a fill is presented in Figure 2.17a along with the main physic signatures, which already include some simplified selections on physics object isolation and identification. The Figure 2.17b shows instead the the total HLT rate with the breakdown of the rates for the main contributions by reconstructed object groups.

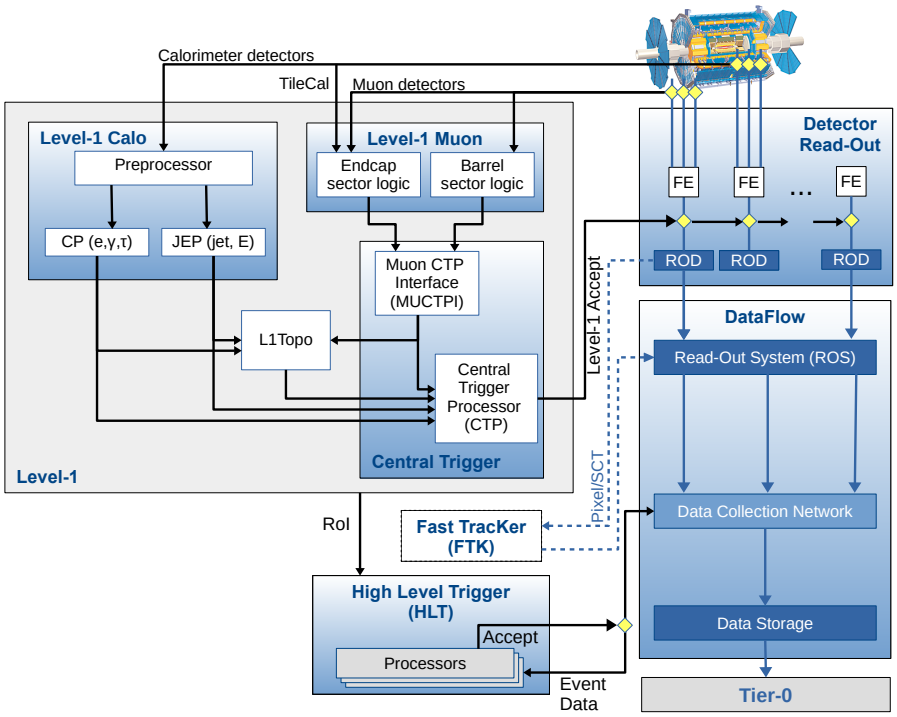

Figure 2.16 – The ATLAS trigger and data acquisition system [73].

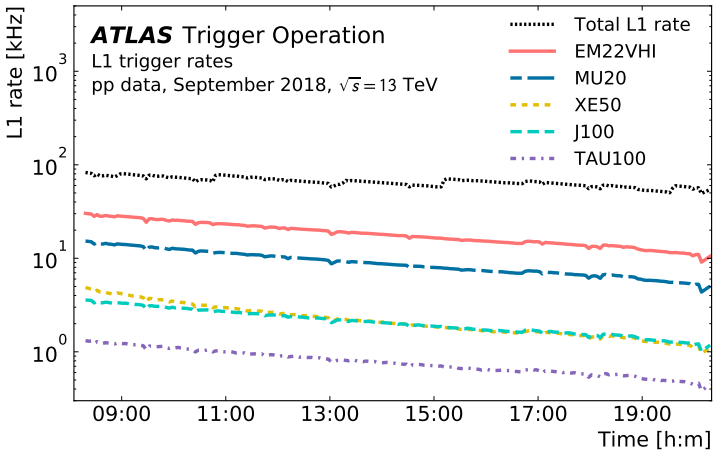

(a) Level1 trigger

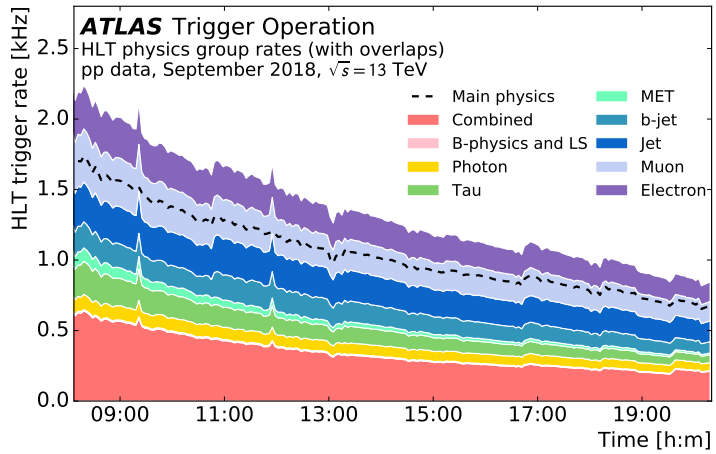

(b) High Level Trigger

Figure 2.17 – Physics trigger rates at the Level-1 (a) and at the High-Level Trigger (b) as a function of time in a fill taken in September 2018 with a peak luminosity of $\mathcal{L} = 2.0 \times 10^{34}\,\mathrm{cm}^{-2}\,\mathrm{s}^{-1}$ and a peak average number of interactions per crossing of $< \mu >= 56$. Rates decrease exponentially with the decreasing luminosity of the LHC fills (see Eq. (2.5)) and they increase periodically due to LHC luminosity re-optimisations; dips are due to dead-time and spikes are caused by detector noise. In (a), the trigger items are based on such objects as electromagnetic clusters (EM), muon candidates (MU), jet candidates (J), missing transverse energy (XE) and tau candidates (TAU). The number in the trigger name denotes the trigger threshold in GeV. The letters following the threshold values refer to details of the selection: variable thresholds (V), hadronic isolation (H), and electromagnetic isolation (I). The total L1 rate is also shown. In (b) presented are the rates of the individual trigger groups specific to trigger physics objects. Overlap between groups is only accounted for in the total main physics stream rate. The combined group represents multiple triggers of different objects, as combinations of electrons, muons, taus, jets and missing transverse energy [75].

CHAPTER 3

Physics objects reconstruction at ATLAS

The particles produced in the pp collisions interact with the detector material and the detected energy is converted into electrical signals which are recorder by the data acquisition system. In the Inner Detector and the Muon Spectrometer, charged particles release a very small fraction of their energy in the various layers. These energy deposits, called hits, are used to reconstruct the tracks of the particles. On the contrary, in the calorimetric system, electrons, photons and hadrons deposit approximately all their energy. The first part of the event reconstruction consists in combining these signals and interpreting them as tracks or energy clusters. The information from the relevant subdetectors is combined in order to reconstruct and identify as accurately as possible a candidate physics object. This chapter describes the reconstruction and identification procedures of the objects used in the analyses discussed in this manuscript, with a focus on photons since these are the key physic objects in the $H \to \gamma\gamma$ decay.

A simple sketch of how information is combined to identify particles is reported in Figure 3.1, while detailed information will be given in the following Sections.

3.1 Tracks and vertexes

Tracking information is essential in the reconstruction and identification of many types of particles, including photons, electrons, muons, and the jets. Charged particles traversing the ID layers deposit some of their energy through ionization, which is converted into electrical signals and read out as hits. These hits are used to reconstruct the trajectory of the charged particles, which is of helicoidal shape and with radius inversely proportional to their momentum, since tracking detectors are immersed in magnetic fields.

Primary tracks, originating from charged particles with a life time $> 3 \times 10^{-11}$ s produced in the hard-scattering vertex, are reconstructed with an inside-out approach [76, 77]: the seed of the reconstruction are three hits in the silicon detector, primarily SCT, and then compatible hits in the other layers of the ID are added with a Kalman filter algorithm [78]. The TRT segments that are not associated with primary tracks are used as starting point to secondary tracks from photon conversion or secondary vertices, with a backward tracking that extrapolates the TRT information to the silicon detectors. Finally an ambiguity solving procedure is applied among tracks which share hits.

Tracks are the starting point for the reconstruction of the primary and secondary vertices. Primary vertices are reconstructed through a vertex finding algorithm [79] which

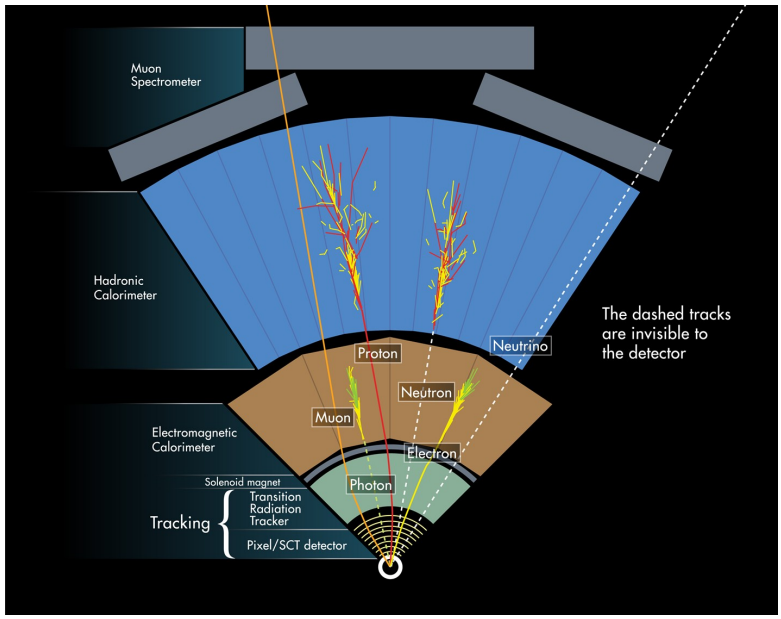

Figure 3.1 – Cartoon of an ATLAS wedge with sub-detectors and different physics objects highlighted. Dashed tracks are invisible to ATLAS.

is robust enough to deal with both mis-associated tracks and mis-measured track errors. The vertex fitting algorithm identifies the vertex position and refits the tracks adding the constraint of the reconstructed interaction point. Multiple primary vertices are reconstructed and the one with the highest sum of the squared transverse momenta of its associated tracks is identified as the hard scattering one. In $H \to \gamma\gamma$ analyses though, the primary vertex is redefined as described in Section 4.3.2.

3.2 Photon and electron reconstruction

Photon and electron reconstruction proceeds simultaneously and it is based on the information collected by the calorimetric system and the Inner Detector. The main signature for these two particles are clusters of energy in the EM calorimeter, with very small or no leakage in the Hadronic one. The tracks reconstructed in the ID are used to distinguish among three cases: electrons, *converted* photons (i.e. photons which have interacted with the ID resulting in a e^+e^- pair) and *unconverted* photons. In case of the presence of tracks, they have to be matched to the barycentre of the energy cluster in the second layer of EM calorimeter. When one track is connected to the cluster the object is considered as an electron, when a conversion vertex is found it is considered as a converted photon, when no tracks connected to the cluster are found the object is considered as an unconverted photon.

The offline electron and photon reconstruction uses group of dynamical, variable-size clusters, called superclusters, [80], which supersedes the fixed-size cluster algorithm [81]. The main advantage of using superclusters is their ability to recover low-

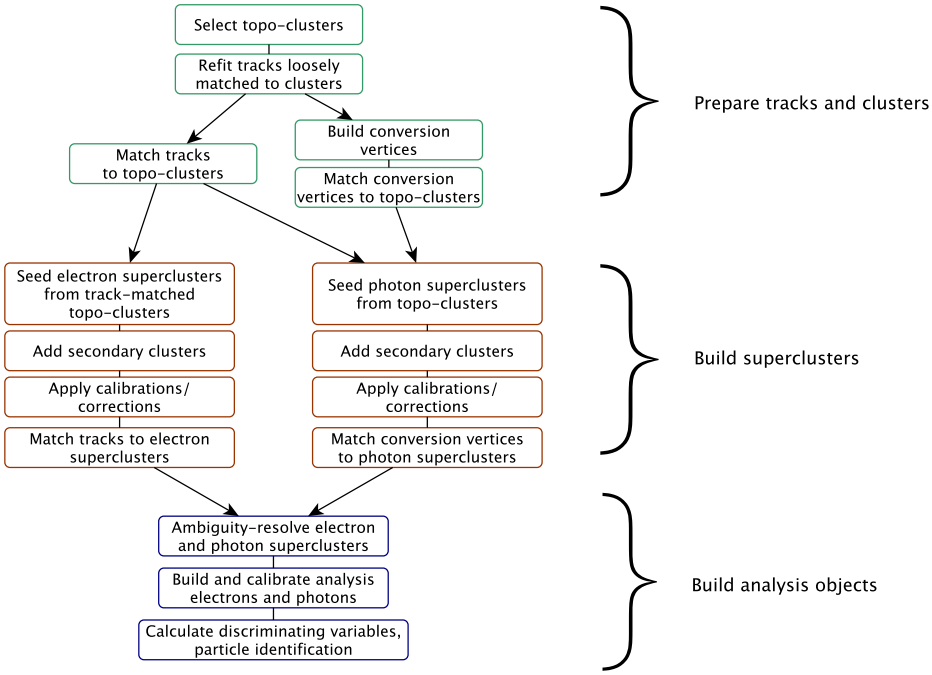

Figure 3.2 – Algorithm flow diagram for the electron and photon reconstruction [80].

energy deposits from bremsstrahlung photons and associate them to the electron cluster. A diagrammatic view of the full reconstruction chain is given in Figure 3.2.

3.2.1 EM calorimeter cluster

The reconstruction of electron and photon candidates starts from energy deposits in the EM calorimeter, where a dynamical clustering method is used (topological clustering). The topocluster reconstruction algorithm proceeds by first identifying a seed cell and then neighbouring cells are iteratively added to the cluster if their energy is above a certain threshold, defined as a function of the expected noise. The first step in the procedure is the calculation of the significance variable which is defined as

$$\zeta_{\text{cell}}^{\text{EM}} = \left| \frac{E_{\text{cell}}^{\text{EM}}}{\sigma_{\text{noise,cell}}^{\text{EM}}} \right| \tag{3.1}$$

where $E_{\text{cell}}^{\text{EM}}$ indicates the cell energy and $\sigma_{\text{noise,cell}}^{\text{EM}}$ the expected cell noise coming from both read-out electronic and an estimate of the pileup noise corresponding to the average instantaneous luminosity. With this variable, the clustering algorithm follows a "4-2-0" scheme:

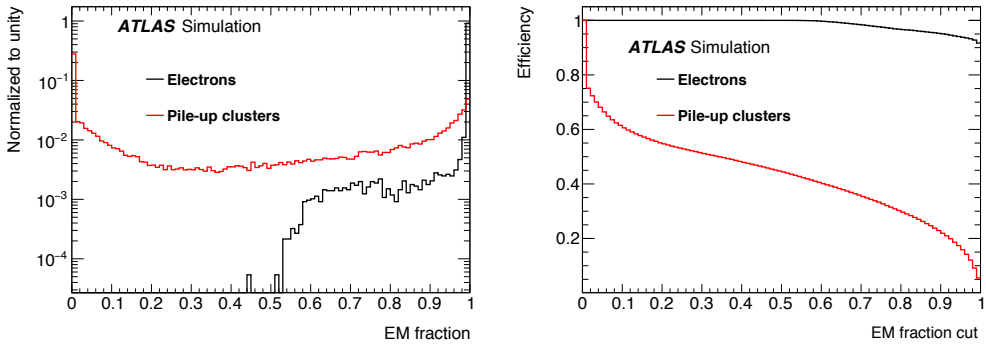

Figure 3.3 – (a) Distribution of f_{EM} and (b) reconstruction efficiency as a function of the f_{EM} selection threshold for simulated true electron (black) and pile-up (red) clusters [80].

1. a proto-cluster seeded from calorimeter cells (excluding Presampler and Layer1) with $\zeta_{\mathrm{cell}}^{\mathrm{EM}} \geq 4$ is formed and used as initial seed;

2. all the neighbouring cells with $\zeta_{\mathrm{cell}}^{\mathrm{EM}} \geq 2$ are added to the proto-cluster. If these selected cells are shared between two proto-clusters, the two are merged together;

3. all the nearest-neighbour cells to the ones added in the first two steps are added.

The algorithm is not limited to one region of the calorimeter and it could create a topocluster with hadronic calorimeter cells too. Therefore, a selection is applied to identify electromagnetic showers based on the fraction of EM energy calculated as

$$f_{\mathrm{EM}} = \frac{E_{L1} + E_{L2} + E_{L3}}{E_{cluster}}. \tag{3.2}$$

where E_{Lx} is the cluster energy in the x-th layer of the calorimeter. If f_{EM} is above 0.5, the cluster is considered as coming from an electromagnetic shower and hadronic cells are removed. This requirement rejects $\sim$ 60% of pileup clusters without affecting the efficiency for selecting true electrons and photons topo-clusters. The threshold on f_{EM} was optimized using simulated samples in order to achieve large rejection of pileup as shown in Figure 3.3. After hadronic cells removal, only topocluster with $E_{\mathrm{T}} > 400\,\mathrm{MeV}$ are considered.

3.2.2 Track-cluster matching

The reconstruction of electrons and photons is completed by including the tracking information. Depending on the number of reconstructed tracks and on the matching of those tracks to the EM clusters, it is possible to identify electrons, unconverted and converted photons. In addition to what is described in Section 3.1, the original tracking is further refined in order to increase the reconstruction efficiency for electrons which undergo

large bremsstrahlung and identification of photon conversion vertexes. Fixed-size clusters compatible with an EM shower are used to create regions-of-interest (ROIs). If the standard pattern recognition fails for a silicon track seed within a ROI, a modified pattern recognition algorithm still based on a Kalman filter formalism is used, but allowing for up to 30% energy loss at each material intersection. In addition, track with silicon hits which are loosely matched to a fixed-size clusters are re-fitted with the Gaussian Sum Filter (GSF) [82], allowing for additional energy loss when the standard track fit fails, in order to further improve track parameter estimation. The loosely matched condition requires the track (with reconstructed charge q) to be within $|\Delta\eta| < 0.05$ from the cluster and with $-0.20 < q \cdot (\phi_{track} - \phi_{clus}) < 0.05$ when using the track energy to extrapolate from the last Inner Detector hit, or $|\Delta\eta| < 0.05$ and $-0.10 < q \cdot (\phi_{track} - \phi_{clus}) < 0.05$ when using the cluster energy to extrapolate from the track perigee. These re-fitted tracks are then used to compute the final matching with the seed cluster: the reconstructed tracks are then matched to an EM calorimeter cluster by extrapolating the track to the second layer of the calorimeter using either the measured track momentum or rescaling the magnitude of the momentum to match the cluster energy (since this improves the matching for electrons with significant energy loss due to bremsstrahlung). A track is considered match if $|\Delta\eta| < 0.05$ and $-0.10 < q \cdot (\phi_{track} - \phi_{clus}) < 0.05$. In case multiple tracks are matched to the same cluster, tracks with pixel hits are preferred over SCT ones and, if in the same category, tracks with smaller ΔR with the cluster barycenter in the second layer of the calorimeter are chosen. The best matched track is used to define the electron candidate properties.

For photon conversion reconstruction, tracks loosely matched to fixed-size clusters serve as input to the reconstruction of the conversion vertex. Both tracks with silicon hits (denoted Si tracks) and tracks reconstructed only in the TRT (denoted TRT tracks) are used for the conversion reconstruction. Two-track conversion vertices are reconstructed from two opposite-charge tracks forming a vertex consistent with that of a massless particle, while single-track vertices are essentially tracks without hits in the innermost sensitive layers. The conversion vertices are then matched to the EM topoclusters: if the conversion vertex has tracks with silicon hits, a conversion vertex is considered matched if, after extrapolation, the tracks match the cluster to within $\Delta\eta < 0.05$ and $\Delta\phi < 0.05$; if the conversion vertex is made of only TRT tracks, then if the first track is in the TRT barrel, a match requires $\Delta\eta < 0.35$ and $\Delta\phi < 0.02$, while if the first track is in the TRT endcap, a match requires $\Delta\eta < 0.2$ and $\Delta\phi < 0.02$. In case multiple conversion vertices are matched to the same cluster, double-track conversions with two silicon tracks are preferred over other double-track conversions, followed by single-track conversions. Within each category, the vertex with the smallest conversion radius is preferred.

3.2.3 Supercluster formation

The reconstruction of electron and photon superclusters proceeds independently, each in two stages: first seed supercluster candidates are identified, secondly additional satellite cluster are added to form the final supercluster.

Seed superclusters are selected from the E_{T} ordered list of topoclusters built as de-

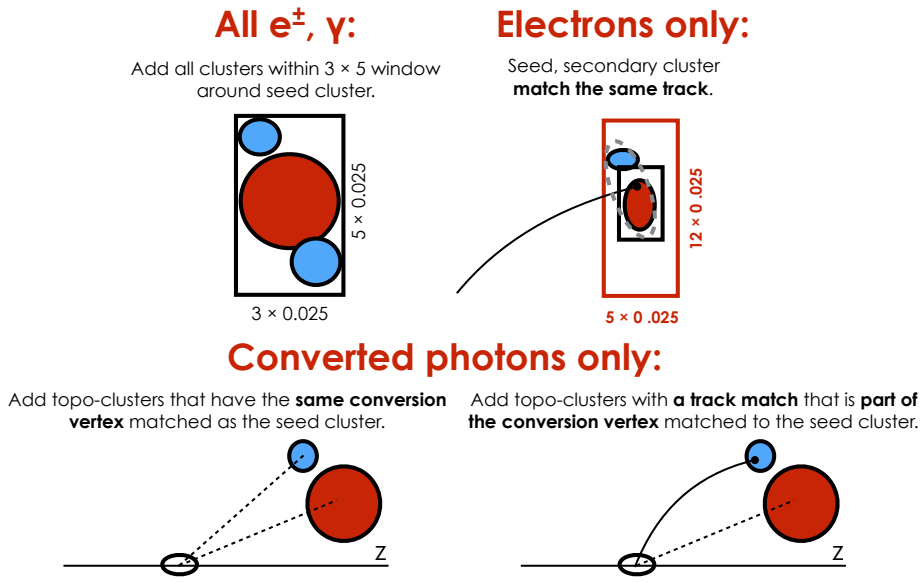

Figure 3.4 – Cartoon showing supercluster formation algorithm for electrons and photons. Supercluster seed for both electron and photons are shown with red circles, while satellite cluster are shown in light blue [80].

scribed in Section 3.2.1. An electron supercluster seed must have $E_{\mathrm{T}} > 1\,\mathrm{GeV}$ and a four silicon hits track associated, while a photon supercluster seed must have $E_{\mathrm{T}} > 1.5\,\mathrm{GeV}$ with no requirement on the tracks. The supercluster is then built as shown in Figure 3.4. First a window of $\Delta\eta \times \Delta\phi = 0.075 \times 0.125$ around the supercluster seed is built and all satellite topoclusters are added. In addition, for electron reconstruction satellite cluster in a $\Delta\eta \times \Delta\phi = 0.125 \times 0.300$ region are included in the supercluster if they have the same best-matched track, in order to recover large bremsstrahlung emission. Instead, for photons reconstruction, a satellite cluster is added if it is matched to the same photon conversion vertex with conversion vertices made up only of tracks containing silicon hits. A cluster is also added as a satellite if its best-matched (electron) track belongs to the conversion vertex matched to the seed cluster, in order to recover a long-range emitted electron. To limit the superclusters sensitivity to pileup noise, the size of each constituent topocluster is restricted to a maximal width of 0.075 or 0.125 in the η direction in the barrel or endcap region, respectively.

3.2.4 Analysis objects

Tracks and vertices are associated to the supercluster with the same procedure described above and supercluster are given an initial energy calibration. Because electron and photon superclusters are built independently, a given seed cluster can produce both an electron and a photon: in these cases the ambiguity resolution detailed in Figure 3.5 is performed. In case a object can be identified only as a good photon (a cluster with no good track attached) or only as an electron (a cluster with a good track attached and

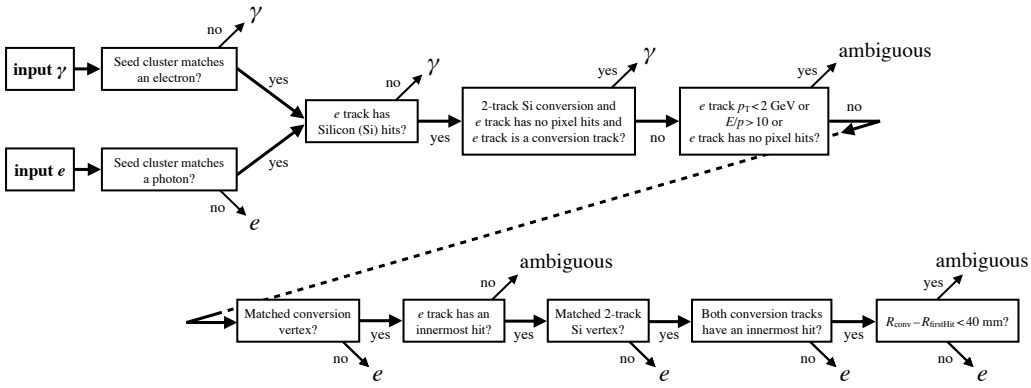

Figure 3.5 – Flowchart showing the logic of the ambiguity resolution for particles initially reconstructed both as electrons and photons. An 'innermost hit' is a hit in the functioning pixel nearest to the beam-line along the track trajectory, E/p is the ratio of the supercluster energy to the measured momentum of the matched track, R_{conv} is the radial position of the conversion vertex, and R_{firstHit} is the smallest radial position of a hit in the track or tracks that make a conversion vertex [80].

no good photon conversion vertex), then only a photon or an electron object is created for analysis; otherwise, both an electron and a photon object are created. This object is marked explicitly as ambiguous, leaving the final classification decision to each analysis. In the $H \to \gamma\gamma$ analyses reported in this manuscript, all the ambiguous objects are retained as photons in order to preserve the maximum photon reconstruction efficiency.

Finally, since the energy calibration depends on matched tracks and conversion vertices, the electrons and photons object are re-calibrated with the procedure outlined in Section 3.4. The performance of the reconstruction efficiency for electron, converted photons and unconverted photons is reported in Figure 3.6. Electron are reconstructed with 80% efficiency if they have a true $E_{\text{T}} > 5\,\text{GeV}$ and with more than 95% for $E_{\text{T}} > 10\,\text{GeV}$. Converted photons have a reconstruction efficiency around 70% with a mild pileup dependence, while unconverted photons are usually very well reconstructed, with a few percent mis-identification fraction in events with high pileup, especially from single track conversions.

3.3 Ambiguous objects classification

As mentioned above, the final decision on the classification of ambiguous objects obtained from the procedure in Figure 3.5 is delegated to the analysis level. Usually, the choice is to classify these candidates all as photons or as electrons. In $H \to \gamma\gamma$ analyses, for example, all the ambiguous objects are classified and calibrated as photons, in order to retain the highest possible selection efficiency. This choice can have drawbacks when a background process producing electrons is enriching a signal region selecting photons (or vice-versa). This is the physics case of $H \to \gamma\gamma$ low mass analysis [83], that searches for light Higgs-like resonances in the diphoton invariant mass

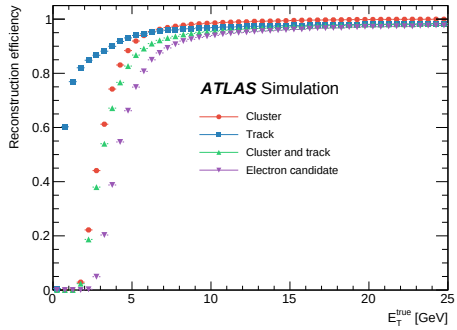

(a) Electron

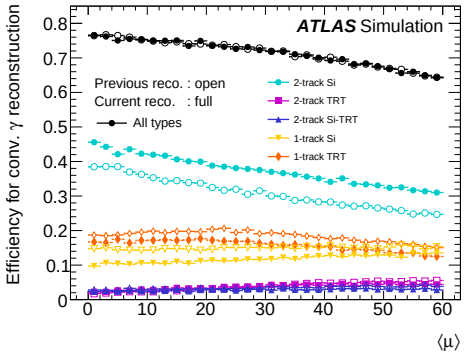

(b) Converted photon

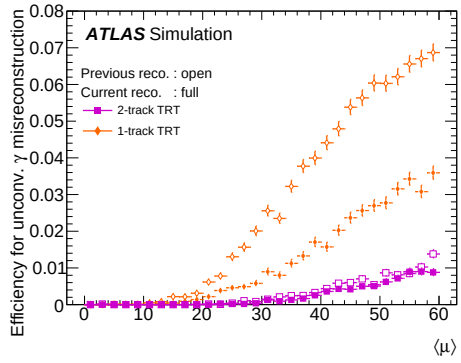

(c) Unconverted photon

Figure 3.6 – (a) The cluster, track, cluster and track, and electron reconstruction efficiencies as a function of the generated electron E_{T}. (b) Converted photon reconstruction efficiency and contributions of the different conversion types as a function of $<\mu>$. (c) Probability of an unconverted photon to be mistakenly reconstructed as a converted photon and contributions of the different conversions types. Figures (b) and (c) report a comparison between the offline reconstruction [80] described in Section 3.2 and the old one based on fixed-size clusters [81].

region $m_{\gamma\gamma} \in [65, 110]$ GeV: in this region, the Drell-Yan $Z \to ee$ process with both electrons mis-identified as photons enters the analysis signal region, generating a peak in the $m_{\gamma\gamma}$ distribution around 90 GeV. The usual choice to retain all ambiguous objects as photons candidates provides the best photon selection efficiency but at the same time the worst background rejection. Therefore in order to allow the analyses to choose the optimal ambiguous object selection for their needs, a BDT algorithm has been developed as detailed in the following.

3.3.1 Algorithm description

In order to create a predictive model, the BDT is trained on simulated single-particle samples of electrons or photons with energy from a few GeV up to a few TeV, with simulated pileup and almost flat p_{T} and η distributions. The training dataset is composed of single particle MC events of electrons or photons, which have been fully reconstructed and classified as ambiguous candidates. Usually, the simulated electron sample is composed by 8% of the objects classified as ambiguous, but in the simulated photon sample this component rises up to 31% of the objects. As can be observed in Figure 3.7, most of the ambiguous objects in the true photon samples are forward candidates, as this reflects the increase in photon conversion probability following the material profile in front of the calorimeter and the denser environment due to pileup.

Each ambiguous candidate is reconstructed both as electron and photon, therefore it carries the properties of both the candidates. The BDT is trained with input variables related to both electron tracks and photon conversion extract for each single ambiguous object.

- Electron tracks variables: the general idea is that true electrons have generally more hits in the ID with respect to photons, because a large amount of the latter are still unconverted in the silicon tracker. Therefore ambiguous candidates coming from electrons usually have higher track hits multiplicity, start sooner in the detector, produce a hit in the innermost available Inner Detector layer. Moreover, real electrons usually have a better match between the energy measured from the track and cluster, while in case of converted photons the associated track might be one of the two conversion tracks. The following variables are therefore considered and shown in Figure 3.7: $B^{trk}_{inmostHits}$ is a boolean variable representing if a track has or not a hit in the first expected layer of the Inner Detector, $N^{trk}_{pixHits}$ and N^{trk}_{SiHits} representing the number of hits for an electron track in Pixel and Silicon detectors respectively, the E/p ratio where E is the energy of the calorimetric cluster associated to the track with momentum p, and finally z_0^{trk} the starting z coordinate of the track.

- Photon conversion variables: true electrons reconstructed as ambiguous objects usually have a photon conversion position closer to the interaction point as their track starts exactly in the primary vertex, a softer conversion track p_{T} distribution due to mis-associated tracks coming from pileup, and they usually have one of the conversion track that carries almost all the conversion system momentum.

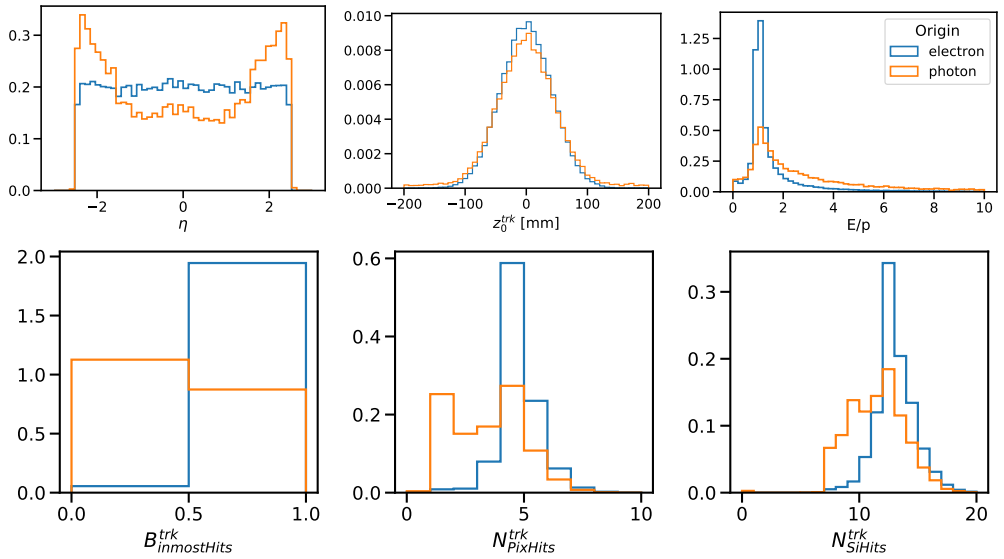

Figure 3.7 – Normalized distributions of electron variables used for BDT training for simulated and reconstructed ambiguous objects when originated by an electron (blue) or a photon (orange) candidate.

Therefore, the following variables are considered and shown in Figure 3.8: the longitudinal z_{conv} and radial R_{conv} coordinates of the conversion, the transverse momentum of the two tracks originating from the conversion ($p_{\mathrm{T}}^{trk1,conv}$ and $p_{\mathrm{T}}^{trk2,conv}$) and the one of the conversion system (p_{T}^{conv}), the ratio of the highest momentum conversion track over the momentum of the conversion system $p_{\mathrm{T}}^{trk1,conv} / p_{\mathrm{T}}^{conv}$.

In addition, the calorimetric cluster energy and η are included as input variables in order to allow the BDT to adapt to different kinematic regimes of the reconstructed ambiguous candidates. The algorithm is trained with the LightGBM package, using the binary cross entropy as optimization loss.

3.3.2 Results

The algorithm performance is visualized by the Receiver Operating Characteristic (ROC) curve: this shows the efficiency of selecting an ambiguous candidate as an electron when it was generated by an electron ($P_{e|e}$) versus the efficiency of selecting an ambiguous object as a photon when generated by a photon ($P_{\gamma|\gamma}$), while varying the classification threshold imposed on the BDT score. Evaluating the integral underneath this curve produces an overall performance score for the algorithm called Area-Under-the-Curve (AUC), which approaches 1 for the optimal classifier. The ROC curve and the corresponding AUC are shown in Figure 3.9. The BDT model hyper-parameters have been optimized in order to obtain the best possible AUC. The most important variables in the training are electron E/p and $B^{trk}_{inmostHits}$.

The BDT was tested in the physics scenario represented by the rejection of the $Z \to ee$

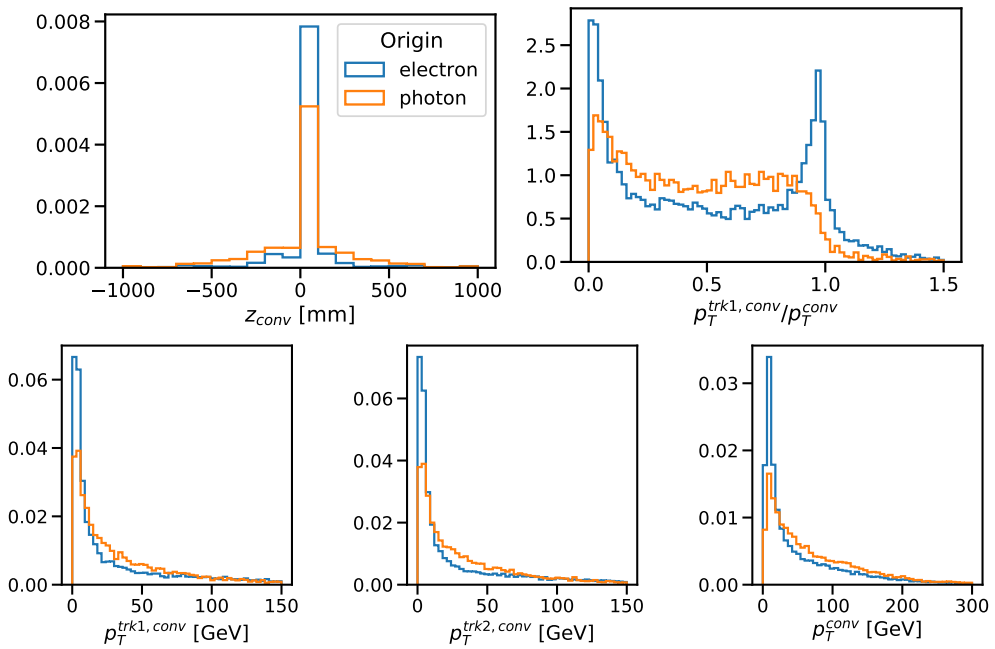

Figure 3.8 – Normalized distributions of photon conversion variables used for BDT training for simulated and reconstructed ambiguous objects when originated by an electron (blue) or a photon (orange) candidate.

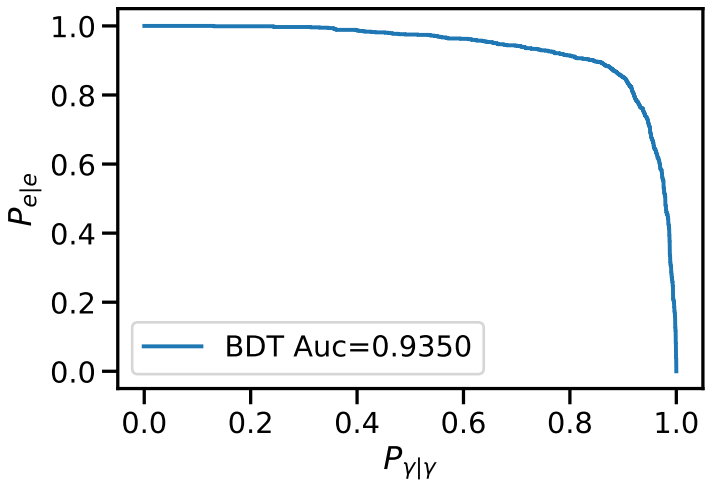

Figure 3.9 – ROC curve and AUC value for the BDT trained to classify ambiguous candidate in electrons and photon. The curve is calculated by varying the threshold applied to the BDT score to classify a object as photon or electron, and computing the probability of selecting a photon when it was simulated as a photon ($P_{\gamma|\gamma}$) or selecting an electron when it was simulated as an electron ($P_{e|e}$).

background in the $H \to \gamma\gamma$ low mass analysis search. As mentioned, the electron and positron produced in the Z boson decay could be both mis-identified as two well reconstructed photons. In particular, converted photons are subject to larger mis-identification rate with respect to unconverted ones due to the additional track-to-cluster association step required. The events are selected by requiring two well reconstructed photons, with similar criteria to the ones reported in Section 4.3. For processes producing prompt photons like $H \to \gamma\gamma$ or QCD $\gamma\gamma$ production, selected events are composed by around 60% of events with both photons directly reconstructed as photons and 40% of the events with at least one object reconstructed as ambiguous and then retained as photon candidate. From these numbers it is clear why in $H \to \gamma\gamma$ analyses it has been decided to retain all ambiguous object selected by the analysis chain as photon candidates: in case the ambiguous objects are classified as electrons, 40% of the signal is lost. On the other hand, the composition dramatically change for a process producing electrons like the Drell-Yan $Z \to ee$, where 94% of the selected events contain at least one object classified as ambiguous and then retained as a photon. The BDT algorithm allows a powerful and flexible resolution of the ambiguity between photons and electrons, by selecting an optimal working point which ensures the largest background rejection but retaining good signal efficiency. In order to apply the BDT to diphoton events, a BDT event score should be built based on the BDT score for each of two objects present in the event. A simple approach is to build an event score as

$$s^{evt} = \min\left(s^{\gamma_1}, s^{\gamma_2}\right)$$

with s^{evt} being the BDT score for the event and s^{γ_i} being the score for the two selected photon candidates; in case only one of the two photons in the event has been classified as ambiguous, the event score reduces to $s^{evt} = s^{\gamma}$. The selection efficiencies computed on simulated MC samples for the $H \to \gamma\gamma$ signal process (with $m_H = 80\,\text{GeV}$), and the two main background processes QCD $\gamma\gamma$ and Drell-Yan $Z \to ee$ are reported in Figure 3.10. Setting the threshold to 0 is equivalent to consider all the ambiguous objects as photon candidates, while setting it to 1 is equivalent to consider all the objects as electrons. It can be observed that choosing a BDT score threshold near 0.25 maintains around 99% signal efficiency while rejecting 70% of the $Z \to ee$ background process in the diphoton selection. The impact is larger in categories in which at least one of the two photons is converted. This large reduction can be also visualized in the diphoton invariant mass plot reported in Figure 3.11, where only the Drell-Yan $Z \to ee$ and QCD $\gamma\gamma$ simulated background processes are shown: the peak around 90 GeV produced by $Z \to ee$ events is smoothed out by the application of this BDT selection, while the global normalization of the QCD $\gamma\gamma$ component is unaffected. The inclusion of this BDT selection in the low mass analysis is currently under discussion.

3.4 Photon and electron energy calibration

A precise calibration of the energy measurement of electrons and photons is required for many ATLAS analyses, among which the studies of the Higgs boson mass measurement

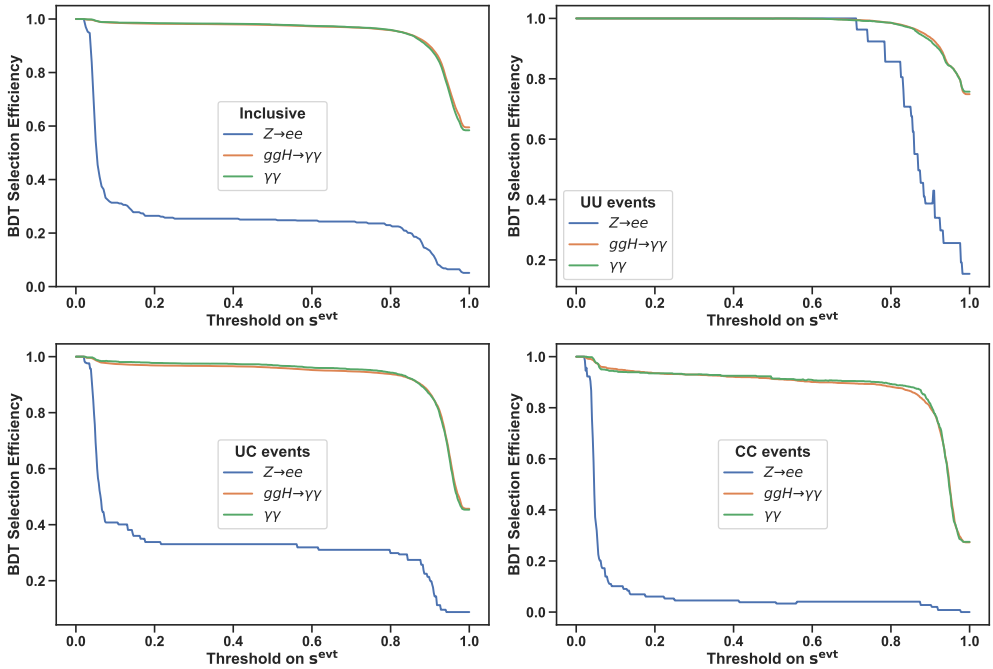

Figure 3.10 – Ambiguity BDT selection efficiency evaluated as function of the BDT event score s^{evt}, for simulated events of Drell-Yan $Z \to ee$ (blue), ggF (orange) and QCD $\gamma\gamma$ production (green) processes, selected with ambiguous objects classified as photons and by requiring two well reconstructed photons. The top left plot shows this inclusive diphoton selection, while in the other three plots the two photons are categorized by their conversion statuses: both photons unconverted (UU, top right), at least one converted (UC, bottom left) and both converted (CC, bottom right).

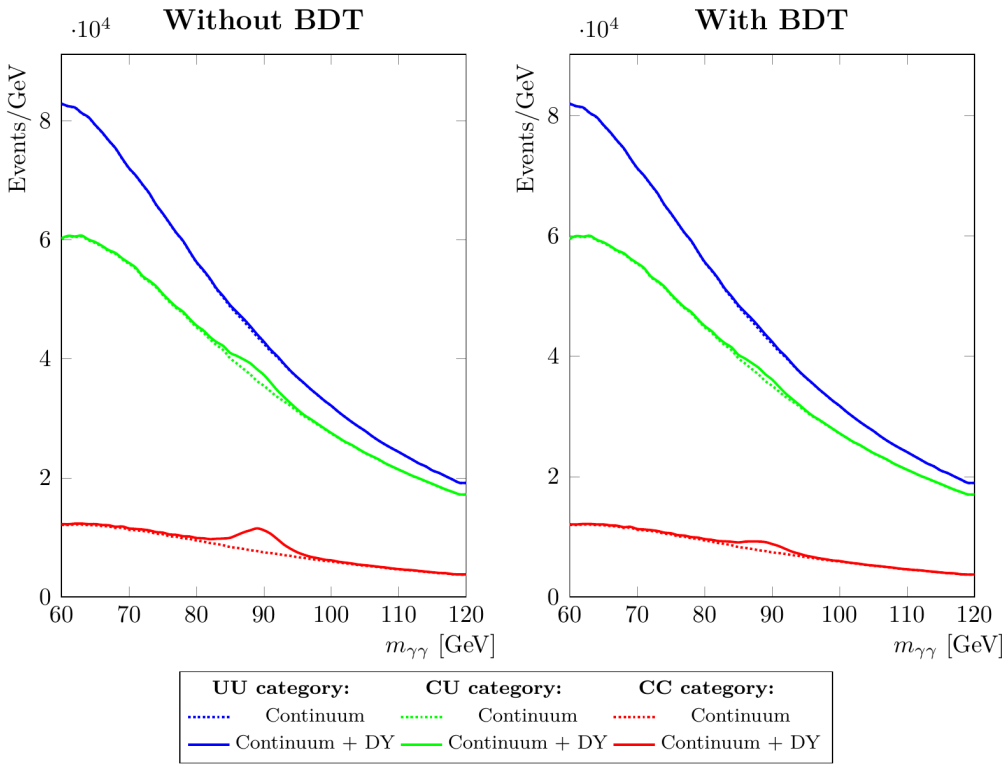

Figure 3.11 – Diphoton invariant mass distributions for simulated continuum QCD $\gamma\gamma$ process (dashed) and summed up with Drell-Yan $Z \to ee$ process (solid), without selection on the BDT score (left) and with a BDT event score selection around 0.25 (right). The colors represent the category based on conversion status of the selected photon candidates, both unconverted (UU, blue), at least one converted (UC, green) and both converted (CC, red). The distributions are not stacked.

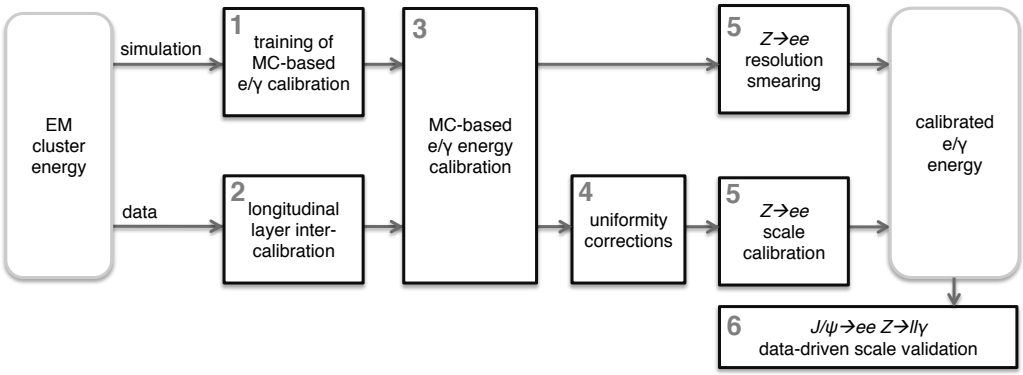

Figure 3.12 – The e/γ calibration procedure applied both on MC simulation (upper part) and data (lower part) [84].

in both the $H \to \gamma\gamma$ and $H \to 4\ell$ decay channels. The full calibration chain is outlined in Figure 3.12.

The starting point of the calibration procedure is the sum of the cell energies contained in the supercluster, (E_{raw}): since the cells are calibrated to the electromagnetic energy deposited in the cells volumes, E_{raw} does not account for the finite dimension of the cluster and the presence of inactive material upstream of and inside the calorimeter. These effects are corrected for both photons and electrons using a MC based multivariate (MVA) regression algorithm using the properties of the shower development in the EM calorimeter, like the ratio of the various E_{raw} energies in different layers, η of the cell edges, the periodicity of the lead absorber in each region, the radius of the conversion, and so on. A *Boosted Decision Tree* (BDT) regression is trained to correct the uncalibrated energies E_{raw} of electrons, converted and unconverted photons candidate separately [85].The MVA algorithm uses information on the correlations between the set of input training variables and the target E_{true}/E_{raw} to derive a correction factor for the target variable. This correction factor is then applied to E_{raw} to retrieve the calibrated energy.

This MVA calibration is applied to both MC and data samples. Since the EM calorimeter is longitudinally segmented, the scales of the different longitudinal layers have to be equalized in data with respect to simulation, prior to the MC based calibration. This is called layer "intercalibration", it is applied to first two layers and it is computed by comparing the energy deposits in data and simulated samples of $Z \to \mu\mu$ events, since the muon signal is not influenced by the amount of material in front of the calorimeter. The results are cross-checked using $Z \to ee$ decays by investigating the variation of the mean of the dielectron invariant mass as a function of the ratio of the energies of the electron or positron candidates in the first two layers. Similarly, also the presampler energy scale is determined from the ratio of the presampler energies in data and simulation. The measured energy in the presampler for electrons from Z boson decays is sensitive to both this scale and the amount of material in front of the presampler.

Moreover, after the MVA energy calibration, data are further corrected to include any

real detector inefficiency which is not included in MC samples: these are due to the non nominal setup of the LAr high voltage system, geometric effects such as the intermodule widening induced by gravity (i.e. the gap between the barrel EM modules are widened due to a gravity-induced sagging effect that is not included in the simulation), and bias introduced by the LAr hardware electronic calibration. The latter is of particular importance for the $H \to \gamma\gamma$ decay: the analogue raw signal reaching front-end electronic of the calorimeter is indeed pre-amplified and then shaped by a multi-gain bipolar filter, which has three overlapping linear gain scales in the ratio 1/10/100 (Low, Medium and High Gain) in order to accommodate the full range of particle energies produced in the collisions; the electrons coming from a Z boson usually have their middle layer cell energies readout using the High Gain (HG) of the LAr electronic, while about the 30% of the $H \to \gamma\gamma$ events have a photon reconstructed with at least one cell in Medium Gain (MG), given their harder p_{T} spectrum. In order to estimate the relative intercalibration between MG and HG, a special dataset with a different threshold between MH and HG has been recorded, so that electrons from Z boson decay have at least the highest-energy cell in Layer 2 recorded in the MG readout. This permits to compute a relative energy scale used for L2 gain correction, which is assigned as a systematic uncertainty (see Section 3.4.1).

Finally, corrections of the energy scale in data and of the energy resolution in simulation are applied. The overall electron response in data is calibrated so that it agrees with the expectation from simulation, using a large sample of $Z \to ee$ events. The MC simulations resolution is smeared to correctly match the one observed in data. The scale factors and smearing are assumed to be valid both for photons and electrons in their whole energy ranges. The invariant mass distribution for $Z \to ee$ candidates for data and simulation after the energy scale correction has been applied to the data and the resolution correction to the simulation is shown in Figure 3.13a, while the relative variation with pileup of the peak position of m_{ee} is shown in Figure 3.13b.

To validate the calibration chain which is based on $Z \to ee$ event reconstruction, low energy electrons from $J/\psi \to ee$ and photons from $Z \to \ell\ell\gamma$ events are used. In particular for photons, the radiative Z decay is employed to derive residual energy data to MC scale factors for the photons, which are usually found to agree with zero within the uncertainty and are therefore not applied.

3.4.1 Systematic uncertainties

Several systematic uncertainties impact the measurement of the energy of electrons or photons in a way that depends on their transverse energy and pseudorapidity [85]. Some of these are of particular importance for the mass analysis described in Chapter 6 and will be briefly discussed in this section. The Figure 3.14 report a summary of the impact for main systematic uncertainties for electrons and photons.

The Z-based calibration fixes the energy scale and its uncertainty for electrons with transverse energy close to the average of those produced in Z decays ($p_{\mathrm{T}} \sim 45\,\mathrm{GeV}$). Photons produced in $H \to \gamma\gamma$ decay have a harder p_{T} spectrum so the uncertainties have to be extrapolated and the impact is generally larger. Most of these impacts on

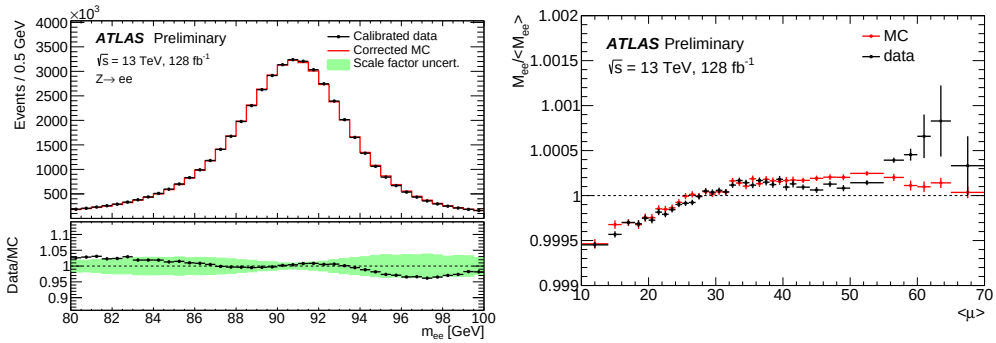

(a) **(b)**

Figure 3.13 – (a) Comparison between data and simulation of the invariant mass distribution of the two electrons in the selected $Z \to ee$ candidates, after the calibration and resolution corrections are applied. The total number of events in the simulation is normalized to the data. The bottom panel presents the resolution correction factors with the uncertainty band which represents the impact of the uncertainties in the calibration. (b) Relative variation of the peak position of the reconstructed dielectron mass distribution in $Z \to ee$ events as a function of the average number of interactions per bunch crossing. The error bars represent the statistical uncertainties [86].

photon energy are computed separately for reconstructed converted and unconverted photons: indeed the converted photons have a shower development more similar to that of electrons and therefore usually smaller energy scale systematic uncertainties than unconverted photons.

- One of the largest impact of photon energy scale systematic, in particular for unconverted photon with $p_{\mathrm{T}} > 60\,\mathrm{GeV}$ is due to the non-linearity of Layer2 gain cell energy measurement (MG/HG gain). The linearity of the readout electronics is better than 0.1% in each of the three gains but the relative calibration of the different readout gains is less well known. The full intercalibration difference (with an average of 0.2% and with a maximum of 0.4% in the $0.8 < |\eta| < 1.37$ region) is taken as systematic uncertainty.

- A similarly large systematic impact on photon energy scale, in particular for unconverted photons, is provided by the intercalibration of Layer1 and Layer2 ($\alpha_{1/2}$). This systematic is computed from $Z \to \mu\mu$ events ($\alpha_{1/2\mu}$) and an additional uncertainty is assigned for this muon-based measurement to electrons. Uncertainties from the intercalibration measurement are propagated to the energy scale with an (E_{T}, $|\eta|$) parametrization and contributing up to $\pm 0.2\%$ impact for unconverted photon with $p_{\mathrm{T}} > 60\,\mathrm{GeV}$. The uncertainties due to the measurement of the presamples energy scale (α_{PS}) is propagated too and it has generally a smaller impact of $\pm 0.1\%$.

- Mis-modeling of the lateral electromagnetic shower development can create differences between data and Monte Carlo simulation on the relative energy response for

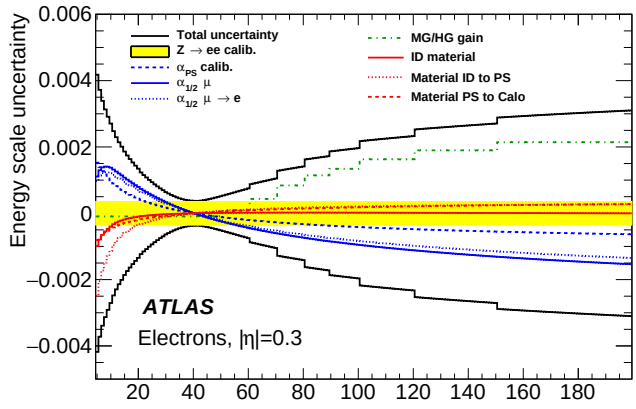

(a) Electron

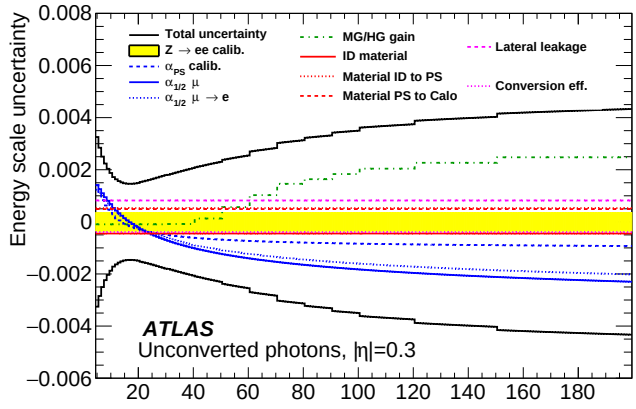

(b) Unconverted photon

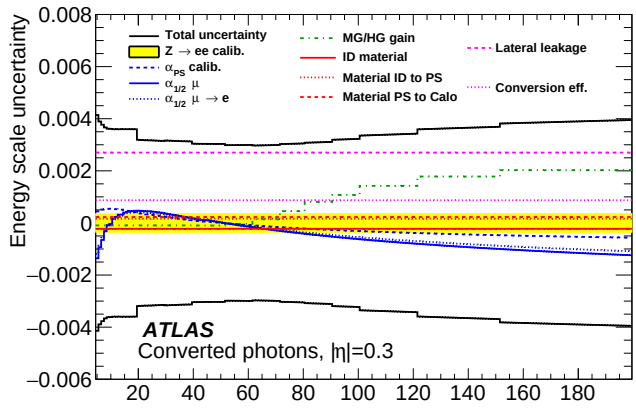

(c) Converted photon

Figure 3.14 – Fractional energy scale calibration uncertainty for (a) electron, (b) unconverted photon and (c) converted photons, as a function of E_{T} for $|\eta| = 0.3$. The total uncertainty is shown as well as the main contributions, which are represented by the signed impact of a one-sided variation of the corresponding uncertainty. Only a one-sided variation for each uncertainty is shown for clarity [85].

electrons and between electron and photons. The first is accounted for by measuring the peak position of the dielectron m_{ee} distribution as a function of the shower width in the first layer (which is very granular in η). The latter is due to the difference interaction probability with the material in front of the calorimeter and it is measured comparing the size of enlarged clusters in Layer2 for electron and photons from $Z \to ee$ and $Z \to ee\gamma$ events. The largest deviation is observed for converted photons with a 0.25% impact, that makes this the dominant uncertainty source for converted photons.

- The Inner Detector, cryostat and calorimeter material uncertainties are obtained by comparing the energy response in Monte Carlo samples simulated with nominal and modified detector geometry. The difference in the energy response are scaled comparing the material variation of the corresponding distorted simulated sample with the actual material measurement uncertainties, yielding to the energy scale uncertainties. These are usually parametrized in many different η bins and subdominant with respect to other sources.

- Since the MVA used to predict the correct cluster energy is trained separately for reconstructed converted and unconverted photons, difference between misclassification rate in conversion category between data and simulation can create a bias on the energy scales for photons. The systematic uncertainty is computed by using $Z \to \mu\mu\gamma$ events comparing the photon longitudinal shower shape estimating photon conversion efficiency and fake rate in both data and simulation. For photons with $E_{\mathrm{T}} = 60\,\mathrm{GeV}$, the uncertainty in the energy scale is about 0.04% (0.2% to 0.02%) in the barrel (endcap) for reconstructed unconverted photon candidates and about 0.05% (0.005%) in the barrel (endcap) for reconstructed converted photon candidates.

The typical photon energy scale systematic uncertainty for $E_{\mathrm{T}} = 60\,\mathrm{GeV}$ ranges between 0.2% to 0.3% averaged over the barrel and 0.45% to 0.8% in the endcap. For this value of E_{T}, the uncertainties from the relative calibration of the different layers is significantly smaller for converted photons than for unconverted photons as they have a longitudinal shower development closer to that of $E_{\mathrm{T}} = 40\,\mathrm{GeV}$ electrons. The cell energy non-linearity uncertainty is higher for unconverted photons as they have a higher probability to use Medium Gain readout in the second layer, given that they deposit a higher energy fraction in the second calorimeter layer.

3.5 Photon performance

In order to target events where a Higgs boson decays in a pair of photons, an excellent rejection of background from jets is needed while maintaining high efficiency for real photons. After reconstruction, additional selections (see Section 4.3) are therefore applied both on photon kinematics and object quality. The identification and isolation selections are discussed in this section.

3.5.1 Photon identification

The photon identification criteria are designed to efficiently select prompt, isolated photons and reject backgrounds from hadronic jets. The photon identification is based on one-dimensional selection criteria over *shower shape* variables, reported in Table 3.1 and depicted in Figure 3.15, constructed using the information collected by the ATLAS calorimeter system and providing a good separation power between prompt photons and jets. Jets in fact are expected to produce deeper and wider showers and therefore the leakage in the hadronic calorimeter should be larger than for photons. The fine segmentation of the EM calorimeter first layer is exploited to identify jets where a neutral meson (for example π^0) carries most of the jet p_{T} and then decays in two photons. Two separated maxima in the first layer are expected to be reconstructed in this case: shower shapes variables are defined to identify these cases.

The identification selections are labeled as Loose, Medium and Tight, with an increasing background rejection capabilities. These photon selections are used for both online and offline algorithm: in particular Loose is the main selection used in the triggering of photon but the Medium selection, which adds a loose cut on E_{ratio}, became the main trigger selection at the beginning of 2017, in order to reduce the rate to an acceptable level. The Medium identification criteria is not supported for offline analysis. Because the shower shapes vary due to the geometry of the calorimeter, the cut-based selection of Loose, Medium are optimized separately in bins of $|\eta|$. The Tight selection is optimized by using a multivariate technique, trained on MC simulations, separately in bins of $|\eta|$, E_{T} and conversion status, since the shower shapes of converted photons differ from unconverted photons due to the opening angle of the conversion pair, which is amplified by the magnetic field, and from the additional interaction of the conversion pair with the material upstream of the calorimeters.

The Loose photon identification provides 99% efficiency for a photon of $E_{\mathrm{T}} > 40\,\mathrm{GeV}$ and the corresponding background rejection factor is about 1000. The Tight selection has a 85% efficiency for a photon of $E_{\mathrm{T}} > 40\,\mathrm{GeV}$ and increases for $E_{\mathrm{T}} > 100\,\mathrm{GeV}$ to around 92% for unconverted photons and 95% for converted ones, as shown in Figure 3.16 and Figure 3.17. The corresponding background rejection factor is about 5000. The photon identification efficiency is measured in data by means of three different methods [87]: the first uses an inclusive-photon production data selection, the second uses photons radiated from leptons in $Z \to \ell\ell\gamma$ decays, and the third uses electrons from $Z \to ee$ decays, with a method that transforms the electron shower shapes to resemble the photon shower shapes. Data to MC scale factors are derived with these methods and their uncertainty is considered as systematic uncertainty on the photon identification selection. These factors differ from one by up to 3–4% at $E_{\mathrm{T}} = 10\,\mathrm{GeV}$ and at most by 1–2% above $E_{\mathrm{T}} = 40\,\mathrm{GeV}$, with an uncertainty decreasing from about 10% at $E_{\mathrm{T}} = 10\,\mathrm{GeV}$ to $<$ 1%–2% at higher E_{T}.

3.5.2 Photon isolation

The activity near photons can be quantified from the tracks of nearby charged particles, or from energy deposits in the calorimeters, leading to two classes of isolation variables.

Category	Description	Name	Loose	Medium	Tight
Hadronic leakage	Ratio of E_{T} in the first sampling of the hadronic calorimeter to E_{T} of the EM cluster (used over the range $\lvert\eta\rvert < 0.8$ or $\lvert\eta\rvert > 1.37$)	R_{had_1}	✓	✓	✓
	Ratio of E_{T} in all the hadronic calorimeter samplings to E_{T} of the EM cluster (used over the range $0.8 < \lvert\eta\rvert < 1.37$	R_{had}	✓	✓	✓
EM 2$^{\mathrm{th}}$ layer	Ratio in η of cell energies in 3×7 cells over 7×7	R_{η}	✓	✓	✓
	Lateral width of the shower	w_{η_2}	✓	✓	✓
	Ratio in ϕ of cell energies in 3×3 cells over 3×7	R_{ϕ}			✓
EM 1$^{\mathrm{th}}$ layer	Shower width calculated from three strips around the strip with maximum energy deposit	w_{s_3}			✓
	Total lateral shower width	$w_{s_{\mathrm{tot}}}$			✓
	Energy outside the core of the three central strips but within seven strips divided by energy within the three central strips	F_{side}			✓
	Difference between the energy associated with the second maximum in the strip layer and the energy reconstructed in the strip with the minimum value found between the first and second maxima	ΔE			✓
	Ratio of the energy difference associated with the largest and second largest energy deposits to the sum of these energies	E_{ratio}		✓	✓

Table 3.1 – Photon shower shape variables and identification criteria definitions [88]

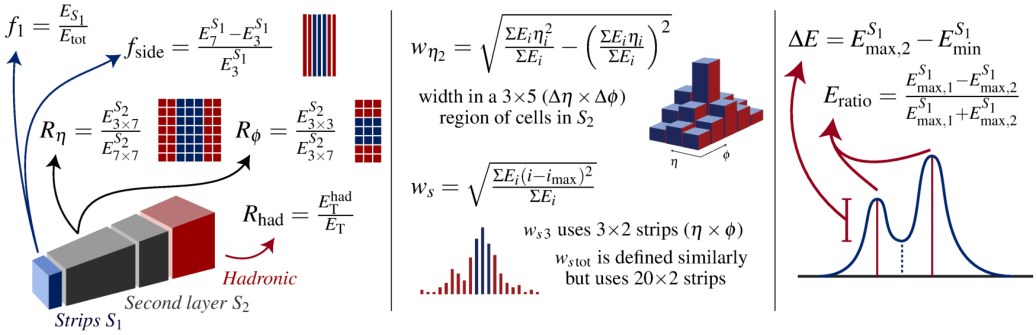

Figure 3.15 – Schematic representation of the photon identification discriminating variables. $E_C^{S_N}$ identifies the electromagnetic energy collected in the N-th longitudinal layer of the electromagnetic calorimeter in a cluster of properties C, identifying the number and/or properties of selected cells. E_i is the energy in the i-th cell, η_i the pseudorapidity centre of that cell [89].

The raw calorimeter isolation $E_{\text{T}}^{\text{iso}}$ is built by summing the transverse energy of positive-energy topological clusters whose barycentre falls within a cone centred around the photon cluster barycentre. The photons energy is removed from the core of the cone eliminating 5×7 cells in $\eta \times \phi$ around the cluster barycentre. This quantity is corrected for the leakage of the EM energy outside this subtraction window, with a photon E_{T} and $|\eta|$ dependent paramaterization. Additionally, a correction for the pile-up and underlying-event contribution to the isolation cone is also estimated on a event-by-event basis. The corrected calorimetric isolation variable obtained with this procedure is called E_{T}^{cone} and can be computed in a cone size of $\Delta R = 0.2$ or 0.4.

Similarly, a track isolation variable p_{T}^{cone} is defined by summing the transverse momenta of selected tracks within a cone centered around the photon cluster direction and excluding tracks matched to the converted photon. The sum is performed over all tracks with $p_{\text{T}} > 1\,\text{GeV}$ and $|\eta| < 2.5$, with at least seven silicon hits and at most one shared hit, two silicon and one pixel missing hits in the track.

Three photon isolation operating points are defined using requirements on the calorimeter and track isolation variables, as summarized in Table 3.2. Photon isolation efficiency is computed with radiative Z boson decay and with inclusive-photon production data selection, similarly to photon identification. The different results are combined to obtain one set of scale factors per working point, data-taking year, and photon conversion status. The evolution of the isolation efficiency from $Z \to \ell\ell\gamma$ measurement as a function of E_{T}, η and conversion status is illustrated in Figure 3.18, together with the data/MC efficiency ratio. For $25 < E_{\text{T}} < 100\,\text{GeV}$, the combination of the two measurement reduces the scale factor uncertainties to about 1% on average.

3.6 Electron performance

Similarly to photons, in order to determine if electron is a prompt object or if it is originated by hadron decays, an identification algorithm is applied to electron candidates,

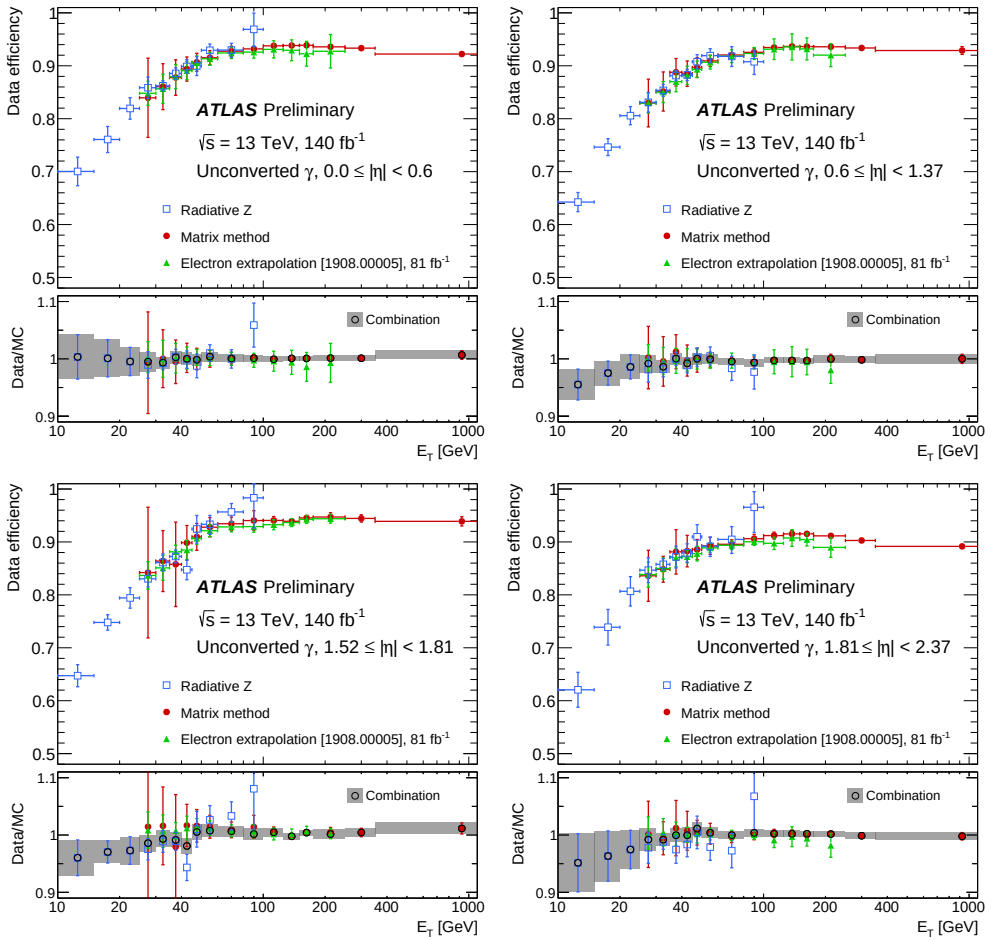

Figure 3.16 – The Tight photon identification efficiency, and the ratio of data to MC efficiencies, for unconverted photons, as a function of E_{T} in four different $|\eta|$ regions. Efficiencies are computed by means of three different measurement. The combined scale factor, obtained using a weighted average of scale factors from the individual measurements, is also presented; the band represents the total uncertainty [90].

Working point	Calorimeter isolation	Track isolation
Loose	$E_{\mathrm{T}}^{cone20} < 0.065 \times E_{\mathrm{T}}$	$p_{\mathrm{T}}^{cone20}/E_{\mathrm{T}} < 0.05$
Tight	$E_{\mathrm{T}}^{cone40} < 0.022 \times E_{\mathrm{T}} + 2.45\,\mathrm{GeV}$	$p_{\mathrm{T}}^{cone20}/E_{\mathrm{T}} < 0.05$
TightCaloOnly	$E_{\mathrm{T}}^{cone40} < 0.022 \times E_{\mathrm{T}} + 2.45\,\mathrm{GeV}$	-

Table 3.2 – Definition of the photon isolation working points [80].

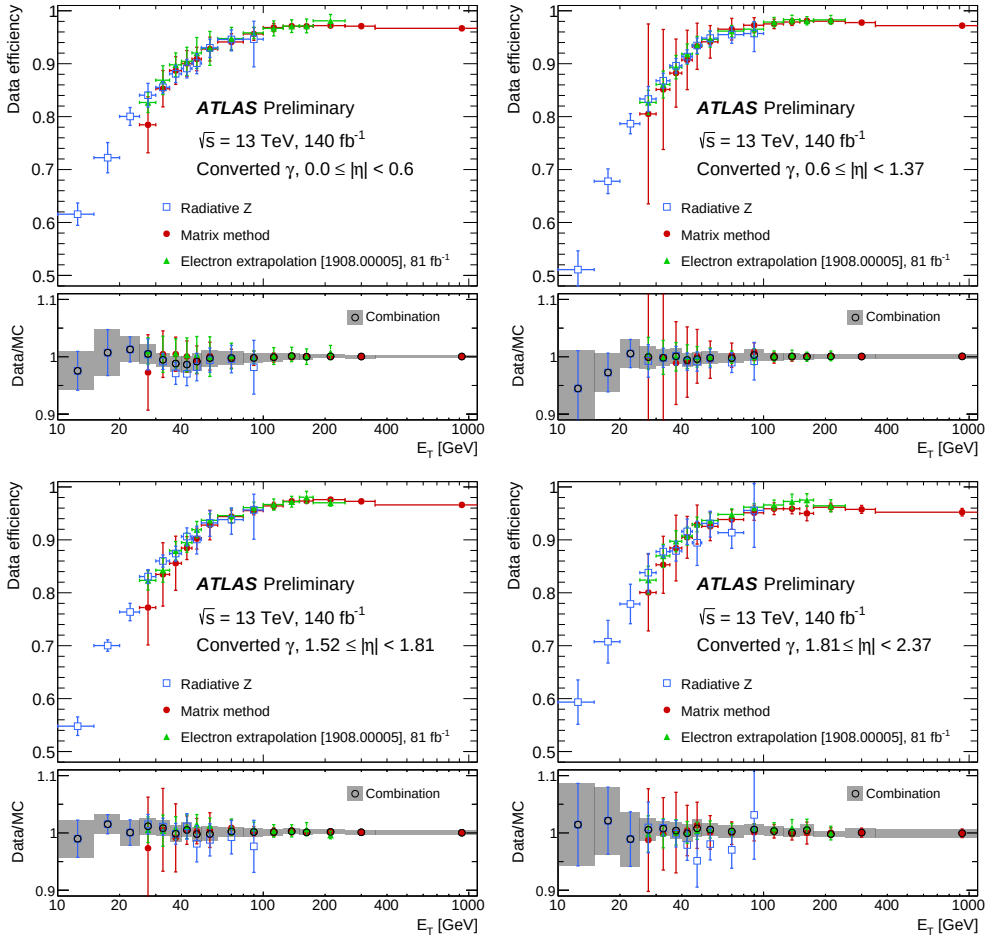

Figure 3.17 – The Tight photon identification efficiency, and the ratio of data to MC efficiencies, for converted photons, as a function of E_{T} in four different $|\eta|$ regions. Efficiencies are computed by means of three different measurement. The combined scale factor, obtained using a weighted average of scale factors from the individual measurements, is also presented; the band represents the total uncertainty [90].

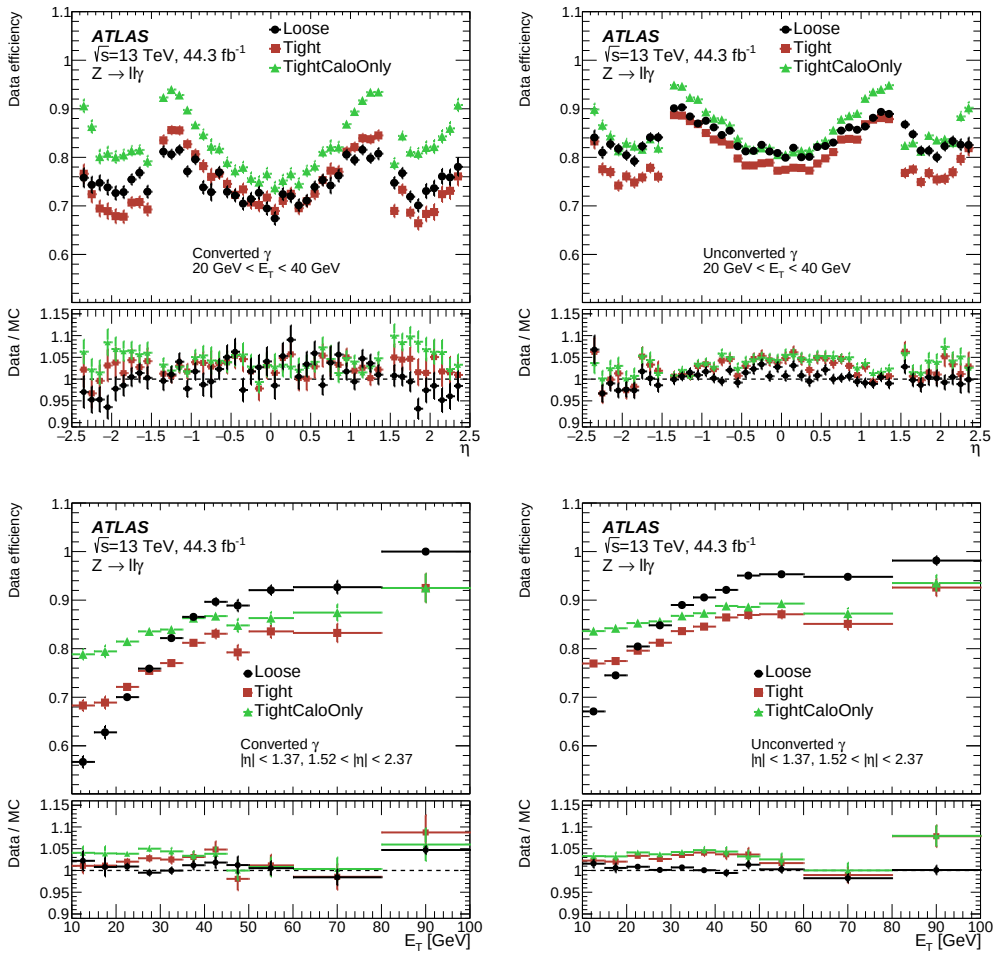

Figure 3.18 – Efficiency of the photon isolation working points, using $Z \to \ell\ell\gamma$ events, for converted (left) and unconverted (right) photons as a function of photon η (top) and E_{T} (bottom). The lower panel shows the ratio of the efficiencies measured in data and in simulation. The total uncertainty is shown, including the statistical and systematic components [80].

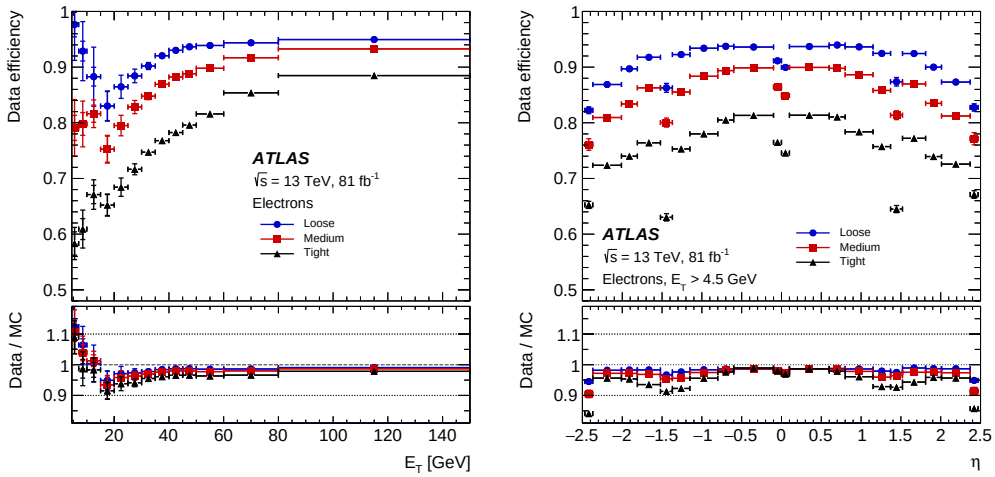

Figure 3.19 – The electron identification efficiency in $Z \to ee$ events in data as a function of E_{T} (left) and as a function of η (right) for the Loose, Medium and Tight operating points [80].

based on a log-likelihood ratio between the probability to originate from signal or background. The probability density functions for both are calculated by smoothing the histograms of 13 typical identification variables with an adaptive kernel density estimator. These distributions are extracted from data, selecting events from $Z \to ee$ and $J/\psi \to ee$ processes using a tag-and-probe technique [91] for the signal and events with at least one electron represents background; this sample is primarily composed by dijets events and genuine electrons from $W \to e\nu$ and $Z \to ee$ processes are suppressed using dedicated selection criteria. The identification variables are similar to the one employed for photon identification with the addition of information extracted from track conditions, TRT identification and track to cluster association, as reported in Table 3.3. Three working points (Loose, Medium and Tight) are provided, based on the likelihood values plus additional rectangular requirements on other identification variables, and are optimized separately in $|\eta|$ and E_{T} bins [80]. The Medium identification selection used in the $H \to \gamma\gamma$ analyses has an efficiency on average of 88% for electrons in typical electroweak processes, with a gradually increase from low to high E_{T} as shown in Figure 3.19.

In addition to the identification criteria described above it is possible to require electrons to fulfill isolation requirements, like for photons, to further discriminate between signal and background. The calorimeter-base variable E_{T}^{cone} is computed in the same way as described in Section 3.5.2, while track-based selection is slightly modified. Since for electrons produced in the decay of high-momentum heavy particles, other decay products can be very close to the electron direction, a variable cone size $p_{\mathrm{T}}^{varcone}$ is used which shrinks for larger transverse momentum as $\Delta R = \min(10/p_{\mathrm{T}}[\mathrm{GeV}], \Delta R_{max})$, where ΔR_{max} is the maximum cone size (usually 0.2). The available selection requirements are reported in Table 3.4. The Gradient working point is designed to give an efficiency of 90% at $p_{\mathrm{T}} = 25\,\mathrm{GeV}$ and 99% at $p_{\mathrm{T}} = 60\,\mathrm{GeV}$, uniform in η. The three other working points, HighPtCaloOnly, Loose and Tight, have a fixed requirement on the calorimeter

Category	Description	Name
Hadronic leakage	Ratio of E_{T} in the first sampling of the hadronic calorimeter to E_{T} of the EM cluster (used over the range $\lvert\eta\rvert < 0.8$ or $\lvert\eta\rvert > 1.37$)	R_{had_1}
	Ratio of E_{T} in all the hadronic calorimeter to E_{T} of the EM cluster (used over the range $0.8 < \lvert\eta\rvert < 1.37$	R_{had}
EM 3$^{\mathrm{th}}$ layer	Ratio of the energy in the back layer to the total energy in the EM accordion. This variable is only used below 100 GeV because it is known to be inefficient at high energies	f_3
EM 2$^{\mathrm{th}}$ layer	Ratio in η of cell energies in 3×7 cells over 7×7	R_η
	Lateral width of the shower	w_{η_2}
	Ratio in ϕ of cell energies in 3×3 cells over 3×7	R_ϕ
EM 1$^{\mathrm{th}}$ layer	Total lateral shower width	$w_{s_{\mathrm{tot}}}$
	Ratio of the energy difference associated with the largest and second largest energy deposits to the sum of these energies	E_{ratio}
	Ratio of the energy in the strip layer to the total energy in the EM accordion calorimeter	f_1
Track conditions	Number of hits in the innermost pixel layer; discriminates against photon conversions	n_{IBL}
	Number of hits in the pixel detector	n_{Pixel}
	Number of total hits in the pixel and SCT detectors	n_{Si}
	Transverse impact parameter with respect to the beam-line	d_0
	Significance of transverse impact parameter defined as the ratio of d_0 and its uncertainty	$d_0/\sigma d_0$
	Momentum lost by the track between the perigee and the last measurement point divided by the original momentum	$\Delta p/p$
TRT	Likelihood probability based on transition radiation in the TRT	eProbabilityHT
Track-cluster matching	$\Delta\eta$ between the cluster position in the strip layer and the extrapolated track	$\Delta\eta_1$
	$\Delta\phi$ between the cluster position in the middle layer and the track extrapolated from the perigee	$\Delta\phi_2$
	Defined as $\Delta\phi_2$, but the track momentum is rescaled to the cluster energy before extrapolating the track from the perigee to the middle layer of the calorimeter	$\Delta\phi_{res}$
	Ratio of the cluster energy to the track momentum	E/p

Table 3.3 – Electron identification variables used in the likelihood [92]

Working point	Calorimeter isolation	Track isolation
Gradient	$\epsilon = 0.1143 \times p_{\mathrm{T}} + 92.14\%$ (with E_{T}^{cone20})	$\epsilon = 0.1143 \times p_{\mathrm{T}} + 92.14\%$ (with $p_{\mathrm{T}}^{varcone20}$)
HighPtCaloOnly	$E_{\mathrm{T}}^{cone20} < \max(0.015 \times p_{\mathrm{T}}, 3.5\,\mathrm{GeV})$	-
Loose	$E_{\mathrm{T}}^{cone20}/pT < 0.20$	$p_{\mathrm{T}}^{varcone20}/pT < 0.15$
Tight	$E_{\mathrm{T}}^{cone20}/pT < 0.06$	$p_{\mathrm{T}}^{varcone20}/pT < 0.06$

Table 3.4 – Definition of the electron isolation working points [80].

and/or the track isolation variable. The Loose isolation criterium used in $H \to \gamma\gamma$ analyses guarantees a 99% efficiency for true electrons, almost flat in η.

3.7 Jet reconstruction, energy calibration and performance

Quarks and gluons could not be observed free due to the color confinement property of the QCD. Hence, when a quark or a gluon is produced in a hard interaction, it first generates a parton shower which in turn hadronizes in a spray of collimated hadrons, called jet. Jet are reconstructed by combining measured energy deposits in the calorimeters and tracks, using a specific algorithm that matches the definition at the theoretical level.

3.7.1 Jet reconstruction

The bunch of generated hadrons leaves tracks in the Inner Detector and clusters of energy both in the EM calorimeter and in the hadronic one. An algorithmic combination of charged-particle tracks with topological clusters (build as described in Section 3.2.1), referred to as the ATLAS particle-flow reconstruction method [93, 94], is used to reconstruct the basic building blocks for jet reconstruction. The algorithm removes calorimeter energy deposits due to charged hadrons during jet reconstruction and uses measurements of the momenta of the matched tracks from the inner tracker. This improves the precision of the charged-hadrons measurement, while retaining the calorimeter measurements of neutral-particle energies. At high energies, the calorimeter energy resolution is superior to the tracker momentum resolution, thus a combination of the two subsystems is preferred for optimal event reconstruction. Outside the geometrical acceptance of the tracker, only the calorimeter information is available. Hence, in the forward region the topo-clusters alone are used as inputs to the particle flow jet reconstruction. Jet reconstruction is then performed on an ensemble of 'particle flow objects' consisting of the remaining calorimeter energy deposits and tracks which are matched to the hard interaction vertex.

From a theoretical point of view, jets must be defined to be "infra-red and collinear safe", so that the number of jets must be stable with respect to the emission of soft or collinear partons. This condition is imposed in order to obtain a finite prediction to all perturbative orders for cross section calculations. The algorithm used by ATLAS to fulfill the above condition is the anti-k_t algorithm [95]. With it, the four-vectors of particle flow

objects are combined by the use of two distance parameters

$$d_i = \frac{1}{p_{\mathrm{T}i}^2} \qquad d_{ij} = \min\left(\frac{1}{p_{\mathrm{T}i}^2}; \frac{1}{p_{\mathrm{T}j}^2}\right)\frac{\Delta_{ij}^2}{R^2} \tag{3.3}$$

where i, j are simple particle flow object indexes, $\Delta_{ij} = \left(\eta_i - \eta_j\right)^2 + \left(\phi_i - \phi_j\right)^2$ and $R = 0.4$ is a fixed distance parameter used to reconstruct jets. The algorithm starts by identifying all possible pairs of input particles and their distance according to the above metrics. If $d_{ij} < d_i$, the objects i and j are combined and removed from the inputs, while the combined object is added as a new input. If instead $d_{ij} > d_i$, then the object i is selected as a jet and removed from the collection of inputs. At each step the distances d_{ij} and d_i are recomputed and the procedure repeated until no further combinations are possible.

3.7.2 Jet calibration

The jet energy scale (JES) is calibrated [94] with MC simulated dijet events following the chain depicted in Figure 3.20.

At the beginning, the pile-up corrections remove the excess energy due to additional pp interactions within the same (in-time) or nearby (out-of-time) bunch crossings. These corrections consist of two components: a correction based on the jet area and transverse momentum density of the event, and a residual correction derived from MC simulation and parameterized as a function of the mean number of interactions per bunch crossing (μ) and the number of reconstructed primary vertices in the event (N_{PV}).

The absolute JES calibration corrects the jet so that it agrees in energy and direction with truth jets from dijet MC events, accounting for non-compensating calorimeter response, energy losses in passive material, out-of-cone effects and biases in the jet η reconstruction. Such biases are primarily caused by the transition between different calorimeter technologies and sudden changes in calorimeter granularity.

Furthermore, the global sequential calibration (derived from dijet MC events) improves the jet p_{T} resolution and associated uncertainties by removing the dependence of the reconstructed jet response on observables constructed using information from the tracking, calorimeter, and muon chamber detector systems. In fact, even after the absolute MC-based calibration, the response can vary from jet to jet depending on the flavour and energy distribution of the constituent particles, their transverse distribution, and the fluctuations of the jet development in the calorimeter.

Finally, a residual in-situ calibration is applied to data only to correct for remaining differences between data and MC simulation. These differences are caused by imperfect simulation of both the detector materials and the physics processes involved: the hard scatter and underlying event, jet formation, pile-up, and particle interactions with the detector. The final in situ calibration measures the jet response in data and MC simulation separately and uses the ratio as an additional correction to be applied to data.

This calibration procedure give rise to 125 systematic sources. The large majority (around 100) stems from the final in-situ calibration in order to cover the various analysis

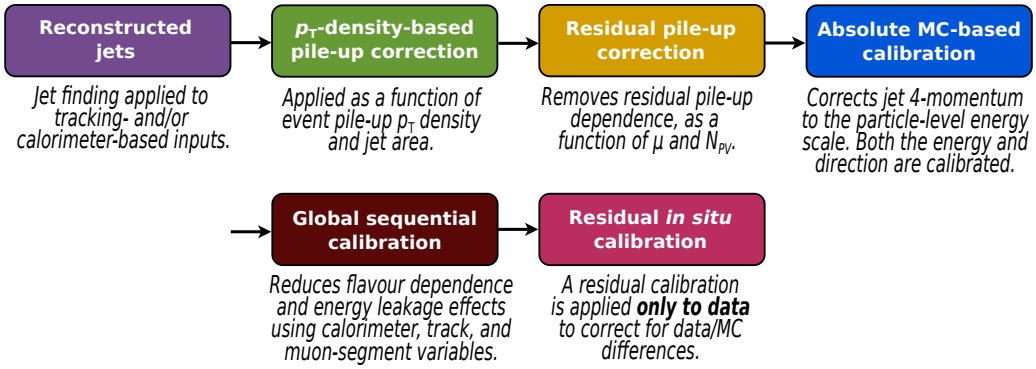

Figure 3.20 – Stages of jet energy scale calibrations. Each one is applied to the four-momentum of the jet [94].

selections performed in data and MC, event topology, MC mis-modelling and statistical limitations. An overview of the various uncertainty sources is reported in Figure 3.21 as function of p_T and η: the largest contributions come from pileup subtraction for low p_T jet (1% averaged) and jet flavor response (1.5% averaged) in the medium p_T range, while at higher p_T and η the in situ calibration uncertainties takes over. The number of nuisance parameters to be used in final analyses is then reduced by means of eigenvector decomposition of in situ components. In $H \to \gamma\gamma$ analysis the *category reduction* scheme is used which combines the p_T dependent in situ uncertainty components in separate groups based on their origin (detector, statistical, modelling, or mixed) and results in 15 reduced components for a total of 30 uncertainty sources.

Concerning instead jet energy resolution (JER), this is particularly important because affects the missing transverse momentum (see Section 3.10), which in turns plays an indispensable role in measurements involving particles that decay into neutrinos (like leptonic decay of V boson in VH Higgs production), and thus rely on well-reconstructed missing transverse momentum. As already mentioned, the resolution in the calorimeter can be parametrized as in Eq. (2.14), with the various terms that are expected to dominate in different p_T regimes: for jets, noise terms dominates up to $\sim 30\,\text{GeV}$ and sampling terms takes over up to $\sim 400\,\text{GeV}$, while very high p_T regime is dominated by the constant term.

In order to measure the JER, jet momentum must be measured precisely. This implies that the jets must either recoil against a reference object whose momentum can be measured precisely, or be balanced against one another in a well-defined dijet system. JER measurements using these events for the dijet balance method rely on the approximate scalar balance between the transverse momenta of the two leading jets. In addition, the noise term of the resolution can also be measured via the fluctuations in the energy deposits due to pileup using data samples that are collected by random unbiased triggers. These measurements are performed using the random cones method in which energy deposits in the calorimeter are summed to the energy scale of the constituents in circular

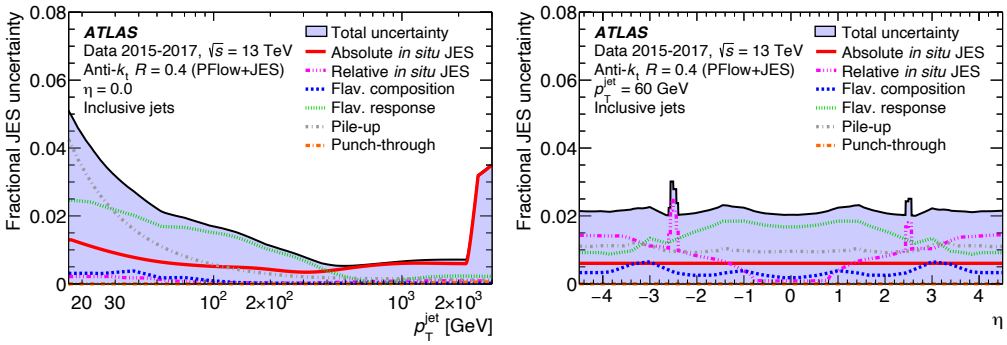

Figure 3.21 – Fractional jet energy scale systematic uncertainty components for anti-k_t $R = 0.4$ jets (a) as a function of jet p_{T} at $\eta = 0$ and (b) as a function of η at $p_{\mathrm{T}} = 60\,\mathrm{GeV}$, reconstructed from particle-flow objects. The total uncertainty, determined as the quadrature sum of all components, is shown as a filled region topped by a solid black line. "*in-situ* JES" contributions refers to the final in situ calibration, while flavor composition, response and 'punch-through" to the global sequential calibration. Flavor-dependent components shown here assume a dijet flavor composition (predominantly gluon). [94].

areas analogous to the jet area for anti-k_t $R = 0.4$ jets. Finally, the two measurements are then combined and the results is presented in Figure 3.22

3.7.3 Jet vertex tagger

Once the jets are reconstructed, different requirements (jet cleaning criteria) are applied in order to reduce the background arising from non-collision background and instrumental effects. In addition, identification and suppression of pileup jets is of paramount importance in particular in the high luminosity enviroment provided by LHC during Run 2. To this end, the jet vertex tagger (JVT) [96] is used to identify and reject jets not originating from the hard-scatter vertex (pileup jets) using information from the tracks matched to each jet. The variable JVT itself is defined by constructing a two-dimensional likelihood based on corrJVF and $R_{p_{\mathrm{T}}}$ defined as

$$\mathrm{corrJVF} = \frac{\sum_m p_{\mathrm{T},m}^{trk}(\mathrm{PV}_0)}{\sum_m p_{\mathrm{T},m}^{trk}(\mathrm{PV}_0) + \frac{\sum_{n\geq 1}\sum_l p_{\mathrm{T},l}^{trk}(\mathrm{PV}_n)}{0.01\cdot n_{trk}^{PU}}} \tag{3.4}$$

$$R_{p_{\mathrm{T}}} = \frac{\sum_m p_{\mathrm{T},m}^{trk}(\mathrm{PV}_0)}{p_{\mathrm{T}}^{jet}} \tag{3.5}$$

where $\sum_m p_{\mathrm{T},m}^{trk}(\mathrm{PV}_0)$ is the scalar sum of the p_{T} of the tracks associated to the jet and originating from the hard-scatter vertex (PV_0), while $\sum_{n\geq 1}\sum_l p_{\mathrm{T},l}^{trk}(\mathrm{PV}_n) = p_{\mathrm{T}}^{\mathrm{PU}}$ is the sum of the p_{T} of the tracks originating from any pileup interactions. This term is corrected for the linear increase of $\left\langle p_{\mathrm{T}}^{\mathrm{PU}} \right\rangle$ with the total number of pileup tracks per event n_{trk}^{PU} not associated to the primary vertex. As shown in Figure 3.23a, corrJVF assumes value

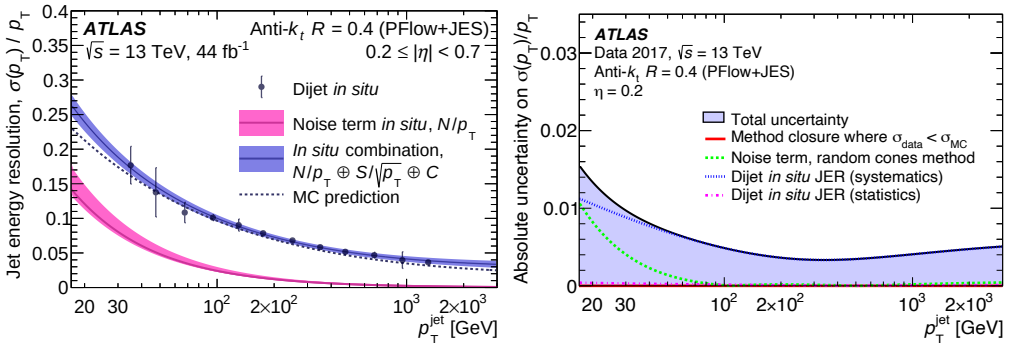

Figure 3.22 – (left) The relative jet energy resolution as a function of p_{T} for fully calibrated PFlow+JES jets. The error bars on points indicate the total uncertainties on the derivation of the relative resolution in dijet events, adding in quadrature statistical and systematic components. The expectation from Monte Carlo simulation is compared with the relative resolution as evaluated in data through the combination of the dijet balance and random cone techniques. (right) Absolute uncertainty on the relative jet energy resolution as a function of jet p_{T}. Uncertainties from the two in situ measurements and from the data/MC simulation difference are shown separately [94].

close to 1 for hard scatter jets and close to 0 for pileup ones. Concerning $R_{p_{\mathrm{T}}}$, the p_{T}^{jet} is the fully calibrated p_{T} of the jet which includes pileup subtraction too. Therefore also $R_{p_{\mathrm{T}}}$ peaks at 0 and steeply falls for pileup jets, while has the meaning of charged p_{T} fraction for hard scatter ones, as shown in Figure 3.23b. The performance of the JVT likelihood for jets up to $|\eta| < 2.5$ is shown in Figure 3.23c using different track-to-vertex-association requirements (TTVA) in the primary hard-scatter vertex when the condition $|\Delta z_0 \sin(\theta_{trk})| < [3, 2, 1.5, 1]$ mm is fulfilled. The longitudinal displacement between the primary HS vertex and the track is Δz_0 and θ_{trk} is the angle of the track in relation to the beam axis. In $H \to \gamma\gamma$ analysis the tight working point for JVT is used ($\mathrm{JVT}_{score} > 0.50$) which corresponds to a hard-scatter jet efficiency of around 96%.

For jets with $2.5 < |\eta| < 4.5$, outside the coverage of the Inner Detector, a different tagger is employed, called *forward JVT* (fJVT) [98]. The basic idea of the forward JVT algorithm is to check if a forward jet closes the momentum conservation for any of the pileup vertices. Indeed pileup jets can be divided into two categories: the QCD pileup jets originating from a single QCD process, occurring in a single pileup interaction, and the stochastic pileup jets that include particles associated with more pileup interactions in the event, without a single prevalent source. To this end, first central jets ($|\eta| < 2.5$) are reconstructed for every pileup vertex and the relevant energy calibration is applied. Then QCD pileup jets are distinguished from stochastic pileup jets in the central region using a modified version of Eq. (3.5), $R^i_{p_{\mathrm{T}}}$ built for the first 10 pileup vertex i and not from the hard-scatter one ($i = 0$). QCD pileup jets are expected to have the majority of the tracks associated to them originating from the same pileup vertex (PV_i), and thus have large values of $R^i_{p_{\mathrm{T}}}$. Tracks associated with stochastic pileup jets are not likely to originate from the same pileup vertex, thus yielding small $R^i_{p_{\mathrm{T}}}$ values. A value of $R^i_{p_{\mathrm{T}}}$ greater than 0.1 is chosen to optimally reject stochastic pileup jets. Subsequently, a cut

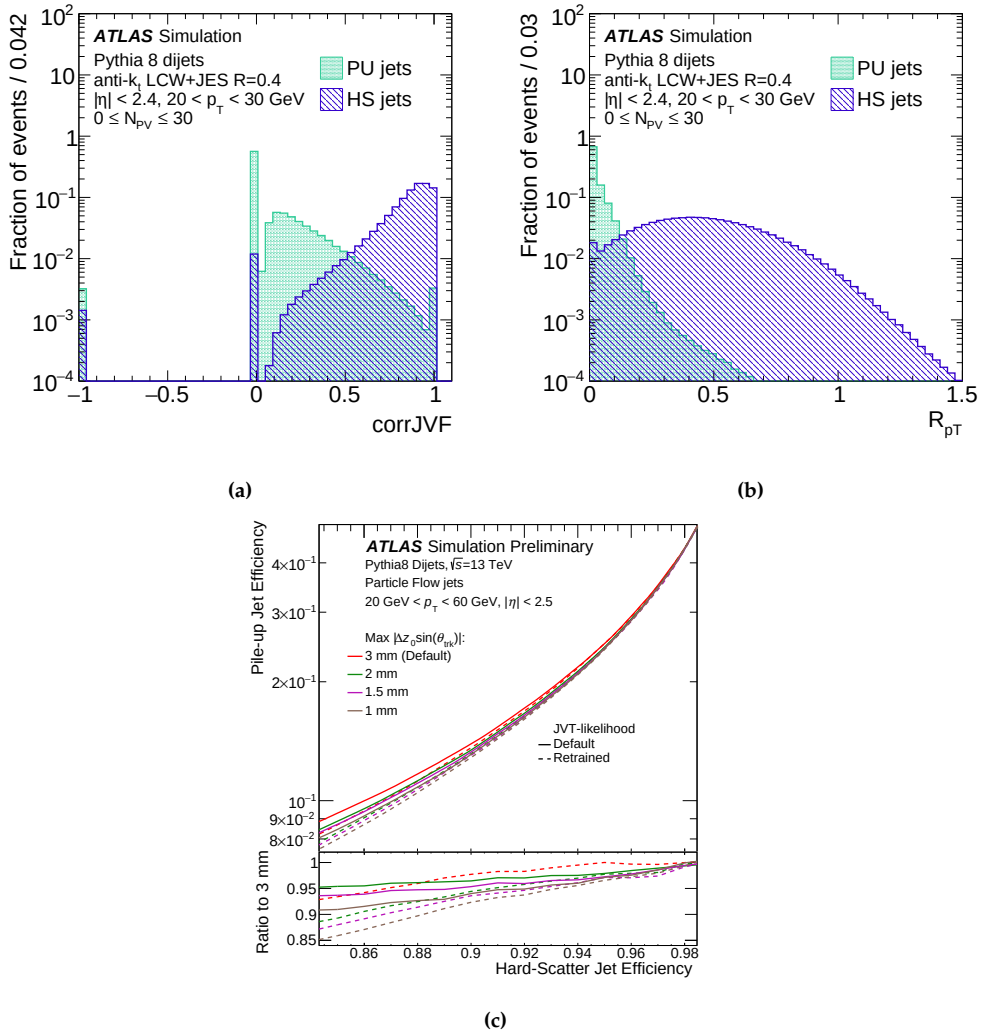

Figure 3.23 – Distribution of corrJVF (a) and R_{p_T} (b) for pileup (PU) and hard-scatter (HS) jets with $20 < p_T < 30$ GeV [96]. (c) Performance of the JVT is evaluated on Monte-Carlo simulation samples using different track-to-vertex-association requirements (TTVA) with and without a retrained JVT-likelihood for Particle Flow jets in multijet events [97].

of $\mathrm{JVT}_{score} < 0.2$, is applied in order to ensure that hard-scatter central jets are excluded. The efficiency of the JVT selection is very high, rejecting 98.8% of the hard-scatter central jets. The missing transverse momentum per vertex i ($\boldsymbol{p}_{\mathrm{T},i}^{\mathrm{miss}}$) is calculated as

$$\boldsymbol{p}_{\mathrm{T},i}^{\mathrm{miss}} = -\left(\sum_{\substack{\text{jets,} \\ p_{\mathrm{T}}^{\mathrm{jet}} > 20\,\mathrm{GeV}}} \boldsymbol{p}_{\mathrm{T}}^{\mathrm{jet}} + \sum_{\substack{\text{tracks} \\ p_{\mathrm{T}}^{\mathrm{jet}} < 20\,\mathrm{GeV}}} \boldsymbol{p}_{\mathrm{T}}^{\mathrm{track}} + \sum_{\substack{\text{tracks} \\ \text{jets fail } R_{p_{\mathrm{T}}}^{i} \text{ cut}}} \boldsymbol{p}_{\mathrm{T}}^{\mathrm{track}} \right) \tag{3.6}$$

where jets refers to central jets and track to the tracks associated to jet. The final fJVT score is computed as the maximum of the normalized projection of $\boldsymbol{p}_{\mathrm{T},i}^{\mathrm{miss}}$ on the forward jet direction:

$$\mathrm{fJVT} = \max_{i} \left(\frac{\boldsymbol{p}_{\mathrm{T},i}^{\mathrm{miss}} \cdot \boldsymbol{p}_{\mathrm{T}}^{fwdj}}{\left| \boldsymbol{p}_{\mathrm{T}}^{fwdj} \right|^2} \right) \tag{3.7}$$

For a forward pileup jet, it is expected that its energy will be balanced by the $\boldsymbol{p}_{\mathrm{T},i}^{\mathrm{miss}}$ leading to fJVT values close to 1. On the contrary, this effect is not present in the case of hard-scatter forward jets, resulting in fJVT values closer to 0. Therefore, a forward jet is tagged as pileup if its fJVT value is above a given threshold (which is the opposite of standard JVT). The distribution of the fJVT is shown in Figure 3.24a and the relative selection efficiency in Figure 3.24b. In the $H \to \gamma\gamma$ analyses, the tight working point for fJVT is used ($fJVT < 0.4$) which corresponds to around 70% efficiency for hard-scatter jet.

3.8 Jet *b*-tagging

For the physics program of the ATLAS experiment, the identification of jets initiated by b-quarks, or b-tagging, is a fundamental tool. Ensuring its optimal performance is particularly important for the study of the Higgs boson as presented in this manuscript. The b-tagging algorithms [99] exploit the long lifetime, high mass and high decay multiplicity of b-hadrons. The procedure consists in two stages. Firstly, low-level algorithms [100, 101] reconstruct the characteristic features of the b-jets via two complementary approaches, one that uses the individual properties of charged-particle tracks, associated with a hadronic jet, and a second which combines the tracks to explicitly reconstruct displaced vertices. Secondly, in order to maximize the b-tagging performance, the results of the low-level b-tagging algorithms are combined in high-level algorithms [102–104] consisting of multivariate classifiers.

The b-tagging algorithm used in $H \to \gamma\gamma$ analyses is called DL1r: the algorithm is based on a deep feed-forward neural network which has a multidimensional output corresponding to the probabilities for a jet to be a b-jet, a c-jet or a light-flavor jet, (p_b, p_c and p_u respectively.) The final DL1r b-tagging discriminant is defined as

$$D_{\mathrm{DL1r}} = \ln \left(\frac{p_b}{f_c \cdot p_c + (1 - f_c) \cdot p_u} \right) \tag{3.8}$$

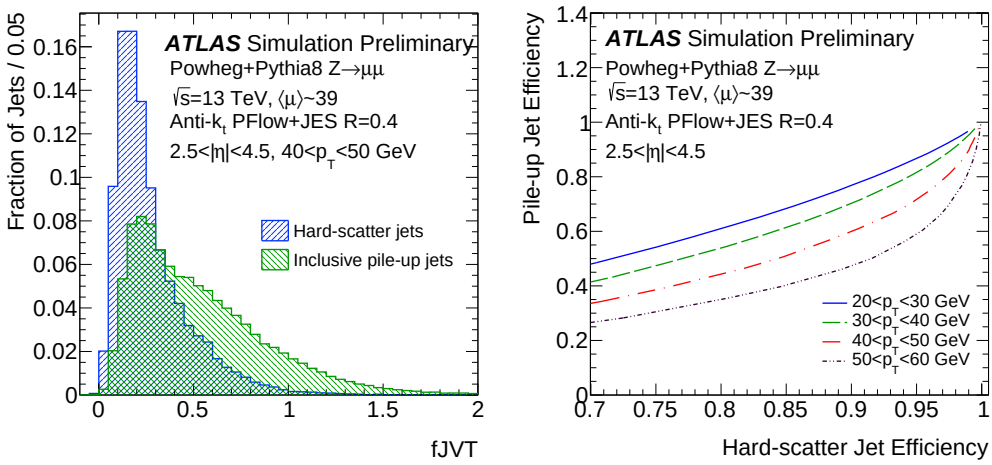

(a) **(b)**

Figure 3.24 – (a) fJVT distributions for hard-scatter (blue) and pile-up (green) forward jets with $40 < p_{\mathrm{T}} < 50$ GeV (b) Efficiency for pileup jets in simulated $Z + jets$ events as a function of the efficiency for hard-scatter jets for different jet p_{T} ranges. For a standard value of hard-scatter jet efficiency the pileup jet efficiency is improving with p_{T} since pileup effects are less dominant in higher p_{T} bins [98].

where f_c controls the importance of the c-jet rejection in the variable, and is optimized separately for the different DL1r variants and different optimization campaigns. Different calibrated working point are usually provided, ensuring an inclusive fixed b-jet efficiency selection (60%, 70%, 77%, 85%). In addition, a pseudo-continuous b-tagging working point is provided too, so that each jet is assigned a integer variable showing which is the tightest working point it fulfills. This is the primary working point used in $H \to \gamma\gamma$ analyses, unless otherwise stated.

The performance of the DL1r tagging algorithm is shown in Figure 3.25, compared to other previous high-level b-tagging algorithm used in ATLAS: the DL1 differs from the DL1r by not including one low-level algorithm to reconstruct b-jet kinematic (RNNIP [101]), while MV2 [102] is the BDT-based version of DL1.

3.9 Muon reconstruction

Muon candidates are reconstructed independently in the Inner Detector (ID), in the Muon Spectrometer (MS) and in the calorimeters and then information is combined. The combination of inputs from several sub-detectors allows to reach almost 100% reconstruction and identification efficiency over a wide range of transverse momenta p_{T}, with background contamination at the per-mil level and good momentum resolution [105].

First of all tracks in the MS are reconstructed and the compatibility with the interaction point is checked. Then, a global muon reconstruction is performed by using the information from ID and calorimeters, leading to five different reconstruction strategies and muon *types*:

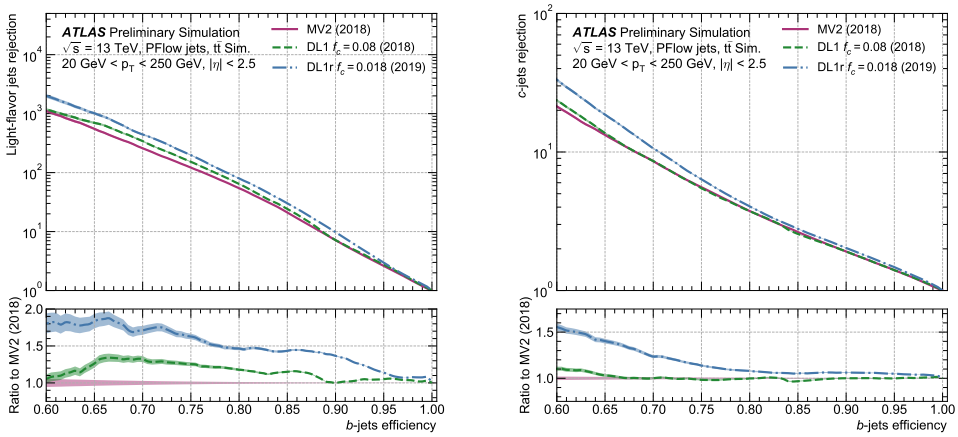

(a) Light-flavor rejection

(b) c-flavor rejection

Figure 3.25 – Comparison of ROC curves for 2018 recommended versions of MV2 and DL1, and 2019 DL1r optimization. The x-axis corresponds to the b-jet efficiency, while the y-axis corresponds to (a) light-flavor jets rejection ($1/\epsilon_u$) and (b) c-jets rejection ($1/\epsilon_c$). The performance is evaluated on anti-k_t $R = 0.4$ particle flow jets with $20 < p_{\mathrm{T}} < 250\,\mathrm{GeV}$ and $|\eta| < 2.5$, on a simulated dataset of $t\bar{t}$ events. The shaded bands represent the statistical uncertainty [103].

- Combined (CB) muons are identified by matching MS tracks to ID tracks and performing a combined track fit based on the ID and MS hits, taking into account the energy loss in the calorimeters.
- Inside-Out combined (IO) muons are reconstructed using a complementary inside-out algorithm, which extrapolates ID tracks to the MS and searches for at least three loosely-aligned MS hits. The ID track, the energy loss in the calorimeters and the MS hits are then used in a combined track fit.
- Muon spectrometer Extrapolated (ME) muons are reconstructed if an MS track cannot be matched to an ID track, so its parameters are extrapolated to the beamline.
- Segment-Tagged (ST) muons are identified by requiring that an ID track extrapolated to the MS satisfies tight angular matching requirements to at least one reconstructed MS segment. A successfully-matched ID track is identified as a muon candidate, and the muon parameters are taken directly from the ID track fit.
- Calorimeter-Tagged (CT) muons are identified by extrapolating ID tracks through the calorimeters to search for energy deposits consistent with a minimum-ionising particle. Such deposits are used to tag the ID track as a muon, and the muon parameters are again taken directly from the ID track fit.

Similarly to electron and photons, high quality prompt muons candidate are selected by means of identification and isolation requirements, in order to suppress candidates

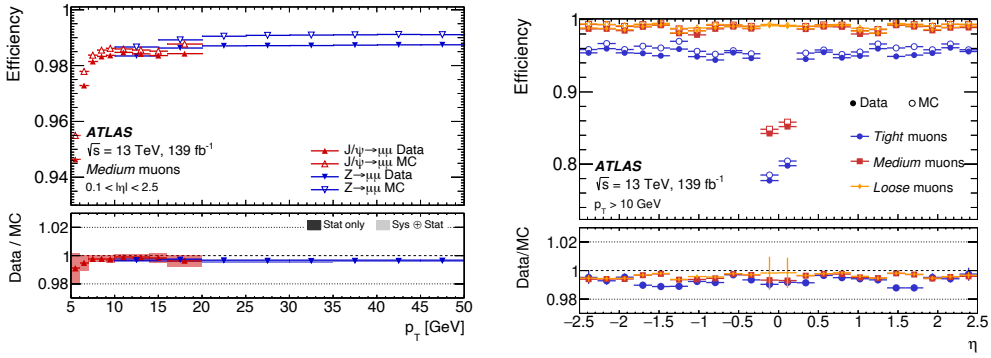

(a) **(b)**

Figure 3.26 – (a) Muon reconstruction and identification efficiencies Medium identification criteria, measured as a function of p_{T} in $J/\psi \to \mu\mu$ and $Z \to \mu\mu$ events for $0.1 < |\eta| < 2.5$. The panel at the bottom shows the ratio of the measured to predicted efficiencies, with statistical and systematic uncertainties. (b) Muon reconstruction and identification efficiencies for the Loose, Medium, and Tight criteria as a function of η for muons with $p_{\mathrm{T}} > 10\,\mathrm{GeV}$ in $Z \to \mu\mu$ events. The panel at the bottom shows the ratio of the measured to predicted efficiencies, with statistical and systematic uncertainties [105].

originating from semileptonic in-flight decay of light hadrons and those from hadrons containing heavy flavors. Bottom and charm decays produce good-quality muon tracks and these can be distinguished from prompt muons, which are more closely associated with the primary vertex and more isolated in the ID and/or in the calorimeters.

The identification algorithm provides five different working points: Loose, Medium, Tight, High-p_{T} and Low-p_{T}. In the majority of physics analyses and in the $H \to \gamma\gamma$ analyses, the Medium working point is used, which guarantees an efficiency and purity suitable for a wide range of physics cases, while keeping the systematic uncertainties in the prompt-muon efficiency small. The Medium selection is based on rectangular cut-based requirements on the track in the ID and MS that selects muons with more than 98% efficiency for $p_{\mathrm{T}} > 10\,\mathrm{GeV}$. The performance of the Medium working point is shown in Figure 3.26.

While muons from light-hadrons decays ares effectively suppressed by the identification requirement, muon isolation provides a way to discriminate between prompt muons and muons from heavy-flavor decays by measuring the amount of hadronic activity in their vicinity. The transverse energy (or momentum if considering only tracks) reconstructed in a cone around a muon and divided by the muon p_{T} defines the muon isolation. Several isolation WPs are defined, balancing prompt-muon efficiency, rejection of non-prompt muons, and performance in proximity to other objects. Similar to electrons, track-based and calorimetric-based isolations are usually combined, with the first providing better energy resolution and low pileup dependence while the latter including neutral particles and particles below the ID track p_{T} threshold. The particle flow algorithm is used to effectively combine the two, allowing removal of overlapping contributions. The particle-flow based isolation variable is defined as the sum of track-

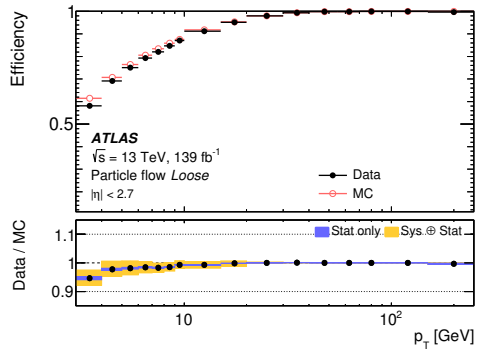

(a) Muon isolation performance

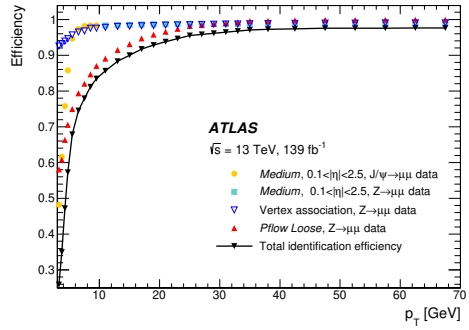

(b) Overall muon performance

Figure 3.27 – (a) Muon isolation efficiency measured in $Z \to \mu\mu$ events for thePflowLoose as a function of p_{T} for muons with $p_{\mathrm{T}} > 3\,\mathrm{GeV}$. The panel at the bottom shows the ratio of the measured to predicted efficiencies, with statistical and systematic uncertainties. (b) Overall reconstruction and identification efficiency measured in data with $Z \to \mu\mu$ and $J/\psi \to \mu\mu$ decays for prompt muons with $p_{\mathrm{T}} > 3\,\mathrm{GeV}$. The total identification efficiency for satisfying simultaneously the Medium, PflowLoose isolation and vertex association criteria (black line) is shown together with its separate components (coloured markers) [105].

based isolation, chosen in the configuration with $p_{\mathrm{T}}^{varcone30}$ for $p_{\mathrm{T}}^{\mu} < 50\,\mathrm{GeV}$ and p_{T}^{cone20} for larger p_{T}^{μ}, and the transverse energy of neutral particle-flow objects in a cone of size $\Delta R = 0.2$ around the muon, labeled as $E_{\mathrm{T}}^{\mathrm{netflow20}}$. The latter is corrected for the contribution from the energy deposit by the muon itself and for pileup effects. In $H \to \gamma\gamma$ analyses, a combination of track-based and calorimetric-based isolations is used, called PflowLoose which is defined as

$$\left(p_{\mathrm{T}}^{varcone30} + 0.4 \cdot E_{\mathrm{T}}^{\mathrm{netflow20}}\right) < 0.16 \cdot p_{\mathrm{T}}^{\mu} \tag{3.9}$$

whose performance is shown in Figure 3.27a. The overall combined muon performance is shown in Figure 3.27b, with the identification, isolation and vertex association (see Section 5.2) requirements used in $H \to \gamma\gamma$ analyses.

3.10 $E_{\mathrm{T}}^{\mathrm{miss}}$ reconstruction

Momentum conservation in the plane transverse to the beam axis implies that the transverse momenta of all particles in the final state should sum to effectively zero. Any momentum imbalance, or missing transverse momentum ($E_{\mathrm{T}}^{\mathrm{miss}}$) may indicate that particles invisible to the detector systems were produced in the collision, such as neutrinos or possibly new particles from physics beyond the Standard Model. The $E_{\mathrm{T}}^{\mathrm{miss}}$ is the most challenging object to be reconstructed as it relies on the reconstruction of all other "hard-objects" (electron, photon, jet, etc.) plus the reconstructed momentum flow not attributed to any object, referred as "soft-term". The $E_{\mathrm{T}}^{\mathrm{miss}}$ is therefore a complicated event-level quantity, susceptible to many imperfections arising from miscalibration and

particles going through un-instrumented regions of the detector.

The missing transverse momentum is defined [106] as the negative sum of all the objects in the event

$$E_{x(y)}^{\text{miss}} = E_{x(y)}^{\text{miss},\mu} + E_{x(y)}^{\text{miss},e} + E_{x(y)}^{\text{miss},\gamma} + E_{x(y)}^{\text{miss},\tau} + E_{x(y)}^{\text{miss,jets}} + E_{x(y)}^{\text{soft}} \tag{3.10}$$

where each term is calculated as the negative vectorial sum of transverse momenta of energy deposits or trajectories of charged particles, and the terms are in reconstruction order; therefore

$$\boldsymbol{E}_{\text{T}}^{\text{miss}} = \left(E_x^{\text{miss}}, E_y^{\text{miss}}\right) \qquad E_{\text{T}}^{\text{miss}} = \left|\boldsymbol{E}_{\text{T}}^{\text{miss}}\right| = \sqrt{\left(E_x^{\text{miss}}\right)^2 + \left(E_y^{\text{miss}}\right)^2} \tag{3.11}$$

An algorithm takes care of removing ambiguities in order to avoid doubly counted object in the sum. Moreover the specific particles and jets selections in a given analysis must be reflected in the $E_{\text{T}}^{\text{miss}}$ for a consistent calculation. For example, the electron selection applied in a given analysis must be applied consistently also to the $E_{\text{T}}^{\text{miss}}$ reconstruction.

The most tricky term is the one related to soft activity in the detector, $E_{x(y)}^{\text{soft}}$: this includes the pileup interactions and missing or badly reconstructed objects. It could be evaluated from calorimetric clusters or tracks. The ATLAS Collaboration uses a soft term called *particle flow Track Soft Term* (PFlow TST) which uses tracks with $p_{\text{T}} > 0.5\,\text{GeV}$ associated to charged particle flow constituents which are not associated to any well-identified reconstructed object and surviving the track-to-vertex association. This last condition makes the TST relatively insensitive to pileup effects but is not able to include neutral particles and particles in forward regions.

The selection of jets used to calculate the $E_{\text{T}}^{\text{miss}}$ has a large impact on $E_{\text{T}}^{\text{miss}}$. In $H \to \gamma\gamma$ analyses, the Tight working point which reduces pileup dependence is used. $E_{\text{T}}^{\text{miss}}$ for this working point is reconstructed by including all the jets with $p_{\text{T}} > 30\,\text{GeV}$ and with a JVT > 0.2 for central ones, but removing forward jets with $|\eta| > 2.4$ and $20 < p_{\text{T}} < 30\,\text{GeV}$. The $E_{\text{T}}^{\text{miss}}$ modeling is shown in Figure 3.28 along with $E_{\text{T}}^{\text{miss}}$ significance which is computed as $E_{\text{T}}^{\text{miss}} / \sqrt{\sum E_{\text{T}}}$, where $\sum E_{\text{T}}$ is the sum of all "hard-objects" entering the $E_{\text{T}}^{\text{miss}}$ computation. The $E_{\text{T}}^{\text{miss}}$ significance shows if the measured $E_{\text{T}}^{\text{miss}}$ value is consistent with the null hypothesis that there is no real $E_{\text{T}}^{\text{miss}}$. Low values indicate $E_{\text{T}}^{\text{miss}}$ comes from resolution effects and hence not from a real physical source and high values suggest the presence of an invisible particle in the event.

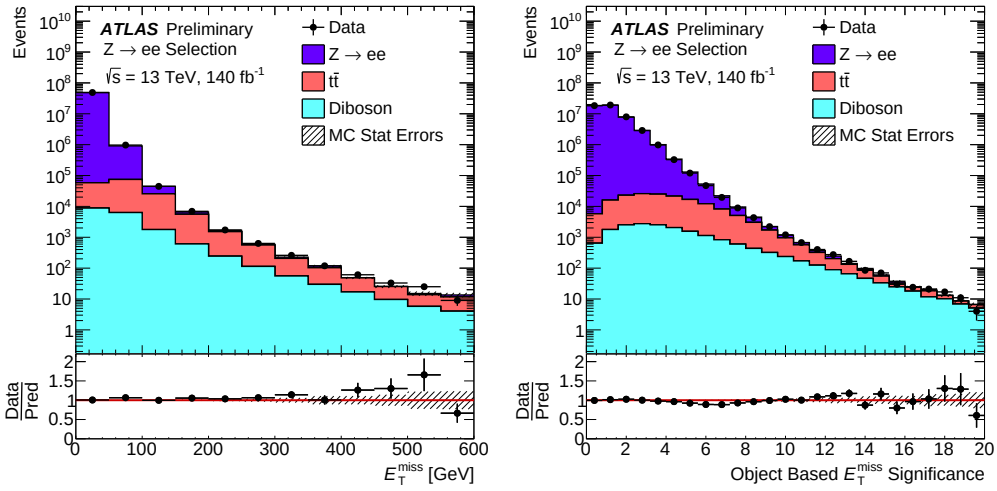

(a) **(b)**

Figure 3.28 – (a) $E_{\mathrm{T}}^{\mathrm{miss}}$ distribution for PFlow TST and Tight working point is shown for the complete Run 2 dataset, compared to Monte Carlo simulation, broken up in to the contribution from each physics process. A $Z \to ee$ selection is applied: $Z \to ee$ events present fake $E_{\mathrm{T}}^{\mathrm{miss}}$ contributions in the low part of the distribution while $t\bar{t}$ and diboson processes create neutrinos in their decay chains, so they present real $E_{\mathrm{T}}^{\mathrm{miss}}$. (b) For the same processes, the $E_{\mathrm{T}}^{\mathrm{miss}}$ significance is shown too [107].

CHAPTER 4

The $H \to \gamma\gamma$ analysis

The analyses presented in this manuscript aimed to measure the properties of the Higgs boson in the $H \to \gamma\gamma$ decay channel using the full Run 2 dataset collected by the ATLAS detector. As already mentioned at the end of Chapter 1, the diphoton decay represents one of the best channel to access the fundamental properties of the Higgs boson. This is due to the excellent photon reconstruction performance, to the clear final state signature of the process and to the robust background description and subtraction.

In this Chapter I will describe the general event selection and the common tools and methods used in both the coupling and mass analyses, that will be discussed extensively in Chapter 5 and Chapter 6.

4.1 Overview of the analysis strategy

The main experimental observable is the invariant mass of the diphoton system, $m_{\gamma\gamma}$: here, the $H \to \gamma\gamma$ process manifests itself as a narrow peak over a continuous falling background composed by $\gamma\gamma$, γj and jj SM production processes. The standard event selection requires two well reconstructed and identified photons, coming from the same interaction vertex and with a reconstructed invariant mass in the 105 GeV to 160 GeV window. The peak will have a resolution between 1 and 2 GeV, therefore the region 120-130 GeV is called *signal region*, while the two remaining windows at 105-120 GeV and 130-160 GeV are called *sidebands*. The main reason to have large sidebands is to extract the background expectation in the signal region.

Events selected with this procedure are then separate into mutually exclusive categories. The categorization is completely analysis dependent, because its design is tightly bounded and optimized on the measurement to be performed. Generally, orthogonal categories are defined in order to enhance particular dataset properties, like to increase the relative presence of a particular Higgs production mode or to optimize the $m_{\gamma\gamma}$ resolution. Once events have been categorized, the shape of the invariant mass spectrum of the two photons for both signal and background is modelled in each category with analytical functional forms. Along with this information, additional systematics effects coming from the experimental and theoretical modelling are taken into account in the model, which is then compare to observed data with a maximum-likelihood fit.

Year	Luminosity [fb^{-1}]	Uncertainty	
		Absolute [fb^{-1}]	Relative [%]
2015+2016	36.2	0.8	2.1
2017	44.3	1.1	2.4
2018	58.5	1.2	2.0
Total	139.0	2.4	1.7

Table 4.1 – Breakdown of the integrated luminosities per year with their absolute and relative uncertainties.

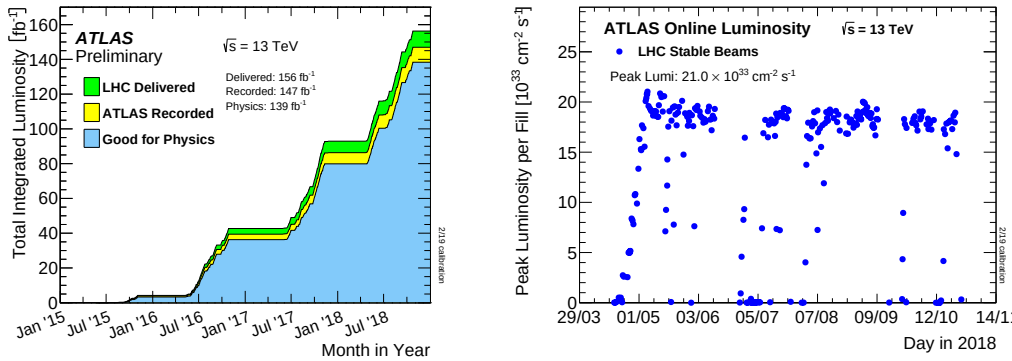

(a) (b)

Figure 4.1 – (a) Cumulative luminosity versus time delivered to ATLAS (green), recorded by ATLAS (yellow), and certified to be good quality data (blue) during stable beams for pp collisions at $\sqrt{s} = 13\,\text{TeV}$ during Run 2. (b) Peak instantaneous luminosity collected by ATLAS day by day during the 2018 for the pp collision. [108].

4.2 Dataset and Monte Carlo samples

4.2.1 Dataset

The results presented in this manuscript are extracted from the dataset collected by ATLAS during the 2015-2018 quadrennium, which amount to 139.0 fb^{-1} after the application of data quality selection. The breakdown of the luminosity for each data-taking year is reported in Table 4.1 with their respective uncertainties. Thanks to an increasingly good understanding of the machine during the years, the LHC behaved particularly well in 2017 and 2018, where most of the Run 2 dataset has been collected as it shown in Figure 4.1a: during 2018 in particular, LHC has constantly outperformed it design values showing a peak luminosity almost constant around $2.0 \times 10^{34}\,\text{cm}^{-2}\,\text{s}^{-1}$ as shown in Figure 4.1b. With this dataset and assuming a total Higgs production cross section at $m_H = 125.09\,\text{GeV}$ of 56 pb [31], the expected number of Higgs bosons produced by the LHC at the ATLAS interaction point is around 7.8 million; considering the $H \to \gamma\gamma$ channel only, which has a theoretical 0.227% branching fraction, the expected number of Higgs bosons in the diphoton final state is reduced to just 18 thousands events.

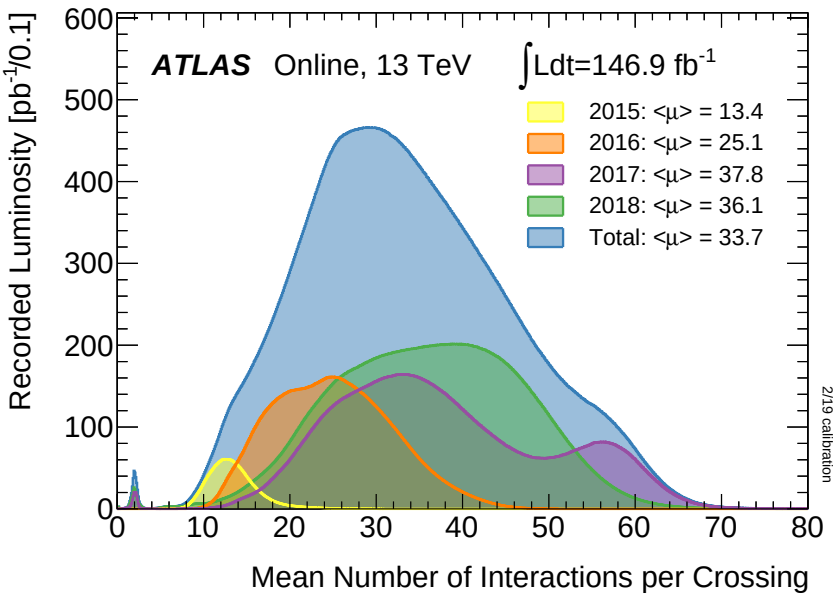

Figure 4.2 – Distribution of the mean number of interactions per bunch crossing recorded by ATLAS during Run 2. Each year is displayed separately and then summed up (blue) [108].

Related to the luminosity, an important quantity to be taken into account is the mean number of inelastic interactions occurring in each bunch crossing, indicated with $<\mu>$. As described in Section 2.1.3, when two bunches of 10^{11} protons collide, several interactions between protons travelling in opposite directions may occur. The number of interactions per bunch crossing is distributed as a Poissonian distribution and its average value depends on the beam parameters, like the number of protons in the bunch, the crossing angle, the longitudinal and transverse size of the bunch (see Table 2.1). In the analyses presented here we are mainly interested in the hard scattering process, but concurring soft interactions have an impact on the measurements because they affect the response of the detector with their additional activity. For the Run 2 dataset, the mean number of interaction per bunch crossing was 33.7 as shown in Figure 4.2, where the pileup profiles recorded by ATLAS during Run 2 quadrennium are reported.

4.2.2 Monte Carlo samples

Monte Carlo (MC) samples are collection of simulated physics events which are widely used at various analysis levels. The simulated samples are used in the analysis to model the detector response in order to estimate signal acceptances, selection efficiencies, signal and background models and to derive expected results. The generated events are passed through a GEANT simulation [109] of the response of the ATLAS detector [110] and reconstructed with the same algorithms as the data.

Nominal Higgs MC samples listed in Table 4.2 are generated with m_H fixed to 125 GeV and the corresponding width fixed to the value predicted by the SM of $\Gamma_H = 4.07$ MeV.

In general, the samples are normalized to the latest available theoretical SM cross section predictions, which are often more precise than the perturbative order of the event generation. Therefore it often happens that the normalization of the simulated sample is more theoretically precise than its actual shape. The normalization takes into account the the $H \to \gamma\gamma$ branching ratio of 2.27×10^{-3} [31] too.

All the Higgs MC samples listed in Table 4.2 are showered with PYTHIA 8, which is able to generate the small background produced by $H \to \gamma\gamma^*$. This background is taken into account in the normalization of the samples.

The ggF is generated at NNLO precision in QCD with the POWHEG NNLOPS generator [111], which implements soft gluons resummation up to next-to-next-to-logarithmic order (NNLL), using the PDF4LHC15 parton distribution function [112], interfaced to PYTHIA 8 [113] for hadronization and underlying event, tuned with the AZNLO parameter set [114]. This sample is then normalized to the latest N^3LO (QCD) + NLO (EWK) cross section [32].

The VBF, VH, $t\bar{t}H$ and $b\bar{b}H$ processes are produced with POWHEG-BOX [115–120] at NLO precision in QCD and interfaced with PYTHIA 8 tuned with AZNLO parameters set for hadronization and underlying event. Then the samples are normalized to the latest NNLO (QCD) + NLO (EWK) cross sections [31], a part the $t\bar{t}H$ production which is normalized at NLO (QCD) + NLO (EWK).

The tH processes are instead modelled using MADGRAPH5_AMC@NLO [121–123] and interfaced with PYTHIA 8 with the A14 parameters set for hadronization and underlying event. The samples are then normalized to NLO (QCD) cross section in the 5 flavour scheme approximation and with no EWK corrections [31].

Alongside nominal signal MC samples, also background events from continuum $\gamma\gamma$, $V\gamma\gamma$ and $t\bar{t}\gamma\gamma$ processes are simulated. The $\gamma\gamma$ production is modelled using SHERPA [124] at NLO order precision ($\gamma\gamma$ plus up to one jet at NLO and plus up to 2/3 jets at LO) and merged with the SHERPA parton shower [125] according to the ME+PS@NLO prescription [126]. The CT10 PDF set and dedicated parton shower tuning developed by the SHERPA authors are used. The $V\gamma\gamma$ processes are generated with a similar setup, but at LO precisions, and with all the possible leptonic decays of the V boson. The $t\bar{t}\gamma\gamma$ processes are simulated with MADGRAPH5_AMC@NLO and showered with PYTHIA 8 at NLO precision and the top quarks are decayed with MadSpin.

Corrections to simulated samples

Corrections to the normalization and shapes of the generated samples should be applied to improve the data-Monte Carlo agreement. In particular, the following corrections are applied:

- the NLO MC generators used provides each event with a weight for each event to be used to correctly obtain NLO observables;
- since the pileup profiles are different among 2015+2016, 2017 and 2018, three sets of MC samples were generated and each MC campaign is weighted to match the corresponding pileup conditions of data, according to the observed distribution of $<\mu>$ shown in Figure 4.2;

Process	Generator	Showering	PDF Set	Stat [M]	Order of calculation	σ [pb]
ggF	POWHEG NNLOPS	PYTHIA 8	PDF4LHC15	18.3	N^{3}LO + NLO	48.52
VBF	POWHEG-BOX	PYTHIA 8	PDF4LHC15	7	approx-NNLO + NLO	3.78
WH	POWHEG-BOX	PYTHIA 8	PDF4LHC15	7.3	NNLO + NLO	1.37
ZH	POWHEG-BOX	PYTHIA 8	PDF4LHC15	7.05	NNLO + NLO	0.76
ggZH	POWHEG-BOX	PYTHIA 8	PDF4LHC15	0.75	NNLO	0.12
$t\bar{t}H$	POWHEG-BOX	PYTHIA 8	PDF4LHC15	7.8	NLO + NLO	0.51
$b\bar{b}H$	POWHEG-BOX	PYTHIA 8	PDF4LHC15	0.4	NNLO	0.49
tHq	MADGRAPH5_AMC@NLO	PYTHIA 8	NNPDF3.0	0.4	NLO (5FS)	0.07
tHW	MADGRAPH5_AMC@NLO	PYTHIA 8	NNPDF3.0	0.21	NLO (5FS)	0.02
$\gamma\gamma$	SHERPA	SHERPA	CT10	720		
$V\gamma\gamma$	SHERPA	SHERPA	CT10	9.45		
$t\bar{t}\gamma\gamma$	MADGRAPH5_AMC@NLO	PYTHIA 8	NNPDF3.0	4.8		

Table 4.2 – Event generators and PDF sets used to model signal and background processes used in the analyses. "Stat" column indicates the number of event generated in millions. The order of the calculated cross section used for normalization is reported in each case with the correspondent value. Where two orders are reported the first one refers to QCD and the second to EW corrections. The order of calculation for the main background processes is omitted, since the background normalisation is determined in fits to the data.

- shifts are applied to the photon shower shape variables and to the photon calorimeter isolation value. Such shifts are determined as the average data-MC difference in photon-enriched control samples;
- scale factors determined from data control samples are applied to correct the objects selection efficiency. Similarly, energy scale and resolution corrections for all simulated objects are included too.

4.3 Event Selection

An event selection is performed in order to reduce the background contamination and enhance the signal over background ratio. The main selection is based on photons kinematic and reconstruction properties, but additional selections on other reconstructed objects are applied as detailed in Section 5.2.

4.3.1 Photons preselection

A first pre-selection is applied, requiring that the events were recorded in the optimal detector condition in which all the ATLAS sub-detectors were fully operational, with no data integrity errors or corruptions due to hardware failure ("Detector DQ" flag) and that events enter the ATLAS *Good Run List* (GRL). Events must fire the HLT trigger `HLT_g35_loose_g25_loose` and `HLT_g35_medium_g25_medium_L12EM20VH` for 2015/16 and 2017/18 data respectively, which requires the presence of two reconstructed photons with E_{T} larger than 35 GeV and 25 GeV passing the *loose* or *medium* identification criteria at trigger level. Additionally, events over the full Run 2 dataset can also be selected with the `HLT_g120_loose` and `HLT_g140_loose` triggers, which require one *loose* photon with E_{T} larger than 120 or 140 GeV respectively. These two triggers are able to recover an

additional 3% signal efficiency in the very high p_T^H phase space, where the photons can be collimated.

At least two photons that fulfill the offline *loose* identification criteria (see Section 3.5.1) are extracted from the list of photon candidates. Pre-selected loose photons are required to have $p_T > 25\,\text{GeV}$ and $|\eta| < 2.37$ and must not fall into the transition region between the barrel and end-cap calorimeter $1.37 < |\eta| < 1.52$. The two loose photons with the highest p_T define the Higgs candidate and are considered for the final selection described below in Section 4.3.3.

4.3.2 Diphoton primary vertex

Differently to all other ATLAS physics analyses which use the vertex with the largest scalar $\sum p_T^2$ of the tracks associated to the vertex, the diphoton analysis makes use of the so called "diphoton primary vertex". In fact, since photons do not leave tracks in the the Inner Detector, the hardest vertex criterium is generally sub-optimal in selecting the correct primary vertex in diphoton events, in particular for Higgs production modes with no additional particles in the final state, like ggF. Therefore a neural network is used to assign a score to each of the vertices reconstructed by ATLAS during a bunch cross and the one with the highest score is used in the analysis. This choice plays a crucial role to make the contribution of the diphoton angle resolution sub-dominant with respect to the photon energy resolution in the $m_{\gamma\gamma}$ uncertainty (see Eq. (4.1)). As can be seen in Figure 4.3, the choice of the diphoton primary vertex leads to a 8% gain in the resolution of the reconstructed $m_{\gamma\gamma}$. This gain is dominated by the improvement for ggF production process, since here the neural network vertex efficiency outperforms the hard selection one considerably, as shown in Table 4.3. The neural network is trained on ggF signal samples and it combines information from the preselected photons direction, exploiting longitudinal segmentation of the EM calorimeter ("pointing"), and tracks related quantities. The following variables have been used as inputs for the neural network:

- $\sum p_T^2$: the scalar sum of the square transverse momenta of the tracks associated to the vertex.
- $\sum p_T$: the scalar sum of transverse momenta of the tracks associated to the vertex.
- Δz: defined as $(z - z_{\text{common}})/z_{\text{error}}$ where z is the position of the candidate primary vertex, z_{common} is the weighted mean of the intersections of the extrapolated photon trajectories given by the calorimeter "pointing" with a constraint from the beam spot position and z_{error} is the standard deviation associated to this quantity.
- $\Delta\Phi$: defined as the azimuthal angle between the di-photon system and the vector sum of the tracks associated to the vertex.

The neural network performs usually better than the standard "hardest vertex" requirement: in ggF simulated events, this algorithm selects a vertex within 0.3 mm form the true one with a 79% efficiency, with respect to the 56% obtained with the hardest vertex criterium. This efficiency ranges between 84% and 97% for the other production modes. However, in $t\bar{t}H$ events, the efficiency of the neural network is slightly lower

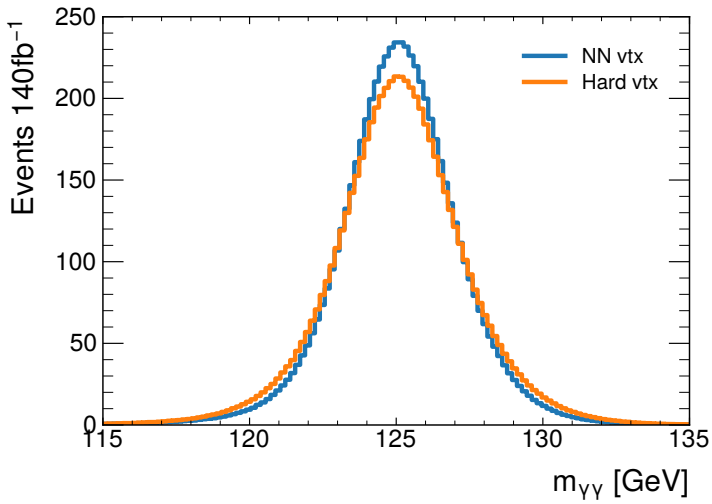

Figure 4.3 – Diphoton invariant mass distributions for the simulated signal events that pass the full analysis selection described in Section 4.3.3 when the selected primary vertex is the nominal ATLAS vertex ("Hardest", orange) compared to the diphoton primary vertex ("NN", blue).

(98% instead of almost 100%) than that of the simpler hardest vertex requirement. This difference, though, has no significant impact on the $t\bar{t}H$ cross section measurement since the acceptance and the sensitivity are found to be unaffected by this choice.

The extracted vertex is then used to update the diphoton kinematic: a straight line between the PV and the centre of the related cluster in the first layer of EM calorimeter is used to redefine η. The p_{T} used for the kinematic cuts and the invariant mass computation takes into account this η correction. Moreover the kinematic variables of all other reconstructed objects are recomputed and this is a particularly important step for the particle flow jets and $E_{\mathrm{T}}^{\mathrm{miss}}$ computation.

Further optimization of diphoton vertex selection

The neural network for vertex classification used in diphoton analyses and for the results presented in this manuscript has been trained on ggF simulated events for the LHC Run 1 results and then used without further modification throughout Run 2. Consequently, the NN is trained with a lower level of pileup with respect to Run 2 data taking conditions and it provides sub-optimal results for production modes different from ggF, as mentioned above. Therefore, a study has been performed in the re-training of this algorithm, in order to adapt it to the Run 2 conditions and including all the Higgs production modes.

The training is implemented based on the BDT algorithm provided by the LightGBM package [127], and it uses the same variables of the original NN version, trained with TMVA [128]. The distributions of the input variables employed are shown in Figure 4.4 for the different signal samples and for pileup vertices. The training dataset is composed

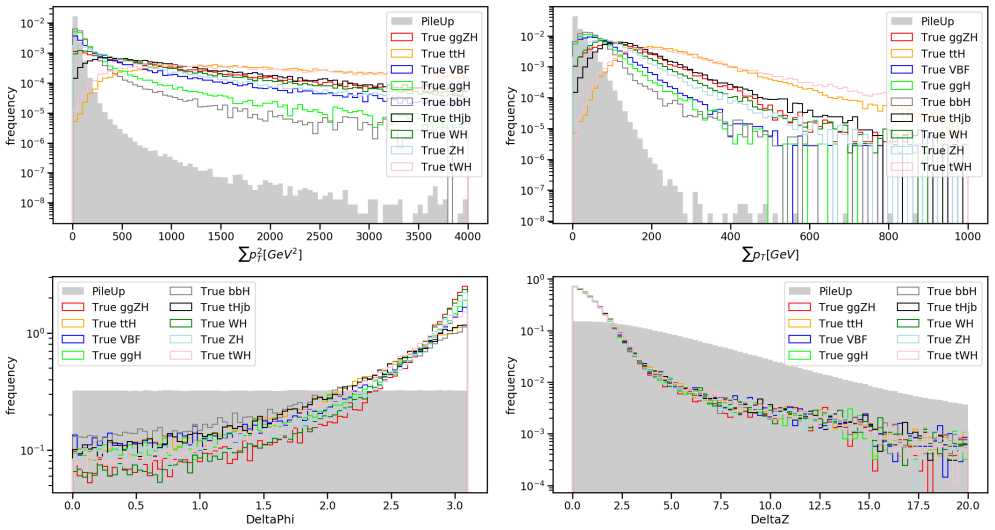

Figure 4.4 – Signal and background distributions for the four input variables used to train both the NN primary vertex selection algorithm and the BDT one. Samples from different data taking conditions are merged according to the corresponding integrated luminosity.

by approximately 30k events (therefore around 1 million background vertices) for each Higgs production mode and for each MC campaigns representing different data taking years. Only the events that fulfil the criteria described in Section 4.3.1 are employed in this dataset. The training is performed inclusively with respect to the photon conversion status, therefore only one BDT is trained to cover all the cases. A score is assigned to each vertex and the vertex with the highest score is selected as the diphoton primary vertex among the vertices belonging to the same event. Vertex selection efficiency is computed by requiring the selected primary vertex position to be within 0.3 mm in the z direction from the true vertex.

The results are reported in Table 4.3 and Figure 4.5. It can be observed that this training achieves better efficiencies compared to both the hardest vertex criterium and the diphoton NN for every Higgs production mode. The selection efficiencies obtained by the BDT are always slightly higher than the one obtained with the NN selections since less degraded by pileup condition. Moreover, in top-quark associated production processes the vertex selection efficiencies match the ones obtained with the selection of the hardest vertex ($\max \sum p_{\mathrm{T}}^2$) as expected, since now all the production modes are considered in the training. This primary vertex selection is not included for the results reported in this manuscript, but will be included for Run 3 results.

4.3.3 Photon selection

To further improve the signal purity, the two preselected photons must be matched to the objects having fired the triggers. Then, these two photons must pass a quality and kinematic selection in order to be considered for the diphoton analysis. In particular:

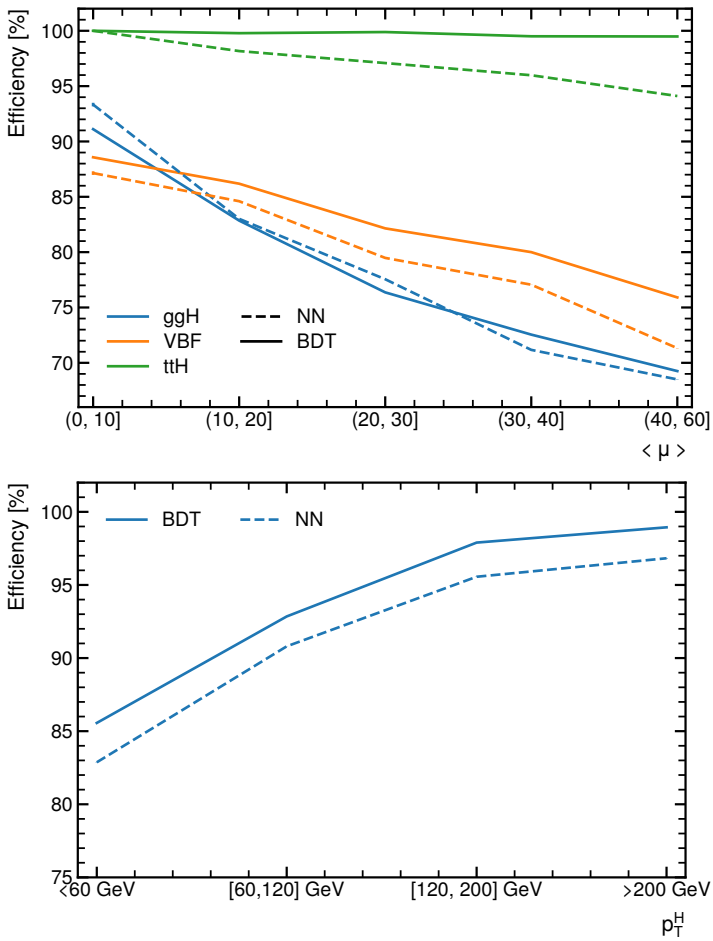

Figure 4.5 – Diphoton primary vertex selection efficiency as a function of the average pileup $<\mu>$ for three main production modes (upper) and as a function of Higgs p_T for the ggF sample (lower), comparing the NN selection (dashed lines) and the re-trained BDT one (solid lines). A vertex is considered correctly selected if its longitudinal z position falls within 0.3 mm from the true vertex.

Efficiency [%]	Hardest	NN	BDT
ggF	53.5	73.9	74.7
VBF	67.9	77.9	81.1
WH (lep)	79.2	83.0	86.7
WH (had)	92.2	92.7	96.4
ZH (lep)	62.7	73.4	78.1
ZH (had)	90.2	92.5	95.2
ggZH (lep)	73.5	82.5	86.0
ggZH (had)	96.4	95.5	98.5
$t\bar{t}H$	99.7	96.4	99.7
tHbj	96.4	92.7	97.5
tHW	99.6	97.0	99.6
$b\bar{b}H$	44.0	68.1	69.8

Table 4.3 – Privary vertex selection efficiency for all Higgs production modes, using with the hardest vertex method, the NN used in the diphoton analyses described in this manuscript, and the re-trained algorithm (BDT). Production modes with different decay modes have been split in their truth leptonic and hadronic parts.

- both photons must satisfy *tight* identification criteria (see Table 3.1);
- both photons must satisfy *FixedCutLoose* isolation criterium, which requires calorimeter-based and track-based isolation to be

$$E_{\mathrm{T}}^{\mathrm{iso}} < 0.065 \cdot p_{\mathrm{T}} \qquad \text{and} \qquad p_{\mathrm{T}}^{\mathrm{iso}} < 0.05 \cdot p_{\mathrm{T}}$$

  where $E_{\mathrm{T}}^{\mathrm{iso}}$ and $p_{\mathrm{T}}^{\mathrm{iso}}$ are calculated in a cone of radius $R = 0.2$ around the photon direction and only the tracks associated to the diphoton primary vertex are considered in the $p_{\mathrm{T}}^{\mathrm{iso}}$ calculation;
- to pass a relative $p_{\mathrm{T}}/m_{\gamma\gamma}$ selection for the leading and sub-leading photon of 0.35 and 0.25 respectively;
- the diphoton invariant mass $m_{\gamma\gamma}$ must fall in the range between 105 GeV and 160 GeV where $m_{\gamma\gamma}$ is defined as

$$m_{\gamma\gamma} = \sqrt{2E_1E_2(1-\cos\theta)}. \tag{4.1}$$

  E_1 and E_2 are the energies of the two photons and θ the angle between them.

4.3.4 Definition of TI and NTI events

Tight and Isolated events (TI events in the following) are events that have passed the full analysis event selection described in Section 4.3.3. In some cases, the invariant mass window requirement could be relaxed (a notable example is reported in Section 5.4.3).

Not Tight or Isolated events (NTI events in the following) are events that fail the tightness or the isolation requirement for at least one of the two photons, while passing all

other requirements, apart from the invariant mass window selection that could be relaxed too. NTI events can be used as a background proxy under the signal region peak, for augmenting the training statistics in case of signal/background classifier or to build background templates.

Data cut flow of diphoton selection

Table 4.4 and Table 4.5 present the cut flow on the data, starting from all recorded events in the `PhysicsMain` data stream. The requirement on $N_{Loose\,\gamma} \geq 2$ appears to be less efficient in 2017 and 2018 than in the previous data years, despite the use of the Medium-ID trigger, as opposed to the previous Loose-ID trigger. This behaviour has already been observed in the past $H \to \gamma\gamma$ analyses and it is related to a relatively higher contamination of electrons passing the 2017-18 trigger.

4.4 Categorization

The diphoton event selected as described in Section 4.3 are usually further divided in a number of categories based on the properties of the events, in order to enhance particular data peculiarities, like the predominant of events from a given Higgs production mode or the events with good $m_{\gamma\gamma}$ resolution. The categorization is therefore tightly bounded the measurement to be performed and more details on the categorizations used for the analyses reported in this manuscript will be given in the following chapters.

The event categorization is of paramount importance since it influences the capability of the maximum likelihood fit to data (see Section 4.8) in constraining its parameters of interest, since the model in these categories makes more stringent statical assumptions on the data. As an example we can consider the statistical significance of a given signal. Assuming we are in a regime where the significance of the i-th category can be approximated as $Z_i = S_i/\sqrt{B_i}$, with $S_i, B_i > 0$ being the number of signal and background events in that category. Two different categories will have a combined statistical significance of

$$Z_c = \sqrt{\frac{S_1^2}{B_1} + \frac{S_2^2}{B_2}} \tag{4.2}$$

while the statistical significance of the signal in the unclassified dataset will be

$$Z_m = \frac{S_1 + S_2}{\sqrt{B_1 + B_2}}. \tag{4.3}$$

With little algebra, it can be shown that the $Z_c \geq Z_m$. In fact,

$$Z_c^2 - Z_m^2 = \frac{S_1^2}{B_1} + \frac{S_2^2}{B_2} - \frac{(S_1 + S_2)^2}{B_1 + B_2} = \frac{B_1 B_2}{B_1 + B_2}\left(\frac{S_1}{B_1} - \frac{S_2}{B_2}\right)^2 \tag{4.4}$$

where the last term is always larger than 0, unless $\frac{S_1}{B_1} = \frac{S_2}{B_2}$. Therefore splitting events in categories usually improves the combined statistical significance of the fit.

Year	2015			2016		
Selection cut	Events	Tot eff [%]	Cut eff [%]	Events	Tot eff [%]	Cut eff [%]
All events	26684852	100	-	221203552	100	-
GRL	26074048	97.71	97.71	216177760	97.73	97.73
Pass trigger	25823600	96.77	99.04	208625888	94.31	96.51
Detector DQ	25821064	96.76	99.99	208619936	94.31	100
Has Primary vertex	25820988	96.76	100	208619904	94.31	100
2 loose photons	3614494	13.55	14	36496988	16.50	17.49
Trigger match	2671858	10.01	73.92	27422184	12.40	75.31
Tight ID	376969	1.41	14.11	3687766	1.67	13.45
Isolation	151476	0.57	40.18	1464740	0.66	39.72
Rel. p_{T} cuts	131391	0.49	86.74	1271547	0.57	86.81
$m_{\gamma\gamma} \in [105, 160]$GeV	28746	0.11	21.88	283205	0.13	22.27

Table 4.4 – Cutflow of the data in 2015 and 2016.

Year	2017			2018		
Selection cut	Events	Tot eff [%]	Cut eff [%]	Events	Tot eff [%]	Cut eff [%]
All events	213511216	100	-	268678304	100	-
GRL	207136448	97.01	97.01	265452832	98.80	98.80
Pass trigger	185083728	86.69	89.35	239147728	89.01	90.09
Detector DQ	185054416	86.67	99.98	239135232	89	99.99
Has primary vertex	185054416	86.67	100	239135232	89	100
2 loose photons	21857452	10.24	11.81	28374152	10.56	11.87
Trigger match	13441074	6.30	61.49	18743580	6.98	66.06
Tight ID	4624282	2.17	34.40	6409828	2.39	34.20
Isolation	1852435	0.87	40.06	2485239	0.92	38.77
Rel. p_{T} cuts	1606093	0.75	86.70	2156352	0.80	86.77
$m_{\gamma\gamma} \in [105, 160]$GeV	370335	0.17	23.06	496814	0.18	23.04

Table 4.5 – Cutflow of the data in 2017 and 2018.

4.5 Signal modelling

The shape of the signal and background $m_{\gamma\gamma}$ distributions is described with analytical functions. Starting from early Run 2 $H \to \gamma\gamma$ analyses [129], the shape of $m_{\gamma\gamma}$ invariant mass distribution for signal events in each category is modelled with a *double-sided Crystal Ball* (DSCB) function, f_{DSCB}. It is a composite function with 6 parameters formed by a Gaussian core and two power-law tails, as detailed in Eq. (4.5):

$$f_{\text{DSCB}}(m_{\gamma\gamma}) = N \times \begin{cases} e^{-t^2/2} & \text{if } -\alpha_{low} \leq t \leq \alpha_{high} \\ \dfrac{e^{-\frac{1}{2}\alpha_{low}^2}}{\left[\frac{1}{R_{low}}\left(R_{low} - \alpha_{low} - t\right)\right]^{n_{low}}} & \text{if } t < -\alpha_{low} \\ \dfrac{e^{-\frac{1}{2}\alpha_{high}^2}}{\left[\frac{1}{R_{high}}\left(R_{high} - \alpha_{high} + t\right)\right]^{n_{high}}} & \text{if } t > \alpha_{high} \end{cases} \tag{4.5}$$

where N is a normalization factor and the six parameters are

- μ_{CB} and σ_{CB} describe the mean and the width of the Gaussian core, which are combined in $t = \left(m_{\gamma\gamma} - \mu_{\text{CB}}\right)/\sigma_{\text{CB}}$;
- α_{low} and α_{high} are the positions of the transitions with respect to μ_{CB} from the Gaussian core to power-law tails, in unit of σ_{CB}, on the low and high mass sides respectively;
- n_{low} and n_{high} are the exponents of the low and high mass tails. With the α's, they define $R_{low} = \frac{n_{low}}{\alpha_{low}}$ and $R_{high} = \frac{n_{high}}{\alpha_{high}}$.

The DSCB parameters are fitted with an unbinned maximum likelihood fit over the simulated Higgs signal samples. The different production modes are merged together according to their SM cross sections. The parameters are then kept fixed when the signal model is included in the final likelihood, but additional parametrization as a function of m_H for μ_{CB} and σ_{CB} is included for the mass analysis, as detailed in Section 6.3.1. An example of this signal fit is shown in Figure 4.6.

The DSCB has been chosen because it showed a good χ^2 in the signal only fit and gives a negligible bias on the fitted signal yield using injection tests with signal MC. The advantage of the DSCB is to well separate the contribution coming from the core and from the tails, making easier to apply systematic variations on the photon energy scale (on μ_{CB}) and on the photo energy resolution (to σ_{CB}).

4.6 Background modelling

As it has been already mentioned at the start of this chapter, one of the advantages of the $H \to \gamma\gamma$ analyses is its robust background modelling and subtraction. The background shape parameters and normalization are directly fit to observed data. Despite this, one

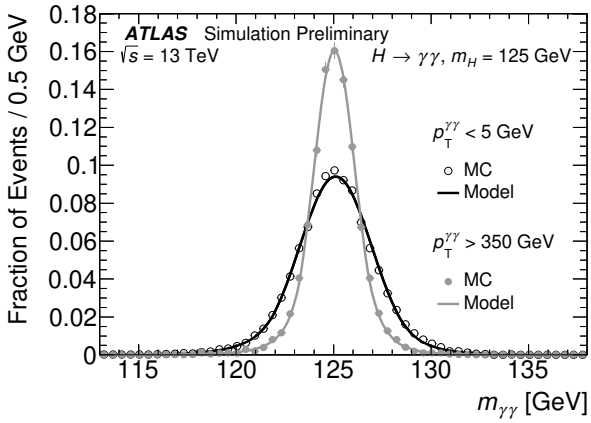

Figure 4.6 – The signal probability distribution functions in two extreme $p_{\mathrm{T}}^{\mathrm{H}}$ regions, demonstrating the variation of the signal $m_{\gamma\gamma}$ resolution. The signal pdfs (solid curves) are compared against the $m_{\gamma\gamma}$ distribution of the signal MC simulation for events in the corresponding $p_{\mathrm{T}}^{\gamma\gamma}$ bins [130].

has to decide the best analytical function to model the background in each reconstructed category and assign a systematic uncertainties on this choice. The general strategy is outlined in this section while further details are given in particular in the Section 5.5.2 since with an increasing number of categories additional complications arise.

The dominant and irreducible background entering the invariant mass spectrum comes from SM continuum $\gamma\gamma$ QCD production. Additionally, photons produced inside jets due to the decays of neutral mesons to photon pairs make γj ad jj events in which the jets are mis-identified as photons a non-negligible source of background. Photon-pairs can be also faked from Drell-Yan events in which both electrons are misidentified as photons. However, this background only contributes with a small fraction ($< 1\%$).

The general strategy starts (Section 4.6.1) by measuring the composition of the continuous background in term of $\gamma\gamma$, γj and jj components by means of data-driven techniques for each category entering the measurement. The background fractions are then used to build $m_{\gamma\gamma}$ background templates for each category: the $\gamma\gamma$ component is obtained from MC, while the γj and jj are included by weighting the $\gamma\gamma$ MC component to reproduce the shape from jet enriched control region in data and normalized used the measured fraction. Finally the spurious signal approach (Section 4.6.2) is used to select a functional form to describe each template, as well as to determine the associated bias that will enter the measurement as a systematic uncertainties.

4.6.1 Background templates

The number of $\gamma\gamma$, γj and jj events entering each category is estimated by means of a double two-dimensional sideband ABCD method [131]. This data-driven method extrapolates the fraction of fake photons within the tight and isolated region from the composition of the control regions built by inverting photon identification and isola-

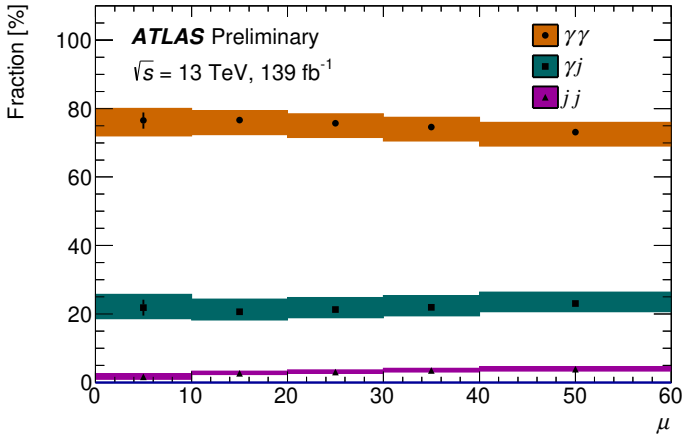

Figure 4.7 – Inclusive $\gamma\gamma$, γj, and jj purities for the Run 2 data as obtained by the double ABCD method as a function of the pileup [130]. The coloured error bands shown in the plots correspond to the sum in quadrature of the statistical and systematic uncertainties.

tion requirements. This criterion is defined by relaxing three strip variables (ω_{s3}, F_{side} and *DeltaE*, see Table 3.1) with respect to the tight criterion. This choice is made to make the photon identification and photon isolation variables independent and to avoid any bias coming from the medium selection made at trigger level for the 2017 and 2018 data taking periods. The full method involves sixteen input equations with nineteen variables and solving them returns the fraction of the three background components. The inclusive results in shown in Figure 4.7 as a function of the pileup. The average diphoton purity in the selected samples amount to $\sim 80\%$.

Once the background fraction have been computed, the simulated $\gamma\gamma$ shape is compared to a γj enriched data control region in which the identification criteria of exactly one of the two photons is inverted. The contamination from $\gamma\gamma$ extracted from simulated samples in this region is subtracted and a linear weighting is derived to make the MC $\gamma\gamma$ shape to match the shape from the control region. The procedure is repeated in a control region in which the identification criteria of both photons is inverted to determine a shape weighting for jj events. These derived shapes are then combined with the measured relative event fractions to obtain the final background template for each category.

4.6.2 Spurious signal test

The background $m_{\gamma\gamma}$ shape for each analysis category is described using an analytic function whose parameters and normalization are fitted to data. The choices for the analytic function that have been considered are

- Exponential Function: $f(m_{\gamma\gamma}) = e^{c \cdot m_{\gamma\gamma}}$
- Exponential Function of 2^{nd} Order Polynomial: $f(m_{\gamma\gamma}) = e^{c_1 \cdot m_{\gamma\gamma}^2 + c_2 \cdot m_{\gamma\gamma}}$

- Exponential Function of 3^{rd} Order Polynomial: $f(m_{\gamma\gamma}) = e^{c_1 \cdot m_{\gamma\gamma}^3 + c_2 \cdot m_{\gamma\gamma}^2 + c_3 \cdot m_{\gamma\gamma}}$
- Bernstein polynomial of order N: $B_N(m_{\gamma\gamma}) = \sum_{i=0}^{N} c_i \cdot b_{i,N}$ with $b_{i,N} = \binom{N}{i} m_{\gamma\gamma}^i (1 - m_{\gamma\gamma})^{N-i}$
- First-Order Power Law Function: $f(m_{\gamma\gamma}) = m_{\gamma\gamma}^c$

The method to select the functional form in each category is based on the *spurious signal* test.

To perform this test, the complete analytic signal plus background model is fitted to the background-only template built as described in Section 4.6.1. All the background functions listed above are tested and the procedure is carried out independently for each reconstructed category. The fit is performed in the nominal diphoton mass range of $105 \leq m_{\gamma\gamma} \leq 160\,\text{GeV}$. The number of fitted signal events as a function of the Higgs mass is computed in intervals of 0.5 GeV within the diphoton mass range of $123 \leq m_{\gamma\gamma} \leq 127\,\text{GeV}$, taking into account also negative fluctuations. The number of spurious signal events N_{sp} is then defined as the maximum of the absolute value of the fitted number of signal events within this range on the background-only MC based template.

One of the above function is considered to pass the spurious signal test if it satisfies at least one of the following criteria:

- $N_{sp} < 10\% N_{s,exp}$ where $N_{s,exp}$ is the number of expected signal events under the SM assumption in the category;
- $N_{sp} < 20\% \sigma_{sig}$ where σ_{sig} is the expected statistical uncertainty on the number of signal events due to the background statical fluctuations.

Moreover, the fit of the analytic function to the background template is required to yield a χ^2 probability of at least 1%. If multiple functions fulfil the requirements, the one with the smallest number of degrees of freedom is chosen. If the functions have the same degrees of freedom, the one with smaller N_{sp} is chosen.

4.7 Systematic uncertainties

Systematic uncertainties are introduced in the statistical model in order to cover for multiple effects that can be due to the choices made at reconstruction level in the analysis chain, use of auxiliary measurements in the analysis, inclusion of prediction from SM parameters with some uncertainties, uncertainties on the corrections applied to object modelling, and many others. The systematic uncertainties can therefore be of *experimental* and *theoretical* nature and they can affect the signal and the background components of the analysis. Systematic uncertainties are brought into the model with *nuisance parameters*, which are allowed to float in the fit to data to best describe the observed dataset. If the same systematic effect has an impact on multiple processes, the nuisance parameters

are correlated, which means that the same nuisance parameter is used to described these multiple impacts.

Concerning the continuum background, the $H \to \gamma\gamma$ analysis features a data driven estimation, so there is only one systematic uncertainty associated to the background modelling which is just the spurious signal assigned on the choice of the analytical model, as described in Section 4.6.2. Since each category has its own background function which is decided in a independent manner, one nuisance parameter for each category is included in the model and this affects the signal normalization as shown in Eq. (4.10).

Besides this, all other systematic uncertainties in the $H \to \gamma\gamma$ channel concerns the signal modelling. As said, these can arise from experimental or theoretical effects and they can impact both the normalization (because for example they are impacting the selection efficiency or the expected SM cross sections) and the shape of the signal model. In the coupling analysis, the systematic with the largest impacts are the ones which affects the signal normalization or the ones that vary the signal over background ratio, while in the mass analysis the largest impacts come from systematic affecting the position of the signal peak.

The computation of the impacts caused by different systematic sources affecting the signal is carried out by variations included in the simulated Monte Carlo samples: usually, the nominal samples are produced alongside systematics samples where each single systematic source has been activated by means of different weights or by different central values of a given observable. The impact is then computed as variations with respect to the nominal Monte Carlo sample and then propagate through the analysis. In case the uncertainty has an impact on the signal normalization, this is computed as the relative difference between the expected number of events and $\pm 1\sigma$ varied yields using signal MC samples:

$$\delta N_{cp}^{\pm 1\sigma} = \frac{N_{cp}^{\pm 1\sigma}}{N_{cp}^{\text{nom}}} - 1 \tag{4.6}$$

where $N_c p$ is the expected number of events in a given category c for the SM process p. In case of theoretical uncertainties, additional care has been taken when computing the systematic impact since it both affects the truth-level and reco-level distributions and we may want to have the two contributions separated (see Section 5.6.1).

4.7.1 Theoretical uncertainties

Theoretical uncertainties are due to the imperfect knowledge of the theoretical parameters used in the MC generation or to the uncertainties that affects the calculation of the Standard Model predictions. Since all of them have an effect on the signal normalization the coupling analysis is more affected then the mass analysis. The predicted number of diphoton events from each of the different Higgs boson production modes have uncertainties arising from the imperfect knowledge of

- the $H \to \gamma\gamma$ branching ratio;
- the missing higher-order terms in the perturbative QCD calculations, referred as

QCD scale uncertainties;

- the parton density functions (PDF) and the value of the strong coupling constant α_S;
- the QCD effects in the soft and collinear regime, hadronization and multi-parton interactions (MPI).

These effects cause signal migrations among the different analysis categories and are therefore computed as variation on the signal yields. Each uncertainty source is considered fully correlated among the various categories.

The uncertainty on the $H \to \gamma\gamma$ branching ratio is due to the dependence on the partial Higgs widths from quark masses and the strong coupling constant. It has a flat asymmetric effect of $+2.90\%$ and -2.84% [31].

The effect of missing higher-order in the perturbative QCD calculations and of PDF and α_S variation are Higgs production process dependent, with their impact reported in Table 1.1. The QCD scale uncertainties are usually computed with variations of the factorization and renormalization scales used at generator-level or with much complex schemes (like the BLPTW one [31, 132]). Additional prescriptions are needed in the case where the Higgs production phase space is sub-divided in kinematic bins, like in the Simplified Template formalism (see Section 5.1) used in the coupling analysis; therefore additional details will be provided in Section 5.6.1. The PDF and α_S uncertainties are evaluated using generator-level variations which follows the PDF4LHC15 at NLO prescriptions [133], which, apart from the central PDF, comes along with 30 error sets. Each of them corresponds to an eigenvector of the covariance matrix in the parameter space of the PDF fit. Two additional PDF sets are provided with a different value of α_S assumed in the PDF fit: the nominal value of 0.118 is varied by ± 0.0015 to compute the α_S uncertainty.

Concerning instead uncertainties due to soft and collinear regime, hadronization and MPI, no general prescriptions have been given by the theoretical community; therefore these are usually accounted for by means of additional MC samples where a different parton shower generator (Herwig++) is used in placed of the nominal one (PYTHIA 8) and the variation of expected number of events in a given category is assigned as systematic impact. These effects are usually taken as uncorrelated among the different production modes, giving rise to 8 different nuisance parameters, and are computed by means of Eq. (4.6).

4.7.2 Experimental uncertainties

Experimental uncertainties affect both the signal shape and normalization. In the $H \to \gamma\gamma$ analysis, the largest experimental sources are the photon reconstruction and selection, in particular concerning photon energy calibration, trigger efficiency, identification and isolation.

The photon energy scale (PES) and the photon energy resolution (PER) variations act both on the signal shape and on the categories yields. Their effect is included in the fit to data as response functions on the mean and the width of the Gaussian core of the DSCB (μ_{CB} and σ_{CB}) respectively. The other parameters of the Double Sided Crystal

Ball function used to model the signal are considered as not affected. These systematic variations are extracted for each analysis category and are treated as fully correlated among categories. Since the PER changes the signal over background ratio, the coupling analysis is more affected by these uncertainties, while the mass analysis is concerned by the PES since it acts on the peak position. The impact of these systematic sources is computed from MC signal samples

- for the PES using the ratio-of-mean technique: the means of $m_{\gamma\gamma}$ are computed for nominal and $\pm 1\sigma$ varied distributions. Then, the systematic uncertainty applied to μ_{CB} is evaluated as

$$\delta_{\mu_{\text{CB}}}^{\pm 1\sigma} = \frac{\left\langle m_{\gamma\gamma}^{\pm 1\sigma} \right\rangle}{\left\langle m_{\gamma\gamma}^{\text{nom}} \right\rangle} - 1. \tag{4.7}$$

  The 69 nuisance parameters related to the PES are included in the fit by multiplying their effects and applying them to μ_{CB}. In the coupling analysis, the material systematics subdivided in many $|\eta|$ bins are grouped together by summing in quadrature their effects in a "barrel" and an "endcap" components, effectively reducing the number of nuisance paramerts to 40.

- for the PER using the ratio of inter-quartile distribution: the inter-quartile is computed as $S = CDF^{-1}(75\%) - CDF^{-1}(25\%)$, where CDF is the cumulative distribution function of the $m_{\gamma\gamma}$ nominal and varied distributions. Then, the uncertainty is evaluated as

$$\delta_{\sigma_{\text{CB}}}^{\pm 1\sigma} = \frac{S^{\pm 1\sigma}}{S^{\text{nom}}} - 1. \tag{4.8}$$

  The 9 nuisance parameters related to the PER are included in the fit by multiplying their effects and applying them to μ_{CB}.

Photon energy scale and resolution have an impact on the signal normalization too, since selection on photons p_{T} is used in the diphoton event selection and may be further used to define the analysis categorization. These effects are accounted for alongside photon trigger efficiency, identification and isolation and MC pileup re-weighting (see Section 4.2.2), which all impact the yield of each category. Additional experimental source of systematics acting on the yields are included in the case additional reconstructed objects are used to defined a categorization, as in the case of the coupling categorization: in this case, the systematic sources associated to that object should be account for the in model to fit the data. All these effects that have an impact on the signal normalization are computed with the Eq. (4.6).

An additional source of experimental uncertainty for the signal comes from the luminosity measurement, which has a flat 1.7% impact on the signal yields as reported in Table 4.1.

4.8 Statistical model

The signal and background models plus all the systematic uncertainties are combined in an extended likelihood function $\mathcal{L}$, built to model the data in each of the analysis categories

$$\mathcal{L}\left(\boldsymbol{\mu}, m_H, \boldsymbol{\theta}; m_{\gamma\gamma}\right) = \prod_{c=1}^{N_c} \text{Pois}\left(n_c | \nu_c\left(\boldsymbol{\mu}, \boldsymbol{\theta}\right)\right) \prod_{i=1}^{n_c} f_c\left(m^i_{\gamma\gamma}; m_H, \boldsymbol{\theta}\right) \prod_j G\left(\alpha_j | \theta_j, 1\right). \quad (4.9)$$

The first product is the likelihood extended term and it spans over the analysis categories: the number of observed events for each category n_c is modelled with a Poisson distribution with mean

$$\nu_c\left(\boldsymbol{\mu}, \boldsymbol{\theta}\right) = s_c(\boldsymbol{\mu}, \boldsymbol{\theta}) + b_c + N^c_{sp} \cdot \theta^c_{sp} \quad (4.10)$$

where s_c is the number of expected Higgs signal events for the c-th category, b_c the number of background events and N^c_{sp} is the spurious signal along with its nuisance parameter θ^c_{sp}. The number of expected events for each category s_c is modelled as

$$s_c\left(\boldsymbol{\mu}, \boldsymbol{\theta}\right) = \sum_p \mu_p \cdot s_{cp}\left(\boldsymbol{\theta}\right) = \sum_p \mu_p \cdot L\left(\theta_{lumi}\right) \cdot \sigma^{\gamma\gamma}_p\left(\boldsymbol{\theta}_{sig}\right) \cdot \epsilon_{ct}\left(\boldsymbol{\theta}_{sig}\right) \quad (4.11)$$

where

- the sum runs over the Higgs production modes p;
- $\sigma^{\gamma\gamma}_p$ are the values of the $H \to \gamma\gamma$ branching ratio times production mode p cross section at $m_H = 125.09\,\text{GeV}$;
- $\boldsymbol{\theta}$ are the related set of nuisance parameters which impact the categories yields;
- the ϵ_{cp} term accounts fro the probability for an event from a given production mode p to end up in the reconstructed category c;
- $\boldsymbol{\mu}$ is a set of signal strengths (see Eq. (1.37)) that can be fitted to the data (for example in the coupling analysis) and it quantifies the agreement between the measured cross sections and the Standard Model predictions.

The second term of Eq. (4.9) represents the diphoton invariant mass probability density function for each category which is built from the signal and background functions as

$$f_c\left(m^i_{\gamma\gamma}; m_H, \boldsymbol{\theta}\right) = \frac{1}{\nu_c}\left[\left(s_c(\boldsymbol{\mu}, \boldsymbol{\theta}) + N^c_{sp}\theta^c_{sp}\right) \cdot f^c_{sig}\left(m^i_{\gamma\gamma}; m_H, \boldsymbol{\theta}_{SS}\right) + \right. \\ \left. + b_c \cdot f^c_{bkg}\left(m^i_{\gamma\gamma}; \boldsymbol{\theta}_{BS}\right)\right] \quad (4.12)$$

where f^c_{sig} and f^c_{bkg} are the analytical functions for signal and background respectively, $\boldsymbol{\theta}_{SS}$ are the shape uncertainties on the peak position and width of the signal shape and $\boldsymbol{\theta}_{BS}$ are background shape parameters, which are free to float in the fit.

The last term in the likelihood function Eq. (4.9) is the product of constraint terms. Indeed, each nuisance parameter θ (except the $\boldsymbol{\theta}_{BS}$) is constrained by a unitary Gaussian probability density function $G(\alpha|\theta, 1)$, with the α called global observable and usually set to 0. Then systematic uncertainties enter the likelihood by multiplying the affected quantity with one of the following response functions:

$$\begin{aligned}
F_{\mathrm{G}}(\delta,\theta) &= (1+\delta\theta) && \text{for a gaussian constraint} \\
F_{\mathrm{LN}}(\delta,\theta) &= e^{\sqrt{\ln\left(1+\delta^2\right)}\theta} && \text{for a log-normal constraint} \\
F_{\mathrm{AS}}(\delta^{\pm},\theta) &= \begin{cases} P_6(\theta;\delta^-,0,\delta^+) & \text{if } \theta \in \left[\delta^-,\delta^+\right] \\ \exp(\theta) & \text{outside} \end{cases} && \text{for an asymmetric constraint}
\end{aligned} \tag{4.13}$$

where δ is the relative uncertainty amplitude estimated ($\delta^{\pm}$ in case of asymmetric $\pm 1\sigma$ variations), $P_6(\theta;\delta^-,0,\delta^+)$ is a six-degree polynomial bound to pass from δ^-, 0 and δ^+, while $\exp(\theta)$ is the exponential extrapolation of P_6 matching the value, first and second derivatives at its boundaries [134]. In general, log-normal constraints are used whenever a negative model parameter has no physical sense. A possible example could be the luminosity with its associated uncertainty, which is given by

$$L\left(\theta_{lumi}\right) = L \cdot e^{\sqrt{\ln\left(1+\delta^2\right)}\theta_{lumi}} \qquad \text{with constraint } G\left(0|\theta_{lumi},1\right) = \frac{1}{\sqrt{2\pi}} e^{\frac{-\theta^2_{lumi}}{2}}. \tag{4.14}$$

The spurious signal implementation is different from all the other uncertainty, since the response function is just $F_{\mathrm{Sp}} = \theta$, as shown in Eq. (4.10).

Correlation among different systematic sources is imposed by using the same nuisance parameter θ with different values of δ.

The dataset for each category is uniformly binned with 220 bins for the coupling analysis and 550 bins for the mass analysis. These binnings are chosen in order to ensure a bias on the fitted parameter of interest below 0.1%, computed on the Asimov dataset (see Section 4.8.2).

4.8.1 Test statistic

The measurements presented in this manuscript are performed by expressing the event yields in each event category in terms of the measurement parameters (like in the case of signal strengths in Eq. (4.11)), and fitting the model of Eq. (4.9) to the data. Best-fit values are reported along with uncertainties corresponding to 68% confidence level intervals obtained from a profile likelihood technique [135]. The profile likelihood ratio

(PRL) is a test statistic computed as

$$\lambda(\boldsymbol{\mu}) = -2\ln\frac{\mathcal{L}\left(\boldsymbol{\mu}, \hat{\boldsymbol{\theta}}_{\boldsymbol{\mu}}\right)}{\mathcal{L}\left(\hat{\boldsymbol{\mu}}, \hat{\boldsymbol{\theta}}\right)} \tag{4.15}$$

where $\hat{\boldsymbol{\mu}}$ and $\hat{\boldsymbol{\theta}}$ are the parameters which maximize the likelihood unconditionally and $\hat{\boldsymbol{\theta}}_{\boldsymbol{\mu}}$ is the set of parameters of interest which maximizes the likelihood for a fixed $\boldsymbol{\mu}$ [135]. The Neyman-Pearson lemma [136] ensures that the test statistics based on the PRL are the most statistically powerful, i.e. for a given signal efficiency, they provide the decision criterion that minimizes the false positive probability. Compatibility with the Standard Model is computed from the value of the profile likelihood ratio of the model in data under the SM hypothesis; a p-value quantifying the compatibility with the SM is computed under the assumption that this quantity follows a χ^2 distribution with a number of degrees of freedom equal to the number of parameters of interest [135].

Uncertainties may be presented as a decomposition into separate components: the statistical component is obtained from a fit in which the nuisance parameters associated with systematic uncertainties are fixed to their best-fit values; the systematic component, corresponding to the combined effect of systematic uncertainties, is computed by subtracting in quadrature the statistical component from the total uncertainty.

4.8.2 Expected results

Expected results for the SM are obtained from a fit to an Asimov dataset [135], a dataset generated from the likelihood model such that when it is used to evaluate the estimators for all parameters, the result is the true parameter values and their expected uncertainties.

This dataset can be built in different ways, according to the hypothesis under test for what concern the parameter of interest, like for example SM ($\boldsymbol{\mu} = \mathbf{1}$) or background-only ($\boldsymbol{\mu} = \mathbf{0}$). Concerning the value of the constrained nuisance parameters, two prescription are used in this manuscript. The first is employed before unblinding of the signal region, as in the case of the mass analysis in Section 6.5, and the so-called "pre-fit" Asimov dataset is generated: in this case the nuisance parameters and the global observables of the model are set to their default values (i.e. both set to 0). The second prescription is used to generated the "post-fit" Asimov dataset, after SR unblinding: in this case the global observables values is set to the best fit values of the corresponding nuisance parameters obtained from a fit on observed data of the model with the largest number of free parameters possible.

CHAPTER 5

Measurement of Higgs Boson production cross sections

After the Higgs boson discovery in 2012 and the study of its properties carried out on Run 1 data (see Section 1.4), ATLAS and CMS experiments have continued to accumulate and analyse collision data produced by the LHC. The Run 2 data taking period spanned four years from 2015 to 2018 and the total luminosity collected is around a factor five larger than Run 1. Moreover, the center-of-mass collision energy has been raised from 8 TeV to 13 TeV, increasing the total expected Higgs production cross section with a mass of $m_H = 125.09\,\text{GeV}$ from 24.5 pb to 55.6 pb [31]. Therefore, with this large amount of data, more precise and detailed measurements have been performed, in particular on the Higgs boson couplings to the other Standard Model particles. This chapter presents the legacy Run 2 measurements of Higgs boson production cross sections following the *Simplified Template Cross Section* (STXS) formalism (Section 5.1) in the $H \to \gamma\gamma$ decay channel [6], and its combination with other analyses [11]. Both represent the core of my work in the ATLAS Collaboration. These results supersede the partial Run 2 results in the $H \to \gamma\gamma$ channel [8, 129] and combination [13].

5.1 The Simplified Template Cross Section framework

In recent years given the larger and larger amount of data available, the Higgs boson production phase space has been sub-divided into mutually exclusive regions, leading to the so called *Simplified Template Cross Sections* (STXS) framework [31, 137, 138]. Simplified template cross sections provide a way to evolve the signal strength measurements that were performed during Run 1, by reducing the theoretical uncertainties that are directly folded into the measurements and by providing finely-grained Higgs production phase space regions (called *truth bins*), which are mutually exclusive. The splits are designed to maximize the experimental sensitivity by using quantities directly measured by experiment, while reducing the underlying Standard Model assumptions dependence and isolating possible BSM effects that may arise. For example, measuring the ggH plus 0, 1 and 2-jet sub-processes allows to avoid to commit to a single prescription for jet bin migration that is needed to extract the ggF total cross section, while, on the other hand, probing regions with very high p_{T}^{H} provides a handle on possible BSM signals. A fundamental separation into production modes is an essential aspect to reduce their model dependence, i.e., to eliminate the dependence of the measurements on the relative fractions of the production modes in the SM.

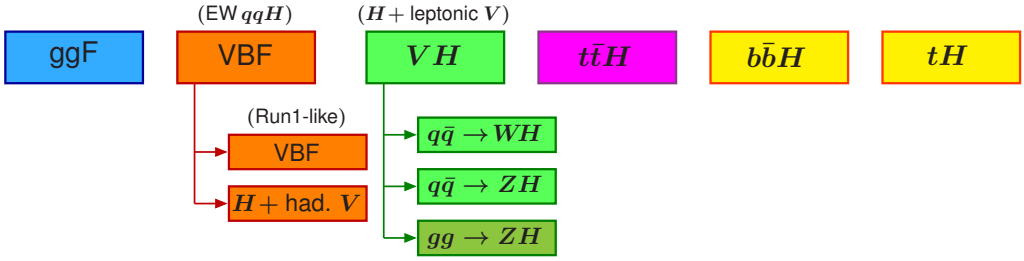

Figure 5.1 – The Stage-0 splitting of the Simplified Template Cross Sections [31].

At the same time, the STXS allows for the use of multivariate analysis techniques and provides a common framework for the combination of measurements in different decay channels and eventually between experiments. Moreover, the splits between bins have been designed to be enough scalable to the sensitivity of the analysis, which varies with the amount of data collected. Indeed, truth bins are defined in three different *stages* with increasing granularity.

The result of their use is a measurement of fully extrapolated and unfolded cross sections that can be also expressed as signal strengths relative to the SM predictions. In additional, given the fact that the production cross sections measurement is carried out in a differential way, the STXS are used as the basis for further interpretations.

The definition of the final state objects, namely leptons, jets, and in particular the Higgs boson itself, are explicitly kept simpler than in the fiducial cross section measurements. The STXS are defined for the production of an on-shell Higgs boson and a global selection cut on the Higgs rapidity at $|y_{\mathrm{H}}| < 2.5$ is enforced in all truth bins. Leptonically decaying vector bosons are defined from the sum of all their leptonic decay products including τ and neutrinos, with no restriction on the transverse momentum or the rapidity of the leptons (or its decays, in case of τ). Truth jets are defined as anti-k_t jets with a jet radius of $R = 0.4$, built from all stables particles after removing Higgs decay products and vector boson leptonic decay products. Truth jets have no rapidity restriction but are required to have $p_{\mathrm{T}} > 30\,\mathrm{GeV}$, in order to experimentally suppress jets from pileup interactions.

5.1.1 Stage 0

The Stage 0 STXS splitting is summarised in Figure 5.1. One truth bin per production mode is defined with Higgs boson rapidity $|y_{\mathrm{H}}|$ less than 2.5. With respect to Run 1 measurements a notable difference is introduced for VBF and VH production processes: indeed, for these production modes, the naive distinction between the two processes becomes ambiguous at higher perturbative orders when the vector boson decays hadronically. For this reason, the VH bin specifically targets Higgs boson production in association with a leptonically decaying V boson. The VH process with a hadronically decaying V boson is considered to be part of what is called "VBF production", which is therefore defined in the following as electroweak $qq \to Hqq$ production, since the VH with hadronic V boson decay and VBF topologies lead to the same final state through

the same interactions and therefore represent the t-channel and s-channel contributions to the same physical process. In a very similar way, the ggF Stage-0 bin includes also the real electroweak radiation, i.e. ggZH process with the Z boson decaying hadronically.

5.1.2 Stage 1.0

The Stage 1.0 of STXS is much more granular with respect to Stage-0 and, like before, the acceptance for each bin is $|y_{\mathrm{H}}| < 2.5$. For $\mathrm{t\bar{t}H}$, $\mathrm{b\bar{b}H}$ and tH production modes no further splitting is defined. For ggF, VBF and VH, instead, the splitting is shown in Figure 5.2. The (+) indicates bins that could be merged together at an intermediate stage: in this sense Stage 1 framework is more flexible than Stage 0.

For the ggF production mode, the primary split is due to the number of jets, following the fact that jet bins are used in Higgs analysis and therefore it avoids folding the associated theoretical uncertainties into the measurement. Each jet bin is further split based on the Higgs transverse momentum values $p_{\mathrm{T}}^{\mathrm{H}}$, where the $p_{\mathrm{T}}^{\mathrm{H}} > 200\,\mathrm{GeV}$ bin targets BSM contributions. The $N_{\mathrm{jets}} \geq 2$ bin with "VBF cuts" is defined in order to measure the ggF contamination in the VBF process and is split in $p_{\mathrm{T}}^{\mathrm{H}jj} \equiv |p_{\mathrm{T}}^{\mathrm{H}} + p_{\mathrm{T,jet1}} + p_{\mathrm{T,jet2}}|$ bins, where $p_{\mathrm{T,jet1}}$ and $p_{\mathrm{T,jet2}}$ are the leading and subleading jet p_{T}. "VBF cuts" targets the typical VBF topology, therefore requires two jets with $\Delta\eta_{jj} > 2.8$ and an invariant mass of the dijet system $m_{jj} > 400\,\mathrm{GeV}$.

For the VBF, the primary split is provided by the p_{T} of the leading jet, where an high value of this observable indicates a BSM contribution. Then, standard VBF selections are applied and bins are defined as in the ggF; two more bins target the VH hadronic decay requiring $60 < m_{jj} < 120\,\mathrm{GeV}$ and all the remaining events (Rest).

As explained before, the VH bins target associated production with a vector boson when it decays to leptons. The split is defined at the production level between $q\bar{q}$ and gg initiated processes and becomes ambiguous at higher orders. Then, $q\bar{q} \rightarrow$ VH bins are divided according to which vector boson takes part in the process. A finer splitting is finally defined on the vector boson p_{T} and the number of jets.

5.1.3 Stage 1.1 and 1.2

The Stage 1.1 [137] and its subsequent evolution in Stage 1.2 [138] have been designed to overcome the limitations of the Stage 1.0, which were brought up by the experimental collaboration after the STXS measurement with partial Run 2 dataset. This new scheme has been designed to be the baseline framework for full Run 2 analyses and is is shown in Figure 5.3. The only difference between schemes 1.1 and 1.2 is the presence of additional $p_{\mathrm{T}}^{\mathrm{H}}$ truth bins ggF ($p_{\mathrm{T}}^{\mathrm{H}} > 200\,\mathrm{GeV}$) regions and in $\mathrm{t\bar{t}H}$, thus these are described together here.

Most of the updates went into the VBF phase space: in particular, the p_{T} requirement is changed from the $p_{\mathrm{T,jet1}}$ to $p_{\mathrm{T}}^{\mathrm{H}}$ (to align the definition with the one adopted for the ggF phase space), the treatment of BSM high $p_{\mathrm{T}}^{\mathrm{H}}$ regions now features additional m_{jj} splits, which are more finely grained in the usual ($p_{\mathrm{T}}^{\mathrm{H}} < 200\,\mathrm{GeV}$) VBF production phase space too and foresees the dropping of the additional $|\Delta\eta_{jj}|$ cut. More m_{jj} bins accounts for the

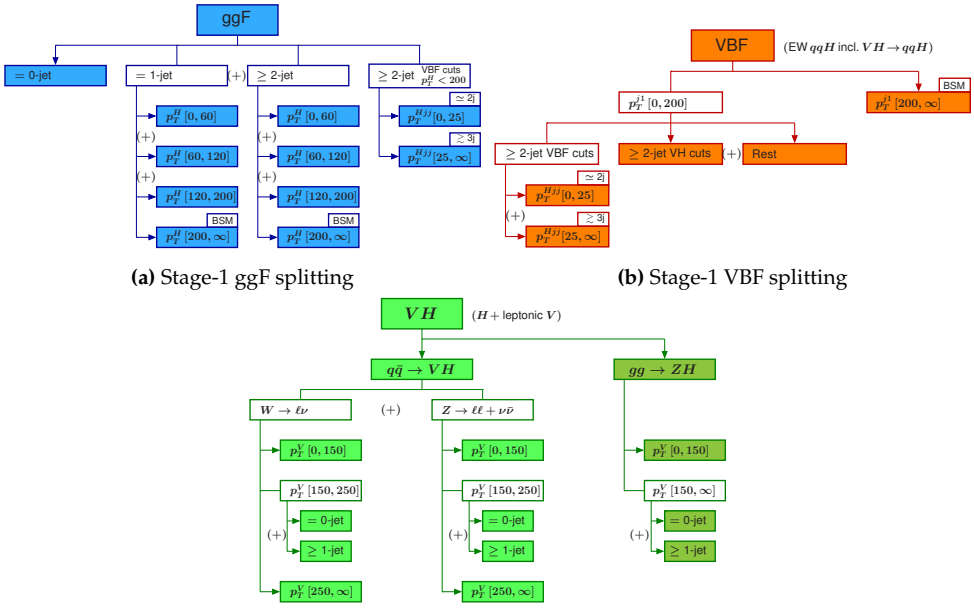

(a) Stage-1 ggF splitting

(b) Stage-1 VBF splitting

(c) Stage-1 VH splitting

Figure 5.2 – ggF, VBF and VH STXS for the Stage 1 splitting. The coloured boxes are the truth bins to be measured. The (+) between bins indicates whether bins could be merged [31].

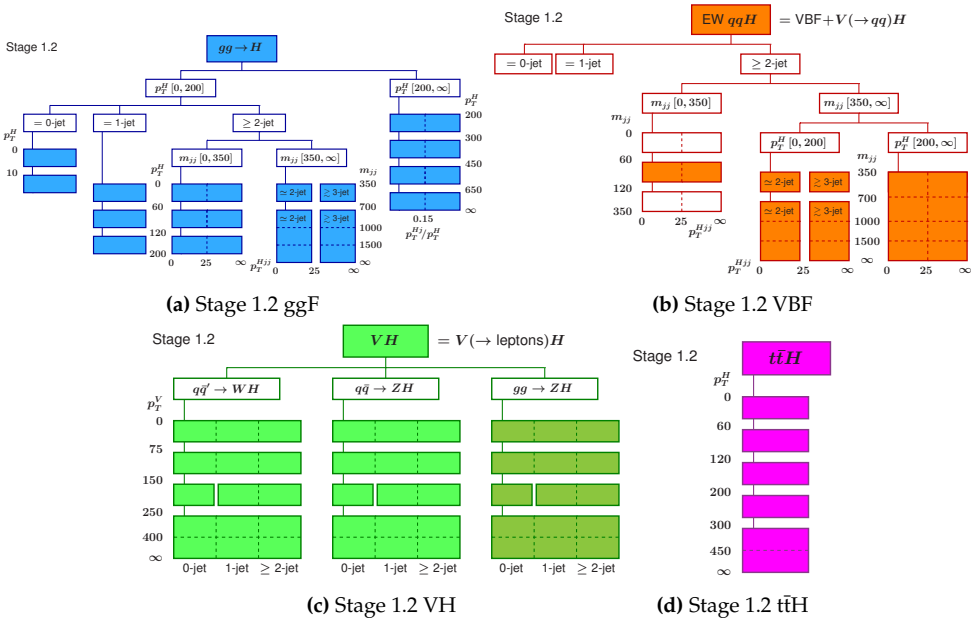

(a) Stage 1.2 ggF

(b) Stage 1.2 VBF

(c) Stage 1.2 VH

(d) Stage 1.2 $t\bar{t}H$

Figure 5.3 – ggF, VBF, VH and $t\bar{t}H$ STXS for the Stage 1.2 splitting [138].

fact that different analyses can have substantially different sensitivities to different m_{jj} regions. The "Rest" bin has been sub-divided in its different components, for an easier treatment for both theoretical uncertainties and experimental modelling.

The ggF truth bins align their definitions to the VBF ones in the $N_{\text{jets}} \geq 2$ regions, while also the BSM sensitive part has been re-designed, with a more differential treatment in p_{T}^{H} for the $p_{\text{T}}^{\text{H}} > 200\,\text{GeV}$ region and being inclusive in the number of jets. The 0-jet region contains now a low p_{T}^{H} split since this contains sizeable fraction of the ggF cross section.

The VH phase space almost matches the one in Stage 1.0, but now additional high p_{T}^{V} splits are included plus an explicit division in number of jets. The ggZH now features the same bins as ZH and WH process.

The $\text{t}\bar{\text{t}}\text{H}$ phase space is for the first time split in p_{T}^{H} bins which allow to constrain possible BSM effects and gain sensitivity to Higgs self-coupling, while $\text{b}\bar{\text{b}}\text{H}$ and tH still remain one single bin each.

Throughout the full Stage 1.2 scheme, additional sub-bins marked with dashed lines are defined. These have been designed primarily to account for theory uncertainties source for analyses that have non-negligible experimental acceptance variations within one bin. The sub-bins can also be viewed as further bin boundaries in case one analysis has sensitivity to them.

In order to visualize each production mode sub-division in the Stage 1.2 scheme, the truth bin acceptances are reported in Table 5.1 and shown in Figure 5.4. The fiducial cuts on $|y_{\text{H}}|$ reduces remove between 1 and 9% of the Higgs events depending on the production process, while in some cases the truth bins cross sections can span three order of magnitudes (like in ggF case).

5.2 Objects selection

Different Higgs production modes, or STXS truth bins, can be tagged by final state particles which are produced alongside the Higgs boson decay products. Therefore on top of the event selection described in Section 4.3 which is uniquely based on photons, additional requirements are imposed on the objects which have been reconstructed in the selected events.

5.2.1 Electrons

Electron candidates are required to:

- have $p_{\text{T}} > 10\,\text{GeV}$ and $|\eta| < 2.47$ (excluding the "crack" region $1.37 < |\eta| < 1.52$);
- have a transverse impact parameter $\left|d_0/\sigma_{d_0}\right| < 5$, and a longitudinal impact parameter $|z_0 \sin\theta| < 0.5\,\text{mm}$;
- satisfy the Medium identification criteria and the Loose isolation criteria (see Section 3.6).

Truth bin acceptances [%]	Production process as modelled in MC								
	ggF	VBF	WH	ZH	ggZH	$t\bar{t}H$	$b\bar{b}H$	tHbj	tHW
gg2H_0J_ptH_0_10	13.7				0.0140				
gg2H_0J_ptH_gt10	42.5				0.357				
gg2H_1J_ptH_0_60	13.4				1.89				
gg2H_1J_ptH_60_120	9.29				4.63				
gg2H_1J_ptH_120_200	1.53				2.81				
gg2H_ge2J_mJJ_0_350_ptH_0_60	2.39				4.63				
gg2H_ge2J_mJJ_0_350_ptH_60_120	3.65				15.3				
gg2H_ge2J_mJJ_0_350_ptH_120_200	1.88				21.3				
gg2H_ge2J_mJJ_350_700_ptH_0_200	1.24				5.47				
gg2H_ge2J_mJJ_700_1000_ptH_0_200	0.293				0.997				
gg2H_ge2J_mJJ_gt1000_ptH_0_200	0.250				0.526				
gg2H_ptH_200_300	0.921				8.17				
gg2H_ptH_300_450	0.212				1.61				
gg2H_ptH_450_650	0.0310				0.159				
gg2H_ptH_gt650	0.00400				0.0120				
qq2Hqq_0J		7.36	4.08	3.33					
qq2Hqq_1J		34.2	21.3	20.7					
qq2Hqq_ge2J_mJJ_0_60		1.32	2.42	2.15					
qq2Hqq_ge2J_mJJ_60_120		2.30	19.5	23.1					
qq2Hqq_ge2J_mJJ_120_350		11.2	9.35	10.3					
qq2Hqq_ge2J_mJJ_350_700_ptH_0_200		13.4	1.65	1.84					
qq2Hqq_ge2J_mJJ_700_1000_ptH_0_200		6.90	0.249	0.267					
qq2Hqq_ge2J_mJJ_gt1000_ptH_0_200		12.3	0.137	0.144					
qq2Hqq_ge2J_mJJ_350_700_ptH_gt200		0.989	0.439	0.439					
qq2Hqq_ge2J_mJJ_700_1000_ptH_gt200		0.777	0.101	0.0990					
qq2Hqq_ge2J_mJJ_gt1000_ptH_gt200		2.14	0.0660	0.0610					
qq2Hlnu_ptV_0_75			15.1						
qq2Hlnu_ptV_75_150			9.61						
qq2Hlnu_ptV_150_250			3.01						
qq2Hlnu_ptV_gt250			0.971						
qq2Hll_ptV_0_75				13.7					
qq2Hll_ptV_75_150				9.10					
qq2Hll_ptV_150_250				2.89					
qq2Hll_ptV_gt250				0.884					
gg2Hll_ptV_0_75					5.28				
gg2Hll_ptV_75_150					13.8				
gg2Hll_ptV_150_250					8.24				
gg2Hll_ptV_gt250					1.62				
ttH_ptH_0_60						23.3			
ttH_ptH_60_120						35.1			
ttH_ptH_120_200						25.0			
ttH_ptH_200_300						10.4			
ttH_ptH_gt300						4.84			
bbH							94.6		
tH								90.9	99.1
gg2H_fwdH	8.78				2.22				
qq2Hqq_fwdH		7.03	8.15	7.74					
qq2Hlnu_fwdH			3.93						
qq2Hll_fwdH				3.28					
gg2Hll_fwdH					0.959				
ttH_fwdH						1.32			
bbH_fwdH							5.36		
tH_fwdH								9.14	0.894

Table 5.1 – Truth bin acceptances in percentage separated for each MC sample. Sum over columns is 100%, within rounding precision. "fwdH" bins are the acceptances for the events with $|y_H| > 2.5$.

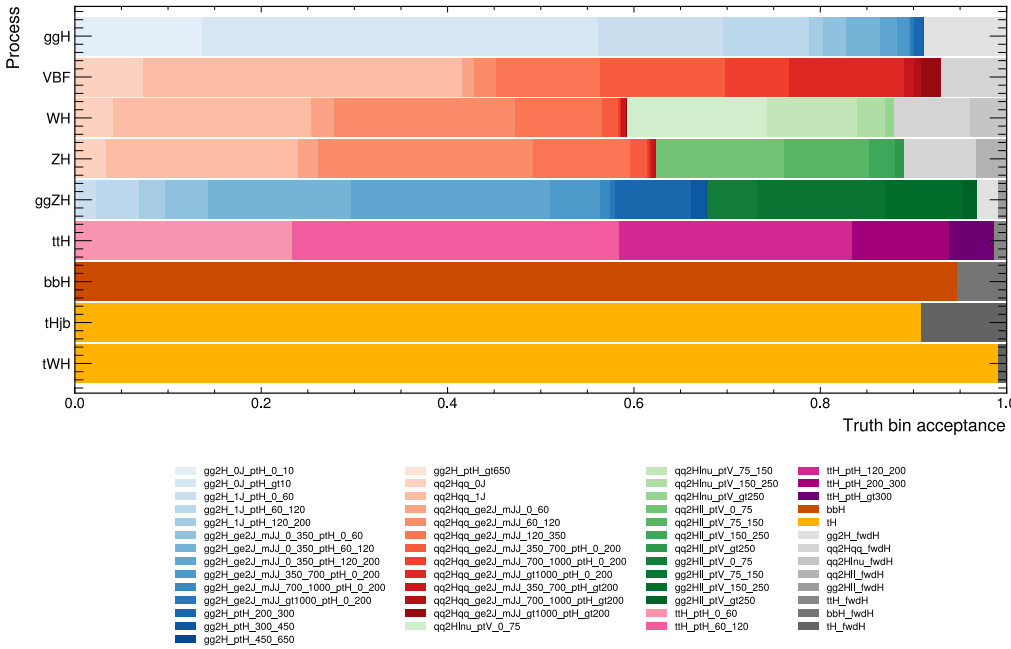

Figure 5.4 – Truth bin acceptances for each MC samples. The colour scheme follows the official STXS one reported in Figure 5.3, while grey truth bins are the forward ones, with $|y_{\mathrm{H}}| > 2.5$.

5.2.2 Muons

Muon candidates are required to:

- have $p_{\mathrm{T}} > 10\,\mathrm{GeV}$ and $|\eta| < 2.7$;
- have a transverse impact parameter $\left|d_0/\sigma_{d_0}\right| < 3$, and a longitudinal impact parameter $|z_0 \sin\theta| < 0.5\,\mathrm{mm}$;
- satisfy the Medium identification, while the isolation follows from the computation of the particle flow algorithm and the PflowLoose_FixedRad isolation criteria is employed (see Section 3.9).

5.2.3 Jets

Jets are reconstructed with the anti-k_t algorithm with distance parameter $R = 0.4$ and are required to have $|y| < 4.4$ and $p_{\mathrm{T}} > 25\,\mathrm{GeV}$. An overlap removal is also applied: reconstructed jets are rejected if they lie within a distance of $\Delta R < 0.4$ of a selected photon or electron.

To reduce the jets originating from pileup collisions, the JVT and fVT algorithms are used, described in Section 3.7.3: their aim is to distinguish between jets coming from a hard scattering vertex or pileup. Jets within $|\eta| < 2.4$ and in the region $20 < p_{\mathrm{T}}^{jet} < 60\,\mathrm{GeV}$ are required to have JVT score greater than 0.5. In the forward region, the fJVT tagger is required to be smaller than 0.4 (Tight working point) for jet with $2.5 < |\eta| < 4.5$ in the region $20 < p_{\mathrm{T}}^{jet} < 120\,\mathrm{GeV}$.

Moreover, jet are b-tagged with the DL1r algorithm and a pseudo-continuous working point on efficiency in the b-jets reconstruction is assigned to each jets used in this analysis with $|\eta|_j < 2.5$, see Section 3.8.

5.3 Top reconstruction

The reconstruction and selection of events from tH and $t\bar{t}H$ associated production is by far the most challenging due to the presence of up to six jets contaminated by pileup and QCD background processes, which poses a tricky combinatorial problem. Therefore, for this analysis a top reconstruction BDT has been developed [139] with the goal of separating random triplets of jets in $t\bar{t}H$ ($\gamma\gamma$) events from the jet triplets that correspond to the top decay products. The training events for the top reconstruction BDT come from the $t\bar{t}H$ Monte Carlo sample requiring 0 reconstructed leptons, ≥ 3 jets and ≥ 1 b-jet, where these latter count as standard jets too. Signal sample consists of jet triplets truth-matched to a top quark while the set of all not truth-matched triplets in this sample is taken as background. The input variables include four vector information of the reconstructed W and b candidates, ΔR between W and b and between the jets comprising the W candidate, the b-tagging scores of all the jets and the tri-jet mass. The BDT is then trained on fully hadronic events but then applied to semi-leptonic events too: it returns the score for the identified primary and secondary top candidates reconstructed from jet triplets. In events with four or five jets, the second top is taken as the sum of the jets left over

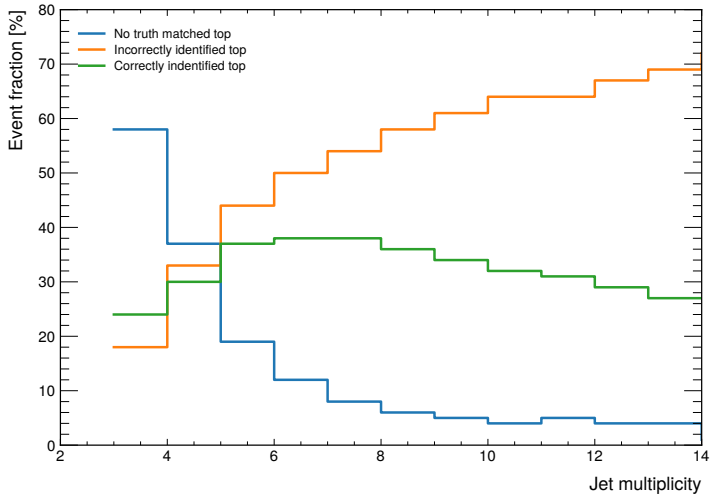

Figure 5.5 – Fraction of hadronic $t\bar{t}H$ ($\gamma\gamma$) MC events containing no correct top candidate, wrongly identified top candidate, and correctly identified top candidate in bins of jet multiplicity. Data taken from [139].

after reconstructing the primary top. In events with exactly three jets, no second top is reconstructed. For semi-leptonic decay, first the W vector boson is reconstructed with leptons and $E_{\mathrm{T}}^{\mathrm{miss}}$ information, and then the BDT is applied to all the (W, jet) combinations, while in di-lepton events, no top is reconstructed since the missing energy cannot be divided easily between the two leptonic W candidates.

The performance of the BDT is quantified by counting the number of events in which the algorithm identifies a top candidate (jet triplet) that is matched to a top quark at truth level. In the hadronic channel, the BDT correctly identifies the top candidate in $t\bar{t}H$ events 37% of the times, with a strong dependency on jet multiplicity as reported in Figure 5.5. At low jet multiplicity, the truth matching efficiency is low since one or more jets may have been removed by jet selection and performance requirements, therefore the fraction of events that contains no truth matched tops (irreducible background) is higher; on the other had at high multiplicity, the possibility to select the wrong jet triplets dominates the signal since the number of jets triplets increases. The BDT performs best in events with five to seven jets. In case of single leptons events, instead, the BDT identifies correctly a top candidate in 76% and 47% of the events for $t\bar{t}H$ and tHW processes respectively.

5.4 Event Categorization

The events passing the diphoton selection described in Section 4.3.3 are further divided in orthogonal categories, in order to measure the cross section of the truth bins of the STXS formalism or the whole Higgs boson production processes. With respect to the previously published analysis in the $H \to \gamma\gamma$ channel with partial Run 2 statistic [8, 129], an improved categorisation approach is employed.

In all the previous coupling analyses, the categorization optimization was performed sequentially starting from categories targeting the production modes with the smallest expected cross sections towards the ones with the largest expected cross section. A stricly ordered number of categories are therefore defined: first, events are selected in categories optimized to measure the tH cross section and the remaining events are left for $t\bar{t}H$ production. After classification in $t\bar{t}H$ categories, events can be classified in VH categories, and so on passing through VBF and, finally, to ggF categories. Thus an event falls in a category if and only if has failed the requirements for all the previous ones. Categories were defined optimizing each step sequentially in a standalone manner using the signal significance as metric for the optimization: this means that the optimal working point for a given production mode depends on the ones optimized before it.

The categorization presented in the following sections, instead, solves the above issue using a global optimization metric, in order to extract the maximal information on the the whole Higgs production phase space. It consists in two general parts: an initial "global" categorisation step, based on the *D-optimality* criterion, aiming to simultaneously divide the events in orthogonal regions targeting each STXS truth bin, followed by a series of dedicated categorizations within the created regions, aiming to further boost the analysis sensitivity by rejecting both the continuum background and the remaining contaminations from other STXS processes.

5.4.1 Categorization overview

The basic idea of the approach is to categorize the events which have passed the diphoton event selection. The categories have been optimized in order to give both the smallest errors and correlations on the final measurement, achieved by optimizing the determinant of the covariance matrix of the fitted POIs.

This approach is performed in many subsequent steps, each step optimized separately.

- The first step foresees a multiclass BDT model trained to separate the different STXS signals and, therefore, to create a number of categories equal to the different STXS bins used in the training. In this training, the STXS bins are treated with equal probability, i.e the model is trained on a dataset that presents a flat prior over the bins.

- To target the final measurement, which needs to take into account different cross sections, a *D-optimality procedure* has been developed: the outputs of the multiclass BDT have been multiplied by weights, optimized in order to give the best (stat-only) measurement precision of the STXS, and each event is assigned to the class with the maximum score. Therefore D-optimal reconstructed categories have been built, one for each STXS bins used during training.

- For each of these categories, a second binary BDT is applied to separate the signal targeted by that category from the continuum background and the resonant one coming from other truth bins.

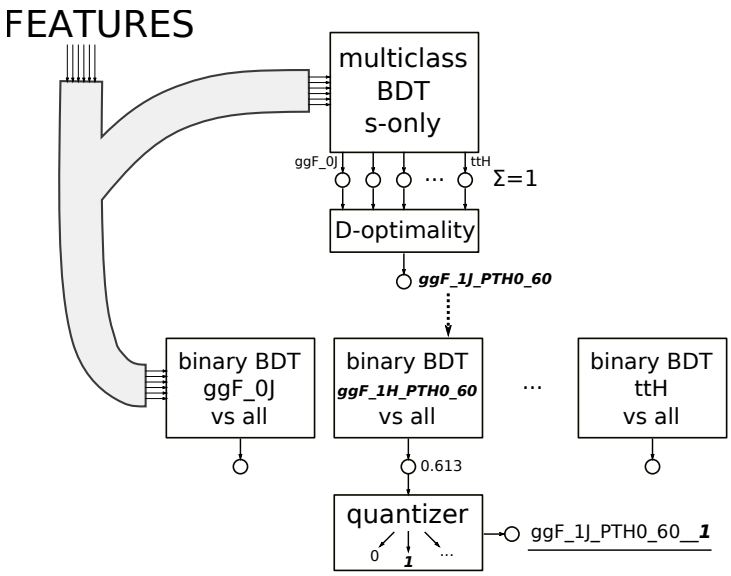

Figure 5.6 – Overview of the categorization approach where all the four steps have been sketched. The STXS names reported in the graph are related to the STXS 1.0 scheme.

- A significance scan is run over the binary BDT output in order to boost the final categorization performance by building categories with different purities.

An overview of the approach is sketched in Figure 5.6. In the following sections, a complete description of the various steps is given. The comparison of the method described in the following sections with past categorizations employed for the $H \to \gamma\gamma$ coupling analysis is reported in Appendix A.2.

5.4.2 The multiclass BDT

A multiclass BDT model has been trained using the Microsoft LightGBM package [127] which provides faster training times while retains the same accuracy with respect to its main competitor XGBoost [140]. The multiclass BDT is trained using only the signal MC simulations described in Section 4.2.2 to discriminate between the STXS truth bin, with the labelling provided by the output of Higgs Template XS Rivet routine [138]. The final classes on which the multiclass BDT has been trained are reported in Table 5.2 and are slightly different from the ones in the full STXS 1.2 granularity, in particular:

- the $b\bar{b}H$ truth bin and events were not considered during the training since they are mostly classified as ggF;

- in the 2 jets phase space, for both ggF and VBF, splits in m_{jj} are preferred with respect to p_{T}^{Hjj} splits, since the analysis is more sensitive to m_{jj} and p_{T}^{Hjj} is modelled at only LO with the current MC samples; moreover, using m_{jj} as splits follows what

ggF + ggZH (hadronic)	VBF + VH hadronic
0. GG2H_0J_PTH_0_10	15. QQ2HQQ_0J
1. GG2H_0J_PTH_GT10	16. QQ2HQQ_1J
2. GG2H_1J_PTH_0_60	17. QQ2HQQ_GE2J_MJJ_0_60
3. GG2H_1J_PTH_60_120	18. QQ2HQQ_GE2J_MJJ_60_120
4. GG2H_1J_PTH_120_200	19. QQ2HQQ_GE2J_MJJ_120_350
5. GG2H_GE2J_MJJ_0_350_PTH_0_60	20. QQ2HQQ_GE2J_MJJ_350_700_PTH_0_200
6. GG2H_GE2J_MJJ_0_350_PTH_60_120	21. QQ2HQQ_GE2J_MJJ_700_1000_PTH_0_200
7. GG2H_GE2J_MJJ_0_350_PTH_120_200	22. QQ2HQQ_GE2J_MJJ_GT100_PTH_0_200
8. GG2H_GE2J_MJJ_350_700_PTH_0_200	23. QQ2HQQ_GE2J_MJJ_350_700_PTH_GT200
9. GG2H_GE2J_MJJ_700_1000_PTH_0_200	24. QQ2HQQ_GE2J_MJJ_700_1000_PTH_GT200
10. GG2H_GE2J_MJJ_GT1000_PTH_0_200	25. QQ2HQQ_GE2J_MJJ_GT100_PTH_GT200
11. GG2H_PTH_200_300	
12. GG2H_PTH_300_450	
13. GG2H_PTH_450_650	
14. GG2H_PTH_GT650	
VH leptonic	**Top**
26. QQ2HLNU_PTV_0_75	38. TTH_PTH_0_60
27. QQ2HLNU_PTV_75_150	39. TTH_PTH_60_120
28. QQ2HLNU_PTV_150_250	40. TTH_PTH_120_200
29. QQ2HLNU_PTV_GT250	41. TTH_PTH_200_300
30. HLL_PTV_0_75	42. TTH_PTH_GT300
31. HLL_PTV_75_150	43. THJB
32. HLL_PTV_150_250	44. TWH
33. HLL_PTV_GT250	
34. QQHNUNU_PTV_0_75	
35. QQHNUNU_PTV_75_150	
36. QQHNUNU_PTV_150_250	
37. QQHNUNU_PTV_GT250	

Table 5.2 – The truth classes used to train the multiclass BDT with their relative indices.

is done in other decay channels, like $H \to WW$ and $H \to \tau\tau$, therefore boosting the combined performance;

- qq2Hll and gg2Hll truth bins have been merged together correspondingly, since the multiclass was unable to discriminate between gg- and qq-initiated ZH processes; moreover the $150 < p_{\mathrm{T}}^{V} < 250\,\mathrm{GeV}$ truth bin has been treated inclusively in the number of jets;

- truth bins targeting ZH leptonic decays are split at truth level in their $\nu\nu$ and $\ell\ell$ counterparts, even if this split is not part of the STXS scheme;

- to improve the classification power of the tH truth bin, two different classes were used during training, one targeting tHW and one targeting tHbj, since they have very different kinematic.

The multiclass BDT optimizes a multiclass cross entropy loss defined by the formula

$$L = -\sum_{i}^{N} \mathbf{y}_i \log \hat{\mathbf{y}}_i = -\sum_{i}^{N} \log \hat{y}_i^c \tag{5.1}$$

for N observations and m classes, with i running over the number of events and where

- $\mathbf{y}$ is a "one-hot encoded" vector with m components representing the truth label information ($\mathbf{y} = (0\,0 \cdots 1 \cdots 0)$, i.e. all zeros apart a 1 in the c-th position)

- $\hat{\mathbf{y}}$ is the BDT score passed through a softmax layer, therefore the n-th component of the $\hat{\mathbf{y}}$ is given by

$$\hat{y}_n = softmax(z_n) = \frac{e^{z_n}}{\sum_j e^{z_j}} \in [0,1]$$

  where z_n is the BDT score for the n-th class and the sums at the denominator runs over the vector components.

The $\log \hat{y}_i^c$ term in Eq. (5.1) represents the error of classifying an event when the truth is the c-th category, therefore the cross entropy is the sum of errors the algorithm commits at each training iteration.

The multiclass BDT makes use of the following variables to discriminate the various truth bin signals:

- **photons**: $p_{\mathrm{T}}^{\gamma\gamma}$, $\left|y_{\gamma\gamma}\right|$, $\eta_{\gamma 1}$, $\eta_{\gamma 2}$
- **di-jets system**: $\underline{m_{jj}}$, p_{T}^{jj}, Δy^{jj}, $\Delta\phi^{jj}$, $\Delta\eta^{j-j}$
- **jets + photons system**: $m_{j\gamma\gamma}$, $p_{\mathrm{T}}^{j\gamma\gamma}$, $m_{jj\gamma\gamma}$, $\underline{p_{\mathrm{T}}^{jj\gamma\gamma}}$, $\Delta\phi^{jj-\gamma\gamma}$, $\Delta y^{jj-\gamma\gamma}$, ΔR_{min}^{y-j}, $m_{\sum j}$
- **leptons and MET**: m_{ee}, $m_{\mu\mu}$, $E_{\mathrm{T}}^{\mathrm{miss}}$, $E_{\mathrm{T}}^{\mathrm{miss}} - E_{\mathrm{T}}^{\mathrm{miss}}{}_{hard} > 30\,\mathrm{GeV}$ (where $E_{\mathrm{T}}^{\mathrm{miss}}{}_{hard}$ is the $E_{\mathrm{T}}^{\mathrm{miss}}$ constructed from the hardest vertex, see Section 4.3.2), $p_{\mathrm{T}}^{\ell\ell}$, $p_{\mathrm{T}}^{\ell E_{\mathrm{T}}^{\mathrm{miss}}}$, $m_{\mathrm{T}}^{\ell E_{\mathrm{T}}^{\mathrm{miss}}}$
- **top**: m, p_{T}, η, ϕ of the two reconstructed tops and their scores, described in Section 5.3, $\Delta R(W,b)_{t2}$ i.e. the ΔR between the W and b candidate for the second reconstructed top in the events
- **counters**: $\underline{N_{\mathrm{jets}}^{|\eta|<2.5}}$, $\underline{N_{\mathrm{jets}}}$, $\underline{N_{b\text{-jets}}}$, N_{lep}
- **others**: p_{T} of the leading jet, η of the most forward jet and the invariant mass of this forward jet+diphton system, $\sum E_{\mathrm{T}}$ (sum runs over all the objects used to build the $E_{\mathrm{T}}^{\mathrm{miss}}$ and contains the soft term), $\frac{E_{\mathrm{T}}^{\mathrm{miss}}}{\sqrt{\sum E_{\mathrm{T}}}}$, H_{T} ($= \sum p_{\mathrm{T}}^{jets}$ for jets with $p_{\mathrm{T}} > 30\,\mathrm{GeV}$), pileup variable μ

Variables underlined are calculated and included twice, one version made with pre-selected jets ($p_{\mathrm{T}} > 25\,\mathrm{GeV}$) and another with harder jets ($p_{\mathrm{T}} > 30\,\mathrm{GeV}$, as in the truth definition of STXS, see Section 5.1). Other jet-related variables uses pre-selected jets. The variable assumes Not-a-Number (NaN) value if it cannot be built from the reconstructed objects in the events. Two variables are further modified: $m_{\sum j}$ is defined only if at least three jets are available, while $N_{b\text{-jets}} = \min(N_{b\text{-jets}}, 3)$. Moreover, when the multiclass BDT is applied to data samples the pileup variable μ is defined as

$$\mu = \begin{cases} < \mu > & \text{for data2015/16} \\ \mu_{actual} & \text{for data2017/18} \end{cases}$$

This last change is due to the fact that MC pileup reweighting is performed on $< \mu >$ and μ_{actual} for samples representing 2015/16 and 2017/18 data respectively, so this choice

improves the data/MC agreement for the pileup variable in the inference. Since $< \mu >$ and μ_{actual} have the same value in MC, there is no impact in the training.

For the training, events from the different multi-class signal classes have been weighted to have equal yield for each STXS bin, therefore providing the algorithm with an input dataset with a flat prior over STXS truth bin cross sections. This choice was performed since the MC dataset used for the training is highly imbalanced, mainly due to the large statistic available for the $t\bar{t}H$ processes. Moreover, it has been observed that a training with classes weighted according to their SM predicted cross sections provides worst classification performance with respect to a flat weighted input dataset, in particular for the processes with the lowest cross sections.

The output of the multiclass BDT for each event consists in a vector of scores with the size equal to the number of classes over which the model has been trained: each of these scores can be interpreted as the probability of the event to be correctly classified in a given signal class, since the scores sum up to 1 for each event. In ML application, it is a common practice to classify an event in the category for which it gets the maximum score: this solution was tested and it has been found that this choice is not optimal for this analysis, since it favours a maximization of the signal efficiencies therefore creating category with poor truth bin purity.

5.4.3 D-optimality criteria

In order to provide the optimal background rejection taking into account the different predicted cross sections for each class and to make use of all the information provided by the output event scores, a completely novel approach has been developed and deployed. First of all, a single metric to be optimized during this step has been defined: the two prerequisites were that it must be a single scalar value and that it must take into account both errors and correlation of the final cross sections measurement. Since these two elements are encoded in the covariance matrix, the metric should be based on that. A natural choice is to take the determinant of this matrix as the metric to be optimized. This intuition can be proved mathematically [141]: the gain in information provided by an experiment in fact is given by

$$\frac{1}{2}\log\frac{\left|\Sigma_{exp}+\Sigma_{theo}\right|}{\left|\Sigma_{exp}\right|}$$

where $|\cdot|$ is the determinant operator, Σ are the expected covariance matrices. Σ_{theo} can be regarded as the covariance matrix of the theoretical SM uncertainties, which is unknown. A given categorization #1 is better than another #2 if it provides more information:

$$\left|\Sigma_{theo}+\Sigma_{exp,1}\right|\cdot\left|\Sigma_{exp,2}\right| > \left|\Sigma_{theo}+\Sigma_{exp,2}\right|\cdot\left|\Sigma_{exp,1}\right|$$

which can be turned into

$$\left|1+\Sigma_{theo}^{-1}\Sigma_{exp,1}\right|\cdot\left|\Sigma_{exp,2}\right| > \left|1+\Sigma_{theo}^{-1}\Sigma_{exp,2}\right|\cdot\left|\Sigma_{exp,1}\right|.$$

If the elements of $\Sigma_{theo}^{-1}\Sigma_{exp,i}$ are small with respect to the unit matrix (and this is true since we are dominated by statistical uncertainties), this is approximatively:

$$\left|\Sigma_{exp,2}\right| > \left|\Sigma_{exp,1}\right|$$

which means we have to find the design that gives the smallest determinant of the covariance matrix, which, geometrically, is proportional to the volume of the ellipsoid in the space of the expected errors. This is called D-optimality.

To evaluate this metric, a complete measurement has to be performed: signal and background ($\gamma\gamma$, $V\gamma\gamma$, $t\bar{t}\gamma\gamma$) MC simulations events have been classified by the multiclass BDT and output scores are computed. A first categorization is built assigning each event to the category where it gets the maximum score over the classes. In each of these categories, a Double Sided Crystal Ball is fitted over the invariant mass distribution of the signal events and the bounds of the smallest $m_{\gamma\gamma}$ region containing 90% of the signal are computed from the fitted pdf. The signal efficiencies and yields for each truth bin are computed in this region ($\epsilon_{S_{90}}$ and S_{90}). The background yield in each category is computed by first mixing the three background MC processes mentioned above using their SM cross sections stored in the MC samples; then, this mixed background sample is normalized to the data TI yield in the $m_{\gamma\gamma}$ region $[90, 105]$ GeV for each reconstructed category produced by the multiclass BDT. Finally the background yield (B_{90}) is computed integrating this background histogram in the 90% signal region.

Given the signal efficiencies for each STXS bin and the background yields in each category in its 90% signal region, a simple counting likelihood can be built with the yields of the various categories modelled as

$$N^c = B^c_{S_{90}} + \sum_t \mu_t \cdot L \cdot \sigma_t^{\gamma\gamma} \cdot \epsilon^{ct}_{S_{90}},$$

where $\epsilon^{ct}_{S_{90}}$ is the efficiency for the t-th truth bin in the 90% signal region of the c-th category. The likelihood can measure the signals strengths μ_t related to the STXS $\sigma_t^{\gamma\gamma}$. With respect to the truth bin used to train the multiclass BDT reported in Table 5.2, the measured POI here are 41, since the two ZH leptonic decays ($Z \to \nu\nu$ and $Z \to \ell\ell$ with $\ell = e, \mu, \tau$) are measured together. From this likelihood, which does not contain any shape information, an Asimov dataset is generated, fixing the signal strengths for each process to the predicted SM value. Fitting the Asimov produces a covariance matrix from which we extract the value of our metric computing the determinant.

To minimize the determinant, each multiclass class output is multiplied by a weight, initially set to one

$$S \circ \vec{w} = (s_{ij} \cdot w_j) = \begin{bmatrix} s_{11} \cdot w_1 & \cdots & s_{1M} \cdot w_M \\ \vdots & \ddots & \vdots \\ s_{N1} \cdot w_1 & \cdots & s_{NM} \cdot w_M \end{bmatrix}$$

where S is the $N \times M$ scores matrix for N events and $M = 45$ training classes, and $\vec{w}$ is

Class	Weight	Class	Weight
GG2H_0J_PTH_0_10	5.10	QQ2HQQ_GE2J_MJJ_350_700_PTH_GT200	1.17
GG2H_0J_PTH_GT10	8.74	QQ2HQQ_GE2J_MJJ_700_1000_PTH_GT200	2.04
GG2H_1J_PTH_0_60	11.1	QQ2HQQ_GE2J_MJJ_GT1000_PTH_GT200	0.254
GG2H_1J_PTH_60_120	10.9	QQ2HLNU_PTV_0_75	0.696
GG2H_1J_PTH_120_200	1.10	QQ2HLNU_PTV_75_150	0.483
GG2H_GE2J_MJJ_0_350_PTH_0_60	37.0	QQ2HLNU_PTV_150_250	0.306
GG2H_GE2J_MJJ_0_350_PTH_60_120	14.6	QQ2HLNU_PTV_GT250	0.514
GG2H_GE2J_MJJ_0_350_PTH_120_200	1.92	QQ2HLL_PTV_0_75	2.91
GG2H_GE2J_MJJ_350_700_PTH_0_200	2.47	QQ2HLL_PTV_75_150	0.182
GG2H_GE2J_MJJ_700_1000_PTH_0_200	2.26	QQ2HLL_PTV_150_250	1.09
GG2H_GE2J_MJJ_GT1000_PTH_0_200	0.655	QQ2HLL_PTV_GT250	0.467
GG2H_PTH_200_300	2.23	QQ2HNUNU_PTV_0_75	5.48
GG2H_PTH_300_450	1.08	QQ2HNUNU_PTV_75_150	2.85
GG2H_PTH_450_650	1.76	QQ2HNUNU_PTV_150_250	0.777
GG2H_PTH_GT650	0.238	QQ2HNUNU_PTV_GT250	0.403
QQ2HQQ_0J	9.68	TTH_PTH_0_60	0.403
QQ2HQQ_1J	4.76	TTH_PTH_60_120	0.181
QQ2HQQ_GE2J_MJJ_0_60	2.30	TTH_PTH_120_200	0.174
QQ2HQQ_GE2J_MJJ_60_120	2.80	TTH_PTH_200_300	0.112
QQ2HQQ_GE2J_MJJ_120_350	9.92	TTH_PTH_GT300	0.205
QQ2HQQ_GE2J_MJJ_350_700_PTH_0_200	1.11	THJB	0.241
QQ2HQQ_GE2J_MJJ_700_1000_PTH_0_200	0.633	THW	0.630
QQ2HQQ_GE2J_MJJ_GT1000_PTH_0_200	0.280		

Table 5.3 – D-optimality weights assigned to each score of a given class.

the weight vector of dimension M, i.e. $s_{ij} \cdot w_j$ represents the weighted output score for the i-th event in the $j-$th class.

Then this weight vector $\vec{w}$ is optimized in order to minimize the value of the chosen metric with the Powell algorithm [142, 143]: it performs sequential one-dimensional minimizations along each vector of the directions set (in our case of 45 dimensions), which is updated at each iteration of the main minimization loop. This method has been chosen since the function does not need to be differentiable and no derivatives are taken. At each iteration step, the counting experiment described above is repeated in all its steps (categorization, signal/background modelling, Asimov generation and fit), categorizing an event in the class that provides the maximum weighted output score over all of them. The final weight vector is reported in Table 5.3. The whole procedure takes around 5000 iterations to converge and takes around 16 hours of CPU time.

D-optimal Multiclass BDT results

BDT outputs The D-optimal scores (after the optimized weight multiplication) outputs are reported in Figure 5.7. As can been observed, the truth bin targeted by each class is usually well separated from the other signals it was trained against. The output classes range from 0 to the D-optimal weight assigned to a given class, reported in Table 5.3. In each plot, all the events are plotted since the multiclass BDT provides to each event to be assigned for output classes, equal to the number of classes in the training. Even if the background is not used in the BDT training, it is interesting to see that the distribution of the background MC used to optimized the D-optimality weights and in the following steps mostly agrees with the data TI in the sidebands and it is also separated from the

main truth bin the class is targeting. NTI data in the sidebands are reported as well since this provide an enriched dataset for γj and jj background components: these may composed large part of the continuum background in some regions of the phase space (usually when low p_{T} photons are selected), therefore it may help in the understanding differences between the MC and data TI histograms.

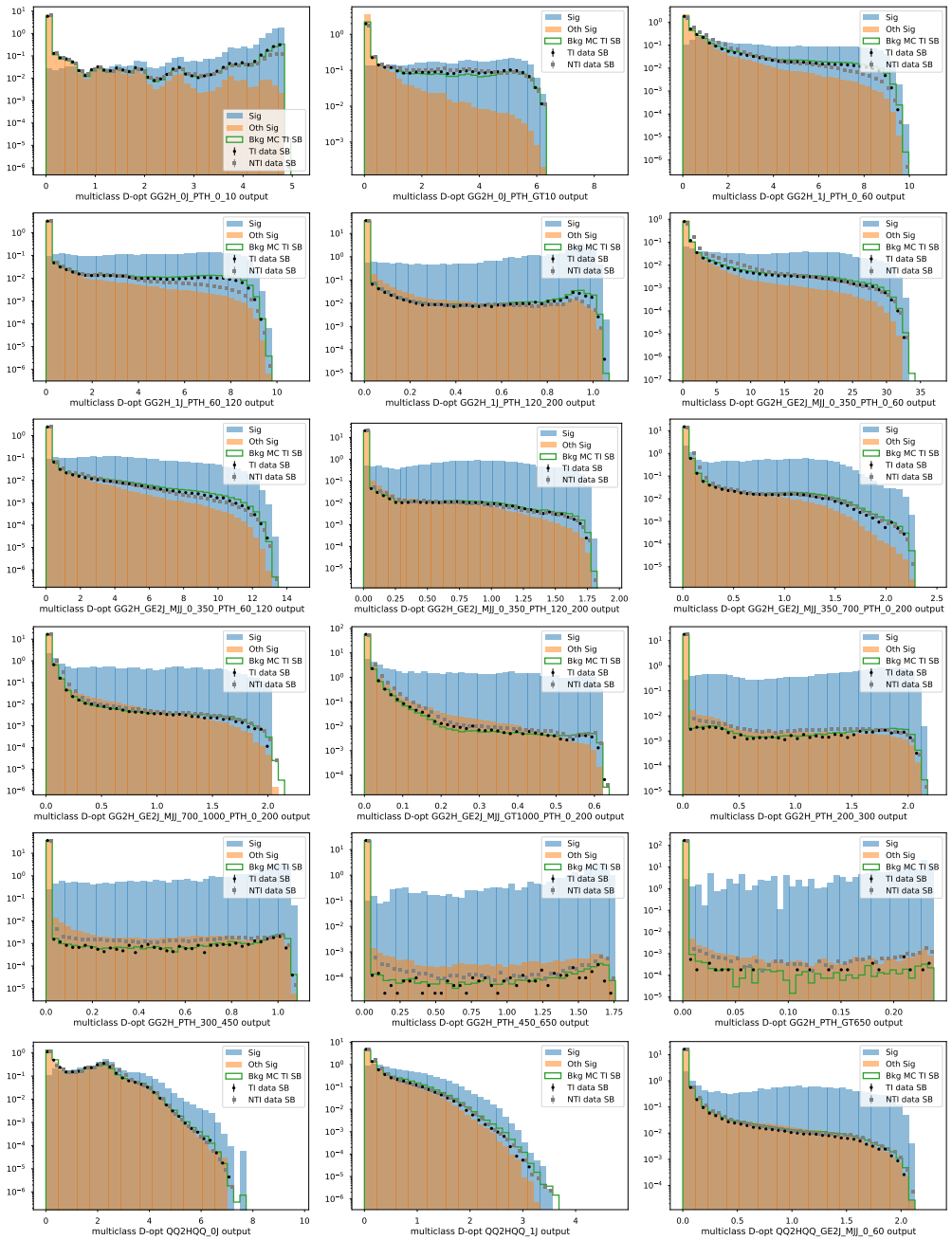

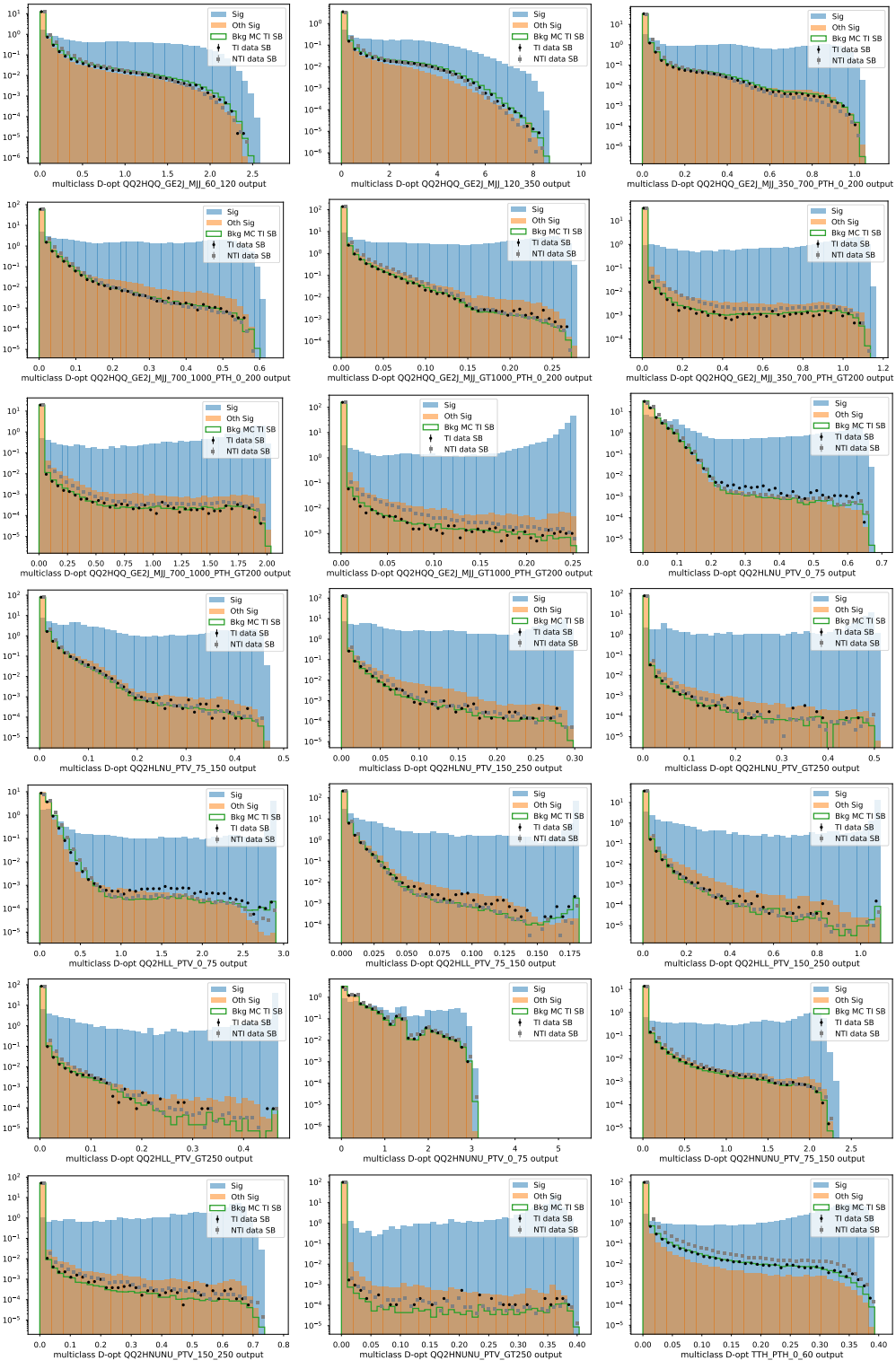
Sig
Oth Sig
Bkg MC TI SB
TI data SB
NTI data SB
multiclass D-opt QQ2HQQ_GE2J_MJJ_60_120 output
multiclass D-opt QQ2HQQ_GE2J_MJJ_120_350 output
multiclass D-opt QQ2HQQ_GE2J_MJJ_350_700_PTH_0_200 output
multiclass D-opt QQ2HQQ_GE2J_MJJ_700_1000_PTH_0_200 output
multiclass D-opt QQ2HQQ_GE2J_MJJ_GT1000_PTH_0_200 output
multiclass D-opt QQ2HQQ_GE2J_MJJ_350_700_PTH_GT200 output
multiclass D-opt QQ2HQQ_GE2J_MJJ_700_1000_PTH_GT200 output
multiclass D-opt QQ2HQQ_GE2J_MJJ_GT1000_PTH_GT200 output
multiclass D-opt QQ2HLNU_PTV_0_75 output
multiclass D-opt QQ2HLNU_PTV_75_150 output
multiclass D-opt QQ2HLNU_PTV_150_250 output
multiclass D-opt QQ2HLNU_PTV_GT250 output
multiclass D-opt QQ2HLL_PTV_0_75 output
multiclass D-opt QQ2HLL_PTV_75_150 output
multiclass D-opt QQ2HLL_PTV_150_250 output
multiclass D-opt QQ2HLL_PTV_GT250 output
multiclass D-opt QQ2HNUNU_PTV_0_75 output
multiclass D-opt QQ2HNUNU_PTV_75_150 output
multiclass D-opt QQ2HNUNU_PTV_150_250 output
multiclass D-opt QQ2HNUNU_PTV_GT250 output
multiclass D-opt TTH_PTH_0_60 output

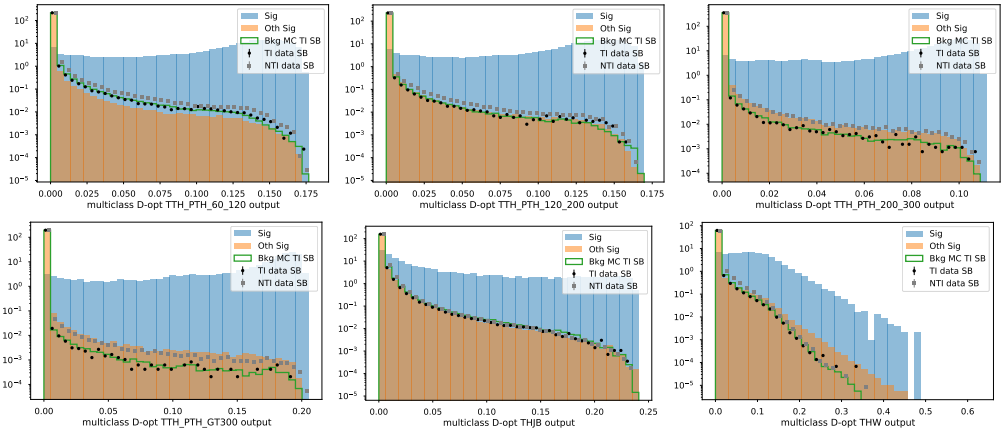

Figure 5.7 – The D-optimal weighted BDT output for each of the category: blue filled histogram represents the targeted signal of a given output class, while the orange filled represents the sum of all the other signals weighted according their SM yields. The green line shows the background-only MC TI distribution over the classes and can be compared to TI data (black dots) and NTI data (grey dots). All the histograms are normalized to the same area.

D-optimal multiclass selection The D-optimal multiclass BDT is able to select each truth signal with high purity with respect to the others signals. The Figure 5.8 and 5.9 show the reco-level distributions of the variables needed to define the STXS scheme in the ggF phase space. Reconstructed variables usually match the truth-level STXS bin definitions, but other interesting features can be observed. For example, as can be observed in Figure 5.8a, in the ggF 0-jets categories, the BDT is able to understand correctly that some truth 0 jets events with 1 reconstructed jet due to pileup belong to this category. Similarly, in the 1 jet categories (see for example Figure 5.8c) some events with 0 reconstructed jet are correctly included. Many other similar plots for all the D-optimal multiclass categories can be found in the Appendix A.1.

D-optimality results The D-optimal multiclass BDT is more accurate in measuring the STXS cross section with respect to the simple multiclass BDT. After the optimization, the determinant of the covariance matrix of the results, measuring 41 POIs with the same counting experiment used during the optimization, is lowered down from $3.2 \cdot 10^{19}$ to $1.1 \cdot 10^{8}$. The statistical errors on the fitted POI is reported in Table 5.4 while the covariance matrices before and after the D-optimality are shown in Figure 5.10.

5.4.4 Binary BDTs

To further boost the performance of the $H \to \gamma\gamma$ categorization for all the truth bins, a background rejection step has been developed. This step is slightly different between ggF/VBF/VH STXS truth bins with respect to the top-quark related ones. In particular,

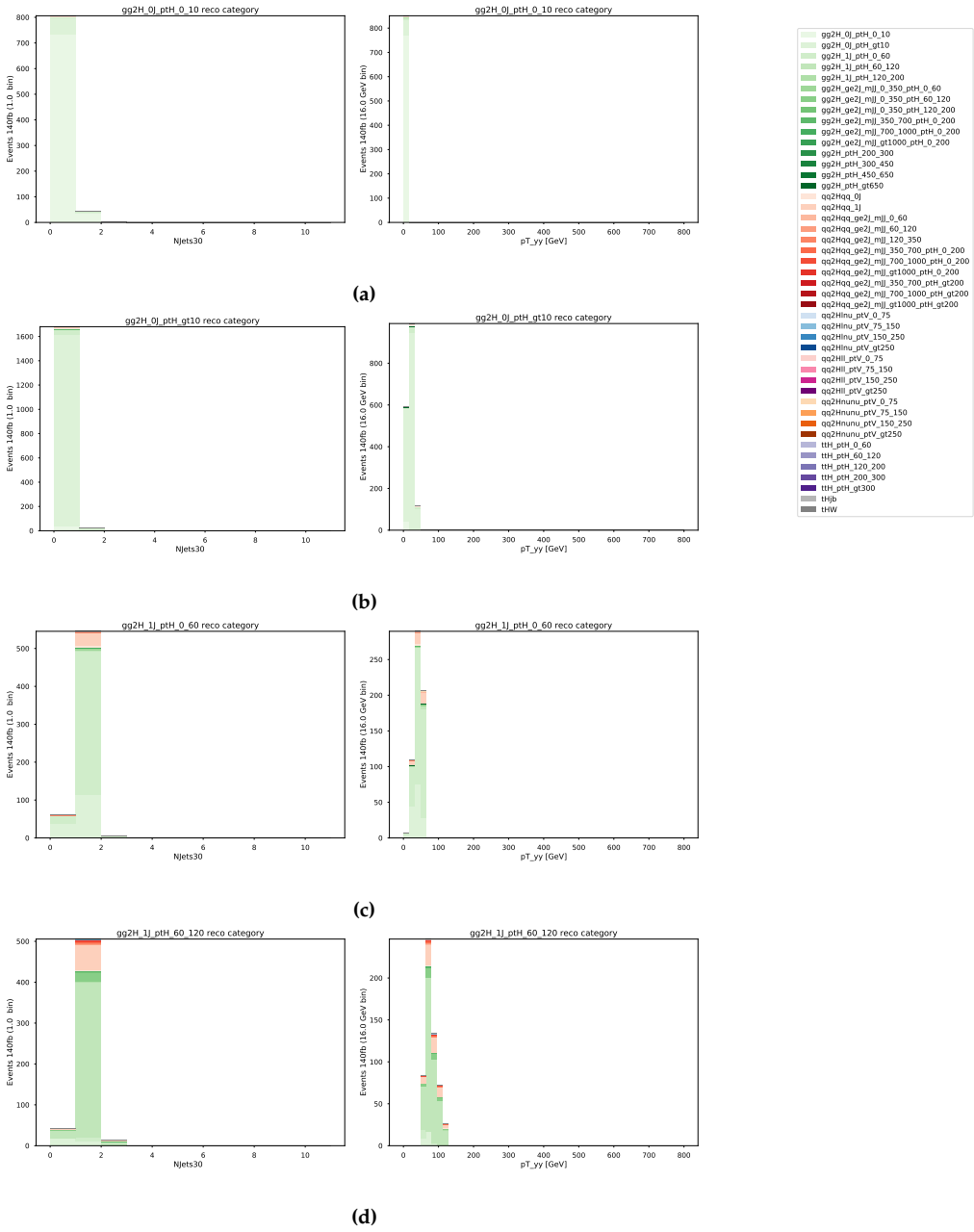

Figure 5.8 – Each row of reports the distributions of events classified in particular categories selected by the D-optimal multiclass BDT for the two variables defining the truth bin at reconstruction level. All the signals are drawn stacked with different colours, therefore showing the purity of the multiclass categories, and the total yield is normalized to 140 fb^{-1}.

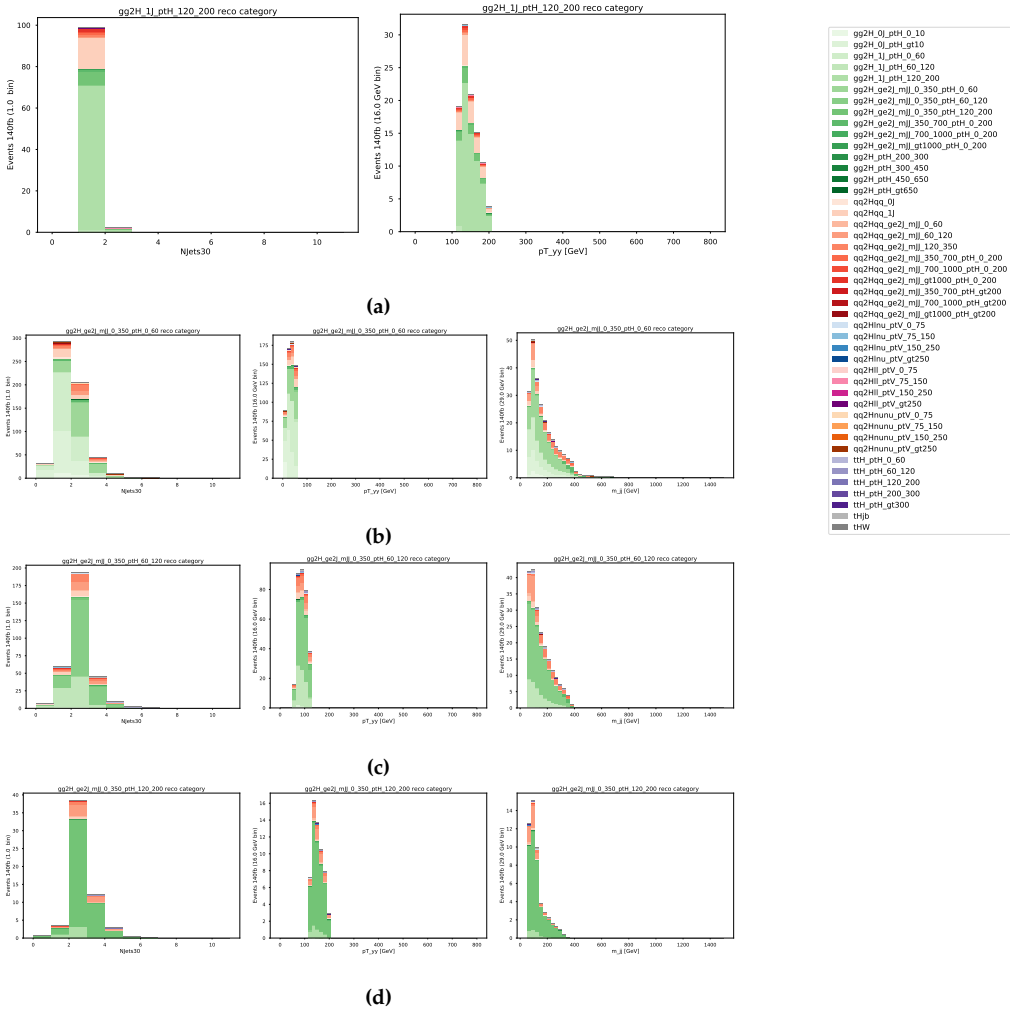

(a)

(b)

(c)

(d)

Figure 5.9 – Each row of reports the distributions of events classified in particular categories selected by the D-optimal multiclass BDT for the two variables defining the truth bin at reconstruction level. All the signals are drawn stacked with different colours, therefore showing the purity of the multiclass categories, and the total yield is normalized to 140 fb^{-1}.

Stat-only error for POI [%]	Multiclass	D-optimal Multiclass
$\mu_{gg2H\_0J\_ptH\_0\_10}$	24.1	24.1
$\mu_{gg2H\_0J\_ptH\_gt10}$	25.1	24.8
$\mu_{gg2H\_1J\_ptH\_0\_60}$	60.1	44.8
$\mu_{gg2H\_1J\_ptH\_60\_120}$	73.2	43.9
$\mu_{gg2H\_1J\_ptH\_120\_200}$	121	66.9
$\mu_{gg2H\_ge2J\_mJJ\_0\_350\_ptH\_0\_60}$	155	160
$\mu_{gg2H\_ge2J\_mJJ\_0\_350\_ptH\_60\_120}$	101	81.5
$\mu_{gg2H\_ge2J\_mJJ\_0\_350\_ptH\_120\_200}$	79.8	72.8
$\mu_{gg2H\_ge2J\_mJJ\_350\_700\_ptH\_0\_200}$	185	160
$\mu_{gg2H\_ge2J\_mJJ\_700\_1000\_ptH\_0\_200}$	412	299
$\mu_{gg2H\_ge2J\_mJJ\_gt1000\_ptH\_0\_200}$	451	268
$\mu_{gg2H\_ptH\_200\_300}$	61.4	48.8
$\mu_{gg2H\_ptH\_300\_450}$	86.5	74.5
$\mu_{gg2H\_ptH\_450\_650}$	181	162
$\mu_{gg2H\_ptH\_gt650}$	444	537
μ_{qq2Hqq_0J}	1440	1440
μ_{qq2Hqq_1J}	461	198
$\mu_{qq2Hqq\_ge2J\_mJJ\_0\_60}$	785	635
$\mu_{qq2Hqq\_ge2J\_mJJ\_60\_120}$	235	122
$\mu_{qq2Hqq\_ge2J\_mJJ\_120\_350}$	393	290
$\mu_{qq2Hqq\_ge2J\_mJJ\_350\_700\_ptH\_0\_200}$	153	93.4
$\mu_{qq2Hqq\_ge2J\_mJJ\_700\_1000\_ptH\_0\_200}$	152	83.0
$\mu_{qq2Hqq\_ge2J\_mJJ\_gt1000\_ptH\_0\_200}$	115	37.0
$\mu_{qq2Hqq\_ge2J\_mJJ\_350\_700\_ptH\_gt200}$	239	234
$\mu_{qq2Hqq\_ge2J\_mJJ\_700\_1000\_ptH\_gt200}$	175	186
$\mu_{qq2Hqq\_ge2J\_mJJ\_gt1000\_ptH\_gt200}$	70.5	47.4
$\mu_{qq2Hll\_ptV\_0\_75}$	722	670
$\mu_{qq2Hll\_ptV\_75\_150}$	437	175
$\mu_{qq2Hll\_ptV\_150\_250}$	255	207
$\mu_{qq2Hll\_ptV\_gt250}$	290	261
$\mu_{qq2Hlnu\_ptV\_0\_75}$	392	129
$\mu_{qq2Hlnu\_ptV\_75\_150}$	318	95.3
$\mu_{qq2Hlnu\_ptV\_150\_250}$	223	138
$\mu_{qq2Hlnu\_ptV\_gt250}$	218	175
$\mu_{ttH\_ptH\_0\_60}$	323	109
$\mu_{ttH\_ptH\_60\_120}$	278	77.9
$\mu_{ttH\_ptH\_120\_200}$	282	76.3
$\mu_{ttH\_ptH\_200\_300}$	359	84.8
$\mu_{ttH\_ptH\_gt300}$	379	106
μ_{tHjb}	746	358
μ_{tHW}	1450	1000

Table 5.4 – The expected stat-only POI errors when measuring a very weakly merged set of truth bin of the STXS 1.2 framework. Results are obtained on a counting Asimov dataset with all the signal strengths fixed to their SM expectations. The two columns report the expected error obtained with the categorization built assigning an event to the class with the maximum score with the simple multiclass output and after the D-optimality step.

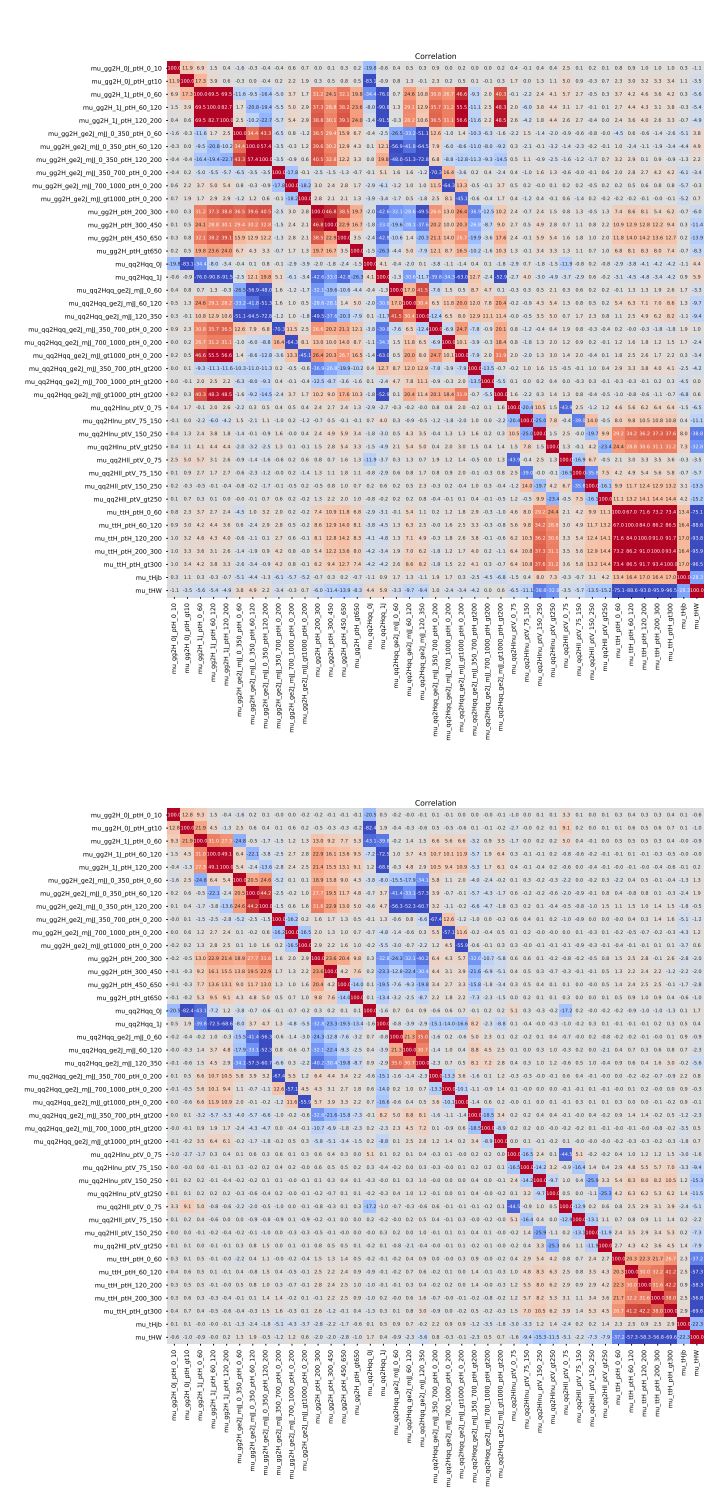

Figure 5.10 – Covariance matrices of the fit results reported in Table 5.4 (upper) before and (lower) after the D-optimality.

for $t\bar{t}H$ a very similar procedure to the one employed for the $t\bar{t}H$ observation with partial Run 2 data [9, 10] is used, since has been proven to lead to better performance. For tHbj production instead, a new categorization has been developed in order to be sensitive to both positive and negative κ_t values. All these further categorizations are always applied on top of the first multiclass BDT selection.

ggF, VBF, VH processes

For each of the ggF, VBF and VH categories, i.e. the first 38 categories built by the D-optimal multiclass BDT, one binary BDT (one for each STXS bin) has been trained to separate the signal from the background of that particular category, using binary cross entropy. For the training of these binary BDTs, the signal is provided by the STXS bin targeted by the reference multiclass reconstructed category, while the background is given by the sum of both continuum and resonant processes. The continuum is composed by the mixture of the background MC samples, while the resonant is composed by the remaining signal contributions from other STXS bins, both selected in a given reconstructed multiclass category. In both continuum and resonant processes, the subcomponents are merged according to their cross sections. Each of these three components (targeted STXS bin signal, continuum background, resonant backgrounds) have been weighted to have an equal yield during the training, with these normalizations computed separately for each of the reconstructed categories.

Binary BDTs use the same features of the multiclass BDT (page 123) plus some features related to the photons and photon-jets systems, needed to separate the signal from the continuum background.

- **diphoton system** $\Delta y_{\gamma\gamma}$, $p_{\mathrm{Tt}}^{\gamma\gamma}$, $\phi^*_{\gamma\gamma}$
- **counters**: N_{e}, N_{μ}
- **others**[12]: $Zepp$, $\cos\theta^*_{\gamma\gamma}$

In addition, before training and in order to avoid any mass sculpting of the $m_{\gamma\gamma}$ shape for the background, a feature is removed from the list of variables used in the training if it shows a linear correlation with $m_{\gamma\gamma}$ larger than 5% either for the signal or the continuum background components. This criterium is always applied to the features of the diphoton system and to $\gamma\gamma j(j)$ features for categories targeting truth bin with 1(2) reconstructed jets. The $p_{\mathrm{T}}^{\gamma\gamma}$ variable has been deemed essential and it can never be removed with this procedure.

Significance scan Over the output score distribution of each binary BDT, a significance scan is performed to split the category in up to three sub-categories. The significance is

[1] $Zepp$ is defined as $\left(\eta_{\gamma\gamma} - (\eta_{j1} + \eta_{j2})\right)/2$

[2] $\cos\theta^*_{\gamma\gamma}$ is defined as $\left| \dfrac{\left(E^{\gamma_1} + p_z^{\gamma_1}\right)\cdot\left(E^{\gamma_2} - p_z^{\gamma_2}\right) - \left(E^{\gamma_1} - p_z^{\gamma_1}\right)\cdot\left(E^{\gamma_2} + p_z^{\gamma_2}\right)}{m_{\gamma\gamma} + \sqrt{\left(m_{\gamma\gamma}^2 + \left(p_{\mathrm{T}}^{\gamma\gamma}\right)^2\right)}} \right|$

computed with the formula

$$S = \sqrt{2 \cdot \left((s+b) \cdot \log\left(1 + \frac{s}{b}\right) - s \right)} \tag{5.2}$$

where $s = S_{90}$ is represented by the truth bin signal targeted by the category while $b = B_{90}$ is the background yield obtained integrating the MC histogram in the 90% signal window computed as the sum of the continuum MC TI background samples normalized in the 95 GeV to 105 GeV data TI range plus the resonant background coming from the contamination of the other STXS truth bins normalized to 140 fb^{-1} according to their SM cross sections.

Three significance values are used to select the event splitting with the highest performance: one with just one category (therefore with no significance scan), one that maximizes the significance with two categories (1D) and one with three categories (2D scan). These last two setups are obtained initially with plain grid scans, which are then further optimized near their minima with a gradient descendent algorithm. Moreover, during the scans, the number of events in the TI data sidebands for each category is required to be larger than 10, in order to create categories where the final maximum likelihood fit can be carried out to extract the continuum background component.

Usually, the three categories setup provides the best result: since having less categories simplifies the analysis, the setup with more categories is selected only if the gain in significance over the setup with one less category is larger than 5%. The category boundaries extracted from these procedure are reported in Table 5.5.

Binary BDTs	Category boundaries	
GG2H_0J_PTH_0_10	0.539	
GG2H_0J_PTH_GT10		
GG2H_1J_PTH_0_60	0.434	
GG2H_1J_PTH_60_120	0.393	
GG2H_1J_PTH_120_200	0.407	
GG2H_GE2J_MJJ_0_350_PTH_0_60	0.434	0.656
GG2H_GE2J_MJJ_0_350_PTH_60_120	0.477	
GG2H_GE2J_MJJ_0_350_PTH_120_200	0.433	
GG2H_GE2J_MJJ_350_700_PTH_0_200	0.339	0.509
GG2H_GE2J_MJJ_700_1000_PTH_0_200	0.334	0.525
GG2H_GE2J_MJJ_GT1000_PTH_0_200	0.351	0.495
GG2H_PTH_200_300	0.444	
GG2H_PTH_300_450	0.365	0.590
GG2H_PTH_450_650	0.386	0.520
GG2H_PTH_GT650		
QQ2HQQ_0J	0.563	0.781
QQ2HQQ_1J	0.433	0.649
QQ2HQQ_GE2J_MJJ_0_60	0.467	0.693
QQ2HQQ_GE2J_MJJ_60_120	0.296	0.536
QQ2HQQ_GE2J_MJJ_120_350	0.389	0.664
QQ2HQQ_GE2J_MJJ_350_700_PTH_0_200	0.350	0.637
QQ2HQQ_GE2J_MJJ_700_1000_PTH_0_200	0.532	
QQ2HQQ_GE2J_MJJ_GT1000_PTH_0_200	0.476	
QQ2HQQ_GE2J_MJJ_350_700_PTH_GT200	0.374	0.632
QQ2HQQ_GE2J_MJJ_700_1000_PTH_GT200	0.541	
QQ2HQQ_GE2J_MJJ_GT1000_PTH_GT200	0.495	
QQ2HLNU_PTV_0_75	0.523	
QQ2HLNU_PTV_75_150	0.442	
QQ2HLNU_PTV_150_250	0.150	
QQ2HLNU_PTV_GT250	0.0681	
QQ2HLL_PTV_0_75	0.861	
QQ2HLL_PTV_75_150	0.540	0.793
QQ2HLL_PTV_150_250	0.241	
QQ2HLL_PTV_GT250		
QQ2HNUNU_PTV_0_75	0.332	0.601
QQ2HNUNU_PTV_75_150	0.540	0.793
QQ2HNUNU_PTV_150_250	0.273	0.541
QQ2HNUNU_PTV_GT250	0.181	

Table 5.5 – Category boundaries for each of the binary BDT for the ggF, VBF and VH processes. If a boundary boundary is not reported, no further category is created on top of the one directly provided by the D-optimal multiclass BDT.

BDT outputs In this paragraph, the binary BDT output for each of the D-optimal reconstructed categories are reported and shown in Figure 5.11. It can be observed that again the background MC TI template reproduce fairly well the data TI sidebands, while differences can be usually be associated to a larger contamination of γj and jj components that are well represented by the NTI data in the sideband. Most of the BDTs can separate the STXS truth bin signal from the continuum background and the contaminations from other STXS processes. The category boundaries are reported in each plots with dashed vertical lines and if no line is shown no further split has been done.

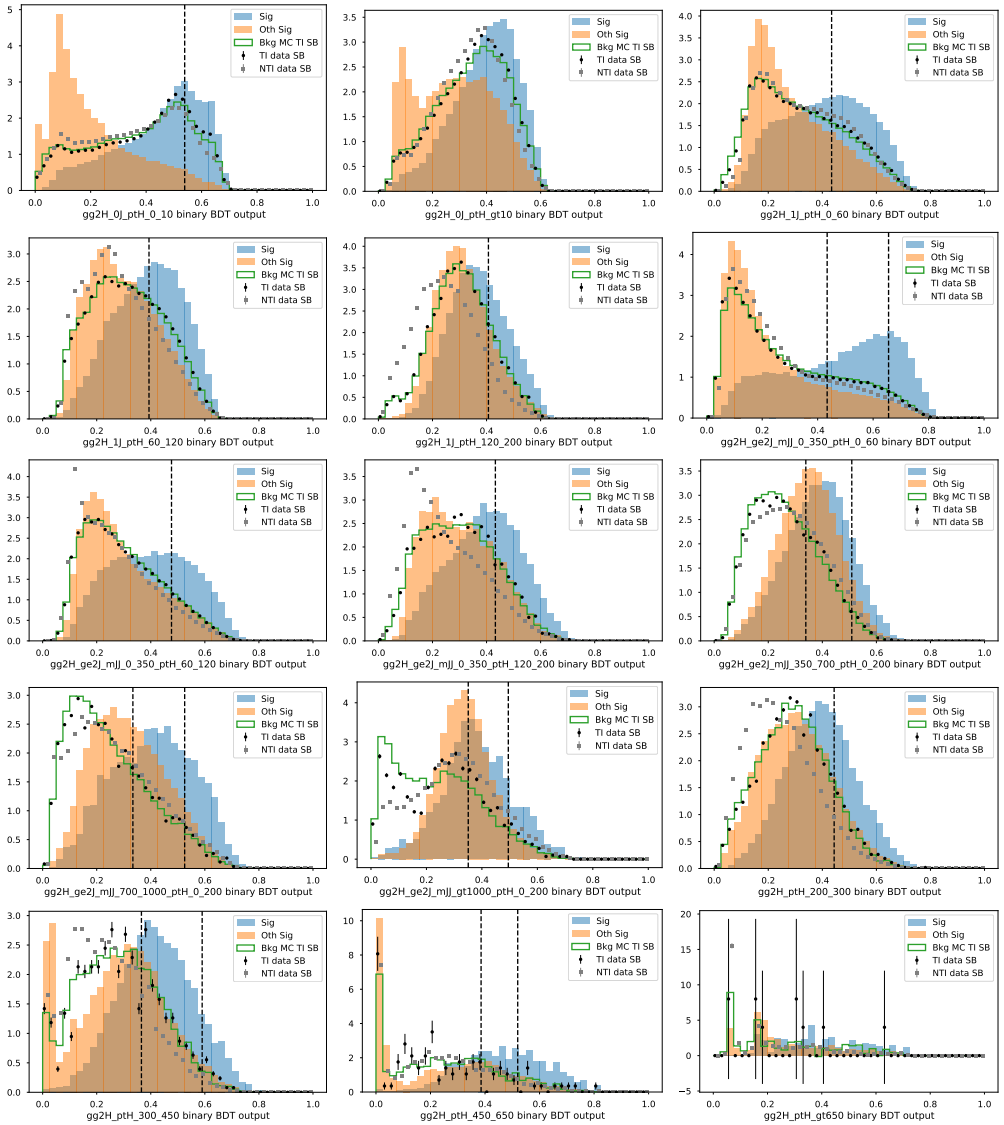

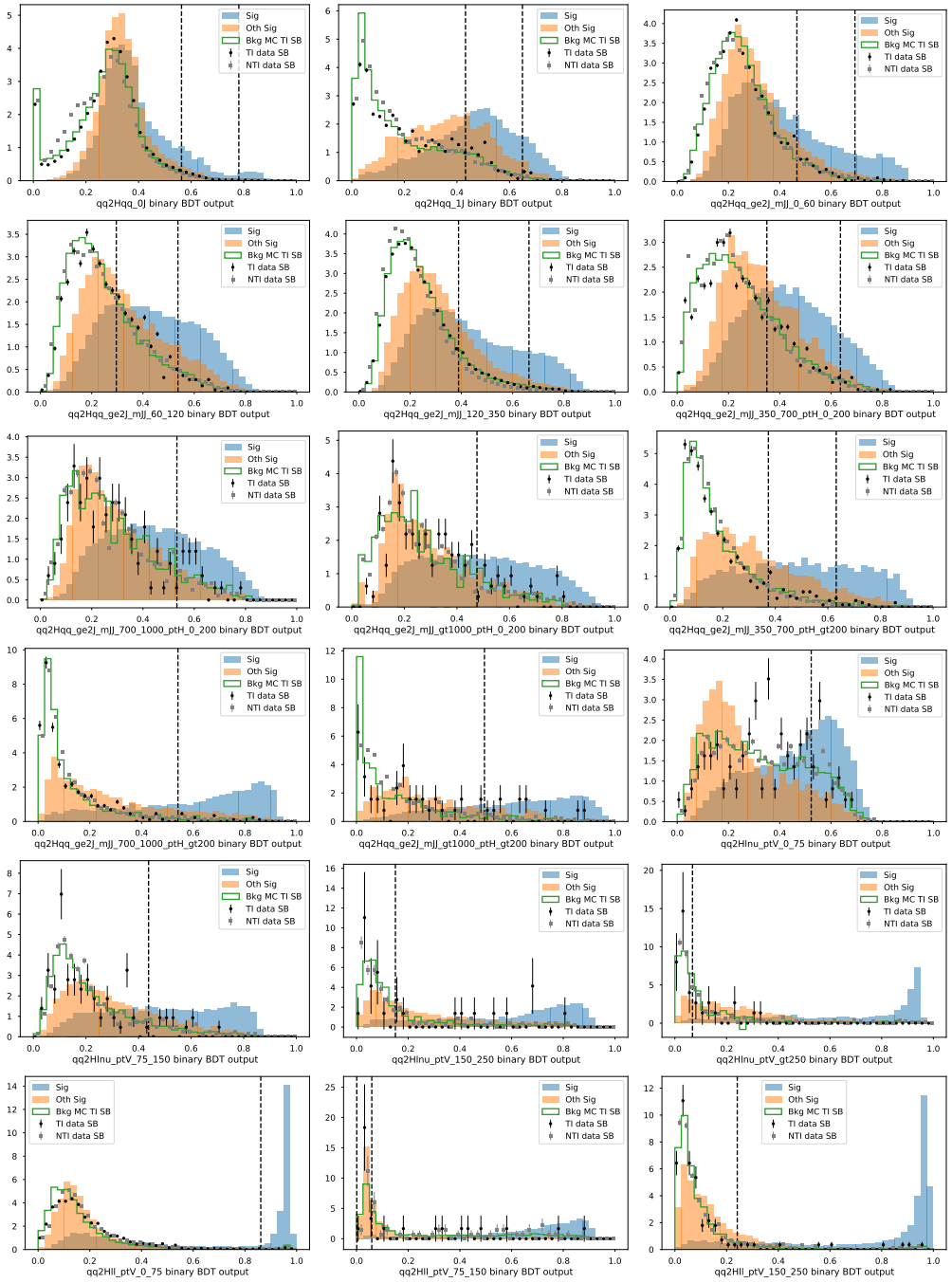
Sig
Oth Sig
Bkg MC TI SB
TI data SB
NTI data SB
qq2Hqq_0J binary BDT output
qq2Hqq_1J binary BDT output
qq2Hqq_ge2J_mJJ_0_60 binary BDT output
qq2Hqq_ge2J_mJJ_60_120 binary BDT output
qq2Hqq_ge2J_mJJ_120_350 binary BDT output
qq2Hqq_ge2J_mJJ_350_700_ptH_0_200 binary BDT output
qq2Hqq_ge2J_mJJ_700_1000_ptH_0_200 binary BDT output
qq2Hqq_ge2J_mJJ_gt1000_ptH_0_200 binary BDT output
qq2Hqq_ge2J_mJJ_350_700_ptH_gt200 binary BDT output
qq2Hqq_ge2J_mJJ_700_1000_ptH_gt200 binary BDT output
qq2Hqq_ge2J_mJJ_gt1000_ptH_gt200 binary BDT output
qq2Hlnu_ptV_0_75 binary BDT output
qq2Hlnu_ptV_75_150 binary BDT output
qq2Hlnu_ptV_150_250 binary BDT output
qq2Hlnu_ptV_gt250 binary BDT output
qq2Hll_ptV_0_75 binary BDT output
qq2Hll_ptV_75_150 binary BDT output
qq2Hll_ptV_150_250 binary BDT output

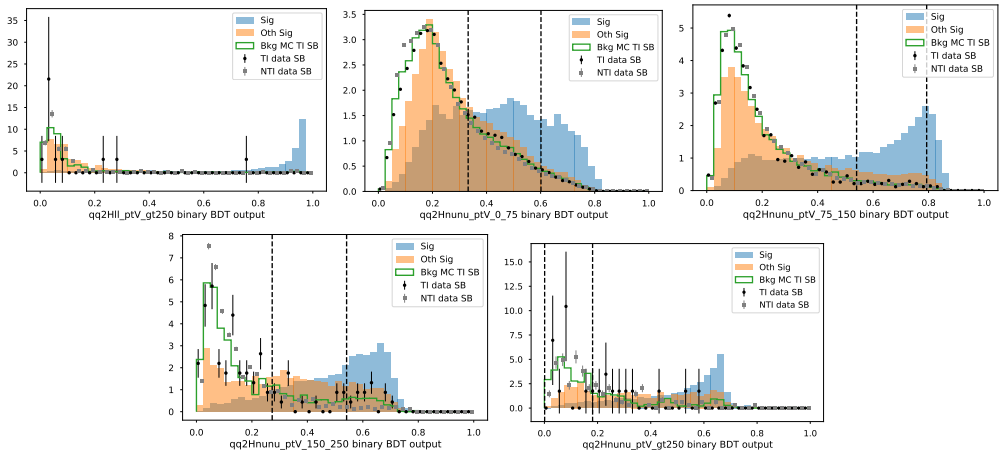

Figure 5.11 – Distributions of BDT output scores for the 38 binary BDTs, trained in each of the D-optimal reconstructed classes: blue filled histogram represents the targeted signal of a given output class, while the orange filled represents the sum of all the other signals weighted according their SM yields. The green line shows the background-only MC TI distribution over the classes and can be compared to TI data (black dots) and NTI data (grey dots). All the histograms are normalized to the same area. Dashed vertical lines represent category boundaries.

$t\bar{t}H$ and tHW processes

In order to boost the performance of $t\bar{t}H$ and tHW categorizations, a slightly different training setup has been used, which follows what has been employed for the $t\bar{t}H$ discovery with partial Run 2 dataset in 2017 and 2018 [9, 10].

The events pre-selected by the D-optimal multiclass BDT in the various top categories are further classified by means of two binary BDTs, one for TTH D-optimal categories and another one for THW category. In particular for $t\bar{t}H$ truth bins, the same TTH binary BDT is applied to all the various multiclass categories targeting different $t\bar{t}H$ $p_{\mathrm{T}}^{\mathrm{H}}$ bins. This is different to what is done for ggF/VBF/VH processes, since only one BDT has been trained to classify many $t\bar{t}H$ truth bins against their background (while above one binary BDT is trained for each truth bin).

For these two ($t\bar{t}H$ and tHW) binary BDTs, all the events pre-selected in one of the TTH D-optimal multiclass categories (or the single TWH category) are used during training: the signal is represented by the $t\bar{t}H$ (tHW) MC sample while the background is represented by NTI data sidebands. These two binary BDTs make use of the following low level variables:

- Photon variables: the transverse momenta, the pseudorapidities and azimuthal angles of the two leading photons;
- Jet variables: the transverse momenta, pseudorapidities, azimuthal angles and pseudo b-tag scores of the six leading jets;

Binary BDTs	Category boundaries	
TTH_PTH_0_60	0.418	0.816
TTH_PTH_60_120	0.354	0.842
TTH_PTH_120_200	0.510	0.842
TTH_PTH_200_300	0.517	
TTH_PTH_GT300	0.215	
THW	0.772	

Table 5.6 – Category boundaries for each of the binary BDT for the $t\bar{t}H$ processes and the tHW process.

- $E_{\mathrm{T}}^{\mathrm{miss}}$ variables: the magnitude and azimuthal angle of the $E_{\mathrm{T}}^{\mathrm{miss}}$ together with the $E_{\mathrm{T}}^{\mathrm{miss}}$ significance, $\left(\frac{E_{\mathrm{T}}^{\mathrm{miss}}}{\sqrt{\sum E_{\mathrm{T}}}}\right)$;

- Top variables: the BDT score of the two leading reconstructed top candidates. See Section 5.3 for additional information about the reconstruction of the $t\bar{t}$ system;

- Lepton variables the transverse momenta, pseudorapidity, azimuthal angle of two leading leptons.

The $t\bar{t}H$ BDT is then applied to the events classified in each of the TTH D-optimal multiclass categories, while the tHW BDT in the THW D-optimal category: to each event, a BDT score is assigned which is used to create either one or two categories, defined by creating cuts on the BDT output. For each of the TTH (THW) categories defined by the multiclass a significance scan for the category boundaries is performed iteratively, looping over all possible cut values starting from high to low scores for a predefined number of categories. The figure of merit is the combined Asimov number counting significance of all categories given in Eq. (5.2), with other Higgs processes and the continuum background summed together as background.

To prevent potential biases, the continuum background is estimated from the NTI data control region, multiplied by a scale factor derived from the TI / NTI ratio after preselection but before any BDT cuts. For Higgs, the yield is taken in the range $m_{\gamma\gamma} \in [123, 127]$ GeV, while for the continuum background, the yield is taken in the range $m_{\gamma\gamma} \in [105, 160]$ GeV excluding the signal region, then scaled by a factor of $4/45$ to mimic the signal window ratio. In order to guarantee enough statistics for a sideband fit, each category must contain at least 0.8 continuum background events (corresponding to $\sim$9 events in the full mass window).

The BDT outputs of the $t\bar{t}H$ and tHW categories are shown in Figure 5.12 for the $t\bar{t}H$ MC sample as well as for the data NTI and TI regions passing the selection. The category boundaries obtained are detailed in Table 5.6. Since the loosest categories have not been optimized with the significance scan described above, they are all merged together in a background-like category.

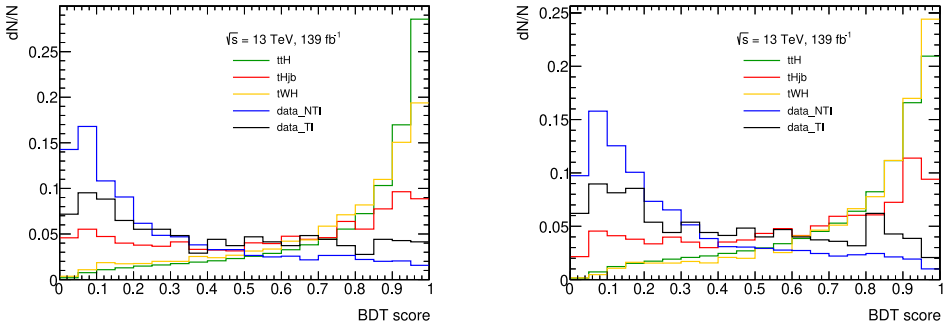

(a) $t\bar{t}H$ BDT output **(b)** tHW BDT output

Figure 5.12 – BDT outputs of the $t\bar{t}H$ and tHW BDT are shown for the whole $t\bar{t}H$, tHq and tHW MC samples as well as for the data NTI and TI regions passing the selection.

tHbj process, maximising sensitivity $\kappa_t = -1$

In order to maximise the analysis sensitivity to the sign of the Higgs-top Yukawa coupling (expressed by the coupling modifier κ_t) when compared to the Standard Model expectation, a Neural Network model is trained to separate tHbj $\kappa_t = +1$ (SM) events from tHbj $\kappa_t = -1$ events. The aim is to use the model to create a new analysis category that is optimised to be sensitive to tHbj events generated with $\kappa_t = -1$, while maintaining the tHbj SM sensitivity.

The model is trained on all tHbj events ($\kappa_t = +1$ vs $\kappa_t = -1$) that pass the diphoton selection while testing is performed on tHbj events that enter the THJB multi-class category. A set of low level variables are defined based on the expected hard scatter particles in the tHbj process: the most forward jet (fwdJet) in each event is selected to target the outgoing light jet in the tHbj process. Angles and invariant masses between the Higgs candidate, the two reconstructed tops (see Section 5.3) and the most forward jet are used in the classification. Variables are recursively added to the training while monitoring its performance, in order not to add useless variables, stopping when the training Area-Under-the-Curve (AUC) becomes stable. The selected input variables are

- Diphoton variables: $p^T_{\gamma\gamma}/m_{\gamma\gamma}$ and $\eta_{\gamma\gamma}$;
- p^T, mass, score, $\Delta R(W,b)$ of the first reconstructed top and p^T, η of the second reconstructed top (see Section 5.3);
- Most forward jet variables j_{fwd}: p_{T}, η;
- Angular variables: $\Delta\eta(t_1,\gamma\gamma)$, $\Delta\theta(t_1,\gamma\gamma)$, $\Delta\theta(j_{\text{fwd}},t_1)$, $\Delta\theta(j_{\text{fwd}},t_2)$, $\Delta\theta(j_{\text{fwd}},H)$ where t_1 and t_2 are the first and second reconstructed top;
- Invariant mass variables: m_{t_1-H}, $m_{t_1-j_{\text{fwd}}}$, $m_{j_{\text{fwd}}-H}$, $m_{t_2-j_{\text{fwd}}}$;
- Other variables: N_{jets} with $p_{\text{T}} > 25\,\text{GeV}$

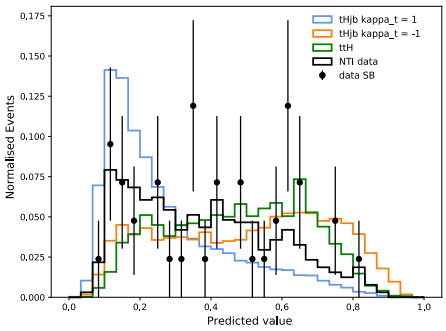

(a) $\kappa_t = +1$ vs $\kappa_t = -1$ model.

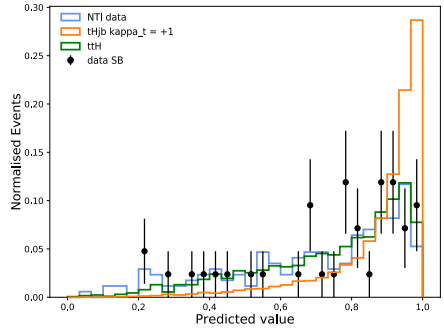

(b) $\kappa_t = +1$ vs NTI model.

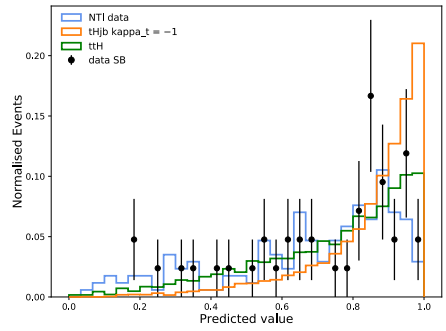

(c) $\kappa_t = -1$ vs NTI model.

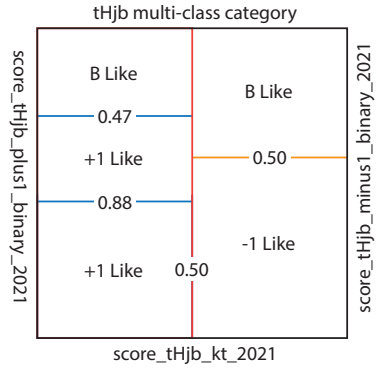

(d) Schematic over view of tHbj categorization.

Figure 5.13 – Distribution of the score of each of the three NN models for $\kappa_t = +1$ vs $\kappa_t = -1$ separation (a) and against continuum background (b,c) for different processes, for all events selected in the THJB multiclass category. (d) Schematic overview of the category boundaries for the final tHbj categories.

Events are weighted to have equal yield for each class during training and binary cross-entropy loss is used as loss. The output of the NN score is shown in Figure 5.13a, for the events that enter the THJB D-optimal multiclass category.

Two additional NN models are trained to separated the $\kappa_t = +1$ and $\kappa_t = -1$ events from their background, using the same algorithm properties above. The sample representing the continuum background for the two trainings is composed by NTI data that are selected into any top-quark related multiclass categories. The performance of these two NN models are reported in Figure 5.13b and Figure 5.13c respectively.

The optimal tHbj categorization is chosen running a three-dimensional scan over the three NN models outputs, where for each point a simple counting experiment in the 90% signal window is run in order to obtain simultaneously the expected statistical uncertainty on the tH cross section and the constraining power on the $\kappa_t = -1$ hypothesis. A schematic illustration of the category boundaries are reported in Figure 5.13d. During this optimization, the continuum background is modelled using the high statistic

$t\bar{t}\gamma\gamma$ MC as it was determined to model the best the TI data sidebands in each NN score used, scaled to the yield of TI data sideband, and it was required that at least 9 events in the sideband integral of data were present. The final categorisation is defined by two categories that are sensitive to the tHbj SM process and one category sensitive to the $\kappa_t = -1$ hypothesis. Events that do not pass any of these three selections are deemed to be background-like and merged with the loosest categories produced by $t\bar{t}H$ and tHW categorizations.

5.4.5 Categorization overview and performance

The final coupling analysis features 101 reconstructed categories, targeting 45 different STXS truth bins. The category optimization described above was slightly modified in the final round of the analysis : it was decided to merge the two GGH_0J_PTH_0_10 categories, since there were some problems in modelling of the background template for the spurious signal method for the "tight" category.

The performance of the categorization procedure is highlighted in Figure 5.14 where the composition of each reconstructed category in terms of STXS truth bins is given. In addition all the details can be found in Table 5.7 in terms of total signal fraction and significance. As can be observed, the purity matrix is almost diagonal for most of the categories. Wherever more than one category is present to target on truth bin, the tight category has better purity than the others. Two notable exceptions to the diagonal are represented by QQ2HQQ categories requiring ≤ 1 reconstructed jet and QQ2HNUNU low-MET categories which are highly contaminated by ggF truth bins because the final state is particularly similar and ggF cross section is overwhelmingly dominant with respect to VH cross section.

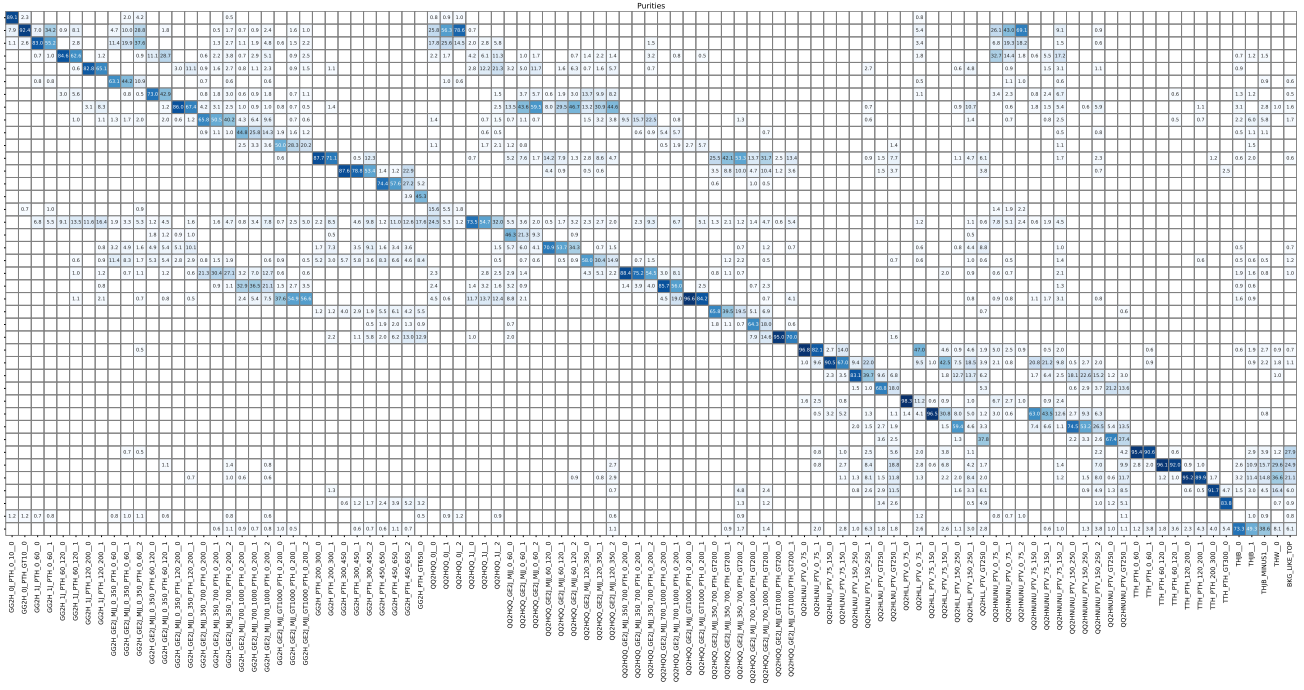

Figure 5.14 – The categories purity for the final categorization: the reconstructed categories are reported on the x-axis, while different truth bins are reported on the y-axis. Sums over columns is 100%, modulo the fact that only values larger than 0.5% are shown.

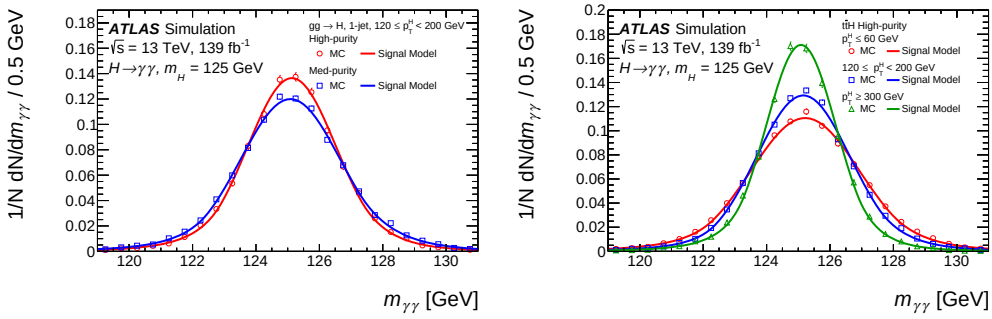

(a) GG2H_1J_PTH_120_200 categories.

(b) Three $t\bar{t}H$ high purity categories.

Figure 5.15 – Shape of the signal $m_{\gamma\gamma}$ distribution for two groups of categories [6], (a) comparing the signal $m_{\gamma\gamma}$ shapes for two categories targeting the same STXS region with different purities and (b) comparing the shapes for three "high-purity" categories targeting different $p_{\mathrm{T}}^{\mathrm{H}}$ regions of the $t\bar{t}H$ process.

5.5 Signal and background modelling

Analytical functions employed to model signal and background processes in each category are chosen with the procedure outlined in Section 4.5 and Section 4.6 respectively. Here, further peculiarities of the modelling are reported, in particular due to the treatment of 101 categories in the background template construction.

5.5.1 Signal modelling

Even if the analysis has some sensitivity to the Higgs mass, the coupling analysis usually keeps the mass value fixed to 125.09 GeV. This is due to the fact that we have a very precise knowledge of the Higgs mass from the Run 1 combination of ATLAS and CMS measurements ($m_H = 125.09 \pm 0.21\,(\mathrm{stat}) \pm 0.11\,(\mathrm{syst})\,\mathrm{GeV}$) [33] and to the relatively small error of the photon energy scale systematics affecting the peak position of the DSCB function ($< 1\%$). Therefore the effect of the variation on m_H is considered negligible on the coupling values and it is possible to parametrize the shape using just one set of MC samples simulated with the Higgs mass m_H fixed at 125 GeV. Then, in the statistical workspace, a 90 MeV shift is applied to fitted value μ_{CB} in order to account for this fact so that the final peak position is given by $\mu_{\mathrm{CB}} = \mu_{\mathrm{CB}}^{125\,\mathrm{GeV}} + 90\,\mathrm{MeV}$.

The signal pdf are fitted over the MC samples in the fixed mass range $[110, 140]$ GeV while leaving floating all the six parameters of the DSCB function. The fit over MC dataset is usually unbinned but it has been decided to revert to a binned dataset if the unbinned fit fails for one category.

A few examples of the fitted signal pdf functions are reported in Figure 5.15 where it can be observed that the signal resolution is usually better for tight categories and for higher and higher $p_{\mathrm{T}}^{\mathrm{H}}$ selections. The width of the smallest signal window containing 68% or 90% of the signal are reported in Table 5.8, where it can be observed the tight category has almost always better resolution.

Category	σ_{90} [GeV]	B_{90}	S_{90}^{tb}	f_{90}^{tb}[%]	Z_{90}^{tb}	S_{90}^{H}	f_{90}^{H}[%]	Z_{90}^{H}
GG2H_0J_PTH_0_10__0	3.4	26 000	690	2.6	4.3	770	2.9	4.8
GG2H_0J_PTH_GT10__0	3.4	47 000	1400	3.0	6.6	1500	3.2	7.0
GG2H_1J_PTH_0_60__0	3.2	4 250	170	3.8	2.6	200	4.5	3.1
GG2H_1J_PTH_0_60__1	3.4	11 500	200	1.7	1.8	350	3.0	3.3
GG2H_1J_PTH_60_120__0	3.1	3 310	190	5.3	3.2	220	6.2	3.8
GG2H_1J_PTH_60_120__1	3.4	7 780	180	2.3	2.0	290	3.5	3.2
GG2H_1J_PTH_120_200__0	2.6	182	23	11	1.7	28	13	2.0
GG2H_1J_PTH_120_200__1	3.0	717	41	5.4	1.5	62	8.0	2.3
GG2H_GE2J_MJJ_0_350_PTH_0_60__0	3.1	1 050	23	2.2	0.72	37	3.4	1.1
GG2H_GE2J_MJJ_0_350_PTH_0_60__1	3.4	4 360	43	0.98	0.65	95	2.1	1.4
GG2H_GE2J_MJJ_0_350_PTH_0_60__2	3.5	16 800	48	0.28	0.37	390	2.3	3.0
GG2H_GE2J_MJJ_0_350_PTH_60_120__0	3.0	901	49	5.2	1.6	67	6.9	2.2
GG2H_GE2J_MJJ_0_350_PTH_60_120__1	3.3	6 440	94	1.4	1.2	220	3.3	2.7
GG2H_GE2J_MJJ_0_350_PTH_120_200__0	2.6	74.8	16	17	1.7	18	19	2.0
GG2H_GE2J_MJJ_0_350_PTH_120_200__1	3.0	343	23	6.2	1.2	34	8.9	1.8
GG2H_GE2J_MJJ_350_700_PTH_0_200__0	2.7	47.5	4.3	8.3	0.62	6.5	12	0.93
GG2H_GE2J_MJJ_350_700_PTH_0_200__1	3.0	380	15	3.9	0.78	30	7.4	1.5
GG2H_GE2J_MJJ_350_700_PTH_0_200__2	3.3	1 080	11	0.97	0.32	26	2.3	0.78
GG2H_GE2J_MJJ_700_1000_PTH_0_200__0	2.8	33.3	2.3	6.6	0.40	5.2	13	0.88
GG2H_GE2J_MJJ_700_1000_PTH_0_200__1	3.1	136	4.2	3.0	0.36	16	11	1.4
GG2H_GE2J_MJJ_700_1000_PTH_0_200__2	3.3	429	3.3	0.77	0.16	23	5.0	1.1
GG2H_GE2J_MJJ_GT1000_PTH_0_200__0	3.0	14.5	1.1	7.3	0.30	2.3	13	0.58
GG2H_GE2J_MJJ_GT1000_PTH_0_200__1	3.1	47.5	2.5	5.0	0.36	8.9	16	1.3
GG2H_GE2J_MJJ_GT1000_PTH_0_200__2	3.4	142	2.5	1.7	0.21	12	7.9	1.0
GG2H_PTH_200_300__0	2.3	38.0	15	29	2.3	17	31	2.6
GG2H_PTH_200_300__1	2.6	236	29	11	1.9	41	15	2.6
GG2H_PTH_300_450__0	2.0	2.13	1.5	42	0.95	1.7	45	1.1
GG2H_PTH_300_450__1	2.2	17.7	6.8	28	1.5	8.6	33	1.9
GG2H_PTH_300_450__2	2.5	43.1	4.7	9.8	0.70	8.7	17	1.3
GG2H_PTH_450_650__0	1.9	1.25	1.0	45	0.81	1.4	52	1.1
GG2H_PTH_450_650__1	2.0	2.00	0.80	29	0.53	1.4	41	0.89
GG2H_PTH_450_650__2	2.2	10.7	0.83	7.2	0.25	3.0	22	0.89
GG2H_PTH_GT650__0	1.7	1.08	0.22	17	0.20	0.47	31	0.43
QQ2HQQ_0J__0	3.3	25.0	0.33	1.3	0.070	2.1	7.7	0.41
QQ2HQQ_0J__1	3.4	471	1.3	0.27	0.060	23	4.7	1.1
QQ2HQQ_0J__2	3.5	18 800	11	0.060	0.080	590	3.0	4.3
QQ2HQQ_1J__0	3.0	2.78	1.1	28	0.61	1.5	35	0.82
QQ2HQQ_1J__1	3.1	26.1	3.5	12	0.67	6.4	20	1.2
QQ2HQQ_1J__2	3.2	145	2.9	2.0	0.24	9.0	5.9	0.74
QQ2HQQ_GE2J_MJJ_0_60__0	2.7	2.10	0.35	14	0.24	0.76	27	0.50
QQ2HQQ_GE2J_MJJ_0_60__1	2.8	19.0	0.67	3.4	0.15	3.1	14	0.70
QQ2HQQ_GE2J_MJJ_0_60__2	2.9	243	1.9	0.78	0.12	21	7.8	1.3
QQ2HQQ_GE2J_MJJ_60_120__0	2.7	6.34	3.5	35	1.3	4.9	43	1.7
QQ2HQQ_GE2J_MJJ_60_120__1	2.9	43.0	5.0	10	0.75	9.3	18	1.4
QQ2HQQ_GE2J_MJJ_60_120__2	3.0	87.3	3.0	3.3	0.32	8.7	9.1	0.92
QQ2HQQ_GE2J_MJJ_120_350__0	2.9	24.4	3.0	11	0.59	5.1	17	1.0
QQ2HQQ_GE2J_MJJ_120_350__1	2.9	204	6.7	3.2	0.47	22	9.8	1.5
QQ2HQQ_GE2J_MJJ_120_350__2	3.0	1 360	8.8	0.64	0.24	59	4.1	1.6
QQ2HQQ_GE2J_MJJ_350_700_PTH_0_200__0	3.0	2.75	2.5	48	1.4	2.9	51	1.5
QQ2HQQ_GE2J_MJJ_350_700_PTH_0_200__1	3.1	34.7	9.2	21	1.5	12	26	2.0
QQ2HQQ_GE2J_MJJ_350_700_PTH_0_200__2	3.3	106	6.0	5.3	0.57	11	9.3	1.0
QQ2HQQ_GE2J_MJJ_700_1000_PTH_0_200__0	2.9	3.00	2.9	49	1.5	3.4	53	1.7
QQ2HQQ_GE2J_MJJ_700_1000_PTH_0_200__1	3.1	22.7	5.6	20	1.1	10	31	2.0
QQ2HQQ_GE2J_MJJ_GT1000_PTH_0_200__0	3.0	3.89	11	74	4.2	11	74	4.3
QQ2HQQ_GE2J_MJJ_GT1000_PTH_0_200__1	3.2	19.0	11	36	2.3	13	40	2.7

Table 5.7 – The table reports the categorization performance in the smallest window (σ_{90}) containing 90% of the total signal. The expected number of background events is shown along with both the number of expected signal events from all signal processes(S_{90}^{H}) or for all the STXS truth bins targeted by a reconstructed category (S_{90}^{tb}). Expected background events are extracted from a fit over TI data sideband of the functions selected in Section5.5.2. The fraction of signal events over total $f = S_{90}/(S_{90} + B_{90})$ and the expected significance computed with the Eq. (5.2) are reported for the case where signal is all the Higgs production processes or only the STXS truth bin targeted by a given category.

Category	σ_{90} [GeV]	B_{90}	S_{90}^{tb}	f_{90}^{tb}[%]	Z_{90}^{tb}	S_{90}^{H}	f_{90}^{H}[%]	Z_{90}^{H}
QQ2HQQ_GE2J_MJJ_350_700_PTH_GT200__0	2.5	2.19	1.3	37	0.81	2.0	48	1.2
QQ2HQQ_GE2J_MJJ_350_700_PTH_GT200__1	2.5	9.22	1.4	13	0.45	3.7	28	1.1
QQ2HQQ_GE2J_MJJ_350_700_PTH_GT200__2	2.5	65.5	1.2	1.7	0.14	7.0	9.6	0.84
QQ2HQQ_GE2J_MJJ_700_1000_PTH_GT200__0	2.4	3.02	2.5	45	1.3	3.9	56	1.9
QQ2HQQ_GE2J_MJJ_700_1000_PTH_GT200__1	2.5	47.4	1.5	3.0	0.22	8.7	15	1.2
QQ2HQQ_GE2J_MJJ_GT1000_PTH_GT200__0	2.4	1.57	5.7	78	3.3	5.9	79	3.4
QQ2HQQ_GE2J_MJJ_GT1000_PTH_GT200__1	2.6	6.31	3.0	32	1.1	4.2	40	1.5
QQ2HLNU_PTV_0_75__0	3.2	4.91	1.9	28	0.81	2.0	29	0.84
QQ2HLNU_PTV_0_75__1	3.3	20.2	2.6	11	0.57	3.2	14	0.69
QQ2HLNU_PTV_75_150__0	3.0	2.05	2.6	56	1.6	2.9	59	1.7
QQ2HLNU_PTV_75_150__1	3.2	12.4	2.1	14	0.58	3.1	20	0.85
QQ2HLNU_PTV_150_250__0	2.8	2.06	1.7	46	1.1	2.1	50	1.3
QQ2HLNU_PTV_150_250__1	3.2	2.90	0.16	5.2	0.090	0.40	12	0.23
QQ2HLNU_PTV_GT250__0	2.4	1.79	1.4	43	0.91	2.0	52	1.3
QQ2HLNU_PTV_GT250__1	3.2	3.12	0.020	0.78	0.010	0.14	4.2	0.080
QQ2HLL_PTV_0_75__0	3.3	1.82	1.1	39	0.78	1.2	39	0.79
QQ2HLL_PTV_0_75__1	3.3	215	1.1	0.49	0.070	9.5	4.2	0.64
QQ2HLL_PTV_75_150__0	3.1	1.58	1.1	40	0.77	1.1	41	0.80
QQ2HLL_PTV_75_150__1	3.1	1.81	0.020	1.2	0.020	0.070	3.6	0.050
QQ2HLL_PTV_150_250__0	2.8	1.79	0.71	28	0.50	1.2	40	0.81
QQ2HLL_PTV_150_250__1	2.9	16.5	0.10	0.62	0.030	2.2	12	0.54
QQ2HLL_PTV_GT250__0	2.5	2.06	0.27	12	0.18	0.71	26	0.47
QQ2HNUNU_PTV_0_75__0	3.5	170	0.60	0.35	0.050	9.0	5.0	0.68
QQ2HNUNU_PTV_0_75__1	3.6	1 020	1.2	0.11	0.040	42	4.0	1.3
QQ2HNUNU_PTV_0_75__2	3.7	2 630	0.87	0.030	0.020	90	3.3	1.7
QQ2HNUNU_PTV_75_150__0	3.0	2.30	0.58	20	0.37	0.92	29	0.57
QQ2HNUNU_PTV_75_150__1	3.3	17.8	1.8	9.3	0.43	4.2	19	0.96
QQ2HNUNU_PTV_75_150__2	3.4	288	2.2	0.75	0.13	17	5.7	1.0
QQ2HNUNU_PTV_150_250__0	2.8	2.00	0.92	32	0.61	1.2	38	0.80
QQ2HNUNU_PTV_150_250__1	2.9	2.54	0.75	23	0.45	1.4	36	0.81
QQ2HNUNU_PTV_150_250__2	3.3	11.7	0.26	2.2	0.080	0.97	7.7	0.28
QQ2HNUNU_PTV_GT250__0	2.5	1.55	0.67	30	0.50	0.99	39	0.73
QQ2HNUNU_PTV_GT250__1	3.1	1.97	0.050	2.6	0.040	0.19	8.8	0.13
TTH_PTH_0_60__0	3.2	4.01	3.0	43	1.4	3.2	44	1.4
TTH_PTH_0_60__1	3.4	13.3	2.8	17	0.74	3.1	19	0.81
TTH_PTH_60_120__0	3.1	4.09	4.3	51	1.9	4.5	52	1.9
TTH_PTH_60_120__1	3.3	8.61	3.0	26	0.97	3.3	27	1.1
TTH_PTH_120_200__0	2.7	3.52	4.7	57	2.1	4.9	58	2.2
TTH_PTH_120_200__1	2.9	4.16	1.7	29	0.77	1.9	31	0.85
TTH_PTH_200_300__0	2.5	2.26	3.4	60	1.9	3.7	62	2.0
TTH_PTH_GT300__0	2.1	1.66	2.7	62	1.8	3.3	66	2.0
THJB__0	3.0	2.16	0.55	20	0.36	0.75	26	0.48
THJB__1	3.5	2.78	0.14	4.9	0.090	0.30	9.8	0.18
THJB_MINUS1__0	3.3	1.86	0.12	6.0	0.090	0.33	15	0.24
THW__0	2.7	6.91	0.16	2.3	0.060	3.5	34	1.2
BKG_LIKE_TOP	3.3	65.8	5.2	7.3	0.63	6.0	8.3	0.72

Table 5.7 – The table reports the categorization performance in the smallest window (σ_{90}) containing 90% of the total signal. The expected number of background events is shown along with both the number of expected signal events from all signal processes(S_{90}^{H}) or for all the STXS truth bins targeted by a reconstructed category (S_{90}^{tb}). Expected background events are extracted from a fit over TI data sideband of the functions selected in Section5.5.2. The fraction of signal events over total $f = S_{90}/(S_{90} + B_{90})$ and the expected significance computed with the Eq. (5.2) are reported for the case where signal is all the Higgs production processes or only the STXS truth bin targeted by a given category.

Category	σ_{68}	σ_{90}
GG2H_0J_PTH_0_10__0	1.95	3.43
GG2H_0J_PTH_GT10__0	1.92	3.41
GG2H_1J_PTH_0_60__0	1.81	3.20
GG2H_1J_PTH_0_60__1	1.91	3.38
GG2H_1J_PTH_60_120__0	1.75	3.10
GG2H_1J_PTH_60_120__1	1.89	3.37
GG2H_1J_PTH_120_200__0	1.49	2.61
GG2H_1J_PTH_120_200__1	1.68	3.00
GG2H_GE2J_MJJ_0_350_PTH_0_60__0	1.76	3.08
GG2H_GE2J_MJJ_0_350_PTH_0_60__1	1.92	3.39
GG2H_GE2J_MJJ_0_350_PTH_0_60__2	1.97	3.51
GG2H_GE2J_MJJ_0_350_PTH_60_120__0	1.72	3.03
GG2H_GE2J_MJJ_0_350_PTH_60_120__1	1.85	3.30
GG2H_GE2J_MJJ_0_350_PTH_120_200__0	1.50	2.64
GG2H_GE2J_MJJ_0_350_PTH_120_200__1	1.67	2.97
GG2H_GE2J_MJJ_350_700_PTH_0_200__0	1.52	2.72
GG2H_GE2J_MJJ_350_700_PTH_0_200__1	1.70	3.02
GG2H_GE2J_MJJ_350_700_PTH_0_200__2	1.85	3.31
GG2H_GE2J_MJJ_700_1000_PTH_0_200__0	1.61	2.84
GG2H_GE2J_MJJ_700_1000_PTH_0_200__1	1.74	3.07
GG2H_GE2J_MJJ_700_1000_PTH_0_200__2	1.83	3.26
GG2H_GE2J_MJJ_GT1000_PTH_0_200__0	1.61	2.97
GG2H_GE2J_MJJ_GT1000_PTH_0_200__1	1.75	3.10
GG2H_GE2J_MJJ_GT1000_PTH_0_200__2	1.87	3.37
GG2H_PTH_200_300__0	1.30	2.28
GG2H_PTH_200_300__1	1.47	2.64
GG2H_PTH_300_450__0	1.10	2.02
GG2H_PTH_300_450__1	1.19	2.16
GG2H_PTH_300_450__2	1.36	2.46
GG2H_PTH_450_650__0	1.02	1.85
GG2H_PTH_450_650__1	1.07	1.98
GG2H_PTH_450_650__2	1.18	2.19
GG2H_PTH_GT650__0	0.98	1.73
QQ2HQQ_0J__0	1.88	3.33
QQ2HQQ_0J__1	1.90	3.35
QQ2HQQ_0J__2	1.96	3.48
QQ2HQQ_1J__0	1.70	2.99
QQ2HQQ_1J__1	1.73	3.11
QQ2HQQ_1J__2	1.83	3.24
QQ2HQQ_GE2J_MJJ_0_60__0	1.57	2.71
QQ2HQQ_GE2J_MJJ_0_60__1	1.59	2.79
QQ2HQQ_GE2J_MJJ_0_60__2	1.66	2.93
QQ2HQQ_GE2J_MJJ_60_120__0	1.47	2.65
QQ2HQQ_GE2J_MJJ_60_120__1	1.59	2.85
QQ2HQQ_GE2J_MJJ_60_120__2	1.68	3.01
QQ2HQQ_GE2J_MJJ_120_350__0	1.68	2.93
QQ2HQQ_GE2J_MJJ_120_350__1	1.65	2.94
QQ2HQQ_GE2J_MJJ_120_350__2	1.67	2.99

Category	σ_{68}	σ_{90}
QQ2HQQ_GE2J_MJJ_350_700_PTH_0_200__0	1.65	2.96
QQ2HQQ_GE2J_MJJ_350_700_PTH_0_200__1	1.71	3.06
QQ2HQQ_GE2J_MJJ_350_700_PTH_0_200__2	1.83	3.27
QQ2HQQ_GE2J_MJJ_700_1000_PTH_0_200__0	1.63	2.90
QQ2HQQ_GE2J_MJJ_700_1000_PTH_0_200__1	1.76	3.11
QQ2HQQ_GE2J_MJJ_GT1000_PTH_0_200__0	1.68	3.01
QQ2HQQ_GE2J_MJJ_GT1000_PTH_0_200__1	1.81	3.23
QQ2HQQ_GE2J_MJJ_350_700_PTH_GT200__0	1.39	2.48
QQ2HQQ_GE2J_MJJ_350_700_PTH_GT200__1	1.38	2.49
QQ2HQQ_GE2J_MJJ_350_700_PTH_GT200__2	1.40	2.54
QQ2HQQ_GE2J_MJJ_700_1000_PTH_GT200__0	1.36	2.43
QQ2HQQ_GE2J_MJJ_700_1000_PTH_GT200__1	1.39	2.54
QQ2HQQ_GE2J_MJJ_GT1000_PTH_GT200__0	1.33	2.39
QQ2HQQ_GE2J_MJJ_GT1000_PTH_GT200__1	1.40	2.55
QQ2HLNU_PTV_0_75__0	1.80	3.17
QQ2HLNU_PTV_0_75__1	1.85	3.28
QQ2HLNU_PTV_75_150__0	1.71	3.02
QQ2HLNU_PTV_75_150__1	1.80	3.23
QQ2HLNU_PTV_150_250__0	1.53	2.78
QQ2HLNU_PTV_150_250__1	1.71	3.17
QQ2HLNU_PTV_GT250__0	1.31	2.41
QQ2HLNU_PTV_GT250__1	1.66	3.15
QQ2HLL_PTV_0_75__0	1.83	3.25
QQ2HLL_PTV_0_75__1	1.85	3.29
QQ2HLL_PTV_75_150__0	1.72	3.08
QQ2HLL_PTV_75_150__1	1.68	3.06
QQ2HLL_PTV_150_250__0	1.51	2.78
QQ2HLL_PTV_150_250__1	1.62	2.88
QQ2HLL_PTV_GT250__0	1.35	2.48
QQ2HNUNU_PTV_0_75__0	1.99	3.50
QQ2HNUNU_PTV_0_75__1	2.00	3.57
QQ2HNUNU_PTV_0_75__2	2.04	3.67
QQ2HNUNU_PTV_75_150__0	1.65	2.97
QQ2HNUNU_PTV_75_150__1	1.81	3.26
QQ2HNUNU_PTV_75_150__2	1.91	3.44
QQ2HNUNU_PTV_150_250__0	1.55	2.75
QQ2HNUNU_PTV_150_250__1	1.64	2.94
QQ2HNUNU_PTV_150_250__2	1.76	3.28
QQ2HNUNU_PTV_GT250__0	1.38	2.46
QQ2HNUNU_PTV_GT250__1	1.61	3.05
TTH_PTH_0_60__0	1.81	3.18
TTH_PTH_0_60__1	1.89	3.37
TTH_PTH_60_120__0	1.72	3.06
TTH_PTH_60_120__1	1.87	3.31
TTH_PTH_120_200__0	1.55	2.73
TTH_PTH_120_200__1	1.67	2.93
TTH_PTH_200_300__0	1.38	2.46
TTH_PTH_GT300__0	1.18	2.12
THJB__0	1.76	3.04
THJB__1	1.87	3.45
THJB_MINUS1__0	1.64	3.25
THW__0	1.54	2.74
BKG_LIKE_TOP	1.84	3.32

Table 5.8 – Width of the smallest windows containing 68% and 90% of the signals in GeV, extracted from the fitted function.

5.5.2 Background modelling

The background modelling strategy for some of the 101 categories has been slightly modified with respect to what is described in Section 4.6.

Concerning background templates, these have been built differently for different regions of the Higgs production phase space. For ggF and VBF categories, the standard strategy detailed in Section 4.6 while, due to the low statistics and significant additional background components, background templates for the VH and $t\bar{t}H$ categories are constructed in the following way:

- VH categories: both MC Sherpa $\gamma\gamma$ and $V\gamma\gamma$ samples are used to provide a diphoton background template by summing them up according to their cross sections;
- $t\bar{t}H$ categories: the standalone $t\bar{t}\gamma\gamma$ MC samples are used to provide a background template

In both cases, they are then normalized to the TI data sideband of the respective category.

Moreover, a smoothing procedure has been applied to the background templates before running the spurious signal test. This is done employing a Gaussian Process regression technique [144–147] on the background template histogram. A Gaussian Process (GP) is defined as a set of random processes, where all finite subsets of these processes have a multivariate normal distribution: one can regards the bin contents of a smooth histogram as generated by such a process. The mean and the covariance of the underlying fundamental process can be fitted from the histogram bin contents including some theoretical model assumptions. For example, the covariance matrix can be simplified through the introduction of a kernel, which analytically determines the level of correlation between two distinct points (i.e., the length scales in X at which points are expected to influence one another in Y). For smoothly-falling functions, it is likely that nearby points will be more correlated in some regions than in others, so a length scale that varies linearly as a function of the observable may be favourable. The Gibbs kernel [148] encodes this variation by including two hyperparameters (the initial scale length and its slope) and is represented by

$$K_{\text{Gibbs}}(x, x') = \frac{\sqrt{2l(x)l(x')}}{l(x)^2 + l(x')^2} \cdot \exp\left\{\frac{-(x-x')^2}{l(x)^2 + l(x')^2}\right\}. \tag{5.3}$$

Since the background templates used in the spurious signal test for the analysis categories are all smooth, roughly exponentially falling distributions with statistical fluctuations, fitting a background template using Gaussian Process Regression (using the Gibbs kernel with the errors as determined by the initial templates) offers a consistent method of estimating the underlying smooth shape of the template, without statistical fluctuations. Notably, the GP smoothing technique makes no assumption on the underlying distribution other than that it is smooth, hence the choice of functional form from the spurious signal test will not be biased. The resulting smoothed shape obtained from the GP fit is then saved as a new histogram. This smoothed histogram is passed as the

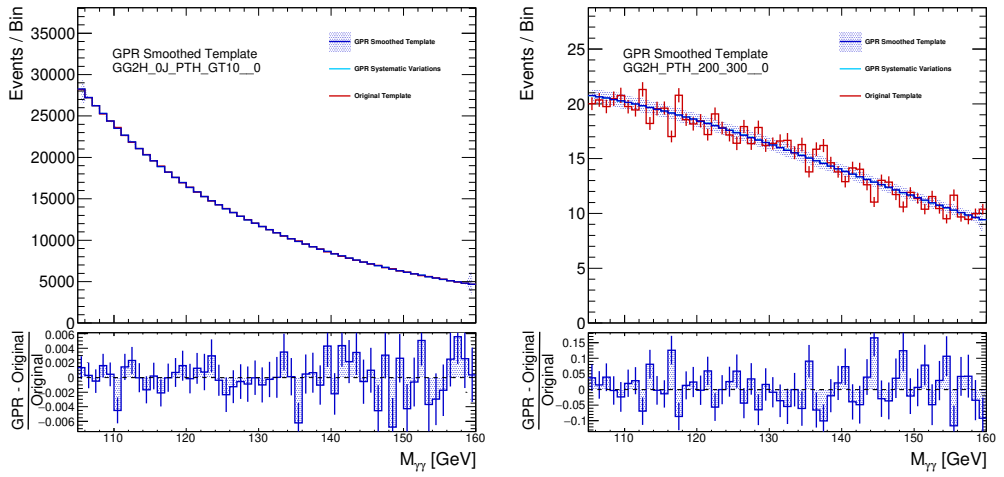

(a) GG2H_0J_PTH_GT10__0 **(b)** GG2H_PTH_200_300__0

Figure 5.16 – Examples of full Run 2 background templates for two of the analysis categories with high (a) and low (b) statistics. The red shape shows the original background template, the blue shape shows the smoothed background template. The bottom panel shows the fractional difference between the smoothed and un-smoothed templates.

background template to the spurious signal test, which then determines the background functional form and spurious signal systematic uncertainty.

Examples of the smoothed templates are presented in Figure 5.16 for a category with a high statistic category and a low statistic one. Extensive validation tests were performed with the GP smoothing technique in order to ensure that the smoothing itself does not introduce a substantial bias. These tests primarily use "toy" templates – randomly-generated background templates constructed from either simulated diphoton events or from the probability distribution function of a known analytic function. The generated toys were first smoothed out with the GPR technique and then fitted with the spurious signal procedure. The results were compared to the results of the spurious signal method on the un-smoothed toy version. These tests were repeated by varying the initial analytical function choice used to generate toys, by varying the statistic of the toys themselves and by varying the slope of the falling background function (in order to model different $p_{\mathrm{T}}^{\gamma\gamma}$ regimes). It was found that that GPR remains effectively unbiased for smoothly-falling templates containing more than an average of 20 effective MC entries per bin [147] and an example of one of these tests can be found in Figure 5.17. In addition, tests were performed with the GP smoothing technique on toys with a signal-like feature injected on top of the background, in order to understand the tendency of the GP to the smooth out real features in the data. The tests followed the logic described above, namely by comparing the biases of the smoothed and unsmoothed version of the toy. It has been found that the bias depends on the yield and the width of the injected feature. The bias can be as large as 50% in the cases where the injected feature is narrow as a SM-like signal and with a decent ($> 10\%$) yield with respect to the background

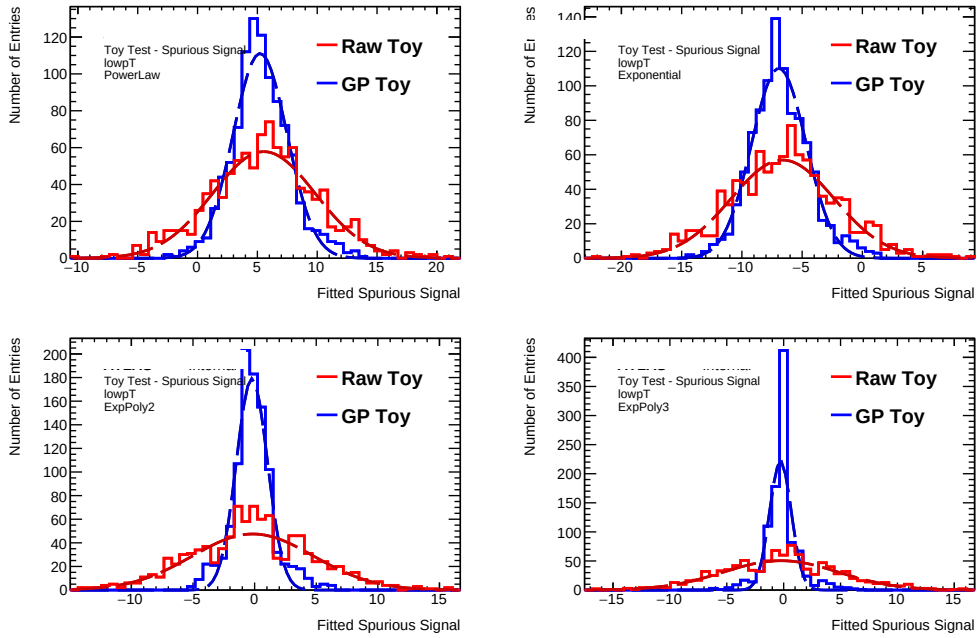

Figure 5.17 – The distributions of spurious signal on the toys for smoothed ("GP toy") and unsmoothed ("Raw toy") templates. Toys are generated from a ExpPoly2 function in the low $p_{\mathrm{T}}^{\gamma\gamma}$ regime and are composed by 10^5 events. These toys are then fitted with a PowerLaw (upper left), Exponential (upper right), ExpPoly2 (lower left) and ExpPoly3 (lower right) function for the spurious signal test, and the obtained *max S* is plotted. The bias can be quantified as the different between the median of the GP and Raw toy distribution, which is 0 in the case the same function is used to generate and fit the toy (lower left plot) while different from 0 but consisted between GP and Raw in the other cases. The GP smoothed toys always have a more peaked SS distribution as expected.

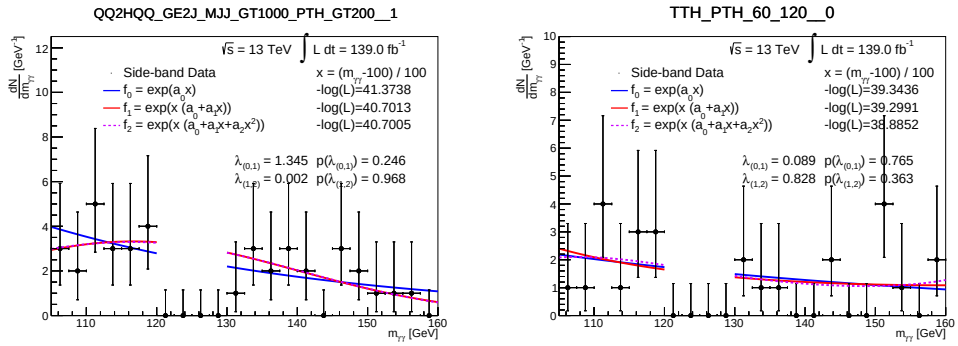

Figure 5.18 – Likelihood ratio test on the low-statistic categories, where all the three exponential functions have been fitted on data sideband and the values of the test statistics are reported.

one; in case where the injected feature has a larger width ($> 3 \times \text{SM} \sim 5\,\text{GeV}$) or a smaller yield with respect to background, the GP process is able to correctly model it and the bias is not significant if compared to the statistical uncertainty extracted from unsmoothed toys.

In case of low statistic categories which are suffering of large statistical fluctuations in the template and where the GP process regression cannot be applied (< 20 effective MC entries per bin), the direct use of spurious signal procedure would potentially lead to select a function with large number of degrees of freedom to accommodate these fluctuations. Therefore, a likelihood ratio test on the data sidebands has been performed in order to initially select the statistically-justified function using a family of exponentials of increasing complexity: a modelling function f_i with a lower number of degrees of freedom is accepted if the addition of one degree of freedom does not lead to a significant improvement in the fit quality of $m_{\gamma\gamma}$ in the data sidebands. To this purpose, the likelihood ratio between the fits to the sideband data with two different background models is computed as

$$\lambda_{(n,n+1)} = -2 \ln \frac{L_{n+1}}{L_n} \tag{5.4}$$

where L_{n+1} and L_n are the likelihood values of higher and lower degrees of freedom fits respectively. We reject the simpler (less parameters) background model by checking if the p-value of the test statistic computed on data-sideband is larger than 5%. A χ^2 with one degree of freedom is used as test statistic distribution. All the categories where this test has been performed selected the exponential function, so the spurious signal test is performed with this function tolerating a bias that could be larger than the criteria used for the high-statistic categories. An example of the likelihood ration test on two categories is reported in Figure 5.18.

The final analytical background function chosen and the relative associated systematic for each reconstructed category is shown in Table 5.9.

Category	LR test	max S	Func	$\frac{S}{\delta S}$ (%)	$\frac{S}{S_{ref}}$ (%)
GG2H_0J_PTH_0_10__0		64.8	Exp2	32.1	7.58
GG2H_0J_PTH_GT10__0		50.5	Exp2	19.9	2.96
GG2H_1J_PTH_0_60__0		20.7	Exp2	26.5	9.26
GG2H_1J_PTH_0_60__1		24.9	Exp2	18.8	6.37
GG2H_1J_PTH_60_120__0		23.7	Exp2	35.1	9.76
GG2H_1J_PTH_60_120__1		21.3	Exp	21.5	6.71
GG2H_1J_PTH_120_200__0		1.48	Exp2	9.83	4.80
GG2H_1J_PTH_120_200__1		5.33	Exp2	17.3	7.71
GG2H_GE2J_MJJ_0_350_PTH_0_60__0		1.51	Exp2	3.92	3.71
GG2H_GE2J_MJJ_0_350_PTH_0_60__1		13.6	Exp2	17.0	12.8
GG2H_GE2J_MJJ_0_350_PTH_0_60__2		15.7	Exp2	10.3	3.58
GG2H_GE2J_MJJ_0_350_PTH_60_120__0		2.26	Exp2	6.38	3.04
GG2H_GE2J_MJJ_0_350_PTH_60_120__1		6.21	Exp2	6.51	2.58
GG2H_GE2J_MJJ_0_350_PTH_120_200__0		0.003 63	Exp2	0.0358	0.0182
GG2H_GE2J_MJJ_0_350_PTH_120_200__1		0.983	Pow	4.85	2.64
GG2H_GE2J_MJJ_350_700_PTH_0_200__0		0.487	Exp	6.85	6.71
GG2H_GE2J_MJJ_350_700_PTH_0_200__1		1.33	Exp2	5.90	3.96
GG2H_GE2J_MJJ_350_700_PTH_0_200__2		5.78	Exp	16.7	20.2
GG2H_GE2J_MJJ_700_1000_PTH_0_200__0		0.560	Exp	9.02	9.71
GG2H_GE2J_MJJ_700_1000_PTH_0_200__1		1.44	Exp	11.5	8.05
GG2H_GE2J_MJJ_700_1000_PTH_0_200__2		4.32	Exp	19.9	17.3
GG2H_GE2J_MJJ_GT1000_PTH_0_200__0		0.192	Exp	4.96	7.66
GG2H_GE2J_MJJ_GT1000_PTH_0_200__1		0.804	Exp	11.3	8.15
GG2H_GE2J_MJJ_GT1000_PTH_0_200__2		1.09	Pow	8.41	8.04
GG2H_PTH_200_300__0		1.68	Exp	25.8	8.68
GG2H_PTH_200_300__1		0.714	Exp	4.31	1.56
GG2H_PTH_300_450__0	✓	0.407	Exp	29.0	21.2
GG2H_PTH_300_450__1		0.259	Exp	6.24	2.72
GG2H_PTH_300_450__2		0.121	Exp	1.81	1.25
GG2H_PTH_450_650__0	✓	0.138	Exp	13.3	9.21
GG2H_PTH_450_650__1	✓	0.391	Exp	28.3	25.4
GG2H_PTH_450_650__2		0.0313	Exp	0.990	0.932
GG2H_PTH_GT650__0	✓	0.448	Exp	46.0	84.9
QQ2HQQ_0J__0		0.180	Exp	3.53	7.71
QQ2HQQ_0J__1		4.73	Exp2	18.1	18.4
QQ2HQQ_0J__2		49.7	Exp2	29.4	7.62
QQ2HQQ_1J__0	✓	0.125	Exp	7.75	7.65
QQ2HQQ_1J__1		0.361	Exp	6.75	5.07
QQ2HQQ_1J__2		1.97	Pow	16.5	19.7
QQ2HQQ_GE2J_MJJ_0_60__0	✓	0.499	Exp	34.6	59.0
QQ2HQQ_GE2J_MJJ_0_60__1		0.489	Exp	11.0	14.1
QQ2HQQ_GE2J_MJJ_0_60__2		1.29	Pow	8.00	5.62
QQ2HQQ_GE2J_MJJ_60_120__0	✓	0.165	Exp	6.59	3.05
QQ2HQQ_GE2J_MJJ_60_120__1		0.520	Exp	8.06	5.02
QQ2HQQ_GE2J_MJJ_60_120__2		1.15	Pow	11.6	11.9
QQ2HQQ_GE2J_MJJ_120_350__0		1.08	Exp	19.9	19.0
QQ2HQQ_GE2J_MJJ_120_350__1		1.07	Exp2	6.41	4.35
QQ2HQQ_GE2J_MJJ_120_350__2		6.34	Pow	15.9	9.68
QQ2HQQ_GE2J_MJJ_350_700_PTH_0_200__0	✓	0.162	Exp	8.82	5.10
QQ2HQQ_GE2J_MJJ_350_700_PTH_0_200__1		0.443	Exp	7.28	3.28
QQ2HQQ_GE2J_MJJ_350_700_PTH_0_200__2		1.17	Exp	11.0	9.57
QQ2HQQ_GE2J_MJJ_350_700_PTH_GT200__0	✓	0.189	Exp	13.2	8.51
QQ2HQQ_GE2J_MJJ_350_700_PTH_GT200__1	✓	0.513	Exp	17.1	12.6

Table 5.9 – The final background modelling decision and the size of spurious signal uncertainties (max S). The δS is the uncertainty on spurious signal found in an Asimov study on background template with signal plus background fit, and S_{ref} is the expected number of Higgs signal events for this category. LR test indicates if the likelihood ratio test has been performed.

Category	LR test	max S	Func	$\frac{S}{\delta S}$ (%)	$\frac{S}{S_{ref}}$ (%)
QQ2HQQ_GE2J_MJJ_350_700_PTH_GT200__2		0.721	Exp	8.90	9.33
QQ2HQQ_GE2J_MJJ_700_1000_PTH_0_200__0	✓	0.670	Exp	36.8	17.7
QQ2HQQ_GE2J_MJJ_700_1000_PTH_0_200__1		0.713	Exp	14.1	6.41
QQ2HQQ_GE2J_MJJ_700_1000_PTH_GT200__0	✓	0.110	Exp	7.68	2.53
QQ2HQQ_GE2J_MJJ_700_1000_PTH_GT200__1		0.193	Exp	2.92	2.01
QQ2HQQ_GE2J_MJJ_GT1000_PTH_0_200__0	✓	1.47	Exp	57.7	11.9
QQ2HQQ_GE2J_MJJ_GT1000_PTH_0_200__1		0.270	Exp	5.99	1.91
QQ2HQQ_GE2J_MJJ_GT1000_PTH_GT200__0	✓	1.30	Exp	1.53	6.09
QQ2HQQ_GE2J_MJJ_GT1000_PTH_GT200__1	✓	0.329	Exp	13.3	7.01
QQ2HLNU_PTV_0_75__0		0.277	Exp	11.6	12.7
QQ2HLNU_PTV_0_75__1		0.609	Exp	12.1	17.4
QQ2HLNU_PTV_75_150__0		0.0686	Exp	4.65	2.13
QQ2HLNU_PTV_75_150__1		0.255	Exp	6.61	7.38
QQ2HLNU_PTV_150_250__0	✓	0.128	Exp	9.06	5.54
QQ2HLNU_PTV_150_250__1		0.150	Exp	9.02	33.7
QQ2HLNU_PTV_GT250__0	✓	0.237	Exp	22.3	10.8
QQ2HLNU_PTV_GT250__1	✓	0.0539	Exp	3.03	35.7
QQ2HLL_PTV_0_75__0		0.0268	Exp	1.66	2.04
QQ2HLL_PTV_0_75__1		2.28	Pow	14.1	21.7
QQ2HLL_PTV_75_150__0		0.0145	Exp	1.08	1.16
QQ2HLL_PTV_75_150__1		0.0157	Exp	1.11	20.6
QQ2HLL_PTV_150_250__0	✓	0.0592	Exp	4.71	4.43
QQ2HLL_PTV_150_250__1		0.194	Exp	4.57	7.78
QQ2HLL_PTV_GT250__0	✓	0.311	Exp	27.2	39.2
QQ2HNUNU_PTV_0_75__0	✓	12.3	Exp	86.8	122
QQ2HNUNU_PTV_0_75__1		4.13	Exp	12.4	8.78
QQ2HNUNU_PTV_0_75__2		9.95	Exp3	16.0	9.95
QQ2HNUNU_PTV_75_150__0	✓	0.407	Exp	27.1	39.4
QQ2HNUNU_PTV_75_150__1	✓	1.30	Exp	29.2	27.7
QQ2HNUNU_PTV_75_150__2		1.96	Exp	10.9	10.2
QQ2HNUNU_PTV_150_250__0	✓	0.121	Exp	8.80	8.71
QQ2HNUNU_PTV_150_250__1	✓	0.184	Exp	13.2	11.7
QQ2HNUNU_PTV_150_250__2	✓	0.644	Exp	18.8	59.4
QQ2HNUNU_PTV_GT250__0	✓	0.237	Exp	19.1	21.2
QQ2HNUNU_PTV_GT250__1	✓	0.201	Exp	13.6	95.0
TTH_PTH_0_60__0		0.0403	Exp	1.73	1.15
TTH_PTH_0_60__1		0.192	Exp	4.79	5.68
TTH_PTH_60_120__0		0.0378	Exp	1.65	0.768
TTH_PTH_60_120__1		0.274	Exp	8.22	7.64
TTH_PTH_120_200__0		0.0182	Exp	0.817	0.340
TTH_PTH_120_200__1		0.0565	Exp	2.66	2.78
TTH_PTH_200_300__0		0.0261	Exp	1.71	0.641
TTH_PTH_GT300__0	✓	0.180	Exp	13.7	5.03
THJB_SM__0	✓	0.371	Exp	24.5	44.8
THJB_SM__1	✓	0.320	Exp	18.6	96.2
THJB_BSM__0	✓	0.496	Exp	32.7	135
THW__0		0.0702	Exp	3.32	1.82
BKG_LIKE_TOP		0.870	Exp	9.72	13.3

Table 5.9 – The final background modelling decision and the size of spurious signal uncertainties (max S). The δS is the uncertainty on spurious signal found in an Asimov study on background template with signal plus background fit, and S_{ref} is the expected number of Higgs signal events for this category. LR test indicates if the likelihood ratio test has been performed.

5.6 Systematic uncertainties

With respect to what has already been discussed in Section 4.7, the coupling analysis has to face additional issues due to the use of the STXS framework on the theoretical side and the use of additional reconstructed objects on the experimental side. These further peculiarities are described in this section.

5.6.1 Theoretical uncertainties

Among the theoretical uncertainties described in the Section 4.7.1, the ones on parton shower have a large impact on the coupling analysis. As can be observed in Figure 5.19, the differences in expected number of events between the nominal samples showered with PYTHIA 8 and the ones showered with Herwig++ for ggF and VBF production processes can be as large as 30% for the principal STXS truth bin targeted by a reconstructed category. This is a long-standing issue, in particular for VBF PS uncertainties. The impact of other PS uncertainty sources is given in Appendix A.3.

Moreover, in the coupling analysis, additional theory uncertainties due to the imperfect knowledge of heavy quarks modelling and due to the use of STXS formalism has to be included. Concerning the first contribution, ggF, VBF and VH production processes can produce heavy quarks in the final state either directly or through gluon splitting in the hadronic shower, but these contributions are not measured nor theoretically well constrained [149]; therefore, in $t\bar{t}H$ categories, where these contributions can play a non-negligible role, a 100% flat uncertainty is assigned to the expected number of events coming from ggF, VBF and VH production modes. The final impact of this large uncertainty is usually small since the $t\bar{t}H$ categories are predominantly composed ($> 90\%$ fraction) by $t\bar{t}H$ signal (see Figure 5.14).

Concerning instead the use of the STXS formalism, additional theory uncertainties due to missing higher order in QCD prediction have to be taken into account when splitting in additional kinematic bins. For example, consider a single bin boundary $x|y$ that splits the cross section $\sigma_{xy} = \sigma_x + \sigma_y$ into two bins with cross sections σ_x and σ_y. In general, the binning threshold has a nontrivial influence on the perturbative structure of σ_x and σ_y, as it can introduce sensitivity to an additional energy scale or separate different jet multiplicities. This implies that the binning threshold corresponds to an additional and a priori non-negligible source of uncertainty that is not present in σ_{xy}. To deal with these additional theory uncertainty sources, the theoretical community has developed the Stewart-Tackmann (ST) method [149, 150] summarized in Table 5.10 for a more complex three bins scenario: the systematic source can be split in a fully correlated contribution which can be interpreted as an overall yield uncertainty of a common source for all bins and a further anticorrelated components for each threshold interpreted as a migration uncertainty between the bins, which must drop out in their sum. The theory community has come up with prescriptions using the ST method for ggF [151, 152], VBF [153], VH [154] and $t\bar{t}H$ [153] processes:

- for ggF Stage 1.2 truth bins (Figure 5.3a) 18 different uncertainty sources are defined: two overall sources cover for fixed-order and resummation effects on the

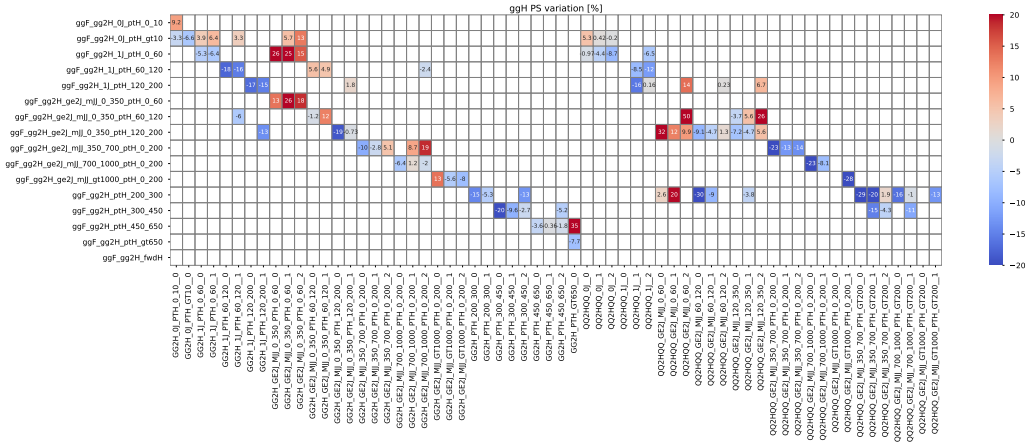

(a) Impact of the ggF PS uncertainty in the ggF STXS bins.

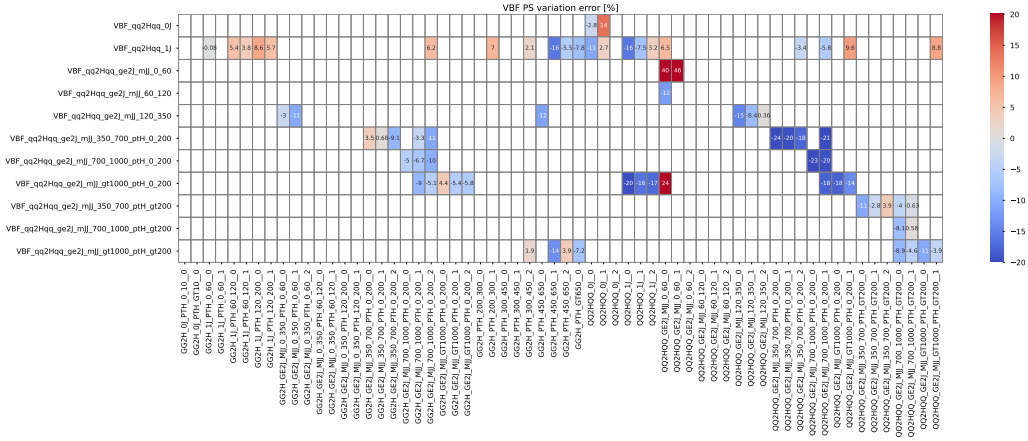

(b) Impact of the VBF PS uncertainty in the VBF STXS bins.

Figure 5.19 – Effect of the ggF (a) and VBF (b) PS uncertainties on the signal yields of both ggF and VBF categories. Each row in the plot is a ggF (a) or VBF (b) STXS truth bin, while each column represents one analysis category. Only the impacts for the STXS truth bins with more than 5% of the total expected yield in a given reconstructed categories are shown. Impacts are computed with Eq. (4.6).

	Kinematic observable x		
Nuisance parameter	$0 \leq x \leq a$	$a < x \leq b$	$x > b$
θ^{y}	δ_y	δ_y	δ_y
θ_a^{mig}	$\rho\delta_a^-$	$\rho\delta_a^+$	$\rho\delta_a^+$
θ_b^{mig}		$\rho\delta_b^-$	$\rho\delta_b^+$

Table 5.10 – Summary table illustrating yield (y) and migration (mig) uncertainties as obtained by the long-range Stewart-Tackmann (ST) method. The δ_y term is the relative uncertainty on the total cross-section, while δ_k^+ is the relative uncertainty on the cross-section in the bin $x \leq k$. δ_k^- is an oppositely-signed relative uncertainty with a value chosen such that it cancels with δ_k^+ when bins are merged. The factor ρ accounts for double-counting of migration uncertainties that cover overlapping regions, by default $\rho = 0.5$ [155].

total ggF cross section, two sources for $0 \leftrightarrow 1$ and $1 \leftrightarrow 2$ jets migrations, three sources for low $p_{\mathrm{T}}^{\mathrm{H}}$ migrations (10, 60, 120 GeV boundaries), the 2 jets phase space is covered with four nuisance parameters for m_{jj} migrations and 1 for $p_{\mathrm{T}}^{\mathrm{H}jj}$, while the BSM ($p_{\mathrm{T}}^{\mathrm{H}} \geq 200\,\mathrm{GeV}$) phase space is covered with two overall uncertainties (for global cross section variation and top quark mass effects) plus 3 sources for $p_{\mathrm{T}}^{\mathrm{H}}$ migrations and one for $p_{\mathrm{T}}^{\mathrm{H}j} / p_{\mathrm{T}}^{\mathrm{H}}$ variations;

- for VBF Stage 1.2 truth bins (Figure 5.3b) 10 different uncertainties sources are accounted: one overall uncertainty on VBF cross section, one for jet migration as in ggF, one for $p_{\mathrm{T}}^{\mathrm{H}}$ migration around 200 GeV, one for $p_{\mathrm{T}}^{\mathrm{H}jj}$ migrations plus 6 more m_{jj} uncertainty sources;
- for VH Stage 1.2 truth bins (Figure 5.3c) 7 different uncertainties sources for each process (WH, ZH, ggZH) are accounted for: one overall uncertainty on VH cross section, two uncertainties for $0 \leftrightarrow 1$ and $1 \leftrightarrow 2$ jets migrations and four more uncertainties for the p_{T}^{V} bin boundaries;
- for $\mathrm{t\bar{t}H}$ Stage 1.2 truth bins (Figure 5.3d) 6 different uncertainties sources are accounted for: one overall uncertainty on $\mathrm{t\bar{t}H}$ cross section plus 5 migration uncertainties around the $p_{\mathrm{T}}^{\mathrm{H}}$ bin boundaries.

An example of impact on the category yields for the overall yield uncertainty and the $0 \leftrightarrow 1$ jet migration uncertainty in the ggF STXS bins on the ggF reconstructed categories is reported in Figure 5.20. The impact of other QCD scale uncertainty sources is given in Appendix A.3.

Uncertainties parametrization

Theoretical uncertainties have an impact on the underlying truth event distribution used to model the Higgs signal and as a consequence on the expected reconstructed number of the events in a given category. The truth- and reco-level effects can be disentangled and their inclusion in the model is slightly different in case the measurement of truth bin

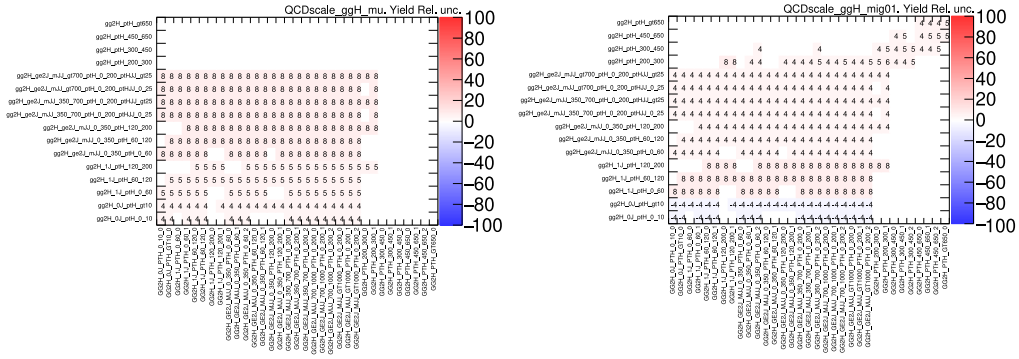

(a) (b)

Figure 5.20 – Impact on the yield for a given ggF reconstructed category (x-axis) and for each ggF STXS truth bins (y-axis) for the overall ggF uncertainty called QCDscale_ggH_mu (a) and for the $0 \leftrightarrow 1$ jet migration uncertainty called QCDscale_ggH_mig01 (b). No impact is reported in the variations for which the nominal or varied yield is 0 or below 0.1 expected events.

cross section or truth bin signal strength is carried out. Indeed for technical convenience, the modifier μ_p on the expected number of events in Eq. (4.11) is always included, but it does have different interpretations: when signal strengths are being fitted, μ_p is the signal strength as defined in Eq. (1.37), while in a cross section measurement μ_p represents the fitted cross-section value in the unit of corresponding SM prediction that needs to be multiplied to the SM prediction. These by consequence translate in a different treatment of systematic uncertainties.

In general, the category selection efficiency can be evaluated as

$$\epsilon_{ct} = \frac{N_{ct}}{N_t} \tag{5.5}$$

with N_{ct} being the expected number of events in the category c for the truth bin t and N_t the total expected number of events for a given truth bin t. In case of theory uncertainty both N_{ct} and N_t are affected by the systematic source. The impact of a systematic source θ on each component are called δ_{ct} and δ_t respectively and, to keep it simple, they can be implemented with a $(1 + \delta\theta)$ response function. Different parametrizations then apply:

- in the signal strength measurement, $\mu = \sigma^{\gamma\gamma}/\sigma^{\gamma\gamma}_{SM}$, the SM is assumed to be known with some degree of uncertainty, so that uncertainty is included in the likelihood and the results are compared with the SM prediction $\mu = 1$ without uncertainty. Therefore the uncertainties on the expected number of events in Eq. (4.11) are parameterized as

$$\sigma_t^{\gamma\gamma}\,(1+\delta_t\theta)\cdot\epsilon_{ct}\cdot(1+\delta_\epsilon\theta) = \sigma_t^{\gamma\gamma}\,(1+\delta_t\theta)\cdot\epsilon_{ct}\cdot\frac{1+\delta_{ct}\theta}{1+\delta_t\theta} = \sigma_t^{\gamma\gamma}\cdot\epsilon_{ct}\cdot(1+\delta_{ct}\theta) \tag{5.6}$$

- in the cross section measurement instead, the SM cross section prediction with its

own uncertainty, which is not included in the likelihood, is compared with the fit results, therefore the parameterization is

$$\sigma_t^{\gamma\gamma} \cdot \epsilon_{ct} \cdot \left(1 + \delta^{\epsilon}\theta\right) = \sigma_t^{\gamma\gamma} \cdot \epsilon_{ct} \cdot \frac{1 + \delta_{ct}\theta}{1 + \delta_t\theta} \sim \sigma_t^{\gamma\gamma} \cdot \epsilon_{ct} \cdot \left[1 + \left(\delta_{ct} - \delta_t\right)\theta\right] \tag{5.7}$$

where in the last step the denominator has been expanded into Taylor series and second order contributions are removed. This parametrization is used when measuring directly the Simplified Template Cross Sections.

Therefore in the cross section measurement, the truth variation δ_t is factored out, while in the signal strength measurement the full variation on the expected yield is taken into account, similarly to what happens for experimental uncertainties (see Eq. (4.6)). Concerning the branching ratio uncertainty, this is completely removed in case of cross section measurements.

In case in the measurement some of the STXS truth bins of the full scheme are merged together, additional theory uncertainties are injected in the likelihood in order to cover for the assumption that truth bins are merged according to their SM cross sections. These additional theory systematics are computed as the weighted average of the truth impact δ_t with the cross sections of the truth bin to be merged.

$$\Delta\delta_t^j = \delta_t^j - \frac{\sum_i \sigma_i \delta_t^i}{\sum_i \sigma_i} \tag{5.8}$$

where $\Delta\delta_t^j$ is the injected theory systematic for the truth bin j, while i runs over the truth bins to be merged with σ_i being their expected SM cross sections. A $\Delta\delta_t$ contribution should be included for all the nuisance parameter affecting at least one of the merged truth bins.

5.6.2 Experimental uncertainties

With respect to what has been discussed in Section 4.7.2, additional experimental uncertainties are included in the coupling analysis. Given the fact that the categorization makes use of reconstructed electrons, muons, jets with b-jet information and $E_{\mathrm{T}}^{\mathrm{miss}}$, all the experimental uncertainties associated to these objects have been included in the likelihood model, amounting to about 80 more uncorrelated nuisance parameters. Examples of the systematic uncertainty impacts described below are reported in Appendix A.3.

Uncertainty sources due to electron and muon reconstruction, identification and isolation are usually pretty small and do not have an impact on the results. A similar situation happens for $E_{\mathrm{T}}^{\mathrm{miss}}$ soft-track term scale and resolution.

Since jets uncertainties are usually large and selections on jets are employed throughout the full analysis chain, jet uncertainties have usually larger impact on the measurements. These can be sub-divided in jet energy scale and energy resolution uncertainties, pileup subtraction uncertainties, flavour uncertainties and JVT and fJVT uncertainties, so large part of the additional NPs included in the coupling measurement comes from jet reconstruction. Among these the uncertainties with the largest variations in signal yields

are the jet flavour modelling and jet energy resolution, which can both have impacts as large as 5%.

Since in the likelihood model, the Higgs mass is kept fixed to the ATLAS and CMS Run 1 combination measurement of $m_H = 125.09\,\text{GeV}$, an additional nuisance parameter with a 0.2% impact is included in the response function applied to the mean μ_{CB} of the DSCB function, alongside all the other photon energy scale contributions.

5.6.3 Summary of systematic uncertainties

More than 300 nuisance parameters is included in likelihood model used to fit the data of Eq. (4.9). The summary of all uncertainties sources and of the actual implementation in the likelihood is given in Table 5.11. Pruning strategies have been employed in order to lower the complexity of the model reducing the number of response functions included, while preserving the accuracy of the results: in particular, the response functions are removed for all that STXS truth bins that compose a maximum of 5% of the number of expected events in a given category, starting from the ones with the lowest yield. For the remaining STXS processes in a given category, the response function is not included if the impact of a given experimental or systematic uncertainty is below the 0.03% threshold.

5.7 Results

Results are presented in terms of several descriptions of Higgs boson production. Different results on the cross section times branching ratio ($\sigma^{\gamma\gamma}$) are reported, each with a different merging scheme for the parameters of interest used in the fit. The following merging scheme are reported below:

- inclusive, single POI to measure the overall rate of Higgs boson production in the $H \to \gamma\gamma$ channel.
- Run 1 like six production modes: ggF, VBF, WH, ZH, $t\bar{t}H$, tH.
- STXS Stage 1.2 measurement (28 POIs): this scheme provides a strong merging with respect to what the categorization can target on the full STXS 1.2 scheme, in order to have expected uncertainties below 100%.
- STXS Stage 1.2 measurement (33 POIs): this scheme provides a minimal merging on the full STXS 1.2 scheme, it is the bases for later EFT interpretations and it defines suitable correlations among POIs.

The extended likelihood model of Eq. (4.9) is fitted with a maximum likelihood estimation over a binned dataset with 220 bins (250 MeV/bin). The bin size is optimized in order to have manageable fitting times with a reduced bias (max 0.2% bias on the central values of the POI extracted from the STXS fit on the Asimov dataset).

Expected results are extracted from a "postfit" Asimov dataset [135] where the values of the global observables in the model has been set to the value of the corresponding nuisance parameters after to the fit to the observed data with the most granular POIs scheme.

		Systematic source	NP	Implementation
Yield	Theo	Branching ratio	1	$N_{\text{tot}}\, F_{\text{LN}}(\delta_i, \theta_i)$
		Heavy Flavor Content	3	$N_{\text{t}}\, F_{\text{LN}}(\delta_i, \theta_i)$
	Exp	Luminosity	1	$N_{\text{tot}}\, F_{\text{LN}}(\delta_i, \theta_i)$
Migrations	Theo	ggF QCD scale	18	$N_{\text{ggF}}\, F_{\text{LN}}(\delta_i, \theta_i)$
		VBF QCD scale	10	$N_{\text{VBF}}\, F_{\text{LN}}(\delta_i, \theta_i)$
		VH QCD scale	21	$N_{\text{VH}}\, F_{\text{LN}}(\delta_i, \theta_i)$
		$t\bar{t}H$ QCD scale	6	$N_{t\bar{t}\text{H}}\, F_{\text{LN}}(\delta_i, \theta_i)$
		Parton shower	8	$N_{\text{t}}\, F_{\text{LN}}(\delta_i, \theta_i)$
		PDF	30	$N_{\text{t}}\, F_{\text{LN}}(\delta_i, \theta_i)$
		α_{S}	1	$N_{\text{t}}\, F_{\text{AS}}(\delta_i, \theta_i)$
	Exp	Photon Trigger	1	$N_{\text{t}}\, F_{\text{LN}}(\delta_i, \theta_i)$
		Photon Isolation	1	$N_{\text{t}}\, F_{\text{AS}}(\delta_i, \theta_i)$
		Photon Identification	1	$N_{\text{t}}\, F_{\text{AS}}(\delta_i, \theta_i)$
		Photon Scale	1	$N_{\text{t}}\, F_{\text{AS}}(\delta_i, \theta_i)$
		Photon Resolution	1	$N_{\text{t}}\, F_{\text{AS}}(\delta_i, \theta_i)$
		Flavor Tagging	12	$N_{\text{t}}\, F_{\text{AS}}(\delta_i, \theta_i)$
		Jet	44	$N_{\text{t}}\, F_{\text{AS}}(\delta_i, \theta_i)$
		Electron	3	$N_{\text{t}}\, F_{\text{AS}}(\delta_i, \theta_i)$
		Muon	11	$N_{\text{t}}\, F_{\text{AS}}(\delta_i, \theta_i)$
		MET	3	$N_{\text{t}}\, F_{\text{AS}}(\delta_i, \theta_i)$
		Pileup	1	$N_{\text{t}}\, F_{\text{AS}}(\delta_i, \theta_i)$
Shape		ATLAS-CMS m_H	1	$\mu_{\text{CB}}\, F_{\text{G}}(\delta_i, \theta_i)$
		Photon Scale	40	$\mu_{\text{CB}}\, F_{\text{G}}(\delta_i, \theta_i)$
		Photon Resolution	9	$\sigma_{\text{CB}}\, F_{\text{AS}}(\delta_i, \theta_i)$
Bkg		Spurious signal	101	$N_{\text{sp},c}\, \theta_{\text{sp},c}$

Table 5.11 – Summary of sources of systematic uncertainty sources included in the likelihood model along with their implementation in the likelihood function, impacting on signal yields, mass scale/resolution and the spurious signals resulting from the background parametrization. When acting on N_{tot} the uncertainty value is the same for all truth bins, whereas the uncertainty has a different value for each signal on the case denoted by N_{t}. The various response functions F are defined in Eq. (4.13), while spurious signal is implemented as in Eq. (4.10).

5.7.1 Inclusive measurement

The expected inclusive cross section from postfit Asimov dataset is measured to be

$$\sigma^{\gamma\gamma}/\sigma^{\gamma\gamma}_{\text{SM}} = 1.0\,^{+0.08}_{-0.08} = 1.0\,^{+0.060}_{-0.060}\,(\text{stat})\,^{+0.056}_{-0.051}\,(\text{syst})$$

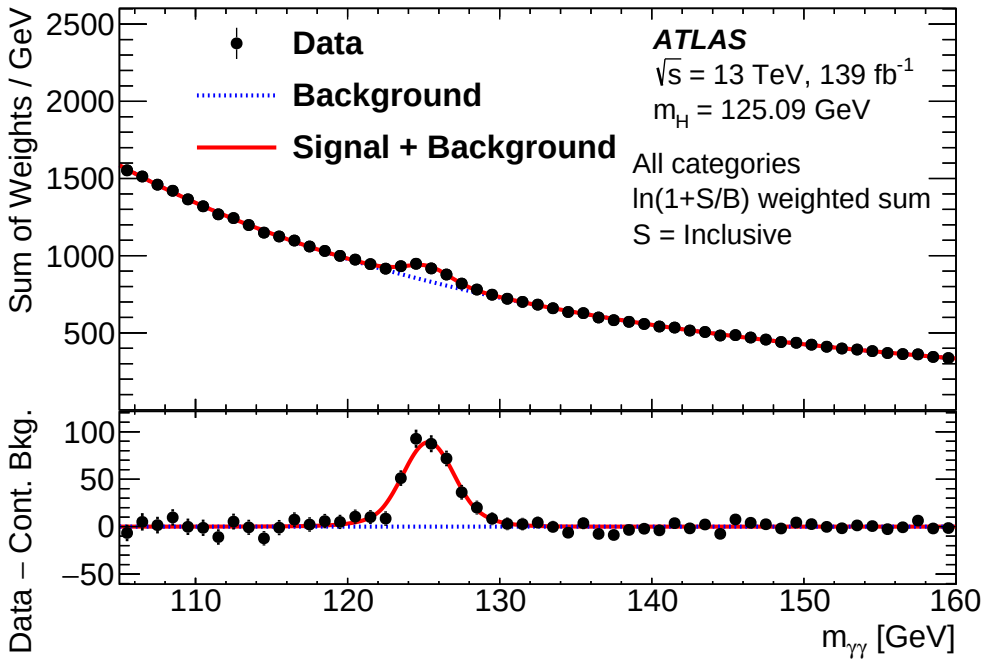

Figure 5.21 – The inclusive diphoton invariant mass distribution of events from all analysis categories [6]. The data events (dots) in each category are weighted by $\ln(1+S/B)$, where S and B are the expected signal and background yields in the category within the smallest $m_{\gamma\gamma}$ window containing 90% of the signal events. The fitted signal plus background PDFs from all categories are also weighted and summed, shown as the solid line. The blue dotted line represents the weighted sum of the fitted background functions from all categories.

while the observed results is

$$\sigma^{\gamma\gamma}/\sigma^{\gamma\gamma}_{SM} = 1.04\ ^{+0.084}_{-0.080} = 1.04\ ^{+0.060}_{-0.059}\ (\text{stat})\ ^{+0.059}_{-0.054}\ (\text{syst})$$

Therefore the Higgs boson production cross section times $H \to \gamma\gamma$ branching fraction is measured to be

$$\sigma^{yy}_{\text{obs}} = 121\ ^{+10}_{-9}\ \text{fb} = 121\ \pm 7\ (\text{stat})\ ^{+7}_{-6}\ (\text{syst})\ \text{fb}$$

with a SM expectation of

$$\sigma^{yy}_{\text{exp}} = 116\ \pm 6\ \text{fb}.$$

Figure 5.21 shows the $m_{\gamma\gamma}$ distribution from the inclusive diphoton sample. The events in each category are weighted by $\ln(1+S/B)$, where S and B are the expected signal and background yields in this category within the smallest $m_{\gamma\gamma}$ window containing 90% of the signal events. This choice of event weight is designed to enhance the contribution of events from categories with higher signal-to-background ratio in a way that approximately matches the impact of these events in the categorized analysis of the data.

Uncertainty source	$\Delta\sigma$[%]					
	ggF + $b\bar{b}H$	VBF	WH	ZH	$t\bar{t}H$	tH
Underlying Event and Parton Shower	$\pm$2.9	$\pm$14	$\pm$3.6	$\pm$14	$\pm$3.7	$\pm$38
Modelling of Heavy Flavor not-$t\bar{t}H$ processes	-	-	-	-	-	$\pm$6
Higher-Order QCD Terms (QCD)	$\pm$1.8	$\pm$3.1	$\pm$4.6	$\pm$51	$\pm$2.3	$\pm$11
PDF and α_S	-	$\pm$1.7	$\pm$1.6	$\pm$7.1	-	$\pm$4.6
Matrix Element	-	$\pm$2.6	-	$\pm$3.7	$\pm$2.5	$\pm$1.6
Photon Energy Resolution (PER)	$\pm$2.9	$\pm$2.2	$\pm$2.3	$\pm$12	$\pm$3.9	$\pm$16
Photon Energy Scale (PES)	-	-	$\pm$2.0	$\pm$17	$\pm$1.1	$\pm$17
Jet/E_T^{miss}	$\pm$1.3	$\pm$5.4	-	$\pm$9.2	$\pm$3.4	$\pm$15
Photon Efficiency	$\pm$2.7	$\pm$2.6	$\pm$3.1	$\pm$11	$\pm$3.0	$\pm$8.9
Background Modeling	$\pm$1.8	$\pm$3.7	$\pm$3.0	$\pm$39	$\pm$2.7	$\pm$24
Flavor Tagging	-	-	-	$\pm$1.7	$\pm$1.6	$\pm$2.9
Leptons	-	-	-	$\pm$1.1	-	$\pm$1.4
Pileup	$\pm$1.6	$\pm$2.3	$\pm$1.9	$\pm$9.7	-	$\pm$3.7
Luminosity	$\pm$1.8	$\pm$1.9	$\pm$2.3	$\pm$4.1	$\pm$2.2	$\pm$4.1
Higgs Boson Mass	-	-	$\pm$1.1	$\pm$9.8	-	$\pm$11

Table 5.12 – The contribution of groups of systematic uncertainties to the total error on the observed cross section times branching ratio. This is shown as the uncertainty due to each group of systematic uncertainties ($\Delta\sigma$), as a fraction of the total observed cross section (σ). For each group of uncertainties symmetric errors are assigned, while "-" means that the impact is below 1%.

5.7.2 Run 1-like production mode measurement

The mechanism of Higgs boson production is probed by considering separately the ggF, VBF, WH, ZH, $t\bar{t}H$ and tH processes separately. The contribution of $b\bar{b}H$ is included into the ggF component. The Figure 5.22 shows the $m_{\gamma\gamma}$ distributions for these production cross section measurements, merging the various categories targeting each production mode. Expected and observed results are reported in Figure 5.23 while the breakdown of the systematic uncertainties is given in Table 5.12.

5.7.3 STXS measurements for strong merging scheme

A measurement of the cross-sections based on the STXS framework is performed. In order to keep uncertainties below 100% for most of the regions, some of the regions are merged with the strong merging scheme presented in Figure 5.24a, which is defined on the expected results, independently of the observed data. The tH and ggF with $p_{\text{T}}^{\text{H}} > 450\,\text{GeV}$ STXS regions have an expected uncertainty which is larger than 100% but are left un-merged for their physical interest. The best fit results and correlation matrices for observed results are shown in Figure 5.25 and Figure 5.26 respectively. The systematic component of uncertainties is everywhere smaller than the statistical one, but reaches similar values for the 0-jet regions of ggF. No significant deviations from the SM expectation are observed and the compatibility between the measurements and the SM predictions corresponds to a p-value of 60%. An upper limit on the rate of the tH production can be obtained by treating the normalization of other Higgs boson production processes as nuisance parameters. Using the CLs method [156], this excludes a tH pro-

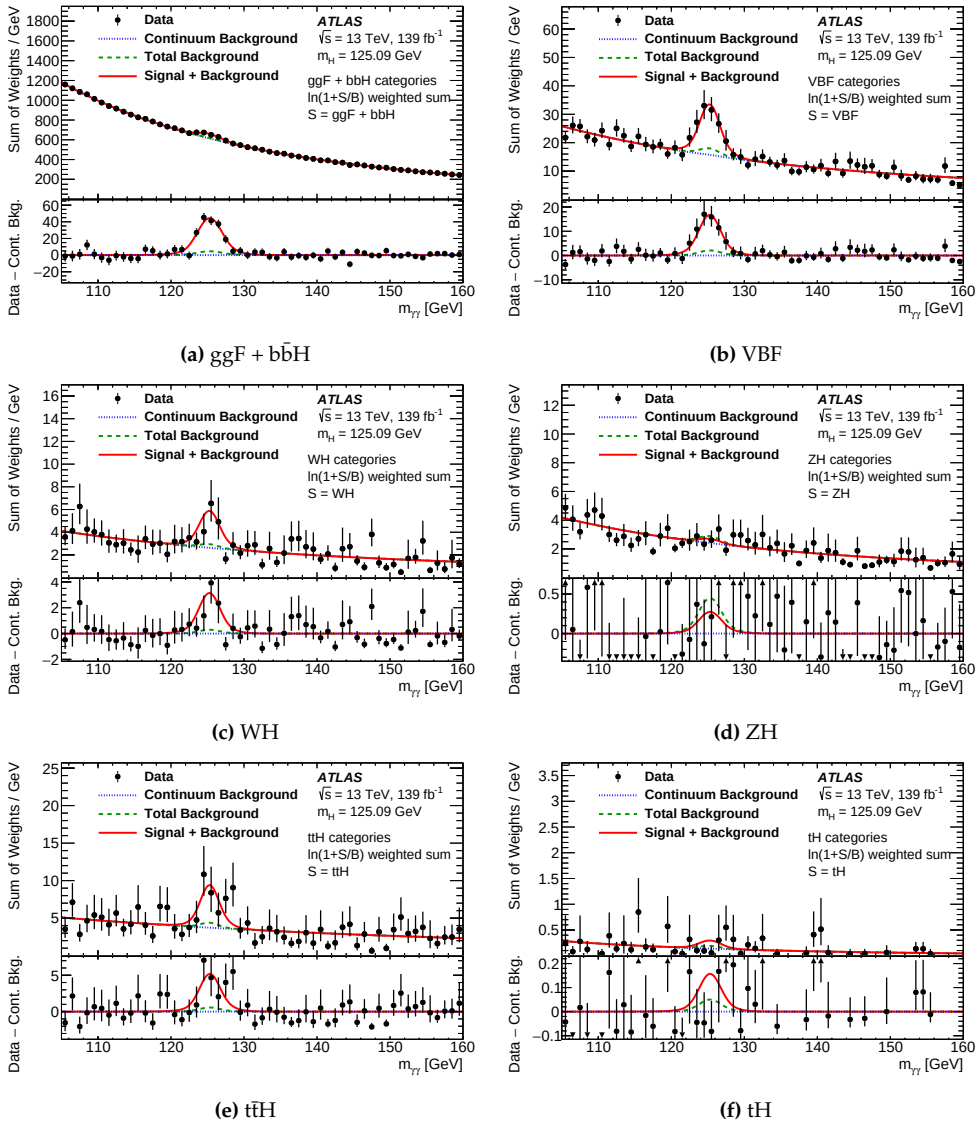

(a) ggF + $b\bar{b}H$ **(b)** VBF

(c) WH **(d)** ZH

(e) $t\bar{t}H$ **(f)** tH

Figure 5.22 – Combined diphoton invariant mass distributions for categories targeting the same production process [6]. In this calculation, only Higgs boson events from the targeted production processes are considered as signal events. Higgs boson events from other processes as well as the continuum background events are considered as background. The fitted signal plus background PDFs from the relevant categories are also weighted and summed, and represented by a solid line. The blue dotted line represents the weighted sum of the fitted continuum background PDFs, while the dashed line combines the weighted contributions of continuum background and other Higgs boson events.

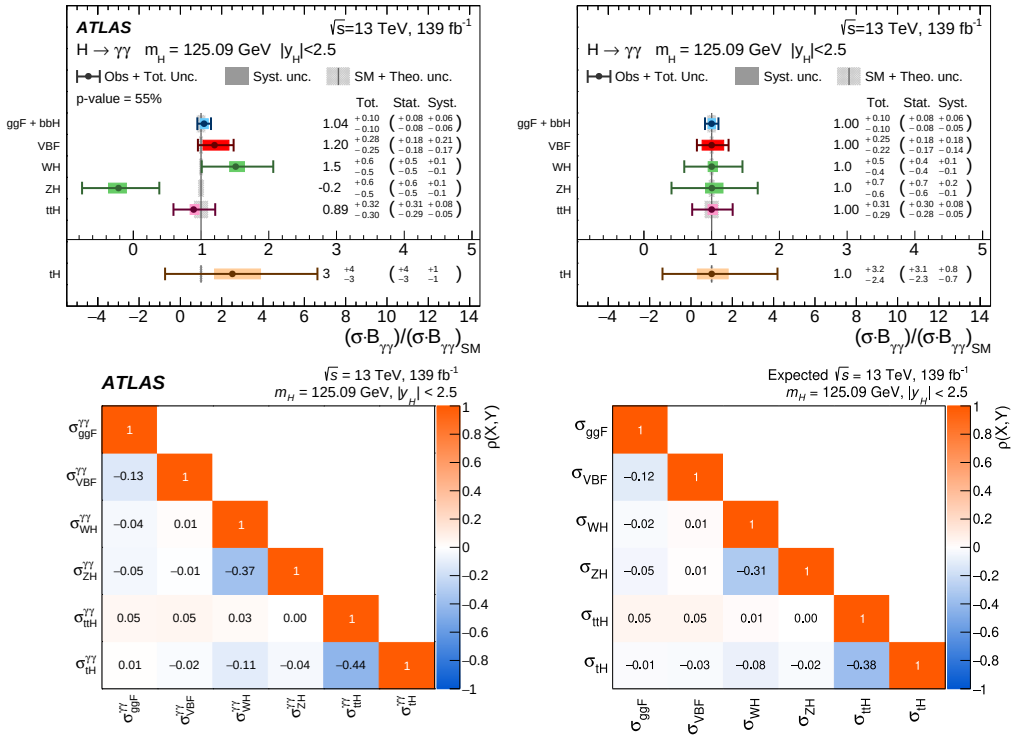

(a) Observed results. **(b)** Expected results.

Figure 5.23 – Observed [6] and expected results for cross sections times branching fraction for ggF +b$\bar{b}$H, VBF, WH, ZH, t$\bar{t}$H and tH production, normalized to their SM predictions. The values are obtained from a simultaneous fit to all categories. The error bars and shaded areas show respectively the total and systematic uncertainties in the measurements. The grey bands show the theory uncertainties in the predictions, including uncertainties due to missing higher-order terms in the perturbative QCD calculations, the PDFs and the value of α_S, as well as the $H \to \gamma\gamma$ branching ratio uncertainty.

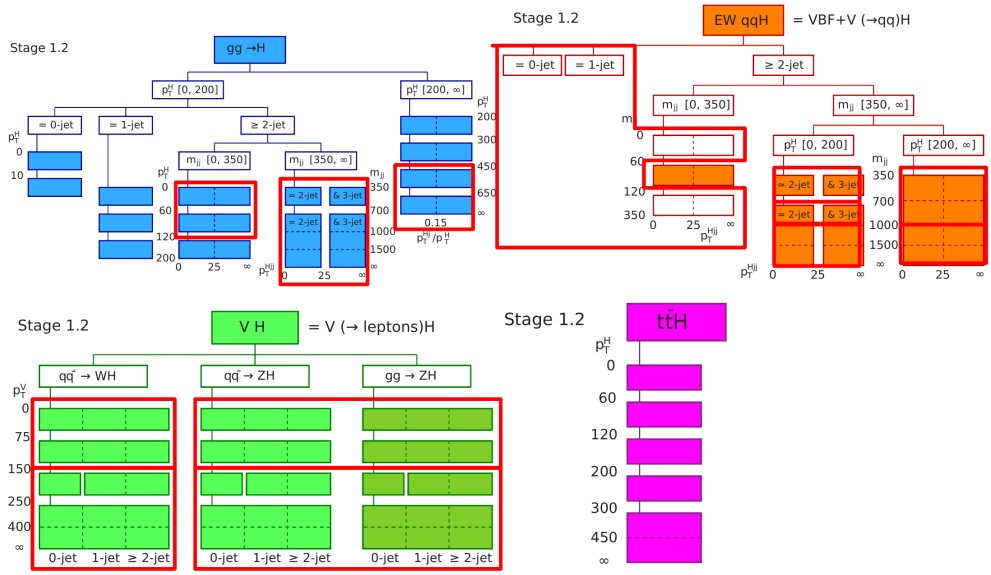

(a) Strong merging scheme.

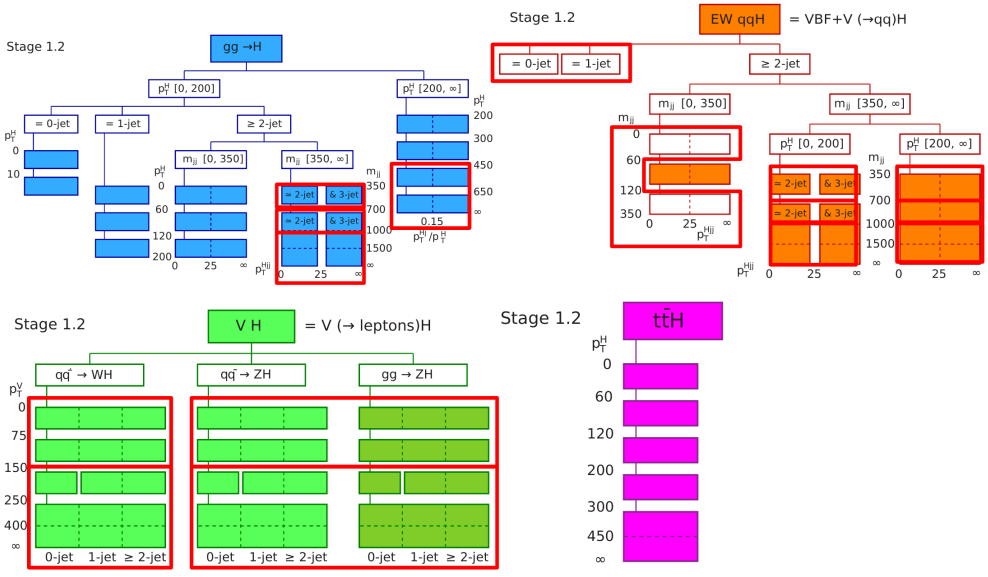

(b) Weak merging scheme.

Figure 5.24 – Strong (a) and weak (b) merging scheme for STXS cross sections measurements. Coloured truth bins are merged standalone unless a red box is draw around them, which shows merged regions. tH truth bin is not shown, but it is always measured separated from $t\bar{t}H$ bins.

duction rate of 10 times its SM prediction or greater at 95% CL while at expected 95% CL limit is set at 6.8 times SM tH production cross section or greater.

5.7.4 STXS measurements for weak merging scheme

Similarly to the STXS measurement scheme described in Section 5.7.3, a measurement of the cross-sections based on the STXS framework is performed in a weaker merging scenario. The merging is performed in order to have expected uncertainties around 100% but also to have more physical correlations among various STXS truth bins. This weaker merging scheme differs from the strong in ggF and VBF STXS bins and it keeps almost the same bin splitting for both the production processes, in order to remove spurious positive correlations observed in Figure 5.26 created by the merging in the 1 and 2 jets regions.The STXS Stage 1.2 scheme was indeed designed to have a correspondence between ggF and VBF bins in the 2 jets phase space to exactly isolate the corresponding resonant backgrounds of each truth bin. The scheme is presented in Figure 5.24b, which is defined on the expected results, independently of the observed data. The best fit results and correlation matrices for observed results are shown in Figure 5.25 and Figure 5.26 respectively. The systematic component of uncertainties is everywhere smaller than the statistical one, but reaches similar values for the 0-jet regions of ggF. No significant deviations from the SM expectation are observed and the compatibility between the measurements and the SM predictions corresponds to a p-value of 70%.

5.8 Interpretation of the results in the κ-framework

Different couplings of the Higgs boson to Standard Model particles contribute to each measured cross sections reported above, as can be observed in Figure 1.4. For example in ggF production the Higgs boson couples mainly with top and bottom quarks, but in $H \to \gamma\gamma$ decay process it couples to W gauge bosons too. The κ-framework has been designed to disentangle the contributions of the various Higgs boson couplings to SM particles considering both production and decay processes: the event rates for processes involving Higgs bosons can be expressed in terms of modifiers applied to the SM Higgs boson couplings, based on the leading-order contributions to each process [31, 157]. These coupling modifiers affect Higgs boson production cross sections and partial decay widths, therefore providing a consistent framework for Higgs boson coupling measurements in both production and decay. While this framework is useful for assessing the level of compatibility of the SM predictions with the data, the interpretation of the physical origin of a discrepancy is out of its scope: this requires, for example, to include high-order corrections to the SM Lagrangian, possibly modifying its tensor structure, like in the case of Effective Field Theory interpretations [12, 31, 158, 159], which are not detailed in this manuscript.

5.8.1 Interpretation framework

The κ-framework interpretation is based on three underlying assumptions. First, the signals observed in the different decay channels originate from a single resonance with a

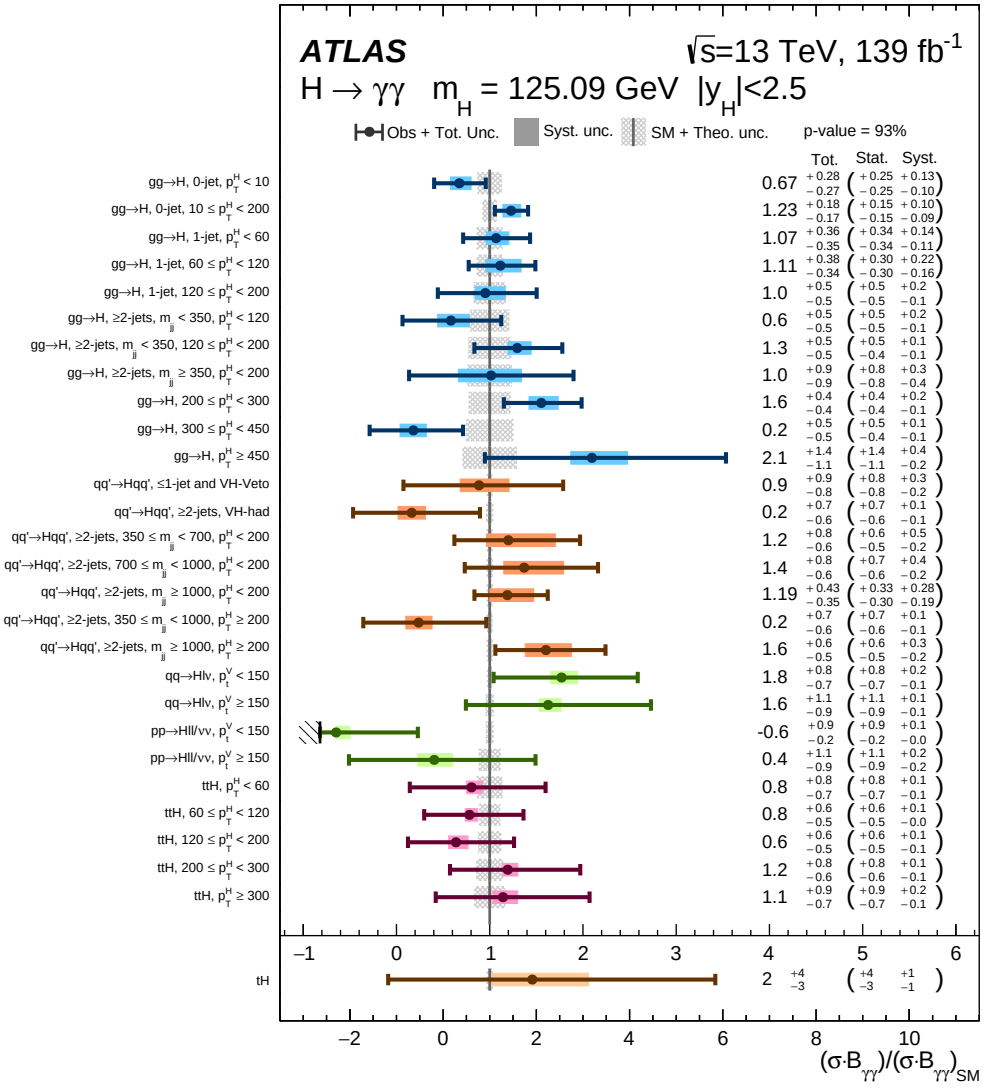

Figure 5.25 – Best-fit values and uncertainties for the cross sections in each measurement region of the strong STXS merging scheme, normalized to the SM predictions for the various parameters [6]. The values for the ggF process also include the contributions from $b\bar{b}H$ production. The error bars and shaded areas show the total and systematic uncertainties in the measurements, respectively. The uncertainties for the $pp \to H\ell\ell/\nu\nu$, $p_{\mathrm{T}}^{V} < 150\,\mathrm{GeV}$ region are truncated at the value for which the model pdf becomes negative. The grey bands around the vertical line at $\sigma^{\gamma}\gamma/\sigma_{SM}^{\gamma}\gamma = 1$ show the theory uncertainties in the predictions, including uncertainties due to missing higher-order terms in the perturbative QCD calculations, the PDFs and the value of α_S, as well as the $H \to \gamma\gamma$ branching ratio uncertainty. The p_{T} and m_{jj} values in the region definitions are indicated in GeV.

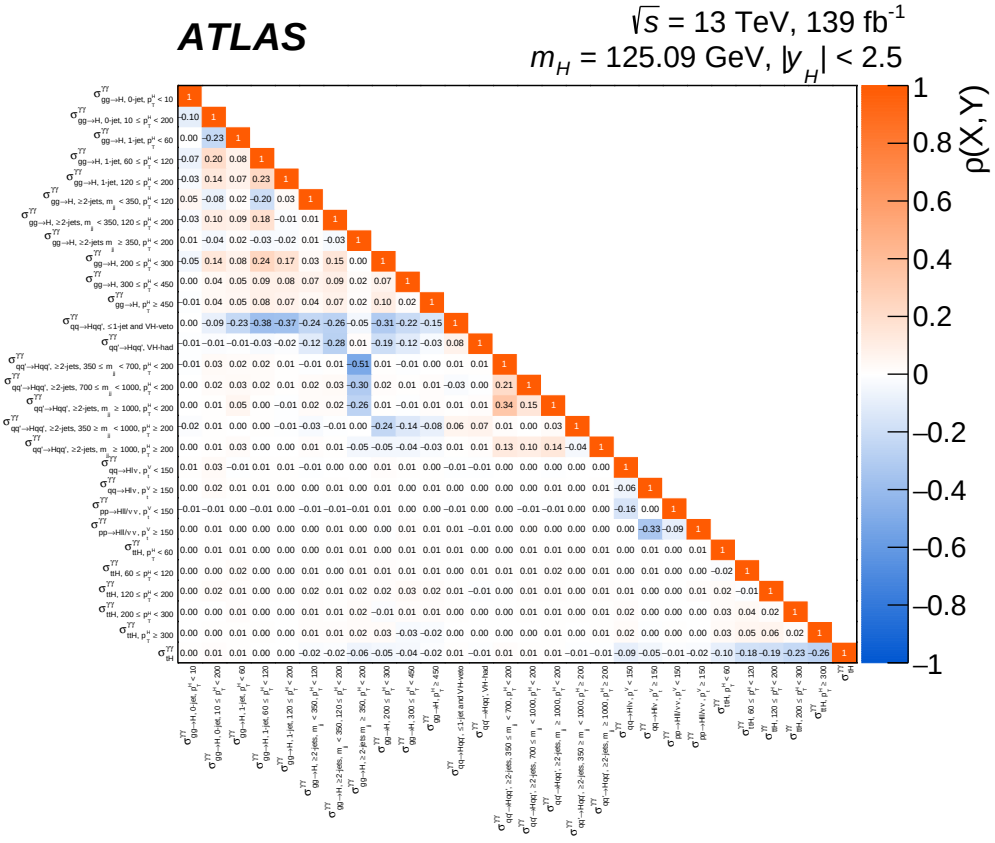

Figure 5.26 – Correlation matrix between the POIs for the measurement of the strong merged STXS scheme [6].

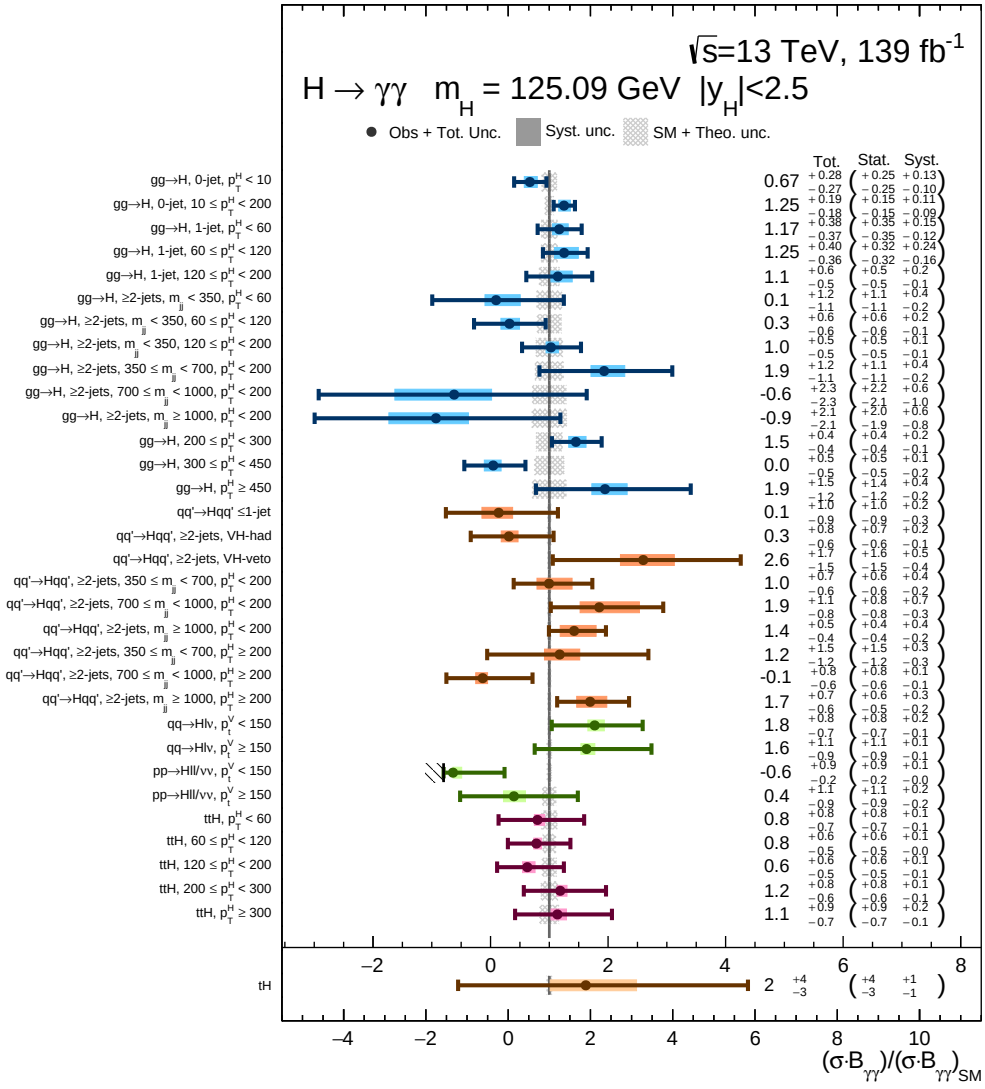

Figure 5.27 – Best-fit values and uncertainties for the cross sections in each measurement region of the weak STXS merging scheme, normalized to the SM predictions for the various parameters. The values for the ggF process also include the contributions from $b\bar{b}H$ production. The error bars and shaded areas show the total and systematic uncertainties in the measurements, respectively. The uncertainties for the $pp \to H\ell\ell/\nu\nu$, $p_{\mathrm{T}}^{V} < 150\,\mathrm{GeV}$ region are truncated at the value for which the model pdf becomes negative. The grey bands around the vertical line at $\sigma^{\gamma}\gamma/\sigma^{\gamma}_{SM}\gamma = 1$ show the theory uncertainties in the predictions, including uncertainties due to missing higher-order terms in the perturbative QCD calculations, the PDFs and the value of α_S, as well as the $H \to \gamma\gamma$ branching ratio uncertainty. The p_{T} and m_{jj} values in the region definitions are indicated in GeV.

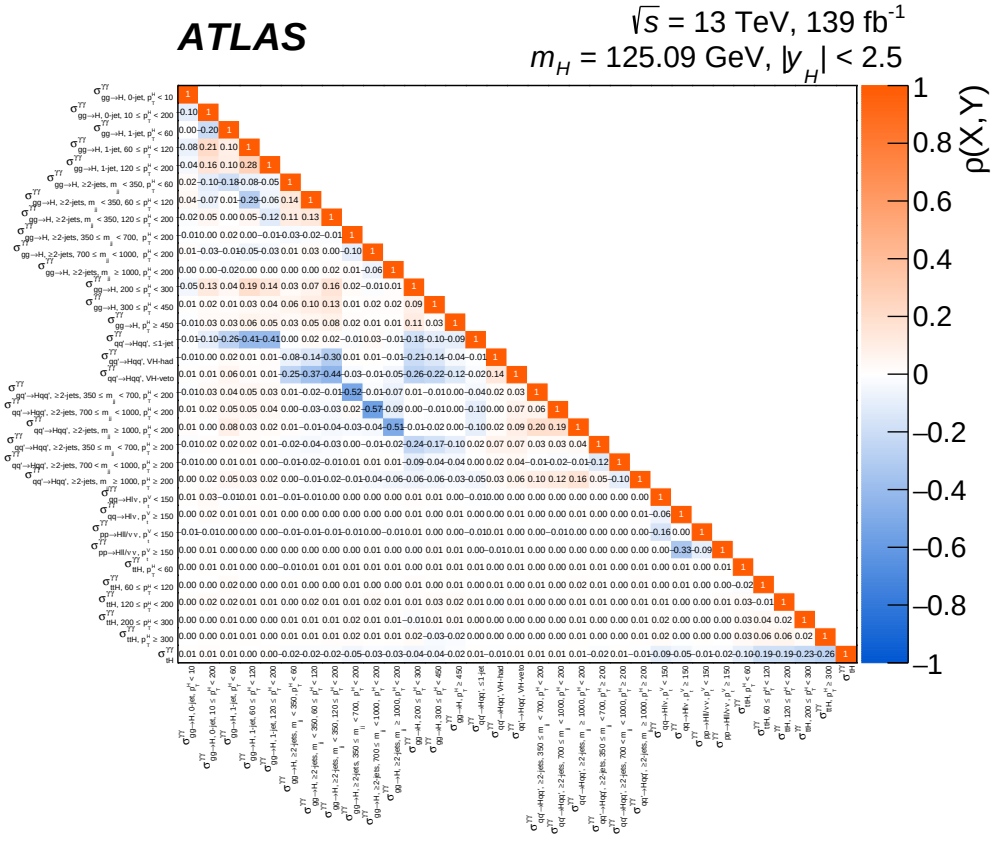

Figure 5.28 – Correlation matrix between the POIs for the measurement of the weak merged STXS scheme [6].

mass close to 125 GeV; the case of several, possibly overlapping, resonances in this mass region is not considered. Secondly, this resonance is assumed to have a narrow width (*narrow width approximation*), hence the production cross section i for each decay process f can be decomposed in the following way

$$\sigma_i \times \mathrm{BR}^f = \frac{\sigma_i \times \Gamma^f}{\Gamma_H} \tag{5.9}$$

where Γ_H is the total width of the Higgs boson and Γ_f is the partial decay width for Higgs boson decay into the final state f. Lastly, only modifications of couplings strengths, i.e. of absolute values of the couplings, are taken into account, while the tensor structure of the couplings is assumed to be the same as in the SM prediction. This means in particular that the observed Higgs state is assumed to be a CP-even scalar. Therefore a general parameterization of the Higgs couplings without referring to any particular model is produced with κ parameters defined as

$$\kappa_j^2 = \frac{\sigma_j}{\sigma_j^{\mathrm{SM}}} \quad \text{or} \quad \kappa_j^2 = \frac{\Gamma_j}{\Gamma_j^{\mathrm{SM}}}. \tag{5.10}$$

The total width of the Higgs boson Γ_H is given by the sum of the partial widths for the SM decay modes, which includes contributions from two additional classes of Higgs boson decays: the first is invisible decays, predicted to be 0.1% in the SM from the $H \to ZZ^* \to 4\nu$ and identified by $\mathrm{B_{i.}}$ for BSM contributions with sizeable $E_{\mathrm{T}}^{\mathrm{miss}}$; the second contribution corresponds to undetected decays, composed by decays to light quarks and gluon pairs, which amount to 11% in the SM and are included in the Γ^{SM}, and decays in BSM final states excluding the invisible ones (for example with low $E_{\mathrm{T}}^{\mathrm{miss}}$) denoted by $\mathrm{B_{u.}}$. Therefore, BSM contributions to the total Higgs boson decay width may manifest themselves as a value of κ_j differing from one, or a value of $\mathrm{B_{i.}}$ or $\mathrm{B_{u.}}$ differing from zero. The Higgs boson total width is then expressed as $\Gamma_H(\vec{\kappa}, \mathrm{B_{i.}}, \mathrm{B_{u.}}) = \kappa_H^2(\vec{\kappa}, \mathrm{B_{i.}}, \mathrm{B_{u.}})\, \Gamma_H^{\mathrm{SM}}$ with

$$\kappa_H^2(\vec{\kappa}, \mathrm{B_{i.}}, \mathrm{B_{u.}}) = \frac{\sum_j \mathrm{B}_j^{\mathrm{SM}} \kappa_j^2}{(1 - \mathrm{B_{i.}} - \mathrm{B_{u.}})} \tag{5.11}$$

where $\mathrm{B}_j^{\mathrm{SM}}$ are the SM branching ratios for the Higgs decay processes. By definition, $\mathrm{B_{u.}}$ is not directly constrained by any measurement, so that extracting values for both the κ parameters and $\mathrm{B_{u.}}$ simultaneously requires additional assumptions or constraints. The simplest assumption is that there are no undetected Higgs boson decays and the invisible branching fraction is as predicted by the SM. An alternative, weaker assumption, is to require $\kappa_W \leq 1$ and $\kappa_Z \leq 1$ [157]. A different approach is instead to rely on measurements of ratios of coupling modifiers, which can be measured without assumptions about the Higgs boson total width, since the dependence on Γ_H of each coupling strength cancels in their ratios.

By definition, the currently best available SM predictions for all $\sigma \times \mathrm{BR}$ are recovered when all $\kappa_j = 1$. These κ_j modifiers can be expressed in terms of individual coupling

modifiers: multiplicative modifiers are introduced for Higgs boson couplings to the W and Z bosons, denoted respectively as κ_W and κ_Z, and for couplings to the top quark, bottom quark and τ lepton, respectively κ_t, κ_b and κ_τ. The couplings to other SM particles are assumed to be fixed to 1, which is the case for κ_u, κ_d and κ_e, or to vary in the same way as other, more sensitive modifiers, so that κ_c varies as κ_t and κ_s varies as κ_b. Two parametrizations are considered for the ggF and $H \to \gamma\gamma$ loop processes: a resolved parameterization in which their rates are expressed using the modifiers to the SM particles involved in the loop, or an unresolved parameterization based on modifiers to the effective couplings of the Higgs boson to the gluon and the photon, respectively denoted κ_g and κ_γ. The ggZH loop process is always described in the resolved parameterization. The κ_Z modifier is assumed to be positive without loss of generality, since all predictions are invariant under a simultaneous flip in the signs of all the κ modifiers. Sensitivity to the sign of the other modifiers is obtained through the interference between processes involving different combinations of modifiers. These include in particular the $H \to \gamma\gamma$, ggF and ggZH loops and tH processes. The relations are summarized in Table 5.13 for the full Higgs production and decays phase space and are used for the results reported in Section 5.8.2 and Section 5.9.2.

The parametrizations in Table 5.13 takes into account only the variation of the cross section as a function of the κ modifiers. For the $H \to \gamma\gamma$ analysis, which is the most sensitive to tH cross section, the parametrization for tHW and tHq is modified in order to account for the the cross section times selection efficiency variations that can be produced by changes in the process kinematics due to the interference effects between the parton-level processes contributing to tHW and tHq. Therefore, a general parametrization $A\,\kappa_t^2 + B\,\kappa_W^2 - C\,\kappa_t\kappa_W$, similar to the one in Table 5.13, is extracted for each of the 101 analysis categories and for both the tHW and tHq processes. The category-dependent (A, B, C) parameters are obtained by computing the expected yields of the given tH process with simulated MC events generated with three different values of κ_t (in particular $\kappa_t = \{-1, 1, 2\}$) and interpolating them with a parabolic function. The parametrization result is then cross checked with a fourth yield value ($\kappa_t = 0.5$).

5.8.2 Results

Three specific models of coupling modifications are considered: the first one targets Higgs to top quark coupling (κ_t), the second tests the universality of fermion and boson couplings to the Standard Model (κ_F and κ_V), while the third is a generic model which probes Higgs loops, total width and couplings to the top quark and vector bosons. For all these results, the different parameterization are applied to a likelihood model that contains the full impact of the theoretical uncertainties (see Section 5.6.1).

In the first model, only the κ_t coupling modifier is left free, while all other couplings are set to their SM expectations ($\kappa_i = 1$). Two configurations are used for the ggF and $H \to \gamma\gamma$ loop processes: they are either described using the resolved parameterization as a function of κ_t or fixed to their SM predictions. In both cases, Γ_H is expressed in terms of κ_t, assuming no contributions from Higgs boson decays other than those predicted in the SM. This model allows to probe the sign of κ_t through interference effects in the tH

Production cross section	Loops	Main interference	Effective modifier	Resolved modifier
$\sigma(\text{ggF})$	✓	t–b	κ_g^2	$1.040\,\kappa_t^2 + 0.002\,\kappa_b^2 - 0.038\,\kappa_t\kappa_b - 0.005\,\kappa_t\kappa_c$
$\sigma(\text{VBF})$	-	-	-	$0.733\,\kappa_W^2 + 0.267\,\kappa_Z^2$
$\sigma(qq/qg \to ZH)$	-	-	-	κ_Z^2
$\sigma(gg \to ZH)$	✓	t–Z	$\kappa_{(ggZH)}$	$2.456\,\kappa_Z^2 + 0.456\,\kappa_t^2 - 1.903\,\kappa_Z\kappa_t$ $- 0.011\,\kappa_Z\kappa_b + 0.003\,\kappa_t\kappa_b$
$\sigma(\text{WH})$	-	-	-	κ_W^2
$\sigma(\text{t}\bar{\text{t}}\text{H})$	-	-	-	κ_t^2
$\sigma(\text{tHW})$	-	t–W	-	$2.909\,\kappa_t^2 + 2.310\,\kappa_W^2 - 4.220\,\kappa_t\kappa_W$
$\sigma(\text{tHq})$	-	t–W	-	$2.633\,\kappa_t^2 + 3.578\,\kappa_W^2 - 5.211\,\kappa_t\kappa_W$
$\sigma(\text{b}\bar{\text{b}}\text{H})$	-	-	-	κ_b^2
Partial decay width				
Γ^{bb}	-	-	-	κ_b^2
Γ^{WW}	-	-	-	κ_W^2
Γ^{gg}	✓	t–b	κ_g^2	$1.111\,\kappa_t^2 + 0.012\,\kappa_b^2 - 0.123\,\kappa_t\kappa_b$
$\Gamma^{\tau\tau}$	-	-	-	κ_τ^2
Γ^{ZZ}	-	-	-	κ_Z^2
Γ^{cc}	-	-	-	$\kappa_c^2\ (=\kappa_t^2)$
$\Gamma^{\gamma\gamma}$	✓	t–W	κ_γ^2	$1.589\,\kappa_W^2 + 0.072\,\kappa_t^2 - 0.674\,\kappa_W\kappa_t$ $+0.009\,\kappa_W\kappa_\tau + 0.008\,\kappa_W\kappa_b$ $-0.002\,\kappa_t\kappa_b - 0.002\,\kappa_t\kappa_\tau$
$\Gamma^{Z\gamma}$	✓	t–W	$\kappa_{(Z\gamma)}^2$	$1.118\,\kappa_W^2 - 0.125\,\kappa_W\kappa_t + 0.004\,\kappa_t^2 + 0.003\,\kappa_W\kappa_b$
Γ^{ss}	-	-	-	$\kappa_s^2\ (=\kappa_b^2)$
$\Gamma^{\mu\mu}$	-	-	-	κ_μ^2
Total width ($\text{B}_{\text{i.}} = \text{B}_{\text{u.}} = 0$)				
Γ_H	✓	-	κ_H^2	$0.581\,\kappa_b^2 + 0.215\,\kappa_W^2 + 0.082\,\kappa_g^2$ $+0.063\,\kappa_\tau^2 + 0.026\,\kappa_Z^2 + 0.029\,\kappa_c^2$ $+0.0023\,\kappa_\gamma^2 + 0.0015\,\kappa_{(Z\gamma)}^2$ $+0.0004\,\kappa_s^2 + 0.00022\,\kappa_\mu^2$

Table 5.13 – Parametrisations of Higgs boson production cross sections σ_i, partial decay widths Γ^f, and the total width Γ_H, normalised to their SM values, as functions of the coupling-strength modifiers κ [12]. The parametrisation reported here for tH processes is used only for Section 5.9.2. The effect of invisible and undetected decays is not considered in the expression for Γ_H. For effective κ parameters associated with loop processes, the resolved scaling in terms of the modifications of the Higgs boson couplings to the fundamental SM particles is given. The coefficients are derived following the methodology in [31, 157].

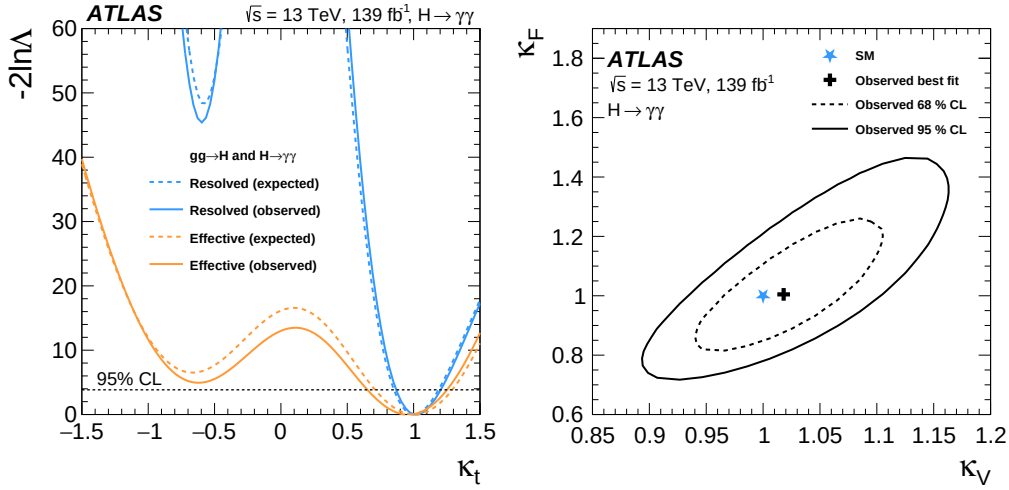

(a) κ_t scan.

(b) (κ_V, κ_F) contour.

Figure 5.29 – (a) Negative log-likelihood scans as a function of κ_t in a model where all other coupling modifiers are fixed to their SM values. The $H \to \gamma\gamma$ and ggF loops are either parameterized as a function of κ_t (blue) or with their effective coupling modifiers (orange). In the latter case, sensitivity to the sign of κ_t is provided only by the tH processes. The solid curves correspond to observed data, and the dotted curves to an Asimov dataset generated under the SM hypothesis. (b) Negative log-likelihood contours at 68% (dashed line) and 95% CL (solid line) in the (κ_V, κ_F) plane of modifiers applied to Higgs boson couplings to gauge bosons (κ_V) and fermions (κ_F). Loop processes and the Higgs boson total width Γ_H are parameterized as a function of κ_V and κ_F. The best-fit point is indicated by a cross while the SM prediction is indicated by a star.

processes, and also in the $H \to \gamma\gamma$ and ggZH loop processes when these are resolved as a function of κ_t. The negative log-likelihood scans for both configurations are shown in Figure 5.29a. Negative values of κ_t are excluded with a significance of 6.7σ when the $H \to \gamma\gamma$ and ggZH loops are included, and at 2.2σ by the tH process alone.

The second model considers two universal coupling modifiers, one for gauge bosons κ_V and one for fermions κ_F built by just equalizing all the relevant coupling modifiers as follows

$$\kappa_V = \kappa_W = \kappa_Z \quad \text{and} \quad \kappa_F = \kappa_t = \kappa_b = \kappa_\tau.$$

In this scheme, all the loops and the Higgs total width are described using the resolved parametrization in terms of κ_V and κ_F. The measurement is performed simultaneously in the (κ_V, κ_F) plane and the result is reported in Figure 5.29b while the the best fit values are $\kappa_V = 1.02\ ^{+0.06}_{-0.05}$ and $\kappa_F = 1.00\ ^{+0.16}_{-0.13}$, with a linear correlation between the two parameters of 77%.

The last model uses of the effective parameterization of the ggF and $H \to \gamma\gamma$ processes, while the total width of the Higgs boson is described using the effective modifier κ_H. A common coupling modifier $\kappa_V = \kappa_W = \kappa_Z$ is introduced for couplings to both W and Z bosons, while κ_τ is fixed to 1 and $\kappa_b = \kappa_t$. The measurement is performed in term

Parameter	Result	Total Uncert.
$\kappa_{g\gamma}$	1.02	± 0.06
λ_{Vg}	1.01	± 0.11
λ_{tg}	0.95	$^{+0.15}_{-0.16}$

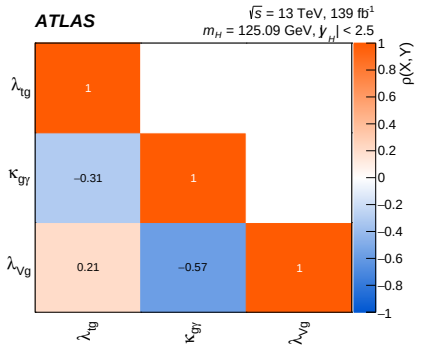

(a)

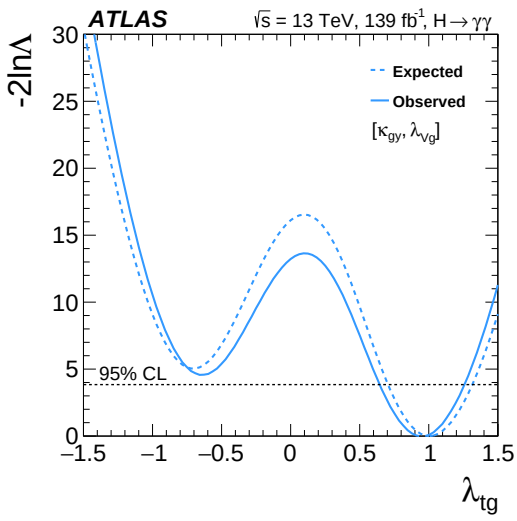

(b)

Figure 5.30 – (a) Best-fit values, total uncertainties and linear correlations for $\kappa_{g\gamma}$, λ_{Vg}, λ_{tg}. (b) Profile likelihood of the observed (solid) and expected (dashed) coupling strength ratio λ_{tg}, with other parameters of interest left floating in the fit [6].

of ratios with the following parameters

$$\kappa_{g\gamma} = \frac{\kappa_g \kappa_\gamma}{\kappa_H} \qquad \lambda_{Vg} = \frac{\kappa_V}{\kappa_g} \qquad \lambda_{tg} = \frac{\kappa_t}{\kappa_g}$$

with the parameter λ_{tg} allowed to be negative to exploit the sensitivity to the relative sign from the tHq, tHW and ggZH processes. Ratios of coupling modifiers allow to make no assumptions about the Higgs boson total width, since the dependence on Γ_H of each coupling strength cancels in their ratios, therefore allowing for BSM Higgs decays. The best fit results are reported in Figure 5.30a along with linear correlations. The likelihood scan of λ_{tg}, obtained by leaving the other two parameters floating in the fit, is shown in Figure 5.30b. Sensitivity to the sign of λ_{tg} is provided by the tH and ggZH processes, and leads to exclusion of the region $< \lambda_{tg} 0$ with a significance of 2.1σ.

5.9 Combination with other Higgs decay channels

In order to further boost the measurement precision of the Higgs boson properties, the various analyses performed in different Higgs decay channels are combined together [11]. The combination of many different analyses makes full use of the Run 2 dataset recorded by ATLAS and it permits to decouple the Higgs production from its decay, which is not possible with a measurement performed in a single channel. The combination of different measurements therefore provides the most stringent tests of the validity of the Standard Model.

Decay channel	Target Production Modes	$\mathcal{L}$ [fb^{-1}]	Ref.	Included for results
$H \to \gamma\gamma$	ggF, VBF, WH, ZH, $t\bar{t}H$, tH	139	[6]	Prod. Modes, κ, STXS
$H \to ZZ^*$	ggF, VBF, WH, ZH, $t\bar{t}H + tH(4\ell)$	139	[160]	Prod. Modes, κ, STXS
	$t\bar{t}H + tH$ (multilepton)	36.1	[161]	Prod. Modes, κ
$H \to WW^*$	ggF, VBF	139	[162]	Prod. Modes, κ, STXS
	WH, ZH	36.1	[163]	Prod. Modes, κ
	$t\bar{t}H + tH$ (multilepton)	36.1	[161]	Prod. Modes, κ
$H \to \tau\tau$	ggF, VBF, WH, ZH, $t\bar{t}H(\tau_{had}\tau_{had})$	139	[164]	Prod. Modes, κ, STXS
	$t\bar{t}H + tH$ (multilepton)	36.1	[161]	Prod. Modes, κ
$H \to b\bar{b}$	WH, ZH	139	[165–167]	Prod. Modes, κ, STXS
	VBF	126	[168]	Prod. Modes, κ, STXS
	$t\bar{t}H + tH$	139	[169]	Prod. Modes, κ, STXS
	inclusive	139	[170]	STXS
$H \to \mu\mu$	ggF + $t\bar{t}H$, VBF + VH	139	[171]	Prod. Modes, κ
$H \to c\bar{c}$	VH	139	[172]	Only κ_c constraints
$H \to Z\gamma$	ggF, VBF, VH, $t\bar{t}H$	139	[173]	Prod. Modes, κ
$H \to inv$	VBF	139	[174]	κ
	VH	139	[175]	κ

Table 5.14 – The decay channels, targeted production modes and integrated luminosity ($\mathcal{L}$) used for each input analysis of the combination [11]. The references for the input analyses and information about which combined measurements they enter are also provided. The $t\bar{t}H(4\ell)$ and $t\bar{t}H(\tau_{had}\tau_{had})$ input analyses are complementary to the multilepton $t\bar{t}H$ analysis [161], with no overlapping event selection criteria.

5.9.1 Input measurements

The decay channels, targeted production modes and integrated luminosities of the input analyses entering the combined measurement presented here are shown in Table 5.14. As can be observed, almost all the analyses included in the combination are based on the full Run 2 dataset and can target at least a subset of STXS Stage 1.2 kinematic bins presented in Section 5.1.

Among all the input analyses, $H \to inv$ analyses are considered only when producing κ-framework results, in particular only for the scenarios in which BSM contributions lead a $H \to inv$ signature. The $t\bar{t}H$ multilepton, $H \to \mu\mu$, $H \to Z\gamma$ and $VH(\to WW^*)$ analyses are excluded from the STXS measurements due to their lack of sensitivity in highly granular STXS kinematic regions. The $H \to c\bar{c}$ analysis is included only when κ_c constraints have been set.

The overlap among the events selected by each analysis included in the combination is found to be negligible. All input analyses use a consistent set of event generators for the Higgs boson Monte Carlo (MC) samples, as described in Section 4.2 and in the individual analysis references.

The results of the combination are obtained by employing the profiled likelihood ratio test defined in Section 4.8.1 on a likelihood function built as the product of the likelihoods of each input analysis. These are themselves products of likelihoods computed for

each mutually exclusive analysis regions, similarly to what is described in Section 4.8. Systematic uncertainties that affect multiple analyses are modeled with common nuisance parameters to propagate the effects of these uncertainties coherently to all measurements. These common nuisances parameters are easily identified in the analyses targeting the full Run 2 statistic since these are based on the same ATLAS reconstruction algorithm and recommendations, while additional care has been taken in the correlation of systematic uncertainties for the analysis based on partial Run 2 dataset.

5.9.2 Results

Similarly to the results of the $H \to \gamma\gamma$ analysis reported in Section 5.7 and Section 5.8, various measurements has been performed at the combination level. The results for inclusive signal strength, production mode cross sections, branching ratios, STXS framework and κ-framework interpretations are reported in the following; nonetheless this is a relatively small but representative subset of the measurements performed with the combined likelihood, fully detailed in [11] and its auxiliary material.

Inclusive, production modes and branching ratio measurements

For a specific production mode p and decay final state d, the signal yield is expressed in terms of a single modifier μ_{pd}, as the production cross section σ_p and the branching fraction B_d cannot be separately measured without further assumptions. The modifiers are defined as the ratios of the measured Higgs boson yields and their SM expectations as reported in Eq. (1.37). An overall scaling of the expected Higgs boson yield in all categories is obtained if all the μ_{pd} are set equal to a global μ modifier in the likelihood model. The observed value of μ for the $|y_H| < 2.5$ fiducial region is

$$\mu = 1.05 \pm 0.06 = 1.05 \pm 0.03\,(\text{stat.}) \pm 0.03\,(\text{exp.}) \pm 0.04\,(\text{sig. th.}) \pm 0.02\,(\text{bkg. th.})$$

where the total uncertainty is decomposed into the statistical uncertainty, experimental systematic uncertainty, and theory uncertainties for the signal and background modeling. The measurement is consistent with the SM prediction with a p-value of 39%. The likelihood scan as a function of μ is shown in Figure 5.31, for the full likelihood and the reduced ones with sets of nuisance parameters sequentially fixed to their best-fit values to obtain the components of the uncertainty.

In addition to the global measurement, Higgs boson production cross section measurements for the main processes is carried out. In this scheme, the underlying assumption is that branching ratios for the different decay modes follow the Standard Model expectations within theoretical uncertainties. The results are reported in Figure 5.32 and the level of compatibility between the measurement and the SM prediction corresponds to a p-value of 65%. The observed (expected) upper limit on the tH production is measured to be 15 (7) times the SM prediction at 95% CL, influenced by a relatively large negative correlation coefficient of 56% between $t\bar{t}H$ and tH measurements. This is due to cross-contamination between the two processes in the set of reconstructed events that provide the highest sensitivity to these production processes and to the smaller than SM

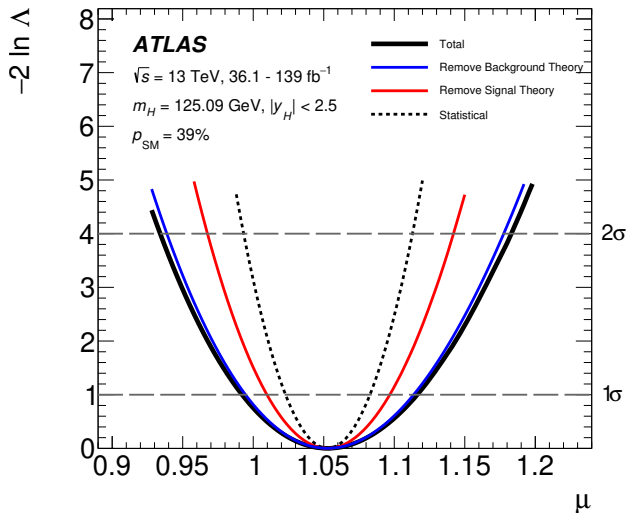

Figure 5.31 – Likelihood scan as a function of μ with all systematic uncertainties included (solid black line), with parameters describing theory uncertainties in background processes fixed to their best-fit values (solid blue line), with the same procedure also applied to theory uncertainties in the signal process (solid red line) and to all systematic uncertainties, so that only statistical uncertainties remain (dotted black line). The dashed horizontal lines show the 1σ and 2σ confidence intervals for μ [11].

observed $t\bar{t}H$ production cross section in the $t\bar{t}H(\rightarrow b\bar{b})$ analysis.

Similarly, branching fractions of individual Higgs boson decay modes are measured by setting the cross sections for Higgs boson production processes to their respective SM values. The results are shown in Figure 5.33. The branching fractions of the $\gamma\gamma$, ZZ, $W^{\pm}W^{\mp}$ and $\tau^{+}\tau^{-}$ decays, which were already observed in the Run 1 data, are measured with a precision ranging from 10% to 12%. The $b\bar{b}$ decay mode is observed with a signal significance of 7.0σ (expected 7.7σ), while the observed (expected) signal significances for the $H \rightarrow \mu\mu$ and $H \rightarrow Z\gamma$ decays are 2.0σ (1.7σ) and 2.3σ (1.1σ), respectively. The p-value for compatibility of the measurement and the SM prediction is 56%.

STXS measurement

Similar to what has been presented for $H \rightarrow \gamma\gamma$ analysis, a combined STXS measurement is also performed. Although $H \rightarrow \gamma\gamma$ channel is the only one that can probe the full STXS with good granularity and sensitivity, the additional measurements brought in the combination allow to probe with higher precision particular regions of the STXS space. In the ggF phase space $H \rightarrow ZZ^{*}$ and $H \rightarrow WW^{*}$ channels present similar sensitivity as $H \rightarrow \gamma\gamma$, with boosted Higgs topology probed mainly by $H \rightarrow \gamma\gamma$ and $H \rightarrow b\bar{b}$ analyses; the $H \rightarrow \gamma\gamma$, $H \rightarrow WW^{*}$ and $H \rightarrow \tau\tau$ dominate the VBF phase space measurements, while VH leptonic regions are dominated by resolved and boosted VH ($H \rightarrow b\bar{b}$) analyses. The $t\bar{t}H$ regions are principally measured by $H \rightarrow \gamma\gamma$ and $t\bar{t}H$ ($H \rightarrow b\bar{b}$) analyses for the low and high $p_{\mathrm{T}}^{\mathrm{H}}$ regions respectively. The only analysis that

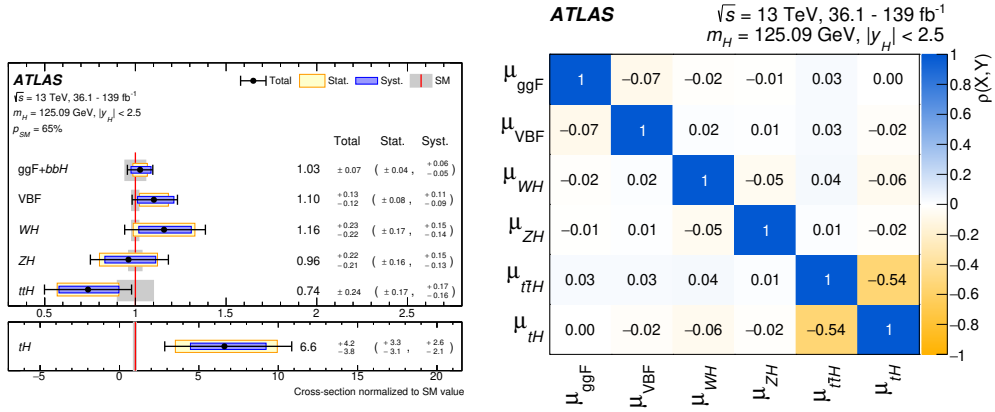

Figure 5.32 – Cross sections for ggF, VBF, WH, ZH, $t\bar{t}H$ and tH production modes and their correlations. The cross sections are normalized to their SM predictions, measured assuming SM values for the decay branching fractions. The black error bars, blue boxes and yellow boxes show the total, systematic, and statistical uncertainties in the measurements, respectively. The gray bands indicate the theory uncertainties on the SM cross-section predictions [11].

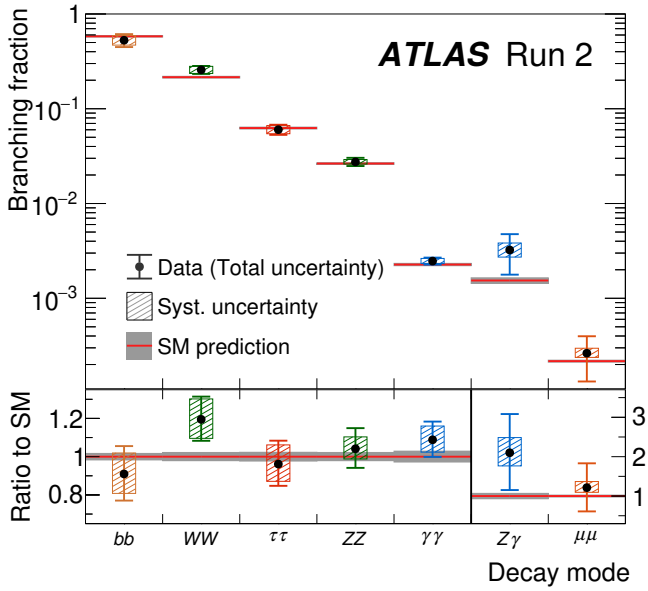

Figure 5.33 – Observed and predicted Higgs boson branching fractions. Branching fractions for different Higgs boson decay modes are measured assuming SM values for the production cross sections. The lower panels show the ratios of the measured values to their SM predictions. The vertical bar on each point denotes the 68% confidence interval [11].

has some sensitivity to tH processes is $H \to \gamma\gamma$.

The fit parameters chosen for the combined STXS measurement are the cross sections for Higgs boson production in STXS region. The branching fractions for the various decay modes follow the Standard Model expectations within theoretical uncertainties.

The best fit results and correlations are shown in Figure 5.34 and Figure 5.35. The results are in agreement with the SM predictions within uncertainties in a wide range of kinematic regions for the different Higgs boson production processes. The level of compatibility between the measurement and the SM prediction corresponds to a p-value of 94%.

κ-framework interpretation

Given the combination of different Higgs decay channels, additional handles are available to disentangle Higgs production and decay processes and therefore to access more easily the Higgs boson coupling to Standard Model particles. The κ-framework described in Section 5.8 is used for this purpose.

Two generic parametrizations are reported here: the first parametrization assumes no BSM particles in loops and decays while the second releases this hypothesis by making use of the effective couplings for loop-mediated processes.

The first model treats independently the scale factors for the coupling strengths to W, Z, t, b, τ and μ. The modifiers of Higgs boson couplings to c-quarks are either assumed to scale as the coupling modifiers for top quark or left free in the fit. The coupling modifiers for s-quark and for first generation quarks and fermion are enforced to the SM. The loop-mediated processes are resolved in terms of these modifiers and no BSM particles are allowed to participate in the loop; in addition, no invisible or undetected decays are assumed to exist. The Figure 5.36 shows the results of this benchmark model in terms of reduced coupling-strength scale factors, derived from Eq. (1.30) and Eq. (1.34) respectively: these are defined as

$$y_V = \sqrt{\kappa_V}\frac{m_V}{v} \quad \text{and} \quad y_F = \kappa_F \frac{m_F}{v}$$

for weak bosons with a mass m_V, fermions with a mass m_F and where $v = 246\,\text{GeV}$ is the vacuum expectation value of the Higgs field. For the b quark and the top quark, the $\overline{MS}$ running mass evaluated at a scale of 125.09 GeV is used. The level of compatibility between the combined measurement and the SM prediction corresponds to a p-value of 56% in the case $\kappa_c = \kappa_t$ and 65% with κ_c as a free parameter. When the coupling strength modifier κ_c is left unconstrained in the fit, an upper limit of $\kappa_c < 5.7(7.6)$ times the SM prediction is observed (expected) at 95% CL. The uncertainty in each of the other parameters increases because of the resulting weaker constraint on the total decay width.

The second model is similar to the one just described but the ggF, $H \to gg$, $H \to \gamma\gamma$ and $H \to Z\gamma$ loop processes are parameterised using the effective coupling-strength modifiers κ_g, κ_γ and $\kappa_{Z\gamma}$. The measured parameters include κ_Z, κ_W, κ_b, κ_t, κ_τ, κ_μ, κ_γ, $\kappa_{Z\gamma}$ and κ_g. The sign of κ_t can be either positive or negative, while κ_Z is assumed to be

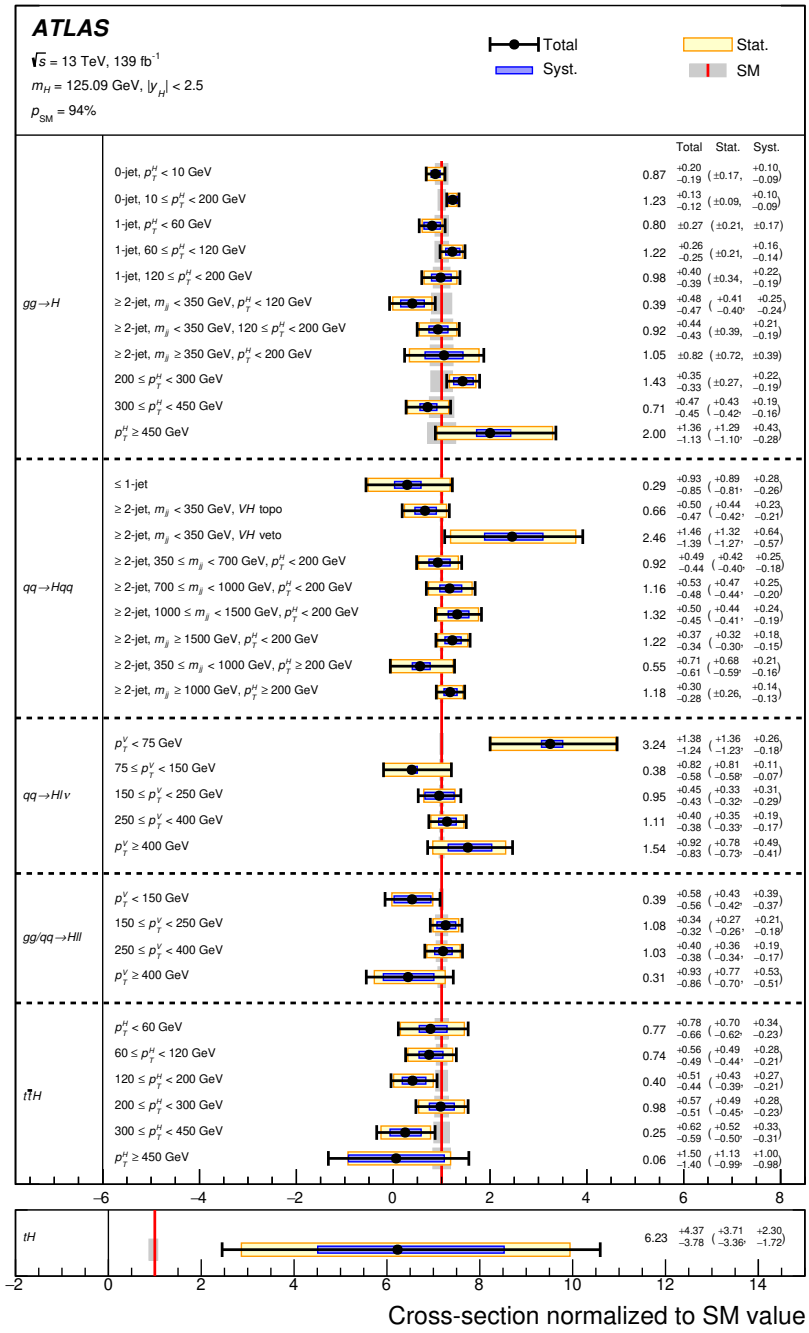

Figure 5.34 – Best-fit values and uncertainties for the cross sections in each measurement region, normalized to the SM predictions for the various parameters. The measurements assume SM branching fractions for all measured decays. The black error bars, blue boxes and yellow boxes show the total, systematic, and statistical uncertainties in the measurements, respectively. The gray bands show the theory uncertainties on the predictions [11].

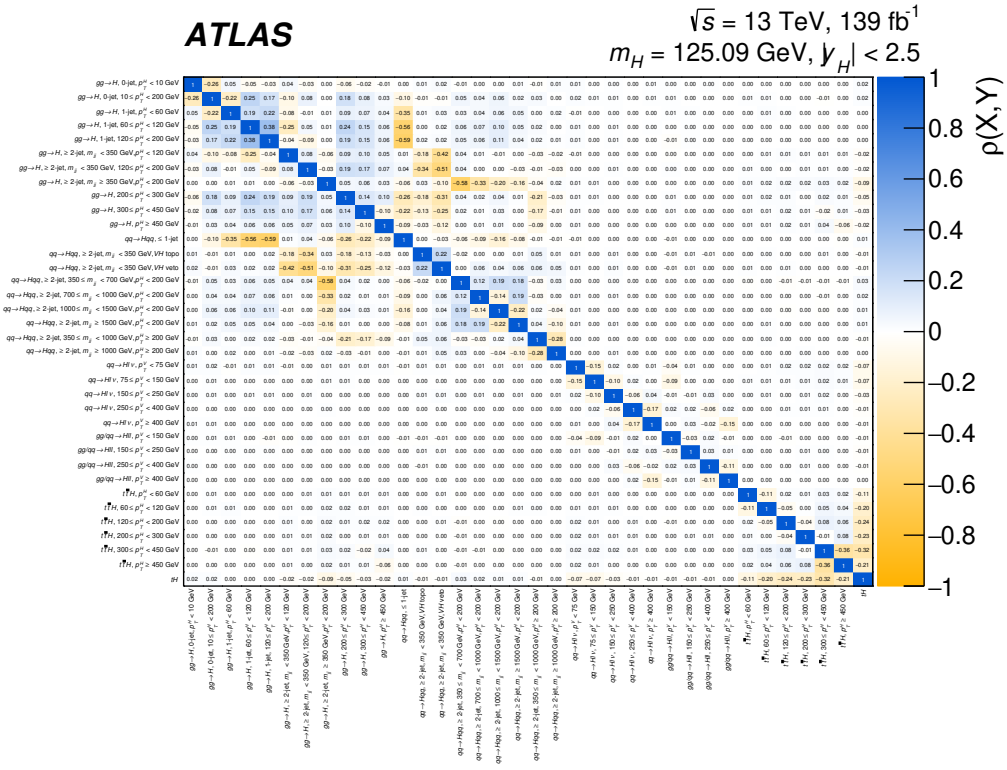

Figure 5.35 – Correlation matrix for the measured values of the simplified template cross sections. The linear correlation coefficient $\rho(X,Y)$ between pairs of observables is indicated in color and given numerically [11].

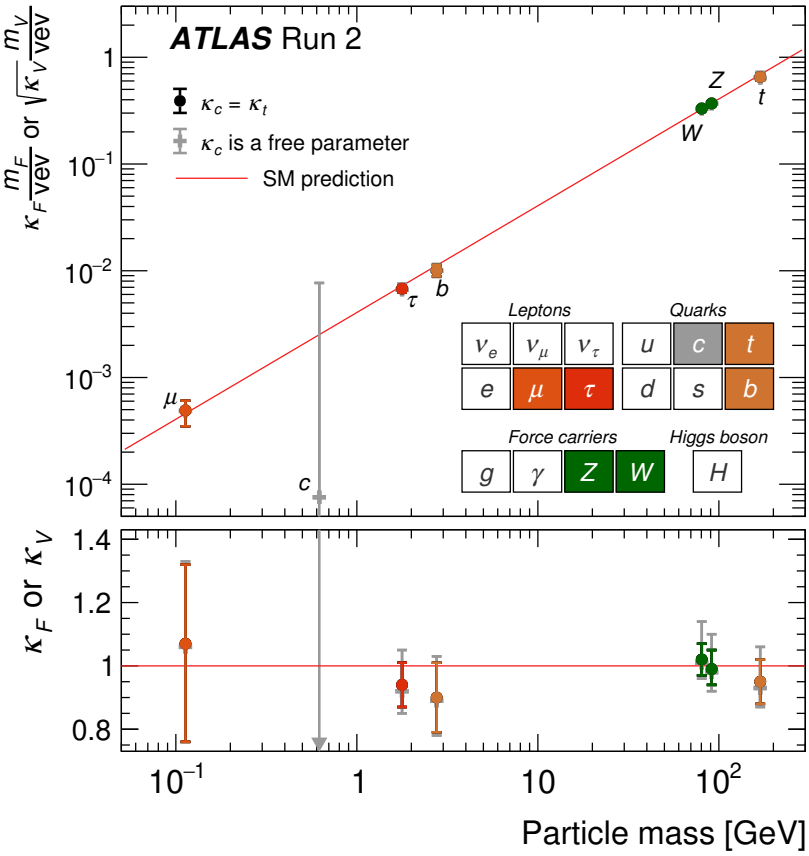

Figure 5.36 – Reduced coupling-strength modifiers $\kappa_F \frac{m_F}{v}$ for fermions ($F = t, b, \tau, \mu$) and $\sqrt{\kappa_V}\frac{m_V}{v}$ for weak gauge bosons ($V = W, Z$) as a function of their masses m_F and m_V, respectively, and the vacuum expectation value of the Higgs field $v = 246\,\text{GeV}$. Two fit scenarios with $\kappa_c = \kappa_t$ (coloured circle markers), or κ_c left free-floating in the fit (grey cross markers) are shown. Loop-induced processes are assumed to have the SM structure, and Higgs boson decays to non-SM particles are not allowed. The SM prediction for both cases is also shown (red straight line). The vertical error bars represent 68% CL intervals for the measured parameters. The lower panel shows the ratios of the values to their SM predictions. The grey arrow points in the direction of the best-fit value and the corresponding grey uncertainty bar extends beyond the lower panel range. [11].

positive without loss of generality. Two scenarios are considered for the total width of the Higgs boson:

(a) No BSM contributions to the total width of the Higgs boson ($B_{i.} = B_{u.} = 0$).

(b) Both $B_{i.}$ and $B_{u.}$ are added as free parameters to the model. The measurement of Higgs boson decays into invisible final states from VBF and VH ($H \rightarrow inv$) analyses is included in the combination and used to provide a constraint on $B_{i.}$. The conditions $\kappa_W \leq 1$ and $\kappa_Z \leq 1$ are included to provide a constraint on $B_{u.}$.

The numerical results for the two scenarios are illustrated in Figure 5.37. All probed fundamental coupling-strength scale factors, as well as the probed loop-induced coupling scale factors are measured to be compatible with their SM expectation. In scenario (a) with no BSM contribution to the total width, a possible negative value for κ_t is excluded at 4.3σ (3.8σ expected) relative to the best-fit value with sensitivity coming from the tH and ggZH processes. The level of compatibility between the SM hypothesis with the best-fit point corresponds to a p-value of 61%. In scenario (b) the observed (expected) 95% CL upper limits on the branching fractions are $B_{i.} < 0.13$ (0.08) and $B_{u.} < 0.12$ (0.21).

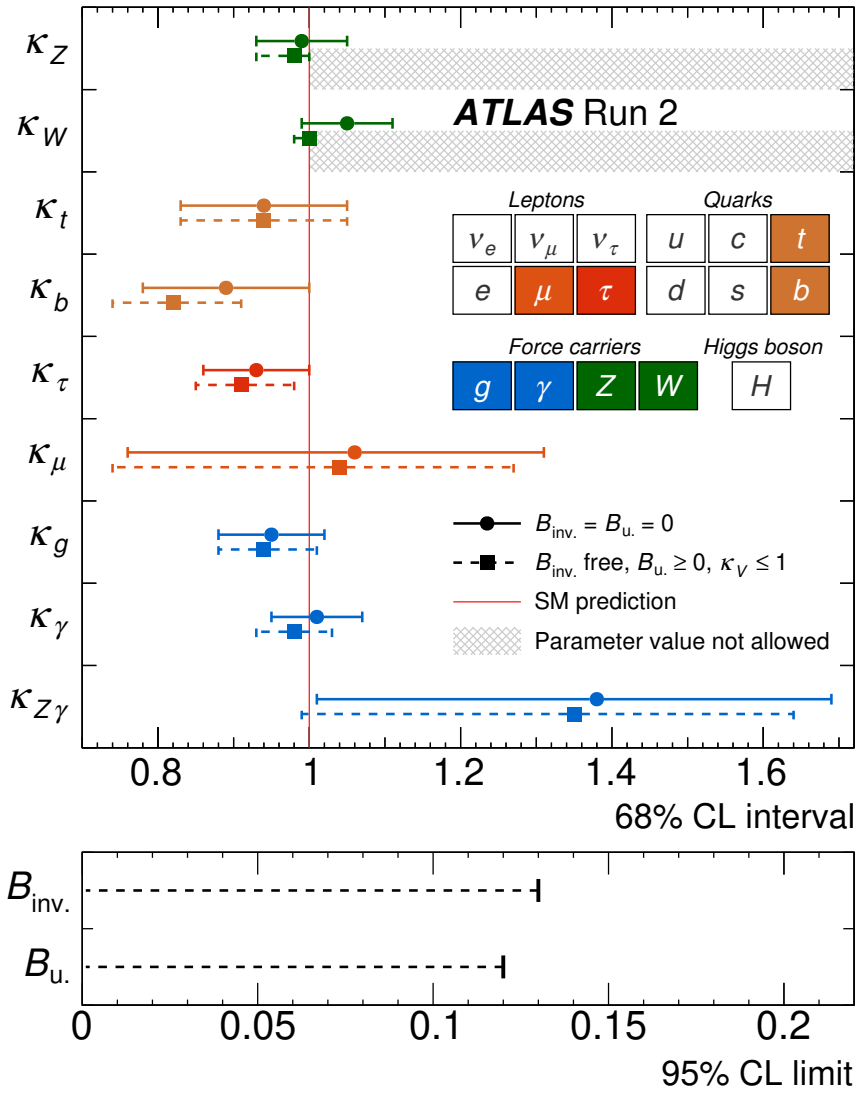

Figure 5.37 – Best-fit values and uncertainties for Higgs boson coupling modifiers per particle type with effective photon, $Z\gamma$ and gluon couplings. The horizontal bars on each point denote the 68% confidence interval. The scenario where $B_{i.} = B_{u.} = 0$ is assumed is shown as solid lines with circle markers. The p-value for compatibility with the SM prediction is 61% in this case. The scenario where $B_{i.}$ and $B_{u.}$ are allowed to contribute to the total Higgs boson decay width while assuming that $\kappa_V \leq 1$ and $B_{u.} \geq 0$ is shown as dashed lines with square markers. The lower panel shows the 95% CL upper limits on $B_{i.}$ and $B_{u.}$. [11].

CHAPTER 6

Measurement of Higgs mass

The observation of a new particle compatible with the Standard Model Higgs boson by the ATLAS and CMS experiments [4, 5], with the LHC Run 1 dataset at center-of-mass energies $\sqrt{s} = 7\,\text{TeV}$ and $8\,\text{TeV}$, has been a major step towards the understanding of the mechanism of electro-weak symmetry breaking. With the increased center-of-mass energy and higher integrated luminosity of the Run 2 LHC data, the Higgs boson properties can be measured with higher accuracy.

As already stated, the Higgs boson mass m_H is a free parameter in the SM and can be measured in the diphoton decay channel from the position of the narrow resonant peak in the $m_{\gamma\gamma}$ distribution due to the Higgs boson decay to two photons. The diphoton invariant mass is computed from the measured photon energies and from their directions relative to the diphoton production vertex selected with a neural-network algorithm (see Section 4.3.2). Differently from the production cross section analysis presented in Chapter 5, the mass analysis presents different challenges due to the fact that it is a systematic limited measurement, as can be noticed by the partial Run 2 $H \to \gamma\gamma$ ATLAS results [176]:

$$m_H = 124.93 \pm 0.40\,\text{GeV} = 124.93 \pm 0.21\,(\text{stat}) \pm 0.34\,(\text{syst})\,\text{GeV}. \tag{6.1}$$

The systematic uncertainty, dominated by the knowledge of the photon energy scale, is larger then the statistical one, so increasing the dataset statistic is of little help in reducing the total uncertainty. Therefore, in order to improve the measurement, additional care must be taken in detector performance understanding and modelling needed to reduce the systematic uncertainties and their impact on the measurement.

This chapter describes the ongoing effort to optimize the categorization for the mass measurement using the full Run 2 dataset and the expected results obtained so far. Since the result is limited by the systematic uncertainties, it is important to take them into account in the category optimization process.

6.1 Additional Monte Carlo samples

Given that the mass analysis has to measure the signal peak position, the signal modelling on both shape and normalization has to feature a parametric dependence on m_H, which is not included in the standard approach described in Chapter 4 where $m_H =$

125.09 GeV is assumed. In order to describe the m_H dependency , additional simulated Monte Carlo samples are generated with m_H set to 110, 122, 123, 124, 126, 127, 130, 140 GeV. For each Higgs boson production process, samples are generated using the same generator, showering algorithm and PDF set employed for the $m_H = 125$ GeV samples reported in Table 4.2, but with a factor ~ 10 smaller data statistic. The samples are then normalised with the state-of-the-art theoretical calculations of the corresponding SM production cross sections and $H \to \gamma\gamma$ branching ratio at different Higgs mass values [31].

6.2 Event Categorization

The events fulfilling the selections detailed in Section 4.3 are further classified in reconstructed categories with different signal over background ratio, invariant mass resolution and systematic errors.

The optimal categorization for the mass analysis is based on the interplay among three quantities:

- the categories **significance** Z of the Higgs signal over the continuum background. This quantity can only be defined once a category is built;
- the $m_{\gamma\gamma}$ peak **resolution** ($\sigma^{\gamma\gamma}$), which depends only on the p_{T}, pseudorapidity, and conversion status of the two photons selected in a given category. This quantity can be simply obtained once a category is built, even if it could be also extracted on a per-event basis with multivariate techniques;
- the $m_{\gamma\gamma}$ shift due to photon energy scale uncertainty, which depends only on the p_{T}, pseudorapidity, and conversion type of the two photons. This is the only quantity that can be easily defined for each diphoton event, since the systematic impact for each is already given as a function of these three quantities.

The first two quantities can be used together to approximate the expected statistical uncertainty on m_H for a given category c. Indeed, assuming a flat background under the peak, it can be shown that

$$\delta^{\mathrm{stat}}_{c,m_H} \sim 0.75 \cdot \frac{\sigma^{\gamma\gamma}_c}{Z_c}. \tag{6.2}$$

Since the total systematic uncertainty on $m_{\gamma\gamma}$ is completely dominated by photon energy scale (PES), the systematic uncertainty can be evaluated by using only PES uncertainty in two different correlation schemes: for a correct evaluation, the full decorrelation scheme of the photon energy scale systematic accounting to 69 nuisance parameters (69NP) should be used in conjunction with a complete shape likelihood model, while for quick evaluation of the impact of the uncertainties the fully correlated scheme with just 1 nuisance parameter (1NP) may be used. A nuisance parameter on the PES will vary the energy of the photons, impacting $m_{\gamma\gamma}$ for each event; therefore the total impact on the $m_{\gamma\gamma}$ distribution for a given category can be computed as reported in Eq. (4.7).

With the goal to define a categorization for the mass analysis, a two-fold approach was pursued. On one side, it was decided to proceed with similar studies carried out for

Run 1 and Run 2 analyses, where different ideas are exploited to minimize the expected uncertainty on the mass measurement, either by using photon kinematics or enhancing the signal significance by isolating events from peculiar production modes; these studies are reported in Section 6.2.2. On the other hand, an innovative approach was developed starting from the categorization of the STXS/coupling analysis in order to use a well defined optimization strategy, directly targeting the total m_H uncertainty to obtain the best possible result; these studies are reported in Section 6.2.3.

All the categorization reported in the following sections are compared among themselves by means of a simple yet complete full shape workspace. For each categorization, the signal and background analytical functions are fitted on signal MC samples and data sideband respectively. The impact of the 69 NPs of the full PES scheme is computed for each category by propagating the effect of each NP to the diphoton invariant mass, computing its impact with Eq. (4.7). Then it is included in the workspace with a Gaussian response function acting on the μ_{CB} peak position parameter. An Asimov dataset is produced with m_H fixed to 125.09 GeV and expected results are extracted.

6.2.1 Review of past categorization

Most of the categorization tests that will be reported in this section are based on the knowledge acquired throughout the development of Run 1 [34] and partial Run 2 [176] categorizations. A brief description of these two designs is reported, in order to give a starting base to the reader.

Run 1 categorization is mostly based on photons kinematics and it provides robust results with a rather small number of categories. All categories are untagged with respect to a particular production process and are defined with the following quantities:

- $|\eta_{S2}|$, the η position of the calorimetric cluster in the second sampling of the EM calorimeter;
- photon conversion status (namely photon converted or unconverted);
- $p_{\text{Tt}}^{\gamma\gamma}$, defined as the orthogonal component of the $p_{\text{T}}^{\gamma\gamma}$ to the so-called thrust-axis $\hat{\boldsymbol{t}}$:

$$p_{\text{Tt}}^{\gamma\gamma} = \left|\boldsymbol{p}_{\text{T}} \times \hat{\boldsymbol{t}}\right| \quad \text{with} \quad \hat{\boldsymbol{t}} = \frac{\boldsymbol{p}_{\text{T}}^{\gamma_1} - \boldsymbol{p}_{\text{T}}^{\gamma_2}}{\left|\boldsymbol{p}_{\text{T}}^{\gamma_1} + \boldsymbol{p}_{\text{T}}^{\gamma_2}\right|}.$$

The best energy resolution can be obtained for photons in the central barrel region and the worst around the transition region between barrel and endcap. At the same time, the resolution is generally better for unconverted photon than converted ones since the latter experience more energy loss before reaching the calorimeter. Categorizing in conversion status and photon pseudorapidity is also beneficial in term of systematic uncertainties: indeed, the largest systematics on photon energy scale stand for unconverted photons, mainly due to the electron to photon scale extrapolation, and for the barrel-endcap transition region, due to the knowledge of the material in this region.

Run 1 reconstructed categories [34] are defined by requiring both photons to be unconverted ("UU") or, conversely, with one of the two converted ("Conv"). These two

categories are then divided in three, based on the $|\eta_{S2}|$ of the two photons: a "central" category ("Cen") with both photons satisfying the $|\eta_{S2}| < 0.75$ selection (near the change in absorber thickness of the barrel calorimeter), a transition category ("Trans") where at least one of the two photons fall in the range $1.3 < |\eta_{S2}| < 1.75$ (excluding the "crack region" $1.37 < |\eta_{S2}| < 1.52$) and a region ("Rest") including the rest of all events. On top of these two selections on the conversion status and $|\eta_{S2}|$, two $p_{\mathrm{Tt}}^{\gamma\gamma}$ bins are defined for the "Cen" and "Rest" categories using the 70 GeV thresholds: this is done in order to improve the signal over background ratio, since the Higgs VBF production is expect to give rise to a harder $p_{\mathrm{Tt}}^{\gamma\gamma}$ spectrum.

The partial Run 2 categorization [176] was instead designed primarily for the Higgs production cross sections measurement and later adapted for the mass analysis. Therefore, all the reconstructed categories are tagged with respect to a production processes. In particular 10 ggF categories, 4 VBF categories, 8 VH categories and 9 top-related categories were present. Among these, most of the sensitivity to m_H was provided by ggF 0 jet category, that was split for the purpose of the mass analysis in a central category (both photons with $|\eta_{S2}| \leq 0.95$) and a forward one (at least one photon with $|\eta_{S2}| > 0.95$). Additional sensitivity on m_H was brought in by the VBF categories: these were based on BDT scores and $p_{\mathrm{T}}^{\mathrm{H}jj}$ requirement in a way that two "tight" categories were defined; it was found that these two contributed to the mass analysis sensitivity thanks to their high signal purity.

The results obtained with this categorization are reported in Table 6.1 and compared to the official partial Run 2 results (scaled to 139 fb^{-1}) and an inclusive categorization including all the diphoton selected events, see Section 4.3. It is important to highlight that photon reconstruction and energy calibration have received substantial updates with the state-of-the-art recommendation reported in Section 3.4.1. In particular, ATLAS reconstruction is now performed with the supercluster algorithm which is known to improve the energy resolution with respect to the "sliding window" approach [81] employed for partial Run 2 mass results. Concerning systematic uncertainties, the partial Run 2 result suffers from the relative large systematic uncertainties in the Inner Detector geometry modeling due to the insertion of IBL between Run 1 and Run 2, which are now reduced

Categorization	N_{cat}	Uncertainty [MeV] Total	Stat	Syst
Mass 2016 (original calibration) [176]	31	335	127	310
Inclusive	1	333	169	287
Mass 2016 [176]	31	308	130	279
Run1 [34]	10	291	132	260

Table 6.1 – Results obtained with the categorization of Run 1 and partial Run 2 results computed with a full shape workspace including the main systematic uncertainties for the mass analysis and the state-of-art photon reconstruction and recommendations. An "Inclusive" categorization is reported as well, to show the gain of a given categorization with respect to the inclusive diphoton selection. The first result is the official Run 2 result [176] scaled to 139 fb^{-1}, therefore obtained with older recommendations.

by a factor of 3.

6.2.2 Run1- and Run2-like approaches

The approaches reported in this section are possible variations of the Run 1 and partial Run 2 categorizations, or combinations of the two. The results are reported in Table 6.2, where each categorization is assigned an identification number. A brief description of the categorization and of the underlying idea is reported in the following for each test performed.

Test 2 divides the Run1 "Conv" categories in the two sub-categories: the first with exactly one photon converted (UC), the second with both photons converted (CC), so that 5 more categories are created in the end. The underlying idea was to maximally exploit the conversion status features.

Test 3 to 7 categorizations are based on a combination of Run 1 and Run 2 categories. The idea is to isolated the four VBF categories of the Run 2 analyis with respect to the others in order to get high signal over background ratios and then to apply in each the Run 1 categorization (Test 3). Possible variations includes: isolate only the two "tight" categories (Test 4), divide with Run 1 categories with conversion split detailed in Test 2 (Test 5), or isolate the ggF and VBF categories from all the rest (Test 6 and 7).

Test 8 and 9 further divide the Run 1 categories in three or four regions based on the value of the average pileup, since there is a mild dependence of the photon energy resolution with increasing pileup. Therefore the idea is to isolated Run 1 categories with even better resolution at low pileup values. Two (Test 8) or three (Test 9) thresholds are used, based on the quantiles of the average pileup distribution.

Test 10 to 21 are possible variations of Run 1 (or Test 3) categorization where different $p_{\mathrm{Tt}}^{\gamma\gamma}$ bins are used: removed $p_{\mathrm{Tt}}^{\gamma\gamma}$ splits (Test 10 and 11), with the $p_{\mathrm{Tt}}^{\gamma\gamma}$ threshold moved from 70 GeV to 100 GeV (Test 12 and 13), with three $p_{\mathrm{Tt}}^{\gamma\gamma}$ regions (Test 14 and 15). Then these test are re-done changing the $p_{\mathrm{Tt}}^{\gamma\gamma}$ thresholds with $p_{\mathrm{T}}^{\gamma\gamma}$ thresholds (Test 16 to 21). The idea is to understand the impact of these thresholds on the final expected uncertainty on m_H. With the full Run 2 statistics it is possible to produce more bins in $p_{\mathrm{Tt}}^{\gamma\gamma}$ without incurring in categories with limited static.

As can be observed from the Table 6.2, all the various tests lead to very similar results, with a total expected uncertainty on m_H of around 290 MeV. The best results are represented by Test 14 and 15, where the additional $p_{\mathrm{Tt}}^{\gamma\gamma}$ region is able to lower down the statistical uncertainty by 8 MeV with respect to Run 1 categorization and, at the same time, to better isolate events with large PES uncertainty in the high $p_{\mathrm{Tt}}^{\gamma\gamma}$. Test 14 is considered the most interesting and it was preferred over Test 15 since it provides almost the same results with halved number of categories.

6.2.3 Global optimization

In order to get rid of the *try-and-error* method of the above approaches, an innovative global optimization approach to the definition of the mass analysis categories was elaborated, with a clear optimization metric. The following approaches are based on the

Test	Categorization	N_{cat}	Uncertainty [MeV] Total	Stat	Syst
1	Run 1	10	292	133	260
2	Run1 with splitting in conversion (UU/UC/CC)	15	292	132	260
3	VBF and (rest+ggH), then Run1	20	291	130	260
4	VBF_{tight} and (rest+ggH), then Run1	20	291	130	260
5	VBF and (rest+ggH), then Run1 with (UU/UC/CC)	30	291	130	261
6	ggF, VBF, rest, then Run1 on ggF,VBF	21	293	133	261
7	ggF, VBF, rest, then Run1 with (UU/UC/CC) on ggF,VBF	31	293	132	262
8	Run1 with 3 $<\mu>$ regions (thresholds $\mu = 15, 30$)	30	291	132	259
9	Run1 with 4 $<\mu>$ regions (thresholds $\mu = 15, 25, 42$)	40	291	132	259
10	Run1 without $p_{\text{Tt}}^{\gamma\gamma}$ split	6	293	149	252
11	Test3 without $p_{\text{Tt}}^{\gamma\gamma}$ split	12	292	144	254
12	Run1 with 2 $p_{\text{Tt}}^{\gamma\gamma}$ regions (threshold 100 GeV)	10	290	129	260
13	Test3 with 2 $p_{\text{Tt}}^{\gamma\gamma}$ regions (threshold 100 GeV)	20	289	128	259
14	Run1 with 3 $p_{\text{Tt}}^{\gamma\gamma}$ regions (thresholds 70,130 GeV)	14	287	125	258
15	Test3 with 3 $p_{\text{Tt}}^{\gamma\gamma}$ regions (thresholds 70,130 GeV)	28	286	122	259
16	Run1 with $p_{\text{T}}^{\gamma\gamma}$ cut at 100	10	292	134	259
17	Test3 with $p_{\text{T}}^{\gamma\gamma}$ cut at 100	20	291	131	260
18	Run1 with $p_{\text{T}}^{\gamma\gamma}$ cut at 130	10	291	132	259
19	Test3 with $p_{\text{T}}^{\gamma\gamma}$ cut at 130	20	289	129	259
20	Run1 with 3 $p_{\text{T}}^{\gamma\gamma}$ regions (130, 190)	14	287	128	257
21	Test3 with 3 $p_{\text{T}}^{\gamma\gamma}$ regions (130, 190)	28	295	129	265

Table 6.2 – Results of the various categorization tests based on Run 1 and partial Run 2 analysis categorizations reported in Section 6.2.2.

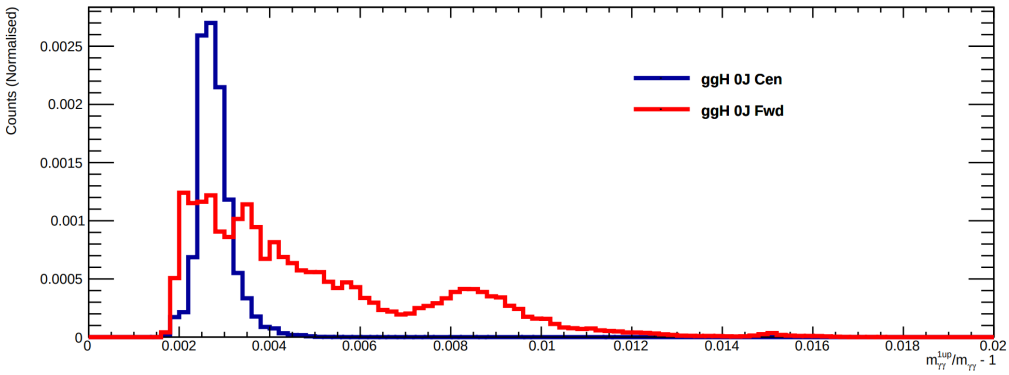

Figure 6.1 – Distribution of the impact on $m_{\gamma\gamma}^{1up}/m_{\gamma\gamma} - 1$ due to the $+1\sigma$ variation associated to the 1NP scheme of the photon energy scale uncertainties shown for the two best categories of the partial Run 2 mass results [176]. The ggH_0J_Cen category select events with no reconstructed jets and both photons with $|\eta|^{\gamma} < 0.95$ while the "Fwd" one retains other events.

$H \to \gamma\gamma$ STXS/coupling categorization employed for the preliminary full Run 2 results [7] that, for what follows, present no differences with the one described in Section 5.4. The idea is to make use of the great signal over background ratios and of the photon energy resolution sub-divisions already embedded in the STXS categorization, the first provided by advanced BDT algorithms and the latter by the many $p_{\mathrm{T}}^{\gamma\gamma}$ bins encoded in the STXS definition. Indeed, Run 1- and Run 2-like categories described in the above section are missing a clear purity or significance optimization, which is instead provided by the STXS categorization and it is helpful to reduce the statistic uncertainty associated to the measurement of m_H. On the other hand, the STXS categorization is made of hundred of categories, which is probably not well justified to measure one single parameter, and it presents no splits on $|\eta|$ and conversion, which are beneficial in reducing the impact of PES systematic.

As can be seen in Table 6.3, the STXS categorization (Test 22) has an improved stat-only uncertainty but a much larger systematic uncertainty with respect to Run1-like categorizations, but with a larger number of categories too. Therefore in order to use the STXS categories, it is needed to optimize the expected systematic uncertainty on m_H and, at the same time, to reduce their number. The former point has been addressed in two different ways:

- directly selecting events with small or large systematic, by calculating the expected impact of the PES on $m_{\gamma\gamma}$ (called "split syst" in the table). An example of the expected impact of the 1NP PES variation on $m_{\gamma\gamma}$ is shown in Figure 6.1: it is possible to directly select events with low, medium or high systematic uncertainty directly from this distribution by using quantiles of order 1/3, producing equally populated categories;

- use Run 1-like $|\eta|$ and conversion status selections (called "split conv/eta"), since these implicitly optimize the systematic uncertainty.

Test	Categorization	N_{cat}	Uncertainty [MeV] Total	Stat	Syst
1	Run1	10	291	132	260
14	Run1 with 3 $p_{\mathrm{Tt}}^{\gamma\gamma}$ regions (thresholds 70,130 GeV)	14	287	125	258
22	STXS	88	320	120	300
23	STXS, split syst	160	280	118	254
24	STXS, split conv/eta	316	274	111	251
25	STXS, split syst/conv/eta	627	273	110	250
26	STXS, merge stat (18 cats, -0.5%), split syst	40	277	117	251
27	STXS, merge stat (18 cats, -0.5%), split syst/conv/eta	162	274	112	250
28	STXS, merge stat (10 cats, -1.7%), split syst/conv/eta	89	276	111	253
29	STXS, merge stat (5 cats, -4.7%), split syst/conv/eta	59	278	114	253
30	STXS, split conv/eta, merge stat, split syst	32	280	113	256
31	STXS, split conv/eta, merge stat in syst bins	32	283	113	259

Table 6.3 – Expected results on m_H for the various global categorization tested in Section 6.2.3.

Both the methods have been proven to be effective in reducing the systematic uncertainty impact, as it is reported in the second block of Table 6.3. The "syst" split and "conv/eta" split has been tested on a STXS categorization (Test 23 and 24, with additional constraints in order to have enough data sideband events to perform the background fit): both these categorizations managed to get a systematic uncertainty on m_H smaller than the Run 1 categorization. An additional test is performed by dividing the 88 STXS coupling categories with a combination of both "eta/conv" and "syst" split, producing 627 categories in the end. The final categorization has found to provide the best results, with a 6% gain over the Run 1 categorization and 11% gain over the partial Run 2 categorization. On the other hand, managing 627 categories in the full analysis chain is prohibitive, but this results is important because it could be regarded as the best possible theoretical limit for the m_H categorization optimization.

In order to reduce the number of categories, a method to merge STXS coupling categories with the smallest possible impact on the m_H statistical uncertainty has been developed. This method makes use of the approximation reported in Eq. (6.2) which validity is demonstrated in Figure 6.2a, where each point in the plot represents one of the STXS coupling categories. On the y-axis the value of $\frac{\sigma}{Z}$ is reported, obtained from $\sigma_{90}^{\gamma\gamma}$, S_{90} and B_{90} computed in the smallest window containing 90% of the signal; on the x-axis is reported the expected stat-only m_H uncertainty obtained from a complete shape fit where one m_H POI for each category has been used to fit the Asimov dataset. It is therefore clear that $\frac{\sigma}{Z}$ can be used to describe with good approximation the expected statistical uncertainty on m_H, while being easier to compute. Given this, since with N categories the expected stat-only m_H uncertainty δ can be computed as

$$1/\delta^2 = \sum_i^N (1/\delta_i)^2 \tag{6.3}$$

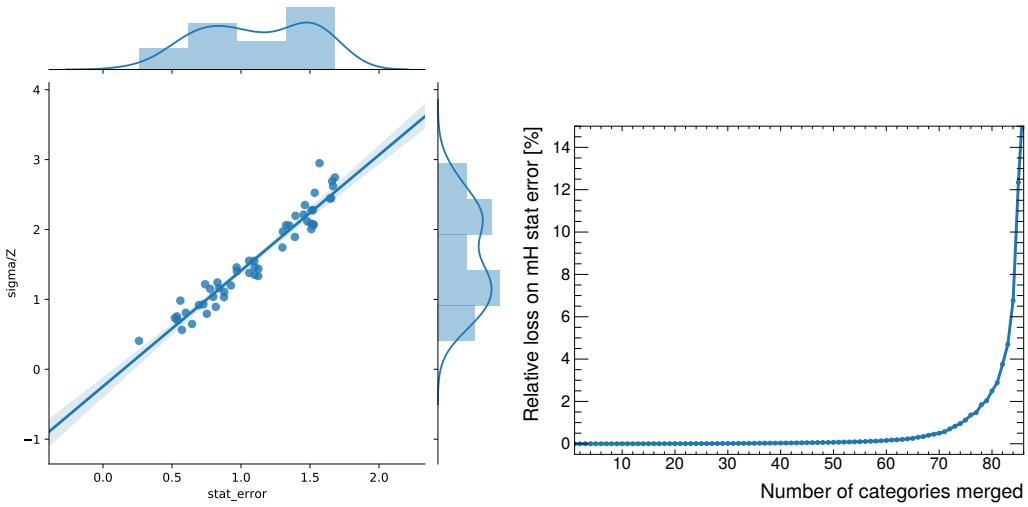

(a) **(b)**

Figure 6.2 – (a) Scatter plot of the STXS coupling categories placed on the plane with their values of $\frac{\sigma}{\Sigma}$ on the y-axis and the expected stat-only uncertainties obtained from the complete STXS shape fit on the x-axis. (b) Statistical merging procedure applied to the STXS coupling categories: on the x-axis is reported the number of categories merged while on the y-axis the relative loss on expected stat-only m_H uncertainty.

where δ_i are the expected stat-only m_H uncertainties for each category computed with Eq. (6.2), it is possible to define a metric to reduce the number of categories by merging the less sensitive ones. Supposing one wants to merge the first two categories, the total uncertainty is given by

$$1/\delta^2 = 1/\delta_1^2 + 1/\delta_2^2 + \sum_{i\geq 3} (1/\delta_i)^2 \tag{6.4}$$

$$1/\delta'^2 = (1/\delta_{1+2})^2 + \sum_{i\geq 3} (1/\delta_i)^2 \tag{6.5}$$

for the unmerged and merged case respectively. By definition $\delta \leq \delta'$, since there is one category less in the second case, and therefore the best possible merging is obtained when $(1/\delta_{1+2})^2 = 1/\delta_1^2 + 1/\delta_2^2$. This in turn means that (applying Eq. (6.2))

$$\frac{(S_1+S_2)^2}{B_1+B_2}\frac{(S_1+S_2)}{S_1\sigma_1^2+S_2\sigma_2^2} = \frac{S_1^2}{B_1\sigma_1^2} + \frac{S_2^2}{B_2\sigma_2^2} \tag{6.6}$$

Therefore, it is possible to define the distance between two categories as

$$d_{ij} = \frac{S_i^2}{B_i\sigma_i^2} + \frac{S_j^2}{B_j\sigma_j^2} - \frac{(S_i+S_j)^2}{B_i+B_j}\frac{(S_i+S_j)}{S_i\sigma_i^2+S_j\sigma_j^2} \tag{6.7}$$

which is positive defined and can be uses to select the two categories to be merged that minimize the increase of statistical uncertainty on the m_H

$$\min\{\delta - \delta'\} \Leftrightarrow \min_{\forall i,j}\{d_{ij}\}. \tag{6.8}$$

The distance d_{ij} can be used algorithmically: first all the distances are computed for each pair of categories, the smallest distance is found, the two categories are merged in one category and this procedure can be repeated until no categories are left. This procedure has been applied to the STXS categories and the results at each merging step are reported in Figure 6.2b. Of course, the merging procedure can only increase the total uncertainty and the only possibility is to set a threshold where to stop this reduction process, in order to reduce enough the number of categories without degrading the statistical uncertainty on m_H. The fourth block of Table 6.3 reports the categorization (Test 26 to 29) where first the STXS categories have been merged according to this algorithm (with the number of remaining categories and the loss on m_H statistical uncertainty stated in the row description) and then split further to reduce the systematic uncertainties impact. These categorization are close to reproduce the theoretical limit obtained with 627 categories but with much less categories.

The Test 30 in Table 6.3 reports instead a variation of this method: the STXS categories are first divided with Run 1-like "conv/eta" splits, then merged with the statistical procedure detailed above and finally split again with the systematic value impact. The number of categories has been tuned in order to obtain around 30 categories, as in the partial Run 2 results. As can be seen, these categorization are usually suboptimal with respect to the results reported in the third block, since the statistical merging does not take into account the mean of the systematic impact in each category, so it may end up in merging two categories that have a clearly different systematic uncertainty impact. To overcome this limitation, one additional categorization (Test 31) has been designed and are reported in the last raw of the table: the STXS categories have been first split with Run 1-like conv/eta splits, but then the categories are labeled in three groups according to the mean value of the 1NP systematic impact; then in each of the three macro-groups a statistical merging procedure is carried out so that only categories with the same level of systematic impact can be merged together. The total number of categories is monitored and the procedure is stopped when the number of categories is around 30.

As can been observed in the table, the approaches reported in this section provide usually a slightly better results with respect to Run 1 categorization and to the selected one in Section 6.2.2. Beside this, it was decided not to use one of these because the gain on the total m_H has been considered minimal with respect the additional complexity these categorizations introduce for the whole analysis, in particular for background modeling and additional reconstructed objects needed to be supported.

6.2.4 Categorization for the mass analysis

Despite the efforts to inject the purity of the STXS categorization into the mass categorization and to provide a more global approach to the mass categorization problem, the

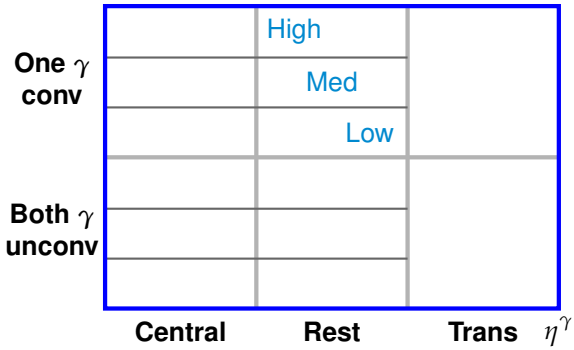

Figure 6.3 – Simple sketch showing the mass analysis categories.

improvements are limited, in particular compared to the amount of extra complication these categorizations introduce. Therefore, given the studies reported in Section 6.2.2, it was decided to use a Run 1-like approach for the Run 2 mass analysis, in particular the Test 14 reported in Table 6.2, since it provides some improvements with respect to the Run 1 categorization, without further complication of the analysis strategy.

A sketch of this categorization is shown in Figure 6.3, while the purities of the categories with respect to the Higgs production modes is shown in Figure 6.4. The SM yields at 139 fb^{-1} and the main features of the designed categories are reported respectively in Table 6.4 and Table 6.5. The two $p_{\mathrm{Tt}}^{\gamma\gamma}$ selections have been chosen to have enough signal events in the selected region with high $p_{\mathrm{Tt}}^{\gamma\gamma}$, given that the 70 and 130 GeV thresholds correspond to the 30% and 10% quantiles of the signal $p_{\mathrm{Tt}}^{\gamma\gamma}$ distribution. The three bins in $p_{\mathrm{Tt}}^{\gamma\gamma}$ are called "Low", "Med", "High". As expected, "Med" and "High" categories feature a large signal fraction coming from non-ggF production modes, with up to 30% VBF contribution. Given their higher purity and the better photon energy resolution due to the selection of high p_{T} photons, these are the ones that provide the lowest stat-only uncertainties. On the other hand, they are affected by larger systematic uncertainties with respect to "low" categories, since PES uncertainties increase with the increase of photon p_{T}.

This categorization is then compared to the latest partial Run 2 results in Table 6.6. The categorization described in this section outperforms the partial Run 2 results scaled to 139 fb^{-1} on the total mass uncertainty by 15%, gain that is reduced to 7% if the results are extracted with the same partial Run 2 categorization but with updated reconstruction and calibrations. With respect to the Run 1-like categorization, the inclusion of one additional $p_{\mathrm{Tt}}^{\gamma\gamma}$ threshold brings a gain of 1.5%.

6.3 Signal and background modeling

Signal and background modeling for the mass analysis follow almost exactly what has been described in Section 4.5 and Section 4.6. In addition, the signal modeling strategy is adapted in order to include a parametric dependence on m_H, since this will be the parameter of interest in the likelihood model of Eq. (4.9).

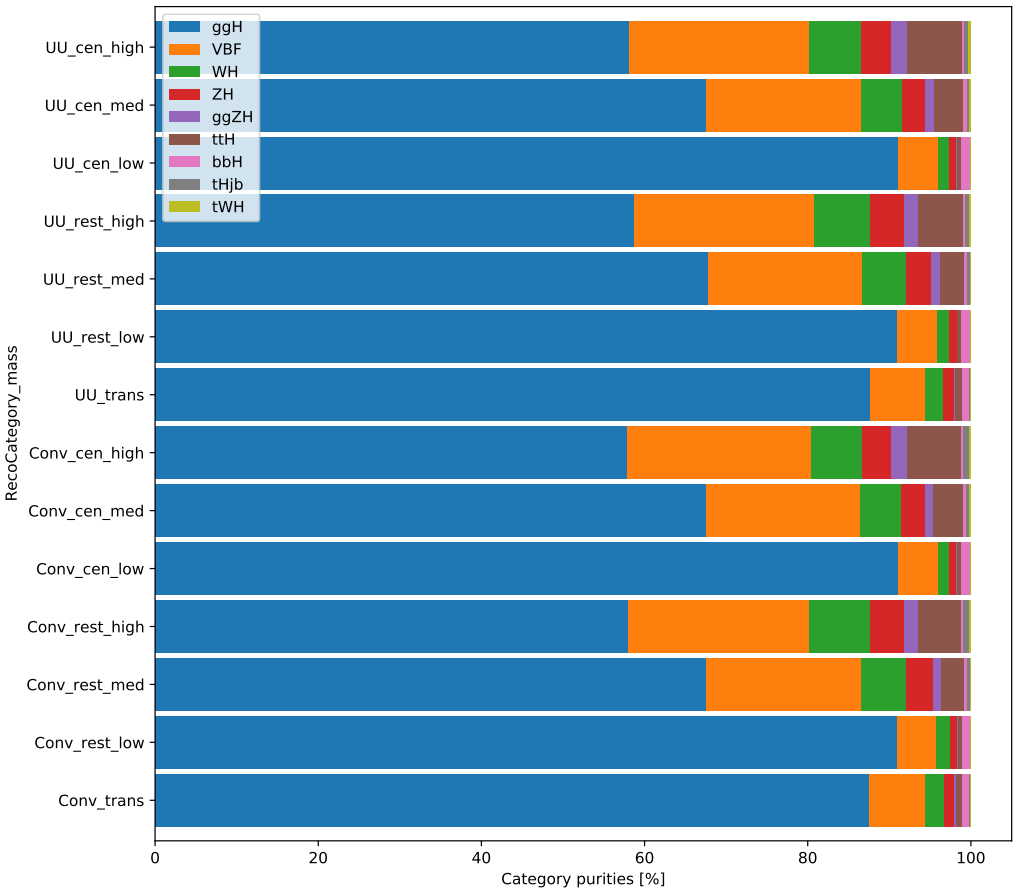

Figure 6.4 – Category composition for the various production modes.

Category	ggF	VBF	WH	ZH	ggZH	$t\bar{t}H$	$b\bar{b}H$	tHbj	tHW
UU Cen high	24.13	9.16	2.66	1.51	0.82	2.80	0.12	0.21	0.11
UU Cen med	67.54	18.97	4.97	2.87	1.13	3.54	0.44	0.35	0.13
UU Cen low	751.50	40.40	11.55	6.54	0.88	4.75	9.02	0.44	0.14
UU Rest high	25.85	9.71	3.06	1.79	0.78	2.40	0.14	0.20	0.10
UU Rest med	114.45	31.86	8.98	5.33	1.69	4.96	0.61	0.65	0.17
UU Rest low	1260.60	66.96	21.30	11.90	1.46	7.03	14.56	1.04	0.22
UU Trans	413.74	32.32	10.57	5.94	0.97	3.63	4.42	0.60	0.10
Conv Cen high	15.41	5.98	1.68	0.91	0.52	1.78	0.06	0.18	0.06
Conv Cen med	42.80	11.95	3.18	1.84	0.67	2.27	0.28	0.24	0.09
Conv Cen low	470.75	24.97	7.17	4.18	0.53	2.98	5.60	0.29	0.10
Conv Rest high	29.40	11.21	3.80	2.11	0.84	2.66	0.15	0.36	0.12
Conv Rest med	129.32	36.28	10.69	6.30	1.82	5.40	0.72	0.71	0.17
Conv Trans	696.22	54.22	18.41	10.18	1.74	6.02	6.96	1.06	0.19
Conv Rest low	1435.81	76.33	25.39	14.15	1.52	7.58	15.73	1.26	0.19

Table 6.4 – SM yields at 139 fb^{-1} for the various Higgs production modes for the mass analysis categorization

Category	$\sigma_{90}^{\gamma\gamma}$[GeV]	S_{90}	B_{90}	f_{90} [%]	Z	$\delta_{m_H}^{stat}$[GeV]	$\delta_{m_H}^{1NP}$[GeV]	N_{data}^{SB}
UU Cen high	1.98	37.37	60.87	38.04	4.39	0.45	0.46	650
UU Cen med	2.40	89.95	491.56	15.47	3.94	0.61	0.38	3912
UU Cen low	2.68	742.70	11832.79	5.91	6.76	0.40	0.33	87934
UU Rest high	2.23	39.61	123.10	24.35	3.40	0.66	0.87	1207
UU Rest med	2.69	151.81	1700.69	8.19	3.63	0.74	0.70	12618
UU Rest low	3.07	1246.56	38417.02	3.14	6.33	0.49	0.62	251877
UU Trans	3.67	425.08	15709.78	2.63	3.38	1.09	1.22	84497
Conv Cen high	2.11	23.94	38.83	38.14	3.52	0.60	0.45	422
Conv Cen med	2.63	56.99	355.21	13.83	2.95	0.89	0.39	2616
Conv Cen low	3.01	464.90	8768.69	5.03	4.92	0.61	0.35	58723
Conv Rest high	2.62	45.58	184.41	19.82	3.23	0.81	0.67	1511
Conv Rest med	3.20	172.25	2447.78	6.57	3.44	0.93	0.50	15021
Conv Rest low	3.70	1420.15	52822.79	2.62	6.15	0.60	0.42	286684
Conv Trans	4.46	715.50	28803.39	2.42	4.20	1.06	0.71	129430

Table 6.5 – Categorization performance in the smallest window containing 90% of signal events: the window width is $\sigma_{90}^{\gamma\gamma}$, the expected number of Higgs signal and background events are S_{90} and B_{90} respectively. B_{90} is obtained by fitting an ExpoPoly2 function over the TI data sidebands and integrating it in the 90% signal window. The fraction of signal events over the total $f = S_{90}/(S_{90} + B_{90})$ and the expected significance Z are computed too. The expected statistical error on m_H is computed as $\delta_{m_H}^{stat} = \sigma^{\gamma\gamma}/Z$ for each category, to provide a feeling of the expected uncertainty on the mass. The shift caused by the PES impact of 1NP scheme computed as $\delta_{m_H}^{1NP} = m_{\gamma\gamma}^{1NP} - m_{\gamma\gamma}^{nom}$ is reported.

Categorization	N_{cat}	Uncertainty [MeV] Total	Stat	Syst
Mass 2016 (original calibration) [176]	31	335	127	310
Inclusive	1	333	169	287
Mass 2016 [176]	31	308	130	279
Run1 [34]	10	291	132	260
Run1-like with 3 $p_{\mathrm{Tt}}^{\gamma\gamma}$ bins	14	287	125	258

Table 6.6 – Results obtained with a full shape workspace including the main systematic uncertainties for the mass analysis. The categorization described in this section is compared to the official ATLAS partial Run 2 results obtained with old recommendations scaled to 139 fb^{-1}, and with three other categorizations built upon updated ATLAS reconstruction and calibration (see Chapter 3.4.1): "Inclusive" where only the standard diphoton selection is applied, the Run 2 mass analysis categorization and the Run 1 categorization.

6.3.1 Signal model

In order to perform the mass measurement, it is mandatory that the signal shape is described by a parametric function of m_H. This is possible using the additional signal MC samples generated at different values of m_H described in Section 6.1 in addition to the 125 GeV ones. To this end, the parameters of the Double Sided Crystal Ball function of Eq. (4.5) have been written as a function of m_H for each category as

$$\begin{aligned}
\mu_{\mathrm{CB}}(m_H) &= m_H + B_{\mu_{\mathrm{CB}}} + A_{\mu_{\mathrm{CB}}}(m_H - 125\,\mathrm{GeV}) \\
\sigma_{\mathrm{CB}}(m_H) &= B_{\sigma_{\mathrm{CB}}} + A_{\sigma_{\mathrm{CB}}}(m_H - 125\,\mathrm{GeV}) \\
\alpha_{\mathrm{Low}}(m_H) &= \alpha_{\mathrm{Low}} \\
\alpha_{\mathrm{High}}(m_H) &= \alpha_{\mathrm{High}} \\
n_{\mathrm{Low}}(m_H) &= n_{\mathrm{Low}}|_{125\,\mathrm{GeV}} \\
n_{\mathrm{High}}(m_H) &= n_{\mathrm{High}}|_{125\,\mathrm{GeV}}
\end{aligned} \tag{6.9}$$

where $n_{\mathrm{Low}}|_{125\,\mathrm{GeV}}$ and $n_{\mathrm{High}}|_{125\,\mathrm{GeV}}$ are the values obtained from the fit of the 125 GeV sample at $m_H = 125$ GeV. The parametrization described in Eq. (6.9) is used in a simultaneous fit over all the MC signal samples with different m_H values. The fitted parameters for each category are thus $B_{\mu_{\mathrm{CB}}}$, $A_{\mu_{\mathrm{CB}}}$, $B_{\sigma_{\mathrm{CB}}}$, $A_{\sigma_{\mathrm{CB}}}$, α_{Low} and α_{High}, while n_{Low} and n_{High} are kept constant since they model the slope in the tails and therefore only negligibly affect the peak position of the DSCB, and in turn they do not affect the mass measurement. After the determination of these *global* coefficients, they are kept fix in the Eq. (4.9) while fitting the observed data. As an example, the result of the simultaneous fit over the MC samples for the category "UU cen low "is shown in Figure 6.5, while Figure 6.6 reports a comparison of the projected simultaneous fit for $m_H = 125$ GeV with a single standalone fit performed over the 125 GeV MC samples for some example categories. For each parameter, Figure 6.7 shows a comparison for the category "UU cen low" between the result of the simultaneous fit and the result of a linear fit performed on the

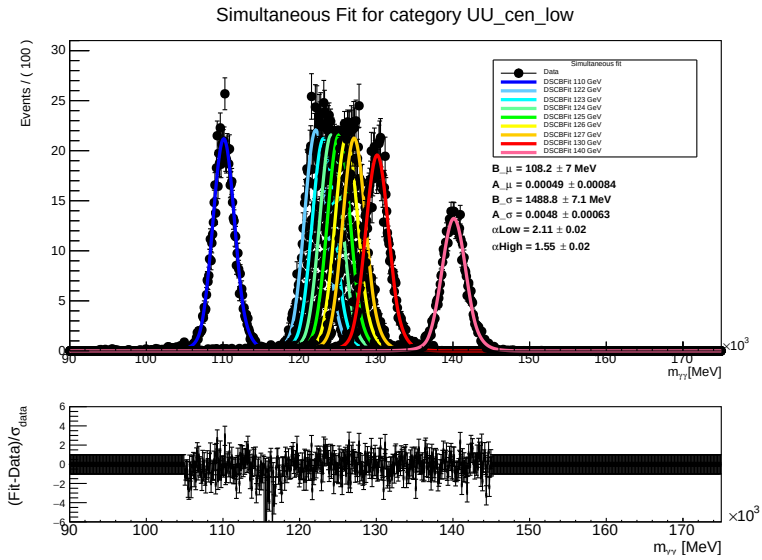

Figure 6.5 – Result of the simultaneous fit for the category UU cen low: the black dots correspond to the various MC samples, whereas each signal PDF (each one for a different m_H value) is shown in a different color, projected from the simultaneous one. The values of the simultaneously fitted parameters are shown in the legend on the right side of the plot. The residuals are shown in the lower part of the plot.

DSCB parameters obtained by fitting each single mass samples.

6.3.2 Background model

The background modeling strategy follows exactly what it is described in Section 4.6. Background $m_{\gamma\gamma}$ templates for all categories are constructed from a combination of the $\gamma\gamma$, γj and jj processes with data-driven normalization and shapes corrections. These background templates are then fitted with a signal+background model with different background functions in order to perform the spurious signal test. The results are reported in Table 6.7.

6.4 Systematic uncertainties

The most important systematic uncertainties for the m_H measurements are the photon energy scale and resolution sources impacting the $m_{\gamma\gamma}$ signal model, in particular peak position and width. These will be detailed in Section 6.4.1. Additional systematic sources are taken into account due to the bias on m_H created by the modeling with analytical function of the signal and background shapes, detailed in Section 6.4.2.

The signal yield uncertainties, like photon efficiency and theoretical uncertainties described in Section 4.7, play a negligible role in the determination the final m_H results. Their impact is limited to a mild variation of the relative importance of different reconstructed categories in the model, therefore only in case of large discrepancies between

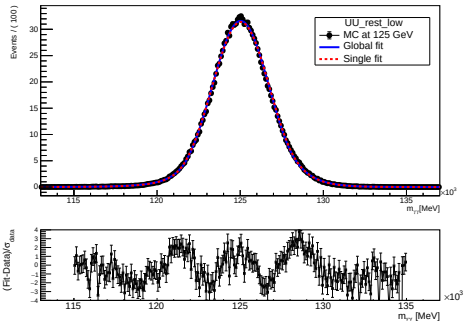

(a) UU Rest Low

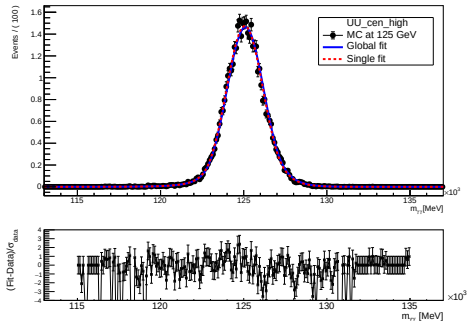

(b) UU Cen High

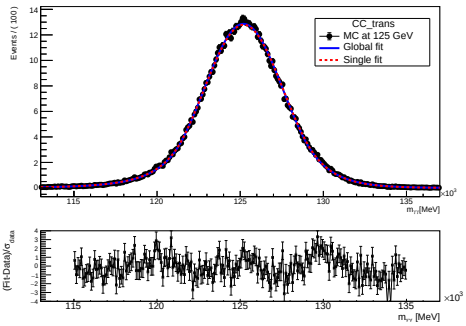

(c) Conv Trans

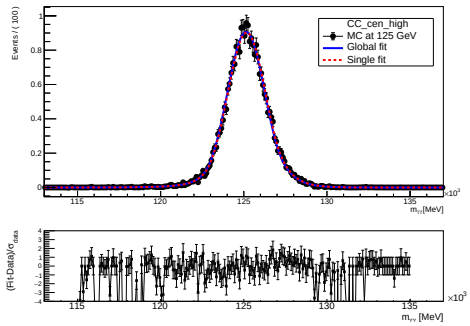

(d) Conv Cen High

Figure 6.6 – Comparison of the simultaneous ("global") fit, projected at $m_H = 125\,\text{GeV}$ for a given category, with the standalone fit ("single") performed over the 125 GeV MC sample for the same category

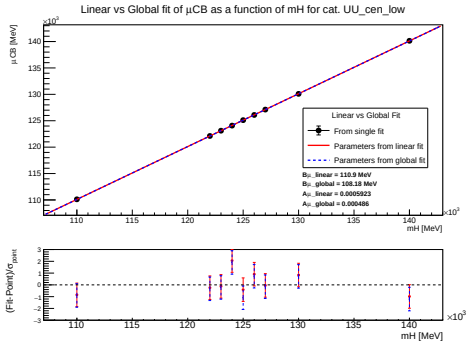

(a) μ_{CB}

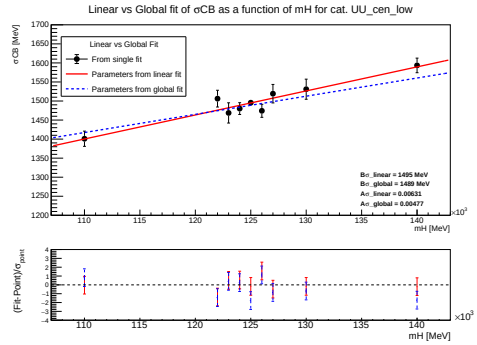

(b) σ_{CB}

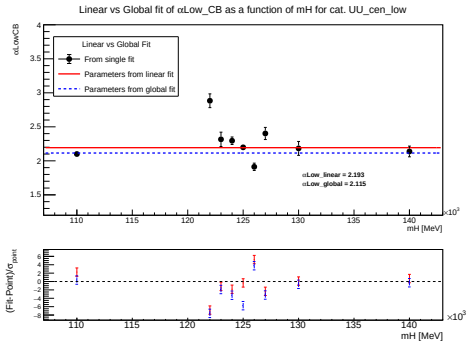

(c) α_{Low}

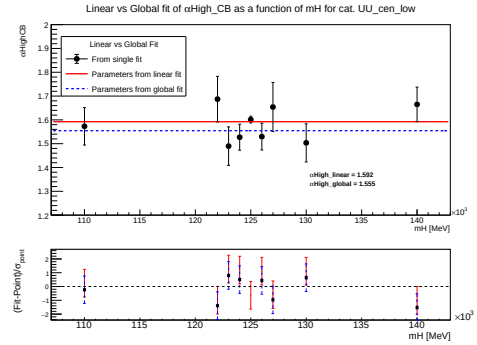

(d) α_{High}

Figure 6.7 – Comparison between the results of the simultaneous fit (dashed blue line) and of the linear fit (solid red line) over the DSCB parameters value obtained by fitting each single MC samples at different m_H values (back dots), for the category "UU cen low" category.

Category	max S	Func	$\frac{S}{\delta S}$ (%)	$\frac{S}{S_{ref}}$ (%)
UU cen high	0.953	Pow	7.28	1.50
UU cen med	2.00	Exp2	6.68	1.65
UU cen low	28.6	Exp2	13.4	1.69
UU rest high	1.06	Exp	12.3	4.79
UU rest med	3.81	Exp2	10.9	4.38
UU rest low	51.7	Exp2	29.3	7.26
UU trans	14.9	Exp2	13.8	6.41
Conv cen high	1.85	Exp	12.7	2.94
Conv cen med	11.7	Exp2	22.1	5.97
Conv cen low	57.0	Exp2	21.8	3.49
Conv rest high	2.37	Exp	22.5	9.35
Conv rest med	7.73	Exp2	18.2	7.93
Conv rest low	43.4	Exp2	21.5	4.20
Conv trans	28.1	Exp2	17.9	7.24

Table 6.7 – The final background modeling decision and the size of spurious signal uncertainties in the mass range 123 to 127 GeV with 0.500 GeV step, "max S" is the maximum fitted spurious signal yield, δS is the uncertainty on spurious signal found on background template with signal + background fit, and S_{ref} is the expected number of Higgs signal events for this category.

data and expectation they may have an impact on m_H.

6.4.1 Signal shape uncertainties

As described in Section 4.7.2, the impact of the PES are computed with the "ratio-of-mean" technique while for PER the "inter-quantile" approach is employed. The impact is computed for each uncertainty component and for each reconstructed category and are implemented in Eq. (4.9) with response functions that multiply directly the μ_{CB} and σ_{CB} parameters, while other parameters of the analytical signal model are considered not affected. The nuisance parameters are fully correlated across different categories.

The Figure 6.8 shows the impact of PES scales for the mass categories, while Figure 6.9 shows the quadrature sum of all the sources for each category. The total effect on the mass ranges from $\sim \pm 0.17\%$ in the "Conv Rest low" category to $\sim \pm 0.58\%$ in the "UU Trans" category. It is clear that "Trans" categories are the most affected by large PES impact, while "Low" categories are the least ones. Comparing one "UU" and the respective "Conv" categories, the systematic are usually larger as expected. Categories with higher and higher $p_{\mathrm{Tt}}^{\gamma\gamma}$ threshold receive larger and larger PES impact, while "Central" category are less affected than "Rest" ones. The dominant systematic sources are the L1 and L2 gain calibration, the layer inter-calibration systematic and the photon cluster lateral leakage systematic, see Section 3.4.1 for their description.

The impact of photon energy resolution systematic components was studied with the interquantile method. The Figure 6.10 shows the squared sum of all the energy resolution systematic up contributions for each category: the total effect on the width of $m_{\gamma\gamma}$

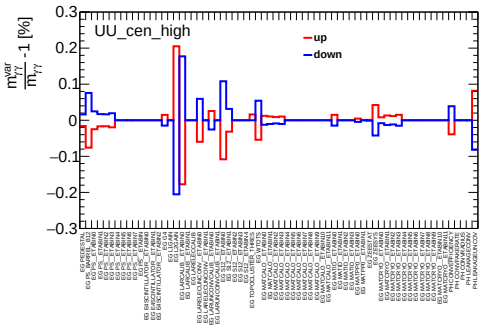

(a) UU cen high

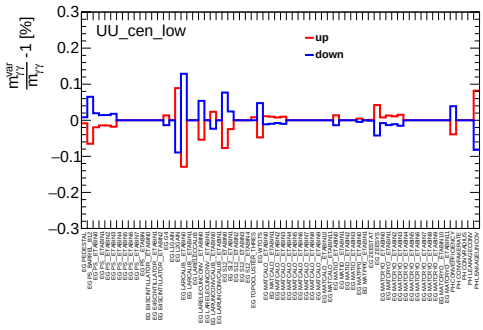

(b) UU cen low

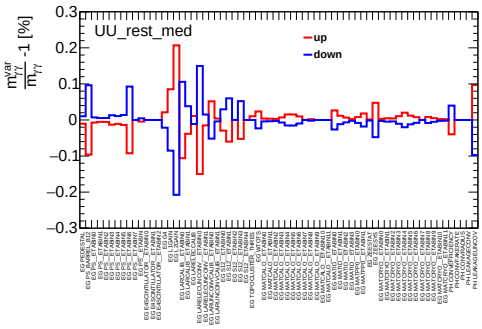

(c) UU rest med

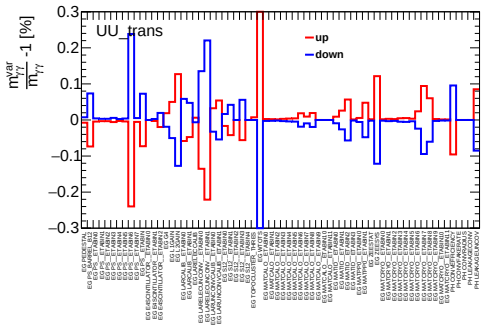

(d) UU trans

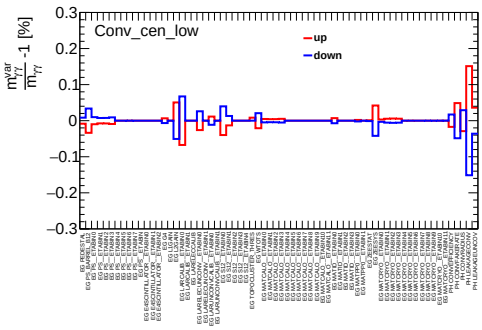

(e) Conv cen Low

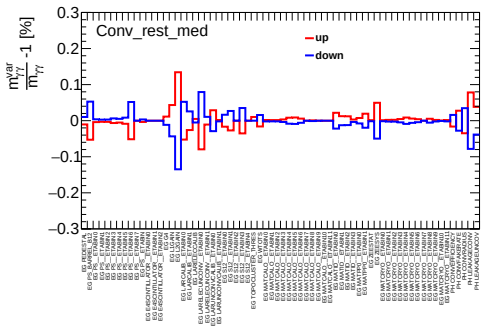

(f) Conv rest med

Figure 6.8 – Evaluation of the impact of each the photon energy scale nuisance parameter for some categories of the mass analysis. The up and down uncertainties (evaluated using respectively the $+1\sigma$ and -1σ varied distributions) are shown in red and blue respectively.

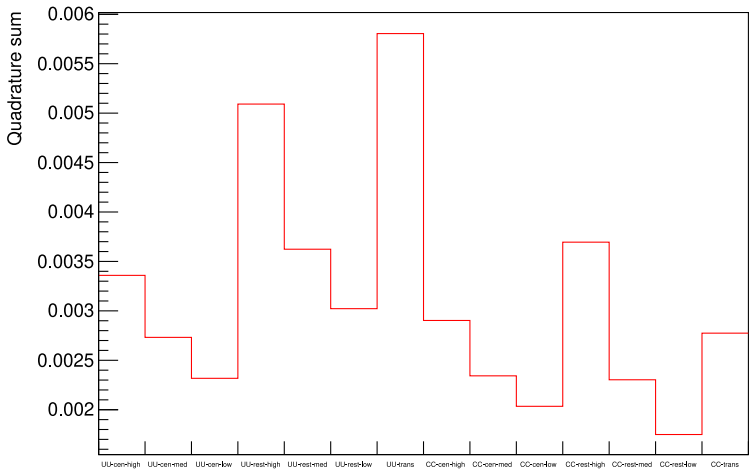

Figure 6.9 – Squared sum of all the PES systematic impacts on the $m_{\gamma\gamma}$ mean for each category. The total effect on the mass ranges from $\sim \pm 0.17\%$ in the Conv rest low category to $\sim \pm 0.58\%$ in the UU trans category.

peak varies from $\sim \pm 5.3\%$ in the "Conv rest low" category to $\sim \pm 20\%$ in the "UU cen high" category. The impact of the resolution uncertainties on the mass has found to be negligible.

6.4.2 Modeling bias on m_H

Since the parameters of the signal model in the model are not allowed to vary in the fit to observed data, a mismodeling of the signal can cause a bias in the mass measurement that has been evaluated. To estimate this bias, a signal injection test is performed: a dataset composed by a background Asimov sample and the signal MC sample at $m_H = 125\,\text{GeV}$ is fitted with the nominal signal plus background model. The shape parameters and the yield of the background only Asimov for each category are extracted from a fit to the data sidebands for each category using the function detailed in Table 6.7. The signal MC sample is then injected on top of the background Asimov and the resulting signal MC plus background Asimov sample is fitted using the nominal signal plus background model of Section 6.3. The signal bias for each category is then evaluated as the relative shift between the fitted and injected ($m_H = 125\,\text{GeV}$) Higgs boson mass, with the result for each category shown in Table 6.8.

The resulting bias is very small compared to the PES uncertainties shown in Figure 6.9 and therefore neglected in the model.

A similar procedure has been applied to evaluate the bias due the background modeling strategy. In this case, a dataset is created by using the Asimov dataset with $m_H = 125.09\,\text{GeV}$ for the signal component on top of the template used for the spurious signal test. This dataset is then fitted with the nominal signal plus background model and the

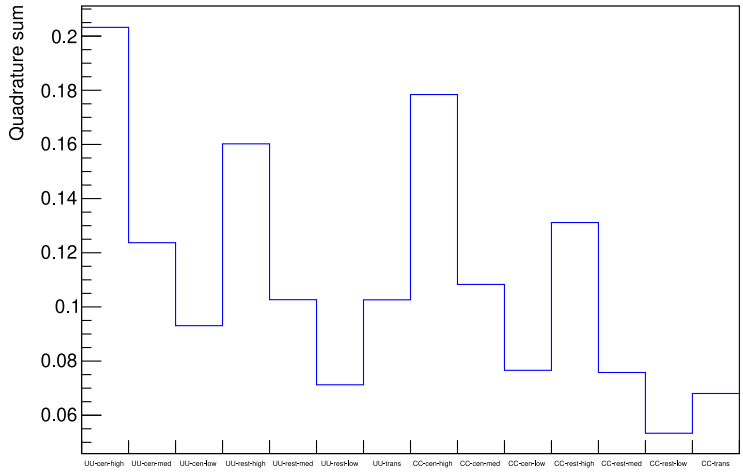

Figure 6.10 – Squared sum of all the PER systematic impacts on the $m_{\gamma\gamma}$ resolution for each category. The total effect on the mass ranges from $\sim \pm 5.3\%$ in the Conv rest low category to $\sim \pm 20\%$ in the UU cen high category.

Category	m_H^{fit} [GeV]	$m_H^{\text{fit}} - m_H^{\text{inj}}$ [MeV]	signal bias [%]
UU cen high	124.966	-34	-0.027
UU cen med	124.996	-4	-0.003
UU cen low	124.992	-8	-0.006
UU rest high	124.985	-15	-0.012
UU rest med	125.010	10	0.008
UU rest low	124.999	-1	-0.001
UU trans	125.009	9	0.007
Conv cen high	125.006	6	0.005
Conv cen med	125.002	2	0.002
Conv cen low	124.996	-4	-0.003
Conv rest high	125.027	27	0.022
Conv rest med	124.966	-34	-0.027
Conv rest low	125.002	2	0.002
Conv trans	124.999	-1	-0.001

Table 6.8 – Signal bias $\left(\frac{m_H^{\text{fit}}}{m_H^{\text{inj}}} - 1\right)$ as relative shift between the fitted (m_H^{fit}) and injected (m_H^{inj}) Higgs boson mass.

Category	m_H^{fit} [GeV]	$m_H^{\text{fit}} - m_H^{\text{inj}}$ [MeV]	Bkg bias [%]
UU cen high	125.140	50	0.040
UU cen med	125.200	110	0.088
UU cen low	125.123	33	0.026
UU rest high	125.076	−14	−0.011
UU rest med	125.172	82	0.066
UU rest low	125.160	70	0.056
UU trans	125.133	43	0.034
Conv cen high	125.085	−5	−0.004
Conv cen med	125.168	78	0.062
Conv cen low	125.208	118	0.094
Conv rest high	125.175	85	0.068
Conv rest med	125.166	76	0.061
Conv rest low	125.244	154	0.123
Conv trans	125.174	84	0.067

Table 6.9 – Background bias $\left(\frac{m_H^{\text{fit}}}{m_H^{\text{inj}}} - 1\right)$ as relative shift between the fitted (m_H^{fit}) and injected (m_H^{inj}) Higgs boson mass.

bias is extracted as the relative shift between the fitted and injected ($m_H = 125.09\,\text{GeV}$) Higgs boson mass, with the result for each category shown in Table 6.9. The bias due to background modeling is generally larger than the signal one, and it is implemented in the model with a single nuisance parameter for each category.

6.5 Results

The summary of all uncertainties sources and of the actual implementation in the likelihood is given in Table 6.10. Since the mass analysis is still in the approval stage, only expected results are reported in this manuscript. In order to estimate the expected values of the uncertainties on the m_H measurement, a fit is performed on an Asimov dataset corresponding to the SM expectations (setting the production mode signal strengths to one and $m_H = 125.09\,\text{GeV}$). The best value obtained for m_H from the fit is:

$$m_H = 125.090\,^{+0.287}_{-0.287}\,\text{GeV} = 125.09\,^{+0.125}_{-0.123}\,(\text{stat})\,^{+0.259}_{-0.259}\,(\text{syst})\,\text{GeV} \tag{6.10}$$

where the total uncertainties have been decomposed in its statistical and systematic components. The statistical-only uncertainty is evaluated by repeating the fit after fixing all the systematic nuisance parameters to their best values (which is by defition ~ 0 on a prefit Asimov dataset) , while the systematic component is evaluated as the quadratic difference between the total and the statistical-only uncertainties. The total uncertainty corresponds to a relative error of 0.23%, while the systematic uncertainty corresponds to a relative uncertainty of 0.21%; as expected, the measurement is therefore still dominated by systematic uncertainty, and in particular by the uncertainties arising from the photon energy scale calibration. These results are in line with the one reported in Table 6.6.

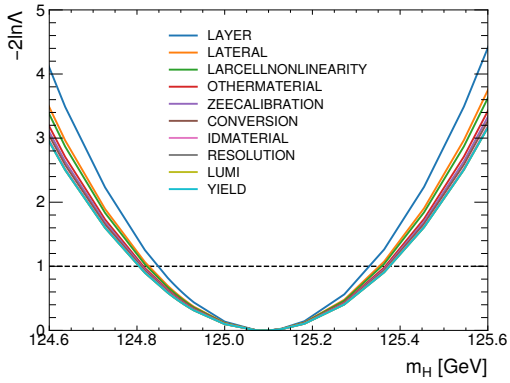

(a) Profile likelihood scan.

Uncertainty on m_{H} [MeV]	Impact	
Systematic group	Down	Up
Layer calibration	144	160
Lateral shower shape	112	124
LAr cell non-linearity	99	114
Other material (not ID)	78	79
$Z \to ee$ calibration	64	65
Conversion reconstruction	50	51
ID material	25	25
Resolution	8	4
Luminosity	0	0

(b) Systematic uncertainty decomposition.

Figure 6.11 – Systematic decomposition on the Asimov dataset. Profile likelihood ratio scans for each systematic group are shown on the left and 68% confidence level intervals obtained from the intersections of the scans at $-2\ln\Lambda = 1$ are reported on the right.

With respect to the expected results from the latest $H \to \gamma\gamma$ Run 2 results [176], the total uncertainty on m_H is reduced from 410 MeV to 287 MeV, corresponding to a 30% improvement: the statistical uncertainty is reduced from 250 MeV to 125 MeV, while the systematic from 310 MeV to 260 MeV. The majority of the statistic improvement is due to the increase in data statistic (36 fb^{-1} against 139 fb^{-1}), while the systematic uncertainty is reduced thanks to better knowledge of the material of the Inner Detector (10% improvement) as mentioned at the end of Section 6.2.1 and to the updated categorization (7% better).

The total systematic is decomposed in its main components, grouping several systematic sources in larger groups. The contribution of a particular set of systematic uncertainties is computed as the quadratic difference between the total uncertainty and a fit with all the nuisance parameters free to float except for the ones under study. This is done always using the same Asimov input dataset and the results are shown in Figure 6.11. As expected the systematic sources with the largest impact are the intercalibration between different layers of the EM calorimeter, the later energy leakage for photon cluster and the non-linearity of the electronic gains for the first two samplings of the EM calorimeter. The final estimation of photon energy scale and resolution systematic is ongoing and will have an impact on the expected and observed results for the mass analysis.

		Systematic source	NP	Implementation
Yield	Theo	Branching ratio	1	$N_{\text{tot}}\, F_{\text{LN}}(\delta_i, \theta_i)$
	Exp	Luminosity	1	$N_{\text{tot}}\, F_{\text{LN}}(\delta_i, \theta_i)$
Migrations	Theo	QCD scale	8	$N_{\text{ggF}}\, F_{\text{LN}}(\delta_i, \theta_i)$
		Parton shower	8	$N_{\text{p}}\, F_{\text{LN}}(\delta_i, \theta_i)$
		PDF	30	$N_{\text{p}}\, F_{\text{LN}}(\delta_i, \theta_i)$
		α_{S}	1	$N_{\text{p}}\, F_{\text{AS}}(\delta_i, \theta_i)$
	Exp	Photon Trigger	1	$N_{\text{p}}\, F_{\text{LN}}(\delta_i, \theta_i)$
		Photon Isolation	1	$N_{\text{p}}\, F_{\text{AS}}(\delta_i, \theta_i)$
		Photon Identification	1	$N_{\text{p}}\, F_{\text{AS}}(\delta_i, \theta_i)$
		Photon Scale	1	$N_{\text{p}}\, F_{\text{AS}}(\delta_i, \theta_i)$
		Photon Resolution	1	$N_{\text{p}}\, F_{\text{AS}}(\delta_i, \theta_i)$
Shape		Photon Scale	68	$\mu_{\text{CB}}\, F_{\text{G}}(\delta_i, \theta_i)$
		Photon Resolution	9	$\sigma_{\text{CB}}\, F_{\text{AS}}(\delta_i, \theta_i)$
		Background bias	14	$\mu_{\text{CB}}\, F_{\text{G}}(\delta_i, \theta_i)$
Bkg		Spurious signal	14	$N_{\text{sp},c}\, \theta_{\text{sp},c}$

Table 6.10 – Summary of sources of systematic uncertainty included in the likelihood model along with their implementation in the likelihood function, impacting on signal yields, mass scale/resolution and the spurious signals resulting from the background parametrization. When acting on N_{tot} the uncertainty value is the same for all Higgs production processes, whereas the uncertainty has a different value for each signal on the case denoted by N_{p}. The various response functions F are defined in Eq. (4.13), while spurious signal is implemented as in Eq. (4.10).

Conclusions

This manuscript presented the measurements of the Higgs boson properties in the diphoton decay channel performed with the pp collision dataset collected by ATLAS at LHC with a center-of-mass energy of $\sqrt{s} = 13\,\text{TeV}$ and amounting to $139\,\text{fb}^{-1}$. The first one is the measurement of the Higgs boson production cross sections in the Simplified Template Cross Section framework and the second is the precision measurement of the Higgs boson mass.

The Higgs boson production cross sections are measured in a number of different parametrizations in order to deeply explore its production phase space. The analysis features a fully redesigned categorization, optimized to measure the STXS truth bin with an innovative multivariate approach, which greatly improves the results with respect to partial Run 2 publication [8]. The total production cross section for $|y_{\text{H}}| < 2.5$ is measured to be

$$\sigma^{\gamma\gamma}_{\text{obs}} = 121\ ^{+10}_{-9}\,\text{fb} = 121\ \pm 7\,(\text{stat})\ ^{+7}_{-6}\,(\text{syst})\,\text{fb}$$

with a SM expectation of

$$\sigma^{\gamma\gamma}_{\text{exp}} = 116\ \pm 6\,\text{fb}.$$

The measurement of the production cross sections for the main Higgs production modes (ggF, VBF, WH, ZH, $\text{t}\bar{\text{t}}\text{H}$, tH) found their signal strengths compatible within one standard deviation with the Standard Model prediction. Except tH, the measured cross sections present relative uncertainties ranging from 11% to 58%. The ggF and VBF present a statistical uncertainty of the size of the systematic one, with the largest uncertainty sources represented by background and parton shower modeling. An upper limit at 95% CL of ten times the SM prediction is set for the associated production of the Higgs boson with a single top quark process (tH). Cross sections are also presented in 28 and 33 different Higgs production regions, defined based on the STXS framework. No significant deviations from the SM expectation are observed and the compatibility between the measurements and the SM predictions corresponds to a p-value of 60% and 70% respectively. Moreover, the $H \to \gamma\gamma$ decay channel has been combined with other analyses performed in the different Higgs decay channel, in order to further boost the measurement sensitivity to the production cross section, to disentangle the production and decay

processes and to enlarge the phase space probed with respect the $H \to \gamma\gamma$ one. No deviations from the SM expectations have been observed.

The preliminary Higgs boson mass measurement in the diphoton decay channel is described as well. A systematic and theoretically motivated investigation of the categorization design has been carried out, consolidating the choice of a categorization similar to the one used for the Run 1 $H \to \gamma\gamma$ results [34] with slight improvements. The expected results obtained from an Asimov dataset generated with $m_H = 125.09\,\text{GeV}$ is

$$m_H = 125.090\,^{+0.287}_{-0.287}\,\text{GeV} = 125.09\,^{+0.125}_{-0.123}\,(\text{stat})\,^{+0.259}_{-0.259}\,(\text{syst})\,\text{GeV}$$

with the largest systematic uncertainty represented by the photon energy scale, in particular the calorimeter layers intercalibration (160 MeV), the shower later leakage (124 MeV) and the LAr cell non-linearity (114 MeV). With respect to the expected results from the latest $H \to \gamma\gamma$ Run 2 results [176], the total uncertainty on m_H presents a 30% improvement, partially due to the increase in dataset statistic, but with sizeable contributions from updated photon energy scale uncertainties (10%) and from the updated categorization (7%). The mass analysis is still in the collaboration revision phase therefore no observed results are presented.

Appendices

APPENDIX A

Additional material for STXS/coupling analysis

This appendix reports additional material related to the $H \to \gamma\gamma$ coupling analysis and referenced in the main body text.

A.1 D-optimal multiclass selection

The plots shown from Figure A.1 to Figure A.9 report the distribution of some representative observables for the events classified in particular categories selected by the D-optimal multiclass BDT: all the signals are drawn stacked with different colors, therefore showing the purity of the multiclass categories, the total yield is normalized to 140 fb^{-1}.

A.2 Performance improvement with respect to partial Run 2 results

The expected results of the "global" categorization described in Section 5.4 are compared to the ones obtained from previous categorizations employed for partial Run 2 datasets (with 36 fb^{-1} [129] and 80 fb^{-1} [8]) results, to demonstrate the improvement brought by the new approach. The study is performed on the same set of simulated MC events and selected data reported in Section 4.2 in order to rule out any performance improvement related to the ATLAS reconstruction introduced in recent years. The comparison is carried out by comparing the expected results with the full Run 2 statistic.

A.2.1 Overview of the partial Run 2 categorizations

The overview of the categorization used for the 80 fb^{-1} results is reported in Table A.1: the categorization was "sequential", namely events were categorized in the first category whose selections are fulfilled in the order $t\bar{t}H$, VH, VBF, ggF, and it features a mix of rectangular cuts and single binary BDTs (in particular 2 for $t\bar{t}H$, 1 for VH hadronic and 2 for VBF). The $t\bar{t}H$ categories used for 80 fb^{-1} results were the ones that led to the ATLAS $t\bar{t}H$ observation [9] and the binary BDTs trained there are similar in structures and inputs to the one used in the analysis presented in this manuscript (see Section 5.4.4).

Concerning instead the categorization for 36 fb^{-1} results, this is very similar to the one reported in Table A.1. The only main difference is in the $t\bar{t}H$ categories: the 36 fb^{-1} analysis was in fact targeting both tH and $t\bar{t}H$, therefore it provided less sensitivity to

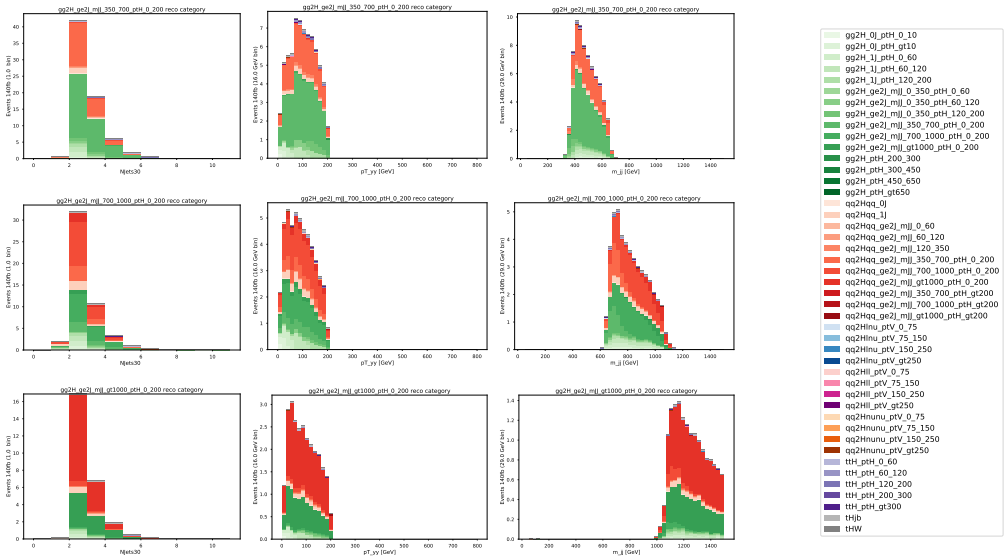

Figure A.1 – Distributions of some representative observables for GG2H_GE2J_MJJ_350_700_PTH_0_200, GG2H_GE2J_MJJ_700_1000_PTH_0_200 and GG2H_GE2J_MJJ_GT1000_PTH_0_200 D-optimal reconstructed category

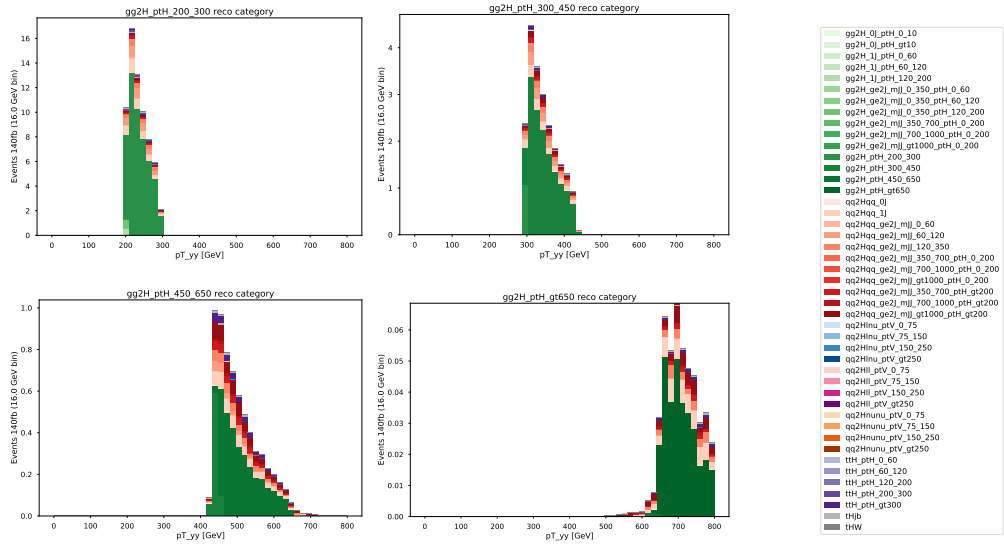

Figure A.2 – Distributions of some representative observables for GG2H_PTH_200_300, GG2H_PTH_300_450, GG2H_PTH_450_650, GG2H_PTH_GT650 D-optimal reconstructed category

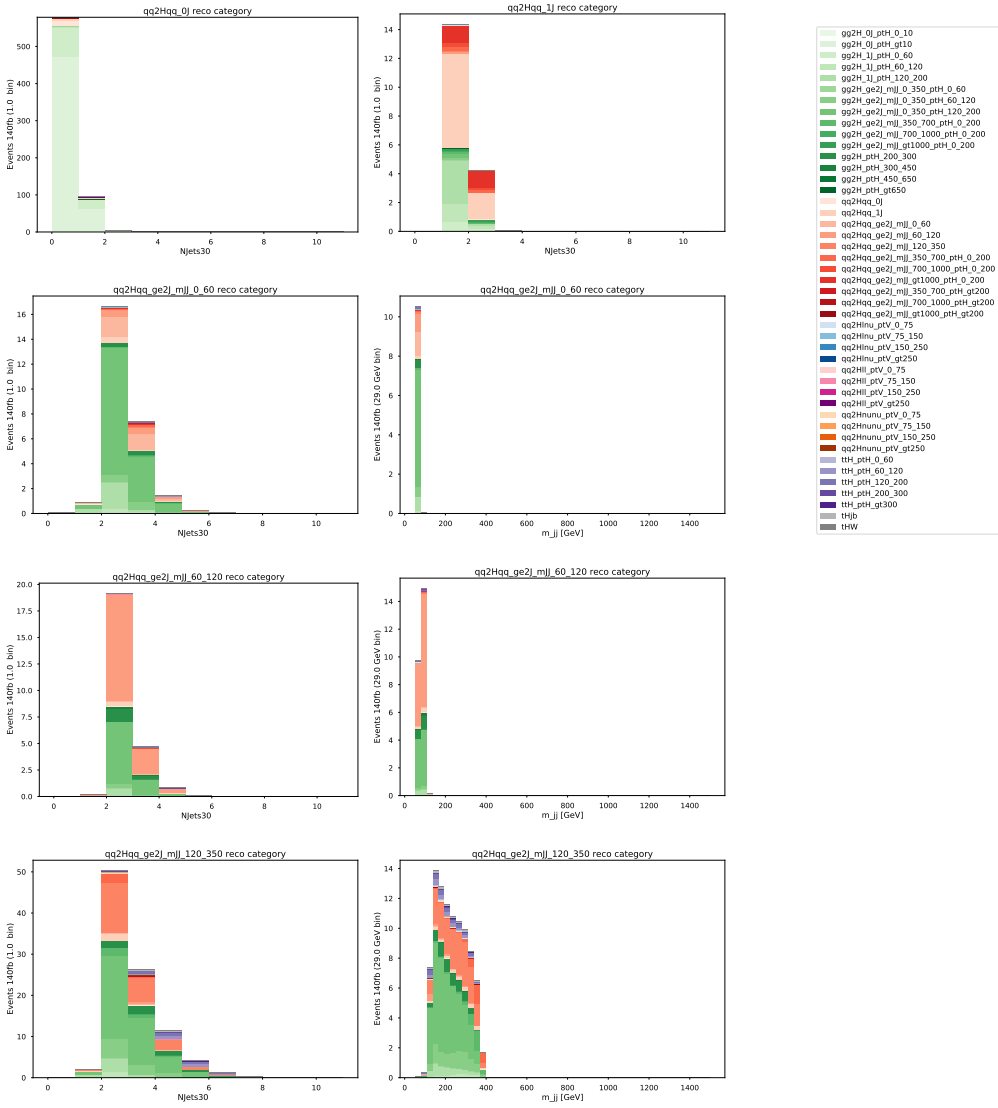

Figure A.3 – Distributions of some representative observables for QQ2HQQ_0J, QQ2HQQ_1J, QQ2HQQ_GE2J_MJJ_0_60, QQ2HQQ_GE2J_MJJ_60_120, QQ2HQQ_GE2J_MJJ_120_350 D-optimal reconstructed category

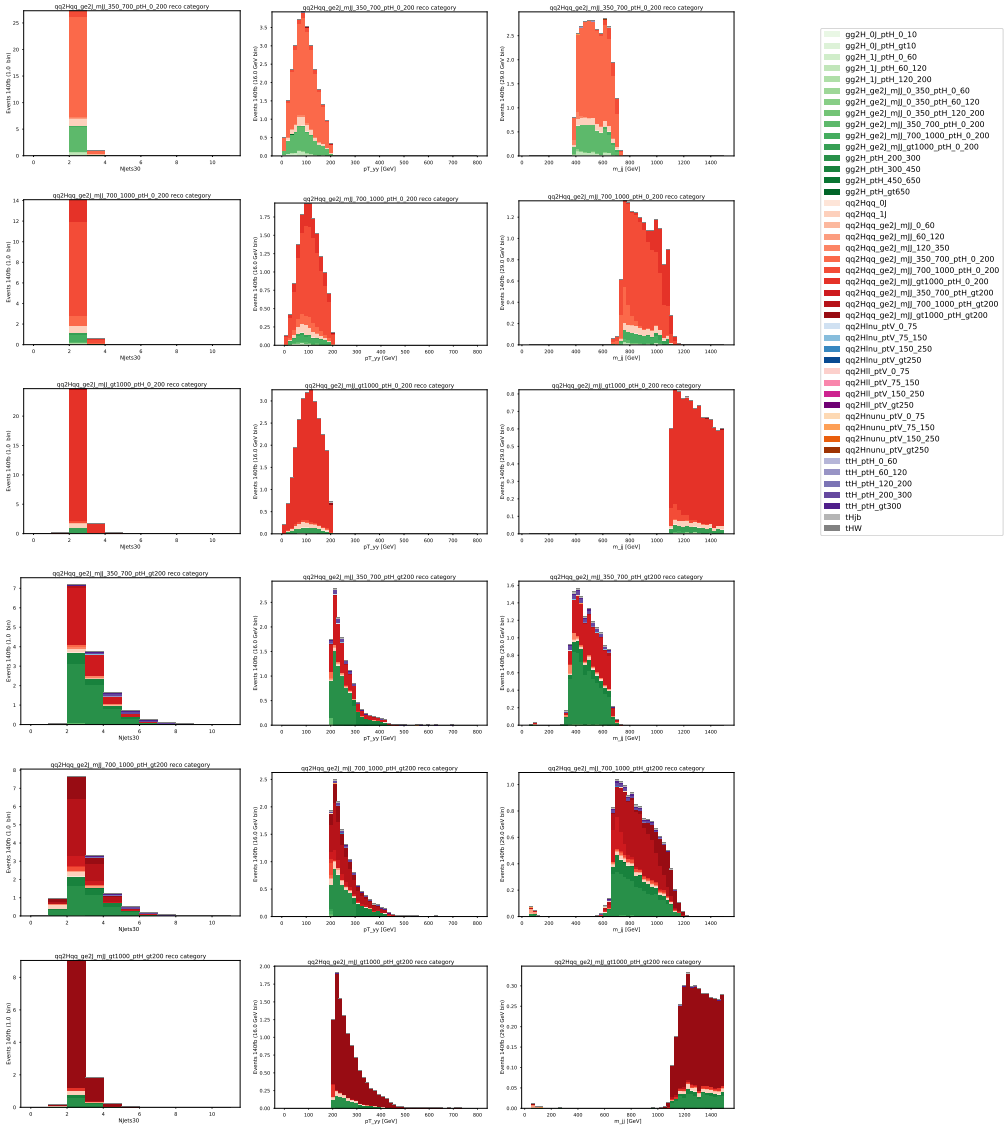

Figure A.4 – Distributions of some representative observables for QQ2HQQ_GE2J_MJJ_350_700_PTH_0_200, QQ2HQQ_GE2J_MJJ_700_1000_PTH_0_200, QQ2HQQ_GE2J_MJJ_GT1000_PTH_0_200, QQ2HQQ_GE2J_MJJ_350_700_PTH_GT200, QQ2HQQ_GE2J_MJJ_700_1000_PTH_GT200, QQ2HQQ_GE2J_MJJ_GT1000_PTH_GT200 D-optimal reconstructed category

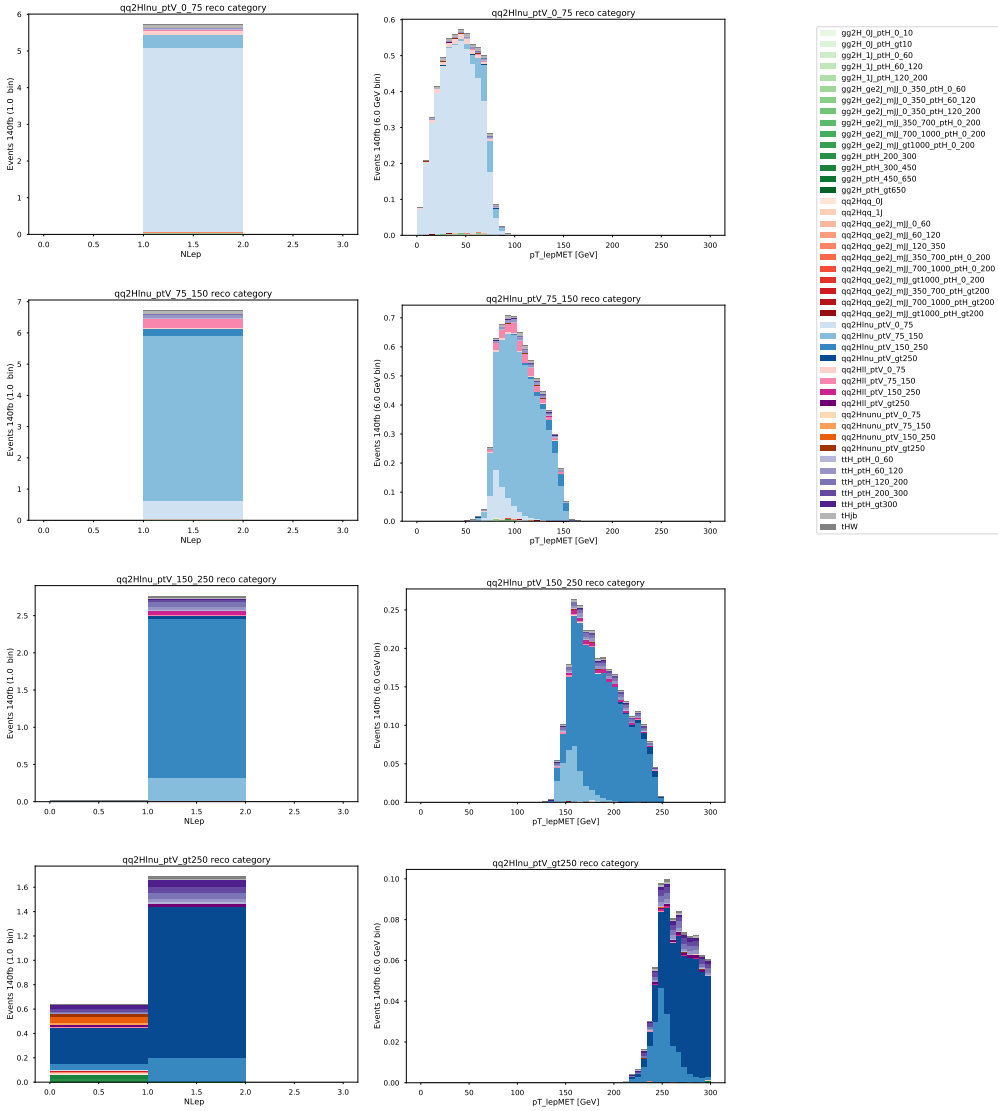

Figure A.5 – Distributions of some representative observables for QQ2HLNU_PTV_0_75, QQ2HLNU_PTV_75_150, QQ2HLNU_PTV_150_250, QQ2HLNU_PTV_GT250 D-optimal reconstructed category

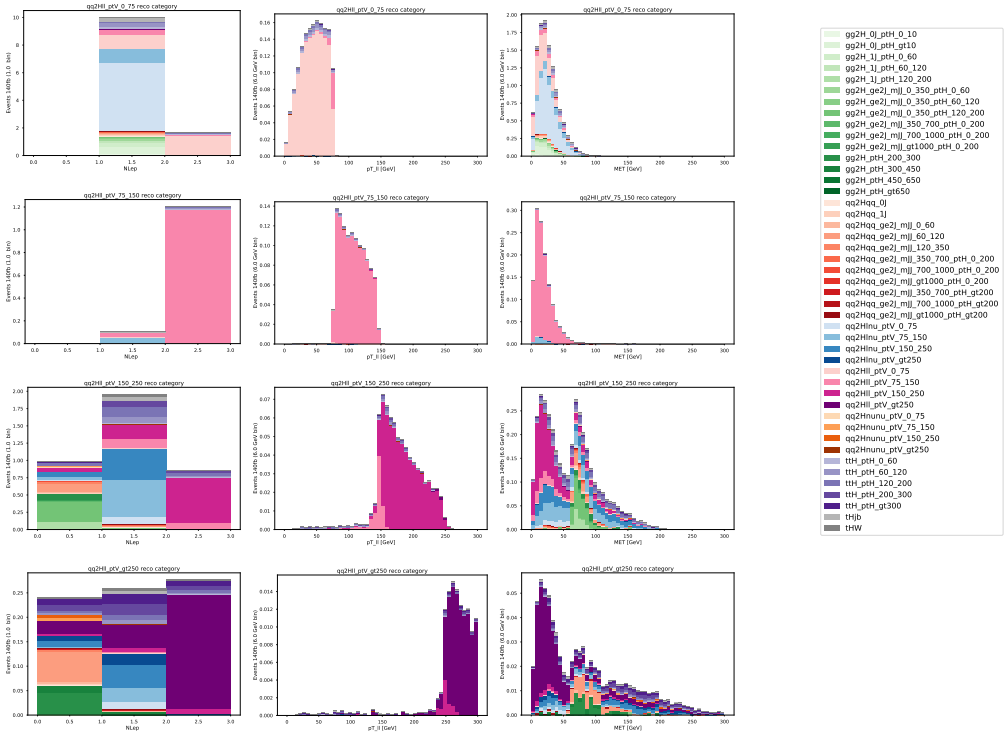

Figure A.6 – Distributions of some representative observables for QQ2HLL_PTV_0_75, QQ2HLL_PTV_75_150, QQ2HLL_PTV_150_250, QQ2HLL_PTV_GT250 D-optimal reconstructed category

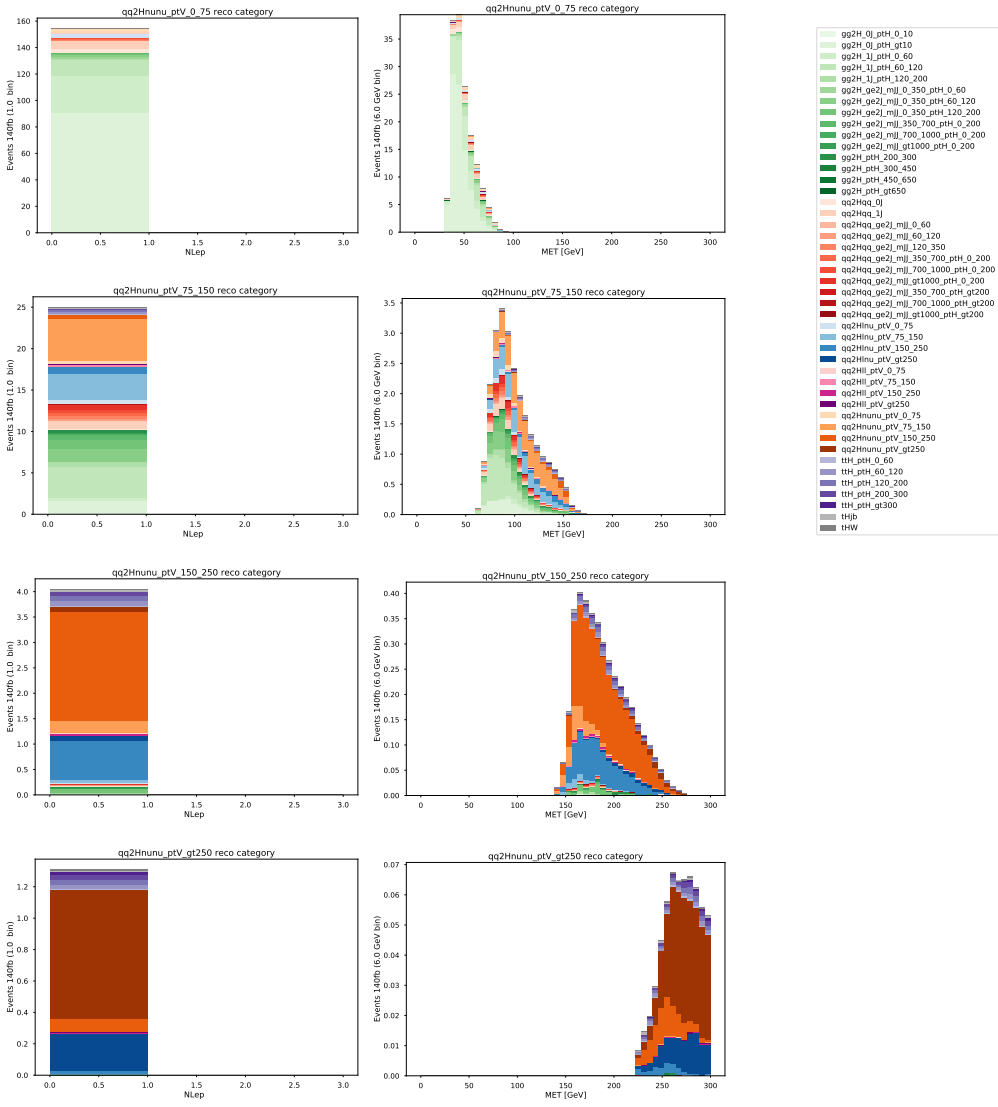

Figure A.7 – Distributions of some representative observables for QQ2HNUNU_PTV_0_75, QQ2HNUNU_PTV_75_150, QQ2HNUNU_PTV_150_250, QQ2HNUNU_PTV_GT250 D-optimal reconstructed category

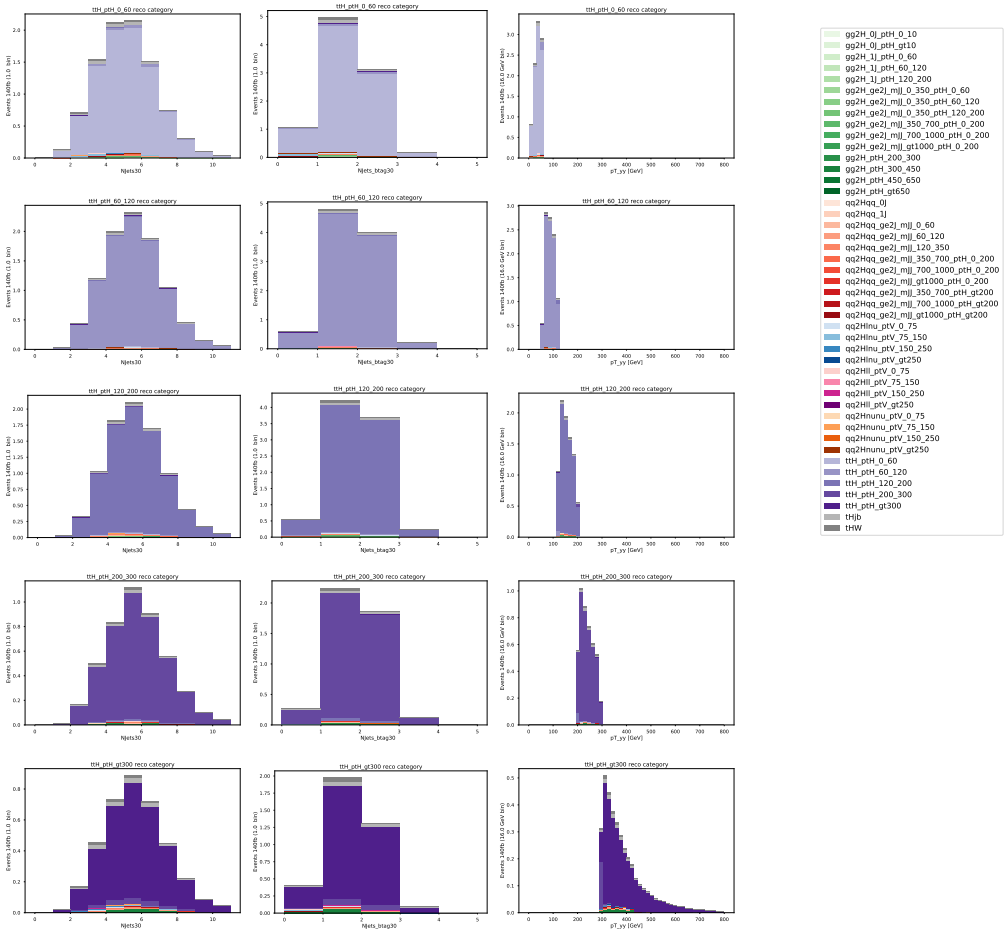

Figure A.8 – Distributions of some representative observables for TTH_PTH_0_60, TTH_PTH_60_120, TTH_PTH_120_200, TTH_PTH_200_300, TTH_PTH_GT300 D-optimal reconstructed category

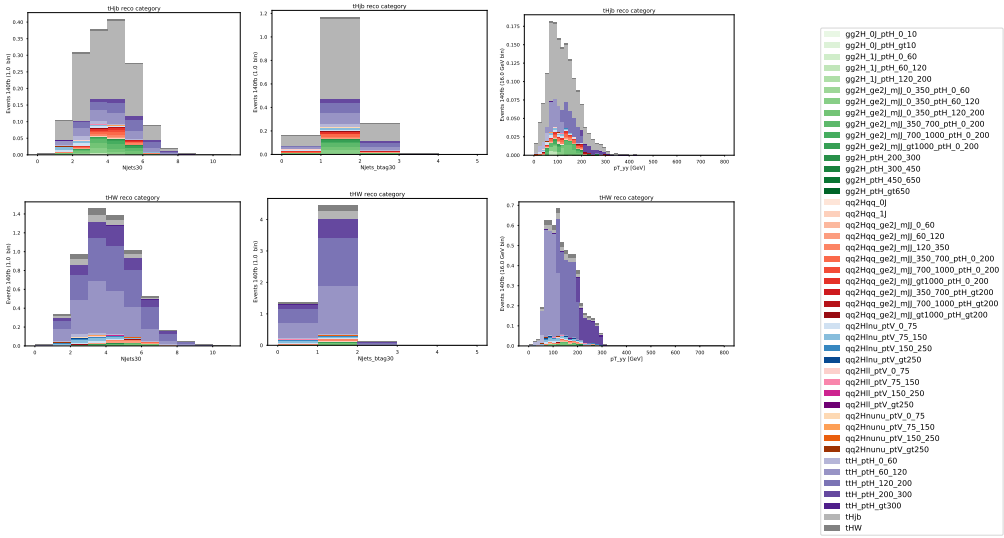

Figure A.9 – Distributions of some representative observables for THJB and TWH D-optimal reconstructed category

$t\bar{t}H$ production mode but larger sensitivity to tH compared to the 80 fb^{-1} categorization.

A.2.2 Retrained global categorization

Since the categorizations described in the previous Section were targeting the STXS 1.0 scheme (see Section 5.1.2), the global categorization has been completely retrained as exactly described in Section 5.4.1 but now based on the STXS 1.0 scheme. This is done in order to ensure a common set of parameter of interests in the comparison fit.

The signals used to train the D-optimal multiclass and the subsequent binary BDTs are reported in Table A.2. This is a merged set of the full STXS 1.0 scheme based on what the previous categorizations were able to target. As can be noticed, TTH and TH signals have been included separately in this retraining.

Results comparison

For each of the signals reported in Table A.2, a signal strength parameter has been fitted simultaneously, by building a counting experiment method as the one described in Section 5.4.3. The expected stat-only uncertainties for 140 fb^{-1} of the past categorizations and the global one are reported in Table A.3, while stat-only correlations are shown in Figure A.10. As can be observed the global approach outperform everywhere the past categorizations (around 30% better) and it is well able to reduce the stat-only correlations among different POIs.

Category	Selection
$t\bar{t}H$ lep BDT 1	$N_{\text{lep}} \geq 1$, $N_{\text{jets}} \geq 0$ ($p_{\text{T}}^{\text{jet}} > 25\,\text{GeV}$), $N_{\text{tags}}^{77} \geq 1$, $\text{BDT}_{t\bar{t}H} > 0.987$
$t\bar{t}H$ lep BDT 2	$N_{\text{lep}} \geq 1$, $N_{\text{jets}} \geq 0$ ($p_{\text{T}}^{\text{jet}} > 25\,\text{GeV}$), $N_{\text{tags}}^{77} \geq 1$, $\text{BDT}_{t\bar{t}H} > 0.942$
$t\bar{t}H$ lep BDT 3	$N_{\text{lep}} \geq 1$, $N_{\text{jets}} \geq 0$ ($p_{\text{T}}^{\text{jet}} > 25\,\text{GeV}$), $N_{\text{tags}}^{77} \geq 1$, $\text{BDT}_{t\bar{t}H} > 0.705$
$t\bar{t}H$ had BDT 1	$N_{\text{lep}} = 0$, $N_{\text{jets}} \geq 3$ ($p_{\text{T}}^{\text{jet}} > 25\,\text{GeV}$), $N_{\text{tags}}^{77} \geq 1$, $\text{BDT}_{t\bar{t}H} > 0.996$
$t\bar{t}H$ had BDT 2	$N_{\text{lep}} = 0$, $N_{\text{jets}} \geq 3$ ($p_{\text{T}}^{\text{jet}} > 25\,\text{GeV}$), $N_{\text{tags}}^{77} \geq 1$, $\text{BDT}_{t\bar{t}H} > 0.991$
$t\bar{t}H$ had BDT 3	$N_{\text{lep}} = 0$, $N_{\text{jets}} \geq 3$ ($p_{\text{T}}^{\text{jet}} > 25\,\text{GeV}$), $N_{\text{tags}}^{77} \geq 1$, $\text{BDT}_{t\bar{t}H} > 0.971$
$t\bar{t}H$ had BDT 4	$N_{\text{lep}} = 0$, $N_{\text{jets}} \geq 3$ ($p_{\text{T}}^{\text{jet}} > 25\,\text{GeV}$), $N_{\text{tags}}^{77} \geq 1$, $\text{BDT}_{t\bar{t}H} > 0.911$
VH dilep high	$N_{\text{lep}} \geq 2$, $70 \leq m_{\ell\ell} \leq 110\,\text{GeV}$
VH lep high	$N_{\text{lep}} = 1$, $\lvert m_{e\gamma} - 89\,\text{GeV}\rvert > 5\,\text{GeV}$, $p_{\text{T}}^{\ell+E_{\text{T}}^{\text{miss}}} > 150\text{GeV}$
VH lep low	$N_{\text{lep}} = 1$, $\lvert m_{e\gamma} - 89\,\text{GeV}\rvert > 5\,\text{GeV}$, $p_{\text{T}}^{\ell+E_{\text{T}}^{\text{miss}}} < 150\text{GeV}$, $E_{\text{T}}^{\text{miss}}\text{sig} > 1$
VH MET high	$150 < E_{\text{T}}^{\text{miss}} < 250\,\text{GeV}$ and $E_{\text{T}}^{\text{miss}}\text{sig} > 9$, or $E_{\text{T}}^{\text{miss}} > 250\,\text{GeV}$
VH MET low	$80 < E_{\text{T}}^{\text{miss}} < 150\,\text{GeV}$, $E_{\text{T}}^{\text{miss}}\text{sig} > 8$
qqH BSM	≥ 2 jets ($p_{\text{T}}^{\text{jet}} > 30\,\text{GeV}$), $p_{\text{T}}^{j1} > 200\,\text{GeV}$
VH had tight	$60\text{GeV} < m_{jj} < 120\text{GeV}$, $\text{BDT}_{\text{VH}\,had} > 0.78$
VH had loose	$60\text{GeV} < m_{jj} < 120\text{GeV}$, $0.35 < \text{BDT}_{\text{VH}\,had} < 0.78$
VBF tight, high $p_{\text{T}}^{\text{H}jj}$	$\Delta\eta_{jj} > 2$, $\eta^{\text{Zepp}} < 5$, $p_{\text{T}}^{\text{H}jj} > 25\,\text{GeV}$, $\text{BDT}_{\text{VBF}} > 0.48$
VBF loose, high $p_{\text{T}}^{\text{H}jj}$	$\Delta\eta_{jj} > 2$, $\eta^{\text{Zepp}} < 5$, $p_{\text{T}}^{\text{H}jj} > 25\,\text{GeV}$, $-0.5 < \text{BDT}_{\text{VBF}} < 0.48$
VBF tight, low $p_{\text{T}}^{\text{H}jj}$	$\Delta\eta_{jj} > 2$, $\eta^{\text{Zepp}} < 5$, $p_{\text{T}}^{\text{H}jj} < 25\,\text{GeV}$, $\text{BDT}_{\text{VBF}} > 0.87$
VBF loose, low $p_{\text{T}}^{\text{H}jj}$	$\Delta\eta_{jj} > 2$, $\eta^{\text{Zepp}} < 5$, $p_{\text{T}}^{\text{H}jj} < 25\,\text{GeV}$, $-0.39 < \text{BDT}_{\text{VBF}} < 0.87$
ggF 2J BSM	$N_{\text{jets}} \geq 2$ ($p_{\text{T}}^{\text{jet}} > 30\,\text{GeV}$), $p_{\text{T}}^{\gamma\gamma} \geq 200\,\text{GeV}$
ggF 2J HIGH	$N_{\text{jets}} \geq 2$ ($p_{\text{T}}^{\text{jet}} > 30\,\text{GeV}$), $p_{\text{T}}^{\gamma\gamma} \in [120, 200]\,\text{GeV}$
ggF 2J MED	$N_{\text{jets}} \geq 2$ ($p_{\text{T}}^{\text{jet}} > 30\,\text{GeV}$), $p_{\text{T}}^{\gamma\gamma} \in [60, 120]\,\text{GeV}$
ggF 2J LOW	$N_{\text{jets}} \geq 2$ ($p_{\text{T}}^{\text{jet}} > 30\,\text{GeV}$), $p_{\text{T}}^{\gamma\gamma} \in [0, 60]\,\text{GeV}$
ggF 1J BSM	$N_{\text{jets}} = 1$ ($p_{\text{T}}^{\text{jet}} > 30\,\text{GeV}$), $p_{\text{T}}^{\gamma\gamma} \geq 200\,\text{GeV}$
ggF 1J HIGH	$N_{\text{jets}} = 1$ ($p_{\text{T}}^{\text{jet}} > 30\,\text{GeV}$), $p_{\text{T}}^{\gamma\gamma} \in [120, 200]\,\text{GeV}$
ggF 1J MED	$N_{\text{jets}} = 1$ ($p_{\text{T}}^{\text{jet}} > 30\,\text{GeV}$), $p_{\text{T}}^{\gamma\gamma} \in [60, 120]\,\text{GeV}$
ggF 1J LOW	$N_{\text{jets}} = 1$ ($p_{\text{T}}^{\text{jet}} > 30\,\text{GeV}$), $p_{\text{T}}^{\gamma\gamma} \in [0, 60]\,\text{GeV}$
ggF 0J FWD	$N_{\text{jets}} = 0$ ($p_{\text{T}}^{\text{jet}} > 30\,\text{GeV}$), one γ with $\lvert\eta\rvert > 0.95$
ggF 0J CEN	$N_{\text{jets}} = 0$ ($p_{\text{T}}^{\text{jet}} > 30\,\text{GeV}$), two γs with $\lvert\eta\rvert \leq 0.95$

Table A.1 – Summary of analysis category definitions for the $H \to \gamma\gamma$ $80\,\text{fb}^{-1}$ results [8].

ggF + ggZH (hadronic)	**VBF + VH** hadronic
1. GG2H_0J	11. QQ2HQQ_VBFTOPO
2. GG2H_1J_PTH_0_60	12. QQ2HQQ_VH_REST
3. GG2H_1J_PTH_60_120	13. QQ2HQQ_PTJET1_GT200
4. GG2H_1J_PTH_120_200	
5. GG2H_1J_PTH_GT200	
6. GG2H_GE2J_PTH_0_60	
7. GG2H_GE2J_PTH_60_120	
7. GG2H_GE2J_PTH_120_200	
9. GG2H_GE2J_PTH_GT200	
10. GG2H_VBFTOPO	
VH leptonic	**Top**
14.HLNU	16. TTH
15. HLL	17. TH

Table A.2 – Targeted STXS signals used for comparing old categorizations with the new global one.

	Categorization			Relative gain of Global [%]	
Stat-only error on [%]	36 fb^{-1}	80 fb^{-1}	Global	wrt 36 fb^{-1}	wrt 80 fb^{-1}
μ_{GG2H_0J}	12	12	11	2.2	2.2
$\mu_{GG2H\_1J\_PTH\_0\_60}$	47	48	34	28	28
$\mu_{GG2H\_1J\_PTH\_60\_120}$	39	39	32	18	18
$\mu_{GG2H\_1J\_PTH\_120\_200}$	61	61	53	13	13
$\mu_{GG2H\_1J\_PTH\_GT200}$	150	90	65	58	28
$\mu_{GG2H\_GE2J\_PTH\_0\_60}$	150	150	110	24	24
$\mu_{GG2H\_GE2J\_PTH\_60\_120}$	86	87	59	32	32
$\mu_{GG2H\_GE2J\_PTH\_120\_200}$	76	76	43	43	43
$\mu_{GG2H\_GE2J\_PTH\_GT200}$	71	72	38	46	46
$\mu_{GG2H\_VBFTOPO}$	160	160	96	38	39
$\mu_{QQ2HQQ\_VBFTOPO}$	40	40	27	32	32
$\mu_{QQ2HQQ\_VH\_REST}$	150	160	110	32	33
$\mu_{QQ2HQQ\_PTJET1\_GT200}$	170	180	50	71	72
μ_{HLNU}	69	72	48	31	34
μ_{HLL}	83	83	73	12	12
μ_{TTH}	42	38	31	27	18
μ_{TH}	750	870	440	41	49

Table A.3 – Stat-only expected uncertainties for the past categorizations (labeled 36 fb^{-1} and 80 fb^{-1}) compared to the results obtained by a categorization (global) optimized in a similar way to the one used for full Run 2 results reported in the main body of this manuscript. All the results are obtained with an integrated luminosity of 140 fb^{-1}.

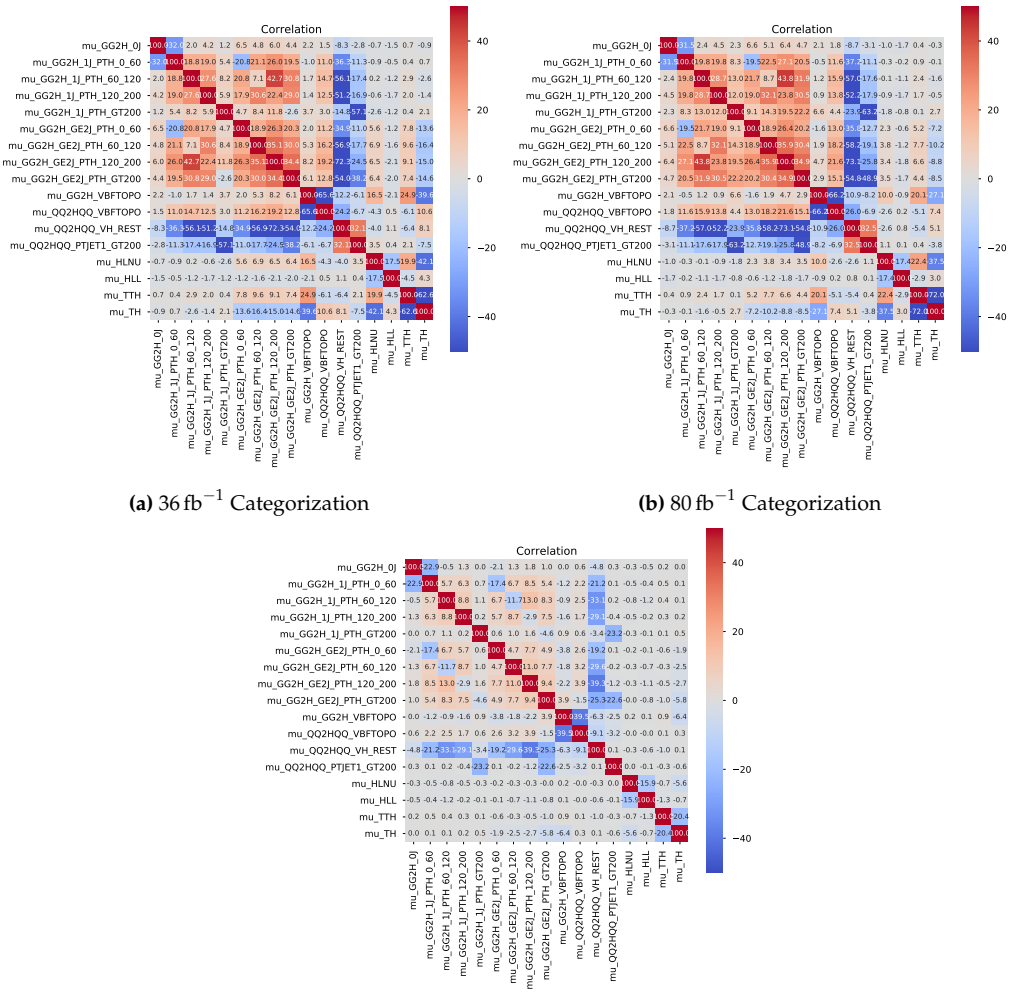

(a) 36 fb^{-1} Categorization

(b) 80 fb^{-1} Categorization

(c) Global categorization

Figure A.10 – Expected stat-only correlations among the measured POIs of a STXS 1.0 scheme. Large positive correlations in the GG2H part are mainly due to the badly measured QQ2HQQ_VH_REST POI which represents a resonant background for these bins.

A.3 Systematic uncertainties

This section reports the values of some of the systematic uncertainty variations that have been computed for the $H \to \gamma\gamma$ coupling analysis. The large number of systematic sources impacting each reconstructed category and each STXS truth bin makes difficult to report all the hundreds of thousands variations computed and included in the likelihood model. Here, it is reported a not exhaustive selection of figures and tables chosen to show the main systematic impacts for the major STXS truth bins and to highlight the complexity of the likelihood function when all the uncertainties are included, with their descriptions given in Section 5.6.

Starting from theoretical uncertainties, the parton shower uncertainties have a large impact on the cross section results and therefore the additional variations for WH, ZH, ggZH, $t\bar{t}H$ and tHbj are reported in Figure A.11 and Figure A.12, which complement the two plots already shown for ggF and VBF in Figure 5.19

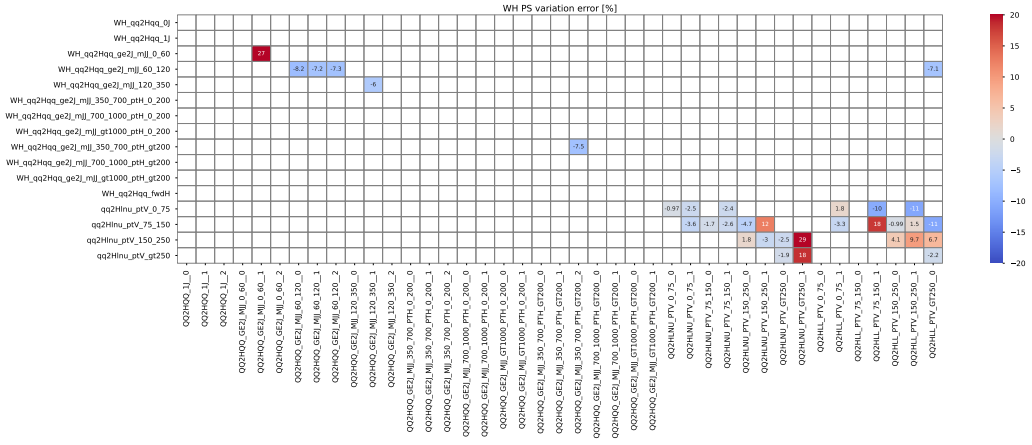

(a) Impact of the PS uncertainty in the WH STXS bins.

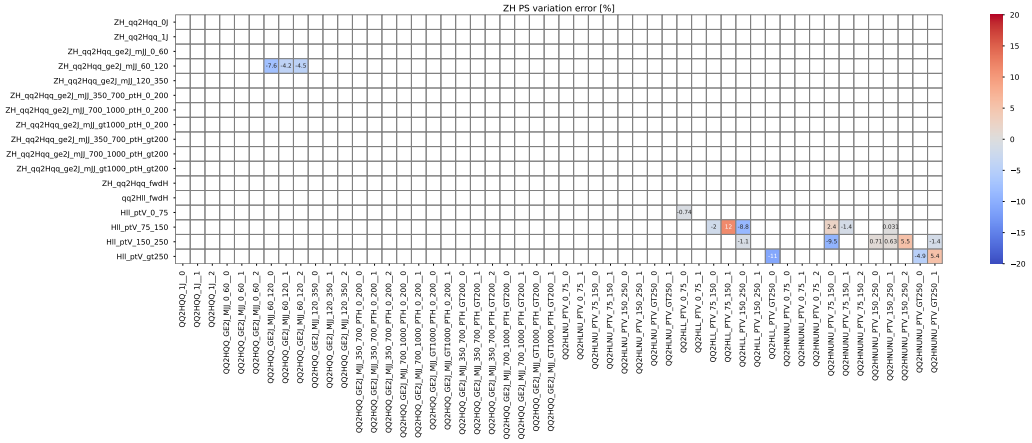

(b) Impact of the PS uncertainty in the ZH STXS bins.

Figure A.11 – Effect of the (a) WH and (b) ZH PS uncertainties on the signal yields of both VBF and VH categories. Each row in the plot is a (a) WH or a (b) ZH STXS truth bin, while each column represents one analysis category. Only the impacts for the STXS truth bins with more than 5% of the total expected yield in a given reconstructed categories are shown. Impacts are computed with Eq. (4.6).

The complex scheme used to model QCD scale uncertainties for the STXS framework generates around 40 nuisance parameters. To complement the examples given in Figure 5.20 referring to the two most important sources for ggF truth bins, additional plots are reported in Figure A.13 for some nuisance parameters impacting ggF, VH and $t\bar{t}H$. The largest impacts are observed for ggZH production processes, even if they do not have an impact in the likelihood since ggZH is a production mode with very small

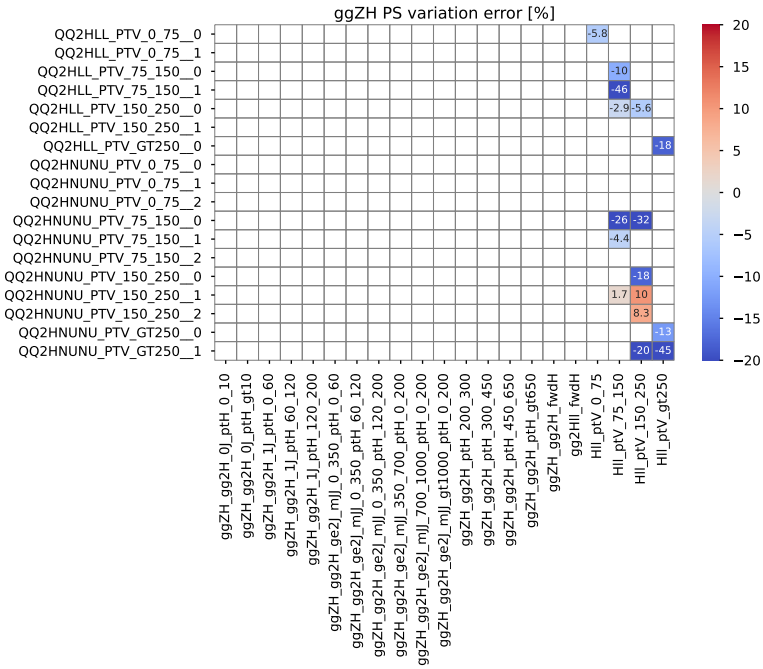

(a) Impact of the PS uncertainty in the ggZH STXS bins.

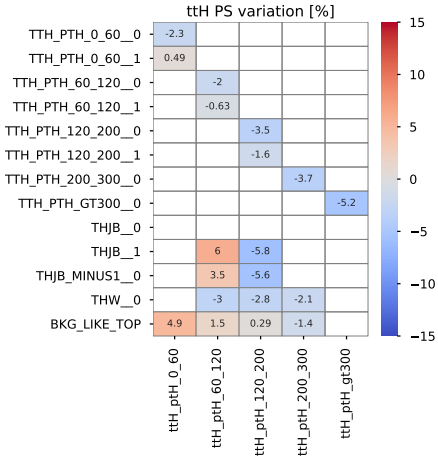

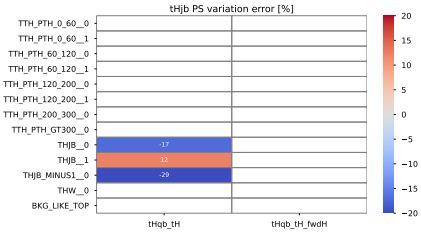

(b) Impact of the PS uncertainty in the $t\bar{t}H$ STXS bins. **(c)** Impact of the PS uncertainty in the tHbj STXS bins.

Figure A.12 – Effect of the (a) ggZH, (b) $t\bar{t}H$ and (c) tHbj PS uncertainties in the relevant reconstructed categories. Please note that the axis are inverted with respect to Figure A.11: the x-axis now represents the truth bins and the y-axis the reconstructed categories. Only the impacts for the STXS truth bins with more than 5% of the total expected yield in a given reconstructed categories are shown. Impacts are computed with Eq. (4.6).

cross section. VBF is the Higgs production process less affected by the QCD scale uncertainties, with relative impacts on the category yields of the order of 1-2%.

Photon energy resolution uncertainties are among the uncertainties that have the

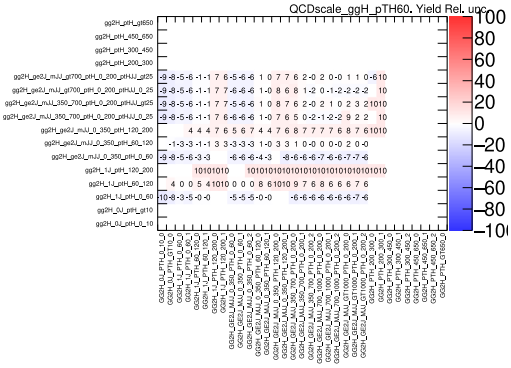

(a) ggF QCD scale $p_{\mathrm{T}}^{\mathrm{H}}$ 60 GeV

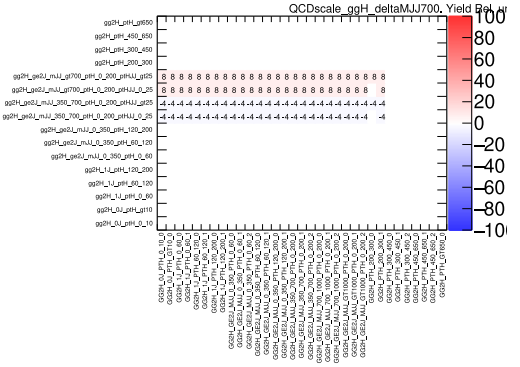

(b) ggF QCD scale m_{jj} 700 GeV

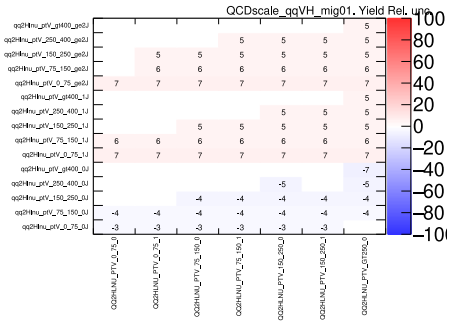

(c) WH QCD scale N_{jets} 0-1 migration

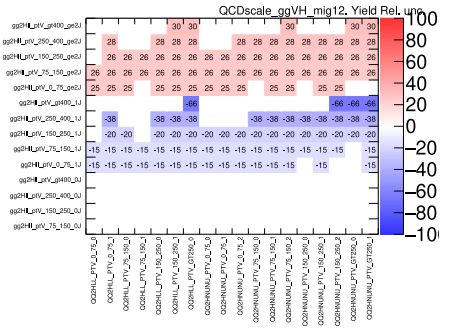

(d) ggZH QCD scale N_{jets} 1-2 migration

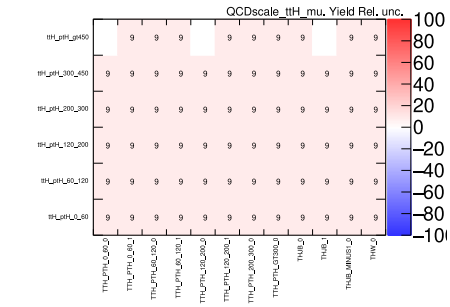

(e) $\mathrm{t\bar{t}H}$ QCD scale global scale

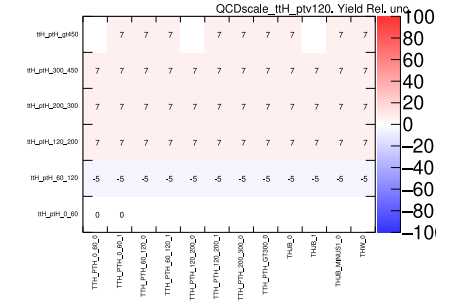

(f) $\mathrm{t\bar{t}H}$ QCD scale $p_{\mathrm{T}}^{\mathrm{H}}$ 120 GeV

Figure A.13 – Relative impact on the yield for the analysis categories (x-axis) and for the relevant STXS truth bins (y-axis) for the some of the nuisance parameters of the STXS uncertainty scheme: (a) $p_{\mathrm{T}}^{\mathrm{H}}$ threshold effects at 60 GeV in ggF, (b) m_{jj} threshold effects at 700 GeV in ggF, (c) $0 \leftrightarrow 1$ jet migration uncertainty in WH, (d) $1 \leftrightarrow 2$ jet migration uncertainty in ggZH, (e) global uncertainty scale for $\mathrm{t\bar{t}H}$ and (f) $p_{\mathrm{T}}^{\mathrm{H}}$ threshold effects at 120 GeV in $\mathrm{t\bar{t}H}$. No impact is reported in the variations for which the nominal or varied yield is 0 or below 0.1 expected events.

largest impact on the measured cross sections, since they vary the S/B ratio of each signal region and they can have up to 15% impact on the $m_{\gamma\gamma}$ resolution. The impact of the 9 nuisance parameters is computed for each category with the interquantile estimator of Eq. (4.8). The impacts for some representative categories are reported in Figure A.14, mainly showing the impact for different bins of $p_{\mathrm{T}}^{\gamma\gamma}$.

The largest group of systematic uncertainties included in the coupling analysis comes from objects reconstruction and selection. The impact of these systematic sources is computed for each analysis category, for each nuisance parameter and for each Higgs production process. An example of the evaluated impacts for the ggF production mode is reported in Table A.4 and Table A.5.

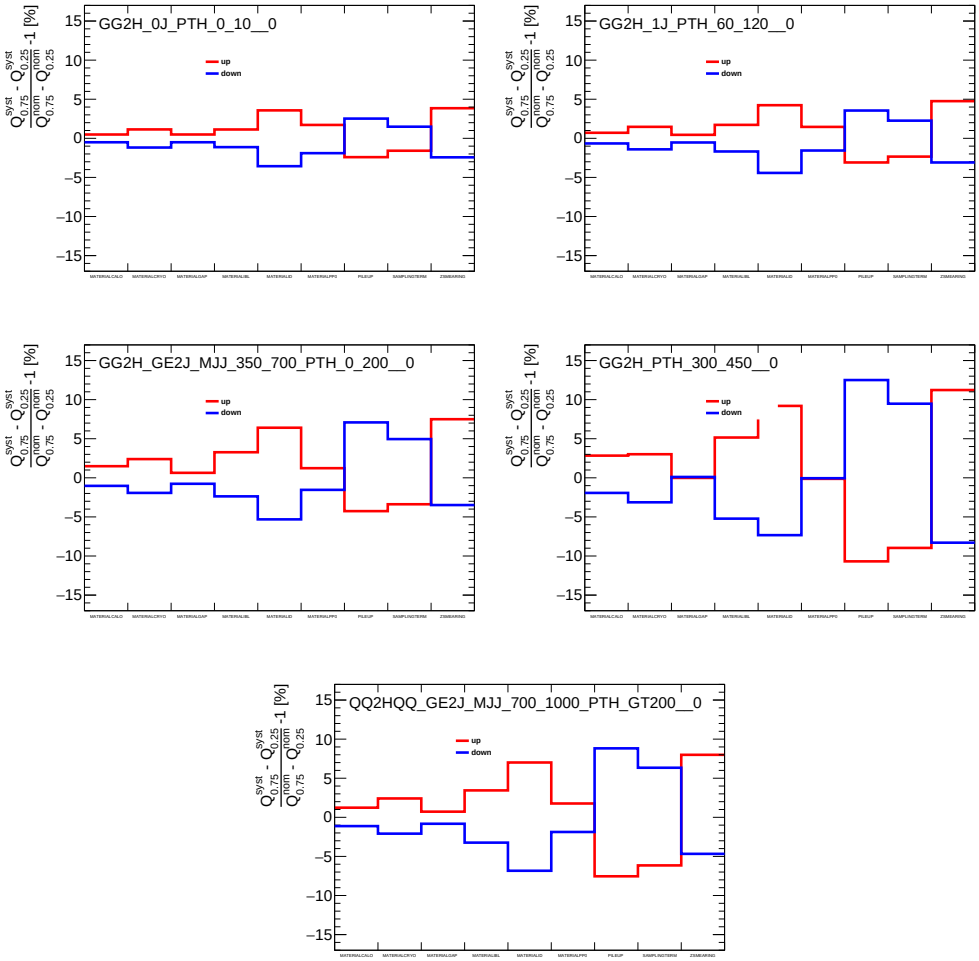

Figure A.14 – Evaluation of the impact of each the photon energy resolution nuisance parameter for some categories of the tight categories of the coupling analysis. The category name is reported at the bottom of each plot. The up and down uncertainties (evaluated using respectively the $+1\sigma$ and -1σ varied distributions) are shown in red and blue respectively.

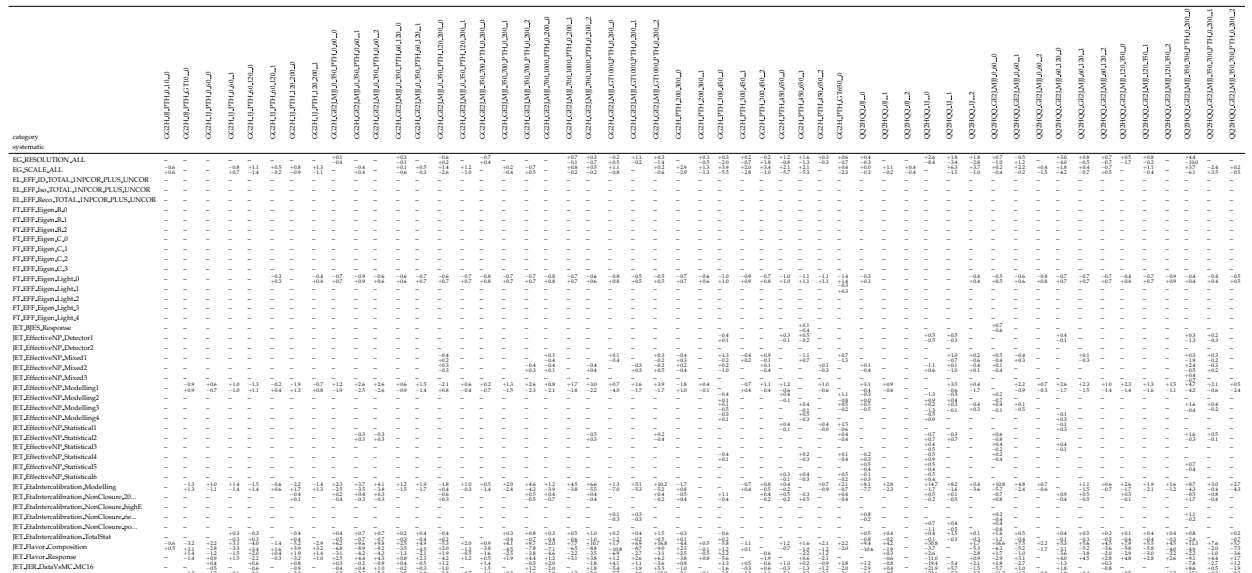

Table A.4 – Table of systematics uncertainty impact for each analysis category using ggF simulated events. Values shown are given in percent representing the relative impact on the category yield

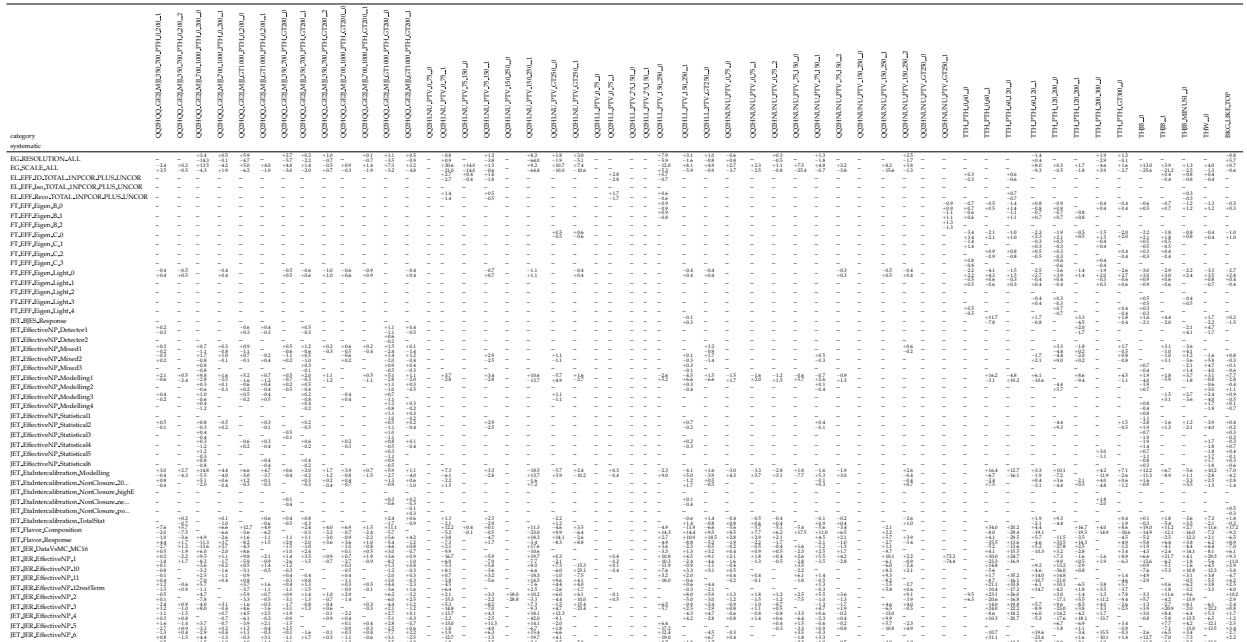

Table A.5 – Table of systematics uncertainty impact for each analysis category using ggF simulated events. Values shown are given in percent representing the relative impact on the category yield. Continued from Table A.4.

Bibliography

[1] ATLAS Collaboration, *The ATLAS Experiment at the CERN Large Hadron Collider*, JINST **3** (2008) S08003 (cit. on pp. ix, 30, 31, 34, 35, 39, 41, 43).

[2] L. Evans and P. Bryant, *LHC Machine*, Journal of Instrumentation **3** (2008) S08001, URL: http://stacks.iop.org/1748-0221/3/i=08/a=S08001 (cit. on pp. ix, 25).

[3] CMS Collaboration, *The CMS experiment at the CERN LHC*, Journal of Instrumentation **3** (2008) S08004, URL: https://doi.org/10.1088/1748-0221/3/08/s08004 (cit. on p. ix).

[4] ATLAS Collaboration, *Observation of a new particle in the search for the Standard Model Higgs boson with the ATLAS detector at the LHC*, Physics Letters B **716** (2012) 1, ISSN: 0370-2693, arXiv: 1207.7214 [hep-ex], URL: http://www.sciencedirect.com/science/article/pii/S037026931200857X (cit. on pp. ix, 1, 18, 187).

[5] CMS Collaboration, *Observation of a new boson at a mass of 125 GeV with the CMS experiment at the LHC*, Physics Letters B **716** (2012) 30, ISSN: 0370-2693, URL: http://www.sciencedirect.com/science/article/pii/S0370269312008581 (cit. on pp. ix, 1, 18, 187).

[6] ATLAS Collaboration, *Measurement of the properties of Higgs boson production at $\sqrt{s} = 13\,TeV$ in the $H \to \gamma\gamma$ channel using $139\,fb^{-1}$ of pp collision data with the ATLAS experiment*, (2022), Accepted by JHEP, arXiv: 2207.00348 [hep-ex] (cit. on pp. xi, 111, 145, 162, 164, 165, 168, 169, 171, 176, 177).

[7] ATLAS Collaboration, *Measurement of the properties of Higgs boson production at $\sqrt{s}$=13 TeV in the $H \to \gamma\gamma$ channel using 139 fb^{-1} of pp collision data with the ATLAS experiment*, tech. rep., All figures including auxiliary figures are available at https://atlas.web.cern.ch/Atlas/GROUPS/PHYSICS/CONFNOTES/ATLAS-CONF-2020-026: CERN, 2020, URL: http://cds.cern.ch/record/2725727 (cit. on pp. xi, 193).

[8] ATLAS Collaboration, *Measurements of Higgs boson properties in the diphoton decay channel using 80 fb^{-1} of pp collision data at $\sqrt{s}$ = 13 TeV with the ATLAS detector*, tech. rep. ATLAS-CONF-2018-028, CERN, 2018, URL: http://cds.cern.ch/record/2628771 (cit. on pp. xi, 111, 119, 211, 215, 224).

[9] ATLAS Collaboration, *Observation of Higgs boson production in association with a top quark pair at the LHC with the ATLAS detector*, Phys. Lett. **B784** (2018) 173, arXiv: 1806.00425 [hep-ex] (cit. on pp. xi, 134, 139, 215).

[10] ATLAS Collaboration, *Measurement of Higgs boson production in association with a $t\bar{t}$ pair in the diphoton decay channel using 139 fb^{-1} of LHC data collected at $\sqrt{s} = 13$ TeV by the ATLAS experiment*, tech. rep., All figures including auxiliary figures are available at https://atlas.web.cern.ch/Atlas/GROUPS/PHYSICS/CONFNOTES/ATLAS-CONF-2019-004: CERN, 2019, URL: http://cds.cern.ch/record/2668103 (cit. on pp. xi, 134, 139).

[11] ATLAS Collaboration, *A detailed map of Higgs boson interactions by the ATLAS experiment ten years after the discovery*, Nature **607** (2022) 52, Auxiliary material is available at https://atlas.web.cern.ch/Atlas/GROUPS/PHYSICS/PAPERS/HIGG-2021-23/, arXiv: 2207.00092 [hep-ex] (cit. on pp. xi, 111, 176–180, 182–184, 186).

[12] ATLAS Collaboration, *Combined measurements of Higgs boson production and decay using up to 139 fb^{-1} of proton-proton collision data at $\sqrt{s} = 13$ TeV collected with the ATLAS experiment*, tech. rep., All figures including auxiliary figures are available at https://atlas.web.cern.ch/Atlas/GROUPS/PHYSICS/CONFNOTES/ATLAS-CONF-2021-053: CERN, 2021, URL: http://cds.cern.ch/record/2789544 (cit. on pp. xi, 167, 174).

[13] ATLAS Collaboration, *Combined measurements of Higgs boson production and decay using up to 80 fb^{-1} of proton–proton collision data at $\sqrt{s} = 13$ TeV collected with the ATLAS experiment*, tech. rep. ATLAS-CONF-2018-031, CERN, 2018, URL: http://cds.cern.ch/record/2629412 (cit. on pp. xi, 111).

[14] ATLAS Collaboration, *A combination of measurements of Higgs boson production and decay using up to 139 fb^{-1} of proton–proton collision data at $\sqrt{s} = 13$ TeV collected with the ATLAS experiment*, tech. rep., All figures including auxiliary figures are available at https://atlas.web.cern.ch/Atlas/GROUPS/PHYSICS/CONFNOTES/ATLAS-CONF-2020-027: CERN, 2020, URL: http://cds.cern.ch/record/2725733 (cit. on p. xi).

[15] P. Zyla et al., *Review of Particle Physics*, PTEP **2020** (2020) 083C01 (cit. on pp. 2, 3).

[16] D. Galbraith and C. Burgard, *Standard Model diagram, CERN Webfest 2012* (cit. on p. 2).

[17] M. Gell-Mann, *A Schematic Model of Baryons and Mesons*, Phys. Lett. **8** (1964) 214 (cit. on p. 3).

[18] G. Zweig, *An SU_3 model for strong interaction symmetry and its breaking; Version 2*, (1964) 80 p, Version 1 is CERN preprint 8182/TH.401, Jan. 17, 1964, URL: http://cds.cern.ch/record/570209 (cit. on p. 3).

[19] JADE Collaboration, *Observation of planar three-jet events in e^+e^- annihilation and evidence for gluon bremsstrahlung*, Physics Letters B **91** (1980) 142, ISSN: 0370-2693, URL: http://www.sciencedirect.com/science/article/pii/0370269380906802 (cit. on p. 3).

[20] R. Feynman and A. Zee, *QED: The Strange Theory of Light and Matter*, Alix G. Mautner memorial lectures, Princeton University Press, 2006, ISBN: 9780691125756, URL: https://books.google.fr/books?id=Uv-uxB0sRKEC (cit. on p. 5).

[21] S. L. Glashow, *Partial-symmetries of weak interactions*, Nuclear Physics **22** (1961) 579, ISSN: 0029-5582, URL: http://www.sciencedirect.com/science/article/pii/0029558261904692 (cit. on p. 5).

[22] P. W. Higgs, *Broken symmetries, massless particles and gauge fields*, Physics Letters **12** (1964) 132, ISSN: 0031-9163, URL: http://www.sciencedirect.com/science/article/pii/0031916364911369 (cit. on p. 7).

[23] P. W. Higgs, *Broken Symmetries and the Masses of Gauge Bosons*, Phys. Rev. Lett. **13** (16 1964) 508, URL: https://link.aps.org/doi/10.1103/PhysRevLett.13.508 (cit. on p. 7).

[24] P. W. Higgs, *Spontaneous Symmetry Breakdown without Massless Bosons*, Phys. Rev. **145** (4 1966) 1156, URL: https://link.aps.org/doi/10.1103/PhysRev.145.1156 (cit. on p. 7).

[25] F. Englert and R. Brout, *Broken Symmetry and the Mass of Gauge Vector Mesons*, Phys. Rev. Lett. **13** (9 1964) 321, URL: https://link.aps.org/doi/10.1103/PhysRevLett.13.321 (cit. on p. 7).

[26] G. S. Guralnik et al., *Global Conservation Laws and Massless Particles*, Phys. Rev. Lett. **13** (20 1964) 585, URL: https://link.aps.org/doi/10.1103/PhysRevLett.13.585 (cit. on p. 7).

[27] S. L. Glashow and S. Weinberg, *Breaking Chiral Symmetry*, Phys. Rev. Lett. **20** (5 1968) 224, URL: https://link.aps.org/doi/10.1103/PhysRevLett.20.224 (cit. on p. 7).

[28] G. 't Hooft, *Renormalization of massless Yang-Mills fields*, Nuclear Physics B **33** (1971) 173, ISSN: 0550-3213, URL: http://www.sciencedirect.com/science/article/pii/0550321371903956 (cit. on p. 7).

[29] G. 't Hooft, *Renormalizable Lagrangians for massive Yang-Mills fields*, Nuclear Physics B **35** (1971) 167, ISSN: 0550-3213, URL: http://www.sciencedirect.com/science/article/pii/0550321371901398 (cit. on p. 7).

[30] J. Goldstone et al., *Broken Symmetries*, Phys. Rev. **127** (3 1962) 965, URL: https://link.aps.org/doi/10.1103/PhysRev.127.965 (cit. on p. 8).

[31] D. de Florian et al., *Handbook of LHC Higgs Cross Sections: 4. Deciphering the Nature of the Higgs Sector*, (2016), arXiv: 1610.07922 [hep-ph] (cit. on pp. 12, 15–17, 90, 92, 106, 111, 112, 114, 167, 174, 188).

[32] C. Anastasiou et al., *High precision determination of the gluon fusion Higgs boson cross-section at the LHC*, Journal of High Energy Physics **2016** (2016) 58, ISSN: 1029-8479, URL: https://doi.org/10.1007/JHEP05(2016)058 (cit. on pp. 13, 92).

[33] ATLAS and CMS Collaborations, *Combined Measurement of the Higgs Boson Mass in pp Collisions at $\sqrt{s} = 7$ and 8 TeV with the ATLAS and CMS Experiments*, Phys. Rev. Lett. **114** (2015) 191803, arXiv: 1503.07589 [hep-ex] (cit. on pp. 18, 20, 145).

[34] ATLAS Collaboration, *Measurement of the Higgs boson mass from the $H \to \gamma\gamma$ and $H \to ZZ^* \to 4\ell$ channels with the ATLAS detector using 25 fb^{-1} of pp collision data*, Phys. Rev. **D90** (2014) 052004, arXiv: 1406.3827 [hep-ex] (cit. on pp. 20, 189, 190, 200, 212).

[35] ATLAS and CMS Collabations, *Measurements of the Higgs boson production and decay rates and constraints on its couplings from a combined ATLAS and CMS analysis of the LHC pp collision data at $\sqrt{s} = 7$ and 8 TeV*, JHEP **08** (2016) 045, arXiv: 1606.02266 [hep-ex] (cit. on pp. 21, 22).

[36] C. N. Yang, *Selection Rules for the Dematerialization of a Particle into Two Photons*, Phys. Rev. **77** (2 1950) 242, URL: https://link.aps.org/doi/10.1103/PhysRev.77.242 (cit. on p. 22).

[37] L. Landau, "On the Angular Momentum of a System of two Photons", *Collected Papers of L.D. Landau*, ed. by D. T. HAAR, Pergamon, 1965 471, ISBN: 978-0-08-010586-4, URL: http://www.sciencedirect.com/science/article/pii/B9780080105864500705 (cit. on p. 22).

[38] J. C. Collins and D. E. Soper, *Angular distribution of dileptons in high-energy hadron collisions*, Phys. Rev. D **16** (7 1977) 2219, URL: https://link.aps.org/doi/10.1103/PhysRevD.16.2219 (cit. on p. 22).

[39] ATLAS Collaboration, *Study of the spin and parity of the Higgs boson in diboson decays with the ATLAS detector*, Eur. Phys. J. **C75** (2015) 476, [Erratum: Eur. Phys. J.C76,no.3,152(2016)], arXiv: 1506.05669 [hep-ex] (cit. on p. 22).

[40] CMS Collaboration, *Constraints on the spin-parity and anomalous HVV couplings of the Higgs boson in proton collisions at 7 and 8 TeV*, Phys. Rev. D **92** (1 2015) 012004, URL: https://link.aps.org/doi/10.1103/PhysRevD.92.012004 (cit. on p. 22).

[41] L. A. Harland-Lang et al., *Parton distributions in the LHC era: MMHT 2014 PDFs*, The European Physical Journal C **75** (2015), ISSN: 1434-6052, URL: http://dx.doi.org/10.1140/epjc/s10052-015-3397-6 (cit. on p. 26).

[42] E. Mobs, *The CERN accelerator complex*, (2018), General Photo, URL: https://cds.cern.ch/record/2636343 (cit. on p. 27).

[43] AC Team, *Diagram of an LHC dipole magnet. Schéma d'un aimant dipôle du LHC*, 1999, URL: https://cds.cern.ch/record/40524 (cit. on p. 28).

[44] J. Caron, *LHC quadrupole cross section.* AC Collection. Legacy of AC. Pictures from 1992 to 2002., 1998, URL: https://cds.cern.ch/record/841485 (cit. on p. 28).

[45] M. Barnes et al., *The PS complex as proton pre-injector for the LHC: design and implementation report*, CERN Yellow Reports: Monographs, Geneva: CERN, 2000, URL: https://cds.cern.ch/record/449242 (cit. on p. 27).

[46] P. Collier et al., *The SPS as Injector for LHC: Conceptual Design*, tech. rep., CERN, 1997, URL: https://cds.cern.ch/record/322782 (cit. on p. 27).

[47] *9th LHC Operations Evian Workshop, Proceedings*, Organisers: Steerenberg, R; Wenninger, J, CERN, Geneva, 2019, URL: https://cds.cern.ch/record/2706427 (cit. on p. 29).

[48] R. Bruce et al., *Review of LHC Run 2 Machine Configurations*, (2019) 187, URL: https://cds.cern.ch/record/2750415 (cit. on p. 29).

[49] B. Salvachua, *Overview of Proton-Proton Physics during Run 2*, (2019) 7, URL: https://cds.cern.ch/record/2750272 (cit. on p. 29).

[50] J. Pequenao, *Computer generated image of the whole ATLAS detector*, 2008, URL: https://cds.cern.ch/record/1095924 (cit. on p. 31).

[51] ATLAS Collaboration, *ATLAS central solenoid: Technical Design Report*, Technical design report. ATLAS, Electronic version not available, Geneva: CERN, 1997, URL: https://cds.cern.ch/record/331067 (cit. on p. 32).

[52] ATLAS Collaboration, *ATLAS barrel toroid: Technical Design Report*, Technical design report. ATLAS, Electronic version not available, Geneva: CERN, 1997, URL: https://cds.cern.ch/record/331065 (cit. on p. 33).

[53] ATLAS Collaboration, *ATLAS end-cap toroids: Technical Design Report*, Technical design report. ATLAS, Electronic version not available, Geneva: CERN, 1997, URL: https://cds.cern.ch/record/331066 (cit. on p. 33).

[54] J. J. Goodson, *Search for Supersymmetry in States with Large Missing Transverse Momentum and Three Leptons including a Z-Boson*, Presented 17 Apr 2012, 2012, URL: https://cds.cern.ch/record/1449722 (cit. on p. 33).

[55] J. Pequenao, *Computer generated image of the ATLAS inner detector*, 2008, URL: https://cds.cern.ch/record/1095926 (cit. on p. 34).

[56] ATLAS Collaboration, *Track Reconstruction Performance of the ATLAS Inner Detector at* $\sqrt{s} = 13$ *TeV*, tech. rep., All figures including auxiliary figures are available at https://atlas.web.cern.ch/Atlas/GROUPS/PHYSICS/PUBNOTES/ATL-PHYS-PUB-2015-018: CERN, 2015, URL: https://cds.cern.ch/record/2037683 (cit. on p. 34).

[57] ATLAS Collaboration, *ATLAS pixel detector: Technical Design Report*, Technical Design Report ATLAS, Geneva: CERN, 1998, URL: https://cds.cern.ch/record/381263 (cit. on p. 35).

[58] M. Capeans et al., *ATLAS Insertable B-Layer Technical Design Report*, (2010), URL: http://cds.cern.ch/record/1291633 (cit. on p. 35).

[59] A. Abdesselam et al., *The barrel modules of the ATLAS semiconductor tracker*, Nuclear Instruments and Methods in Physics Research Section A: Accelerators, Spectrometers, Detectors and Associated Equipment **568** (2006) 642, ISSN: 0168-9002, URL: http://www.sciencedirect.com/science/article/pii/S016890020601388X (cit. on p. 35).

[60] A. Abdesselam et al., *The ATLAS semiconductor tracker end-cap module*, Nuclear Instruments and Methods in Physics Research Section A: Accelerators, Spectrometers, Detectors and Associated Equipment **575** (2007) 353, ISSN: 0168-9002, URL: http://www.sciencedirect.com/science/article/pii/S0168900207003270 (cit. on p. 35).

[61] ATLAS TRT Collaboration, *The ATLAS TRT Barrel Detector*, Journal of Instrumentation **3** (2008) P02014, URL: http://stacks.iop.org/1748-0221/3/i=02/a=P02014 (cit. on p. 36).

[62] ATLAS TRT Collaboration, *The ATLAS TRT end-cap detectors*, Journal of Instrumentation **3** (2008) P10003, URL: http://stacks.iop.org/1748-0221/3/i=10/a=P10003 (cit. on p. 36).

[63] ATLAS Collaboration, *ATLAS IBL Impact parameter resolution*, URL: https://atlas.web.cern.ch/Atlas/GROUPS/PHYSICS/PLOTS/IDTR-2015-007/ (cit. on p. 37).

[64] ATLAS Collaboration, *Particle Identification Performance of the ATLAS Transition Radiation Tracker*, tech. rep., All figures including auxiliary figures are available at https://atlas.web.cern.ch/Atlas/GROUPS/PHYSICS/CONFNOTES/ATLAS-CONF-2011-128: CERN, 2011, URL: https://cds.cern.ch/record/1383793 (cit. on p. 37).

[65] CMS Collaboration, *CMS Physics: Technical Design Report Volume 1: Detector Performance and Software*, Technical Design Report CMS, Geneva: CERN, 2006, URL: https://cds.cern.ch/record/922757 (cit. on p. 37).

[66] J. Pequenao, *Computer Generated image of the ATLAS calorimeter*, 2008, URL: https://cds.cern.ch/record/1095927 (cit. on p. 39).

[67] ATLAS Collaboration, *ATLAS liquid-argon calorimeter: Technical Design Report*, Technical Design Report ATLAS, Geneva: CERN, 1996, URL: https://cds.cern.ch/record/331061 (cit. on pp. 40–42).

[68] ATLAS Collaboration, *Readiness of the ATLAS liquid argon calorimeter for LHC collisions*, The European Physical Journal C **70** (2010) 723, ISSN: 1434-6052, URL: https://doi.org/10.1140/epjc/s10052-010-1354-y (cit. on p. 40).

[69] ATLAS Collaboration, *ATLAS tile calorimeter: Technical Design Report*, Technical Design Report ATLAS (1996), URL: https://cds.cern.ch/record/331062 (cit. on p. 41).

[70] ATLAS Collaboration, *Readiness of the ATLAS Tile Calorimeter for LHC collisions*, The European Physical Journal C **70** (2010) 1193, ISSN: 1434-6052, URL: https://doi.org/10.1140/epjc/s10052-010-1508-y (cit. on p. 41).

[71] A. Artamonov et al., *The ATLAS Forward Calorimeter*, Journal of Instrumentation **3** (2008) P02010, URL: http://stacks.iop.org/1748-0221/3/i=02/a=P02010 (cit. on p. 42).

[72] ATLAS Collaboration, *ATLAS muon spectrometer: Technical Design Report*, Technical Design Report ATLAS (1997), URL: https://cds.cern.ch/record/331068 (cit. on pp. 42–44).

[73] ATLAS Collaboration, *Operation of the ATLAS trigger system in Run 2*, Journal of Instrumentation **15** (2020) P10004, ISSN: 1748-0221, URL: http://dx.doi.org/10.1088/1748-0221/15/10/P10004 (cit. on pp. 43, 46).

[74] ATLAS Collaboration, *Performance of the ATLAS Trigger System in 2015*, Eur. Phys. J. C **77** (2017) 317, arXiv: 1611.09661 [hep-ex] (cit. on p. 43).

[75] ATLAS Collaboration, *ATLAS Trigger operation public results*, URL: https://twiki.cern.ch/twiki/bin/view/AtlasPublic/TriggerOperationPublicResults (cit. on p. 47).

[76] T. Cornelissen et al., *Concepts, Design and Implementation of the ATLAS New Tracking (NEWT)*, tech. rep., All figures including auxiliary figures are available at https://atlas.web.cern.ch/Atlas/GROUPS/PHYSICS/PUBNOTES/ATL-SOFT-PUB-2007-007: CERN, 2007, URL: https://cds.cern.ch/record/1020106 (cit. on p. 49).

[77] ATLAS Collaboration, *Performance of the ATLAS Track Reconstruction Algorithms in Dense Environments in LHC Run 2*, Eur. Phys. J. **C77** (2017) 673, arXiv: 1704.07983 [hep-ex] (cit. on p. 49).

[78] R. Frühwirth, *Application of Kalman filtering to track and vertex fitting*, Nuclear Instruments and Methods in Physics Research Section A: Accelerators, Spectrometers, Detectors and Associated Equipment **262** (1987) 444, ISSN: 0168-9002, URL: http://www.sciencedirect.com/science/article/pii/0168900287908874 (cit. on p. 49).

[79] W. Waltenberger et al., *Adaptive vertex fitting*, Journal of Physics G: Nuclear and Particle Physics **34** (2007) N343, URL: https://doi.org/10.1088/0954-3899/34/12/n01 (cit. on p. 49).

[80] ATLAS Collaboration, *Electron and photon performance measurements with the ATLAS detector using the 2015–2017 LHC proton-proton collision data*, JINST **14** (2019) P12006, arXiv: 1908.00005 [hep-ex] (cit. on pp. 50–52, 54–56, 71, 73, 74, 76).

[81] W. Lampl et al., *Calorimeter Clustering Algorithms: Description and Performance*, tech. rep. ATL-LARG-PUB-2008-002. ATL-COM-LARG-2008-003, CERN, 2008, URL: https://cds.cern.ch/record/1099735 (cit. on pp. 50, 56, 190).

[82] ATLAS Collaboration, *Improved electron reconstruction in ATLAS using the Gaussian Sum Filter-based model for bremsstrahlung*, tech. rep., All figures including auxiliary figures are available at https://atlas.web.cern.ch/Atlas/GROUPS/PHYSICS/CONFNOTES/ATLAS-CONF-2012-047: CERN, 2012, URL: https://cds.cern.ch/record/1449796 (cit. on p. 53).

[83] ATLAS Collaboration, *Search for resonances in the 65 to 110 GeV diphoton invariant mass range using 80 fb^{-1} of pp collisions collected at $\sqrt{s} = 13$ TeV with the ATLAS detector*, tech. rep., All figures including auxiliary figures are available at https://atlas.web.cern.ch/Atlas/GROUPS/PHYSICS/CONFNOTES/ATLAS-CONF-2018-025: CERN, 2018, URL: http://cds.cern.ch/record/2628760 (cit. on p. 55).

[84] ATLAS Collaboration, *Electron and photon energy calibration with the ATLAS detector using LHC Run 1 data*, Eur. Phys. J. C **C74** (2014) 3071. 48 p, URL: https://cds.cern.ch/record/1744017 (cit. on p. 63).

[85] ATLAS Collaboration, *Electron and photon energy calibration with the ATLAS detector using 2015–2016 LHC proton-proton collision data*, Journal of Instrumentation **14** (2019) P03017, ISSN: 1748-0221, URL: http://dx.doi.org/10.1088/1748-0221/14/03/P03017 (cit. on pp. 63, 64, 66).

[86] ATLAS Collaboration, *ATLAS EGamma public plots: energy calibration using LHC Run2 data (2018)*, URL: https://atlas.web.cern.ch/Atlas/GROUPS/PHYSICS/PLOTS/EGAM-2018-008/ (cit. on p. 65).

[87] ATLAS Collaboration, *Measurement of the photon identification efficiencies with the ATLAS detector using LHC Run 2 data collected in 2015 and 2016*, Eur. Phys. J. C **79** (2019) 205, arXiv: 1810.05087 [hep-ex] (cit. on p. 68).

[88] ATLAS Collaboration, *Measurement of the photon identification efficiencies with the ATLAS detector using LHC Run-1 data*, Eur. Phys. J. C **76** (2016) 666. 57 p, URL: https://cds.cern.ch/record/2158117 (cit. on p. 69).

[89] J. Saxon, *Discovery of the Higgs Boson, Measurements of its Production, and a Search for Higgs Boson Pair Production*, Presented 13 06 2014, 2014, URL: https://cds.cern.ch/record/1746004 (cit. on p. 70).

[90] ATLAS Collaboration, *ATLAS EGamma public plots: Photon identification efficiencies and scale factors in Run 2*, URL: https://atlas.web.cern.ch/Atlas/GROUPS/PHYSICS/PLOTS/EGAM-2021-01 (cit. on pp. 71, 72).

[91] ATLAS Collaboration, *Electron efficiency measurements with the ATLAS detector using 2012 LHC proton–proton collision data*, Eur. Phys. J. C **77** (2017) 195, arXiv: 1612.01456 [hep-ex] (cit. on p. 74).

[92] ATLAS Collaboration, *Electron efficiency measurements with the ATLAS detector using the 2015 LHC proton-proton collision data*, tech. rep. ATLAS-CONF-2016-024, CERN, 2016, URL: https://cds.cern.ch/record/2157687 (cit. on p. 75).

[93] ATLAS Collaboration, *Jet reconstruction and performance using particle flow with the ATLAS Detector*, Eur. Phys. J. C **77** (2017) 466, arXiv: 1703.10485 [hep-ex] (cit. on p. 76).

[94] ATLAS Collaboration, *Jet energy scale and resolution measured in proton–proton collisions at $\sqrt{s} = 13$ TeV with the ATLAS detector*, Eur. Phys. J. C **81** (2021) 689, arXiv: 2007.02645 [hep-ex] (cit. on pp. 76–80).

[95] M. Cacciari et al., *The anti-k_t jet clustering algorithm*, JHEP **04** (2008) 063, arXiv: 0802.1189 [hep-ph] (cit. on p. 76).

[96] ATLAS Collaboration, *Performance of pile-up mitigation techniques for jets in pp collisions at $\sqrt{s} = 8$ TeV using the ATLAS detector*, Eur. Phys. J. C **76** (2016) 581, arXiv: 1510.03823 [hep-ex] (cit. on pp. 79, 81).

[97] ATLAS Collaboration, *ATLAS Jet/ETMiss public plots: Optimisation of the jet vertex tagger for Particle Flow jets through track-to-vertex-association improvements*, URL: https://atlas.web.cern.ch/Atlas/GROUPS/PHYSICS/PLOTS/JETM-2021-001/ (cit. on p. 81).

[98] ATLAS Collaboration, *Forward jet vertex tagging using the particle flow algorithm*, tech. rep., All figures including auxiliary figures are available at https://atlas.web.cern.ch/Atlas/GROUPS/PHYSICS/PUBNOTES/ATL-PHYS-PUB-2019-026: CERN, 2019, URL: http://cds.cern.ch/record/2683100 (cit. on pp. 80, 83).

[99] ATLAS Collaboration, *ATLAS b-jet identification performance and efficiency measurement with $t\bar{t}$ events in pp collisions at $\sqrt{s} = 13$ TeV*, Eur. Phys. J. C **79** (2019) 970, arXiv: 1907.05120 [hep-ex] (cit. on p. 82).

[100] ATLAS Collaboration, *Performance of b-Jet Identification in the ATLAS Experiment*, JINST **11** (2016) P04008, arXiv: 1512.01094 [hep-ex] (cit. on p. 82).

[101] ATLAS Collaboration, *Identification of Jets Containing b-Hadrons with Recurrent Neural Networks at the ATLAS Experiment*, tech. rep., All figures including auxiliary figures are available at https://atlas.web.cern.ch/Atlas/GROUPS/PHYSICS/PUBNOTES/ATL-PHYS-PUB-2017-003: CERN, 2017, URL: https://cds.cern.ch/record/2255226 (cit. on pp. 82, 83).

[102] ATLAS Collaboration, *Optimisation and performance studies of the ATLAS b-tagging algorithms for the 2017-18 LHC run*, tech. rep., All figures including auxiliary figures are available at https://atlas.web.cern.ch/Atlas/GROUPS/PHYSICS/PUBNOTES/ATL-PHYS-PUB-2017-013: CERN, 2017, URL: https://cds.cern.ch/record/2273281 (cit. on pp. 82, 83).

[103] ATLAS Collaboration, *Expected performance of the 2019 ATLAS b-taggers*, URL: http://atlas.web.cern.ch/Atlas/GROUPS/PHYSICS/PLOTS/FTAG-2019-005/ (cit. on pp. 82, 84).

[104] ATLAS Collaboration, URL: http://atlas.web.cern.ch/Atlas/GROUPS/PHYSICS/PLOTS/FTAG-2019-005/ (cit. on p. 82).

[105] ATLAS Collaboration, *Muon reconstruction and identification efficiency in ATLAS using the full Run 2 pp collision data set at $\sqrt{s} = 13$ TeV*, Eur. Phys. J. C **81** (2021) 578, arXiv: 2012.00578 [hep-ex] (cit. on pp. 83, 85, 86).

[106] ATLAS Collaboration, *E_T^{miss} performance in the ATLAS detector using 2015-2016 LHC p-p collisions*, tech. rep., All figures including auxiliary figures are available at https://atlas.web.cern.ch/Atlas/GROUPS/PHYSICS/CONFNOTES/ATLAS-CONF-2018-023: CERN, 2018, URL: http://cds.cern.ch/record/2625233 (cit. on p. 87).

[107] ATLAS Collaboration, *Missing transverse momentum performance using the full run 2 pp data at 13 TeV*, URL: https://atlas.web.cern.ch/Atlas/GROUPS/PHYSICS/PLOTS/JETM-2019-03/ (cit. on p. 88).

[108] ATLAS Collaboration, *ATLAS Public Results - Run 2 Luminosity*, URL: https://twiki.cern.ch/twiki/bin/view/AtlasPublic/LuminosityPublicResultsRun2 (cit. on pp. 90, 91).

[109] GEANT4 Collaboration, *GEANT4: a simulation toolkit*, Nucl. Instrum. Meth. A **506** (2003) 250 (cit. on p. 91).

[110] ATLAS Collaboration, *The ATLAS Simulation Infrastructure*, Eur. Phys. J. **C70** (2010) 823, arXiv: 1005.4568 [physics.ins-det] (cit. on p. 91).

[111] K. Hamilton et al., *NNLOPS simulation of Higgs boson production*, JHEP **10** (2013) 222, arXiv: 1309.0017 [hep-ph] (cit. on p. 92).

[112] J. Butterworth et al., *PDF4LHC recommendations for LHC Run II*, J. Phys. G **43** (2016) 023001, arXiv: 1510.03865 [hep-ph] (cit. on p. 92).

[113] T. Sjöstrand et al., *A brief introduction to PYTHIA 8.1*, Comput. Phys. Commun. **178** (2008) 852, arXiv: 0710.3820 [hep-ph] (cit. on p. 92).

[114] ATLAS Collaboration, *Measurement of the Z/γ^* boson transverse momentum distribution in pp collisions at $\sqrt{s}$ = 7 TeV with the ATLAS detector*, JHEP **09** (2014) 145, arXiv: 1406.3660 [hep-ex] (cit. on p. 92).

[115] P. Nason, *A New method for combining NLO QCD with shower Monte Carlo algorithms*, JHEP **11** (2004) 040, arXiv: hep-ph/0409146 (cit. on p. 92).

[116] S. Frixione et al., *Matching NLO QCD computations with parton shower simulations: the POWHEG method*, JHEP **11** (2007) 070, arXiv: 0709.2092 [hep-ph] (cit. on p. 92).

[117] S. Alioli et al., *A general framework for implementing NLO calculations in shower Monte Carlo programs: the POWHEG BOX*, JHEP **06** (2010) 043, arXiv: 1002.2581 [hep-ph] (cit. on p. 92).

[118] P. Nason and C. Oleari, *NLO Higgs boson production via vector-boson fusion matched with shower in POWHEG*, JHEP **02** (2010) 037, arXiv: 0911.5299 [hep-ph] (cit. on p. 92).

[119] J. M. Campbell et al., *NLO Higgs boson production plus one and two jets using the POWHEG BOX, MadGraph4 and MCFM*, JHEP **07** (2012) 092, arXiv: 1202.5475 [hep-ph] (cit. on p. 92).

[120] G. Luisoni et al., *$HW^{\pm}$/HZ + 0 and 1 jet at NLO with the POWHEG BOX interfaced to GoSam and their merging within MiNLO*, JHEP **10** (2013) 083, arXiv: 1306.2542 [hep-ph] (cit. on p. 92).

[121] J. Alwall et al., *The automated computation of tree-level and next-to-leading order differential cross sections, and their matching to parton shower simulations*, JHEP **07** (2014) 079, arXiv: 1405.0301 [hep-ph] (cit. on p. 92).

[122] M. Wiesemann et al., *Higgs production in association with bottom quarks*, JHEP **02** (2015) 132, arXiv: 1409.5301 [hep-ph] (cit. on p. 92).

[123] S. Frixione et al., *Electroweak and QCD corrections to top-pair hadroproduction in association with heavy bosons*, JHEP **06** (2015) 184, arXiv: 1504.03446 [hep-ph] (cit. on p. 92).

[124] T. Gleisberg et al., *Event generation with SHERPA 1.1*, JHEP **02** (2009) 007, arXiv: 0811.4622 [hep-ph] (cit. on p. 92).

[125] S. Schumann and F. Krauss, *A Parton shower algorithm based on Catani-Seymour dipole factorisation*, JHEP **03** (2008) 038, arXiv: 0709.1027 [hep-ph] (cit. on p. 92).

[126] S. Höche et al., *QCD matrix elements + parton showers: The NLO case*, JHEP **04** (2013) 027, arXiv: 1207.5030 [hep-ph] (cit. on p. 92).

[127] G. Ke et al., "LightGBM: A Highly Efficient Gradient Boosting Decision Tree", *Advances in Neural Information Processing Systems 30*, ed. by I. Guyon et al., Curran Associates, Inc., 2017 3146, URL: http://papers.nips.cc/paper/6907-lightgbm-a-highly-efficient-gradient-boosting-decision-tree.pdf (cit. on pp. 95, 121).

[128] A. Hoecker et al., *TMVA - Toolkit for Multivariate Data Analysis*, 2007, arXiv: physics/0703039 [physics.data-an] (cit. on p. 95).

[129] ATLAS Collaboration, *Measurements of Higgs boson properties in the diphoton decay channel with 36 fb^{-1} of pp collision data at $\sqrt{s} = 13$ TeV with the ATLAS detector*, (2018), arXiv: 1802.04146 [hep-ex] (cit. on pp. 101, 111, 119, 215).

[130] ATLAS Collaboration, *Measurements and interpretations of Higgs-boson fiducial cross sectios in the diphoton decay channel using 139 $fb^{-}1$ of pp collision data at $\sqrt{s} = 13$ TeV with the ATLAS detector*, tech. rep., All figures including auxiliary figures are available at https://atlas.web.cern.ch/Atlas/GROUPS/PHYSICS/CONFNOTES/ATLAS-CONF-2019-029: CERN, 2019, URL: http://cds.cern.ch/record/2682800 (cit. on pp. 102, 103).

[131] ATLAS Collaboration, *Measurement of the production cross section of pairs of isolated photons in pp collisions at 13 TeV with the ATLAS detector*, JHEP **11** (2021) 169, arXiv: 2107.09330 [hep-ex] (cit. on p. 102).

[132] R. Boughezal et al., *Combining resummed Higgs predictions across jet bins*, Phys. Rev. D **89** (7 2014) 074044, URL: https://link.aps.org/doi/10.1103/PhysRevD.89.074044 (cit. on p. 106).

[133] J. Butterworth et al., *PDF4LHC recommendations for LHC Run II*, J. Phys. G **43** (2016) 023001, arXiv: 1510.03865 [hep-ph] (cit. on p. 106).

[134] K. Cranmer et al., *HistFactory: A tool for creating statistical models for use with RooFit and RooStats*, tech. rep., New York U., 2012, URL: https://cds.cern.ch/record/1456844 (cit. on p. 109).

[135] G. Cowan et al., *Asymptotic formulae for likelihood-based tests of new physics*, The European Physical Journal C **71** (2011) 1554, ISSN: 1434-6052, URL: https://doi.org/10.1140/epjc/s10052-011-1554-0 (cit. on pp. 109, 110, 160).

[136] J. Neyman and E. S. Pearson, *On the Problem of the Most Efficient Tests of Statistical Hypotheses*, Philosophical Transactions of the Royal Society of London. Series A, Containing Papers of a Mathematical or Physical Character **231** (1933) 289, ISSN: 02643952, URL: http://www.jstor.org/stable/91247 (cit. on p. 110).

[137] N. Berger et al., *Simplified Template Cross Sections - Stage 1.1*, 2019, arXiv: 1906.02754 [hep-ph] (cit. on pp. 111, 113).

[138] LHC Higgs WG, WG2, *Simplified Template Cross Sections, Stage 1.2*, URL: https://twiki.cern.ch/twiki/bin/view/LHCPhysics/LHCHWGFiducialAndSTXS?rev=24 (cit. on pp. 111, 113, 114, 121).

[139] J. E. Dickinson, *ATLAS Measurements of the Higgs Boson Coupling to the Top Quark in the Higgs to Diphoton Decay Channel*, Presented 29 May 2020, 2020, URL: https://cds.cern.ch/record/2719502 (cit. on pp. 118, 119).

[140] T. Chen and C. Guestrin, *XGBoost: A Scalable Tree Boosting System*, CoRR (2016), arXiv: 1603.02754 (cit. on p. 121).

[141] D. V. Lindley, *On a Measure of the Information Provided by an Experiment*, Ann. Math. Statist. **27** (1956) 986, URL: https://doi.org/10.1214/aoms/1177728069 (cit. on p. 124).

[142] M. J. D. Powell, *An efficient method for finding the minimum of a function of several variables without calculating derivatives*, The Computer Journal **7** (1964) 155, ISSN: 0010-4620, eprint: https://academic.oup.com/comjnl/article-pdf/7/2/155/959784/070155.pdf, URL: https://doi.org/10.1093/comjnl/7.2.155 (cit. on p. 126).

[143] W. H. Press et al., *Numerical Recipes in C (2nd Ed.): The Art of Scientific Computing*, USA: Cambridge University Press, 1992, ISBN: 0521431085 (cit. on p. 126).

[144] M. Ebden, *Gaussian Processes: A Quick Introduction*, 2015, arXiv: 1505.02965 [math.ST] (cit. on p. 149).

[145] C. Rasmussen and C. Williams, *Gaussian Processes for Machine Learning*, Adaptive Computation and Machine Learning, Cambridge, MA, USA: MIT Press, 2006 248 (cit. on p. 149).

[146] R. J. Hyneman, *Measuring Higgs Boson Couplings, including to the Top Quark, in the Diphoton Decay Channel with Run 2 Data Collected by the ATLAS Detector*, (2020), Presented 04 Feb 2020, URL: https://cds.cern.ch/record/2712576 (cit. on p. 149).

[147] G. W. Merz, *Precision Measurements of Higgs Boson Couplings in the Diphoton Decay Channel with Run-2 of the ATLAS Detector*, Presented 2021, 2021, URL: https://cds.cern.ch/record/2776271 (cit. on pp. 149, 150).

[148] M. Gibss, *Bayesian Gaussian Processes for Regression and Classification*, (1997) (cit. on p. 149).

[149] J. Bendavid et al., *Les Houches 2017: Physics at TeV Colliders Standard Model Working Group Report*, 2018, arXiv: 1803.07977 [hep-ph] (cit. on p. 155).

[150] I. W. Stewart and F. J. Tackmann, *Theory uncertainties for Higgs mass and other searches using jet bins*, Physical Review D **85** (2012), ISSN: 1550-2368, URL: http://dx.doi.org/10.1103/PhysRevD.85.034011 (cit. on p. 155).

[151] LHC Higgs WG, WG2, *Summary of recommended ggF STXS Stage 1.2 uncertainty scheme after discussion between ATLAS, CMS, and theorists*, URL: https://twiki.cern.ch/twiki/pub/LHCPhysics/LHCHWGFiducialAndSTXS/simplifiedXS%5C_ggF%5C_1.2%5C_theory%5C_uncertainty.pdf (cit. on p. 155).

[152] LHC Higgs WG, WG2, *WG activity on STXS ggF uncertainties (1.2): Summary and presentation of final results*, URL: https://indico.cern.ch/event/1018653/contributions/4624873/attachments/2356989/4022408/TheorySysggF.pdf (cit. on p. 155).

[153] LHC Higgs WG, WG2, *Uncertainties for VBF, VH and ttH STXS Stage 1.2*, URL: https://indico.cern.ch/event/922192/contributions/4057339/attachments/2140439/3606411/STXS-uncertainties-VBF-11-2020.pdf (cit. on p. 155).

[154] ATLAS Collaboration, *Evaluation of theoretical uncertainties for simplified template cross section measurements of V-associated production of the Higgs boson*, tech. rep., All figures including auxiliary figures are available at https://atlas.web.cern.ch/Atlas/GROUPS/PHYSICS/PUBNOTES/ATL-PHYS-PUB-2018-035: CERN, 2018, URL: https://cds.cern.ch/record/2649241 (cit. on p. 155).

[155] ATLAS Collaboration, *ATLAS Higss public plots for ggH STXS 1.2 uncertainties*, URL: https://atlas.web.cern.ch/Atlas/GROUPS/PHYSICS/PLOTS/HIGG-2021-01/ (cit. on p. 157).

[156] A. L. Read, *Presentation of search results: the CLs technique*, Journal of Physics G: Nuclear and Particle Physics **28** (2002) 2693, URL: https://doi.org/10.1088/0954-3899/28/10/313 (cit. on p. 163).

[157] S. Heinemeyer et al., *Handbook of LHC Higgs Cross Sections: 3. Higgs Properties: Report of the LHC Higgs Cross Section Working Group*, ed. by S. Heinemeyer, CERN Yellow Reports: Monographs, Comments: 404 pages, 139 figures, to be submitted to CERN Report. Working Group web page: https://twiki.cern.ch/twiki/bin/view/LHCPhysics/CrossSections, 2013, URL: https://cds.cern.ch/record/1559921 (cit. on pp. 167, 172, 174).

[158] I. Brivio and M. Trott, *The standard model as an effective field theory*, Physics Reports **793** (2019) 1, ISSN: 0370-1573, URL: http://dx.doi.org/10.1016/j.physrep.2018.11.002 (cit. on p. 167).

[159] ATLAS Collaboration, *Methodology for EFT interpretation of Higgs boson Simplified Template Cross-section results in ATLAS*, tech. rep., All figures including auxiliary figures are available at https://atlas.web.cern.ch/Atlas/GROUPS/PHYSICS/PUBNOTES/ATL-PHYS-PUB-2019-042: CERN, 2019, URL: http://cds.cern.ch/record/2694284 (cit. on p. 167).

[160] ATLAS Collaboration, *Higgs boson production cross-section measurements and their EFT interpretation in the 4ℓ decay channel at $\sqrt{s} = 13$ TeV with the ATLAS detector*, Eur. Phys. J. C **80** (2020) 957, arXiv: 2004.03447 [hep-ex] (cit. on p. 177), Erratum: Eur. Phys. J. C **81** (2021) 29.

[161] ATLAS Collaboration, *Evidence for the associated production of the Higgs boson and a top quark pair with the ATLAS detector*, Phys. Rev. D **97** (2018) 072003, arXiv: 1712.08891 [hep-ex] (cit. on p. 177).

[162] ATLAS Collaboration, *Measurements of Higgs boson production by gluon–gluon fusion and vector-boson fusion using $H \to WW^* \to e\nu\mu\nu$ decays in pp collisions at $\sqrt{s} = 13$ TeV with the ATLAS detector*, (2022), arXiv: 2207.00338 [hep-ex] (cit. on p. 177).

[163] ATLAS Collaboration, *Measurement of the production cross section for a Higgs boson in association with a vector boson in the $H \to WW^* \to \ell\nu\ell\nu$ channel in pp collisions at $\sqrt{s} = 13$ TeV with the ATLAS detector*, Phys. Lett. B **798** (2019) 134949, arXiv: 1903.10052 [hep-ex] (cit. on p. 177).

[164] ATLAS Collaboration, *Measurements of Higgs boson production cross-sections in the $H \to \tau^+\tau^-$ decay channel in pp collisions at $\sqrt{s} = 13$ TeV with the ATLAS detector*, (2022), arXiv: 2201.08269 [hep-ex] (cit. on p. 177).

[165] ATLAS Collaboration, *Measurements of WH and ZH production in the $H \to b\bar{b}$ decay channel in pp collisions at 13 TeV with the ATLAS detector*, Eur. Phys. J. C **81** (2021) 178, arXiv: 2007.02873 [hep-ex] (cit. on p. 177).

[166] ATLAS Collaboration, *Measurement of the associated production of a Higgs boson decaying into b-quarks with a vector boson at high transverse momentum in pp collisions at $\sqrt{s} = 13$ TeV with the ATLAS detector*, Phys. Lett. B **816** (2021) 136204, arXiv: 2008.02508 [hep-ex] (cit. on p. 177).

[167] ATLAS Collaboration, *Combination of measurements of Higgs boson production in association with a W or Z boson in the $b\bar{b}$ decay channel with the ATLAS experiment at $\sqrt{s} = 13$ TeV*, tech. rep., CERN, 2021, URL: https://cds.cern.ch/record/2782535 (cit. on p. 177).

[168] ATLAS Collaboration, *Measurements of Higgs Bosons Decaying to Bottom Quarks from Vector Boson Fusion Production with the ATLAS Experiment at $\sqrt{s} = 13$ TeV*, (2020), arXiv: 2011.08280 [hep-ex] (cit. on p. 177).

[169] ATLAS Collaboration, *Measurement of Higgs boson decay into b-quarks in associated production with a top-quark pair in pp collisions at $\sqrt{s} = 13$ TeV with the ATLAS detector*, JHEP **06** (2021) 097, arXiv: 2111.06712 [hep-ex] (cit. on p. 177).

[170] ATLAS Collaboration, *Constraints on Higgs boson production with large transverse momentum using $H \to b\bar{b}$ decays in the ATLAS detector*, Phys. Rev. D **105** (2021) 092003, arXiv: 2111.08340 [hep-ex] (cit. on p. 177).

[171] ATLAS Collaboration, *A search for the dimuon decay of the Standard Model Higgs boson with the ATLAS detector*, Phys. Lett. B **812** (2021) 135980, arXiv: 2007.07830 [hep-ex] (cit. on p. 177).

[172] ATLAS Collaboration, *Direct constraint on the Higgs-charm coupling from a search for Higgs boson decays into charm quarks with the ATLAS detector*, (2022), arXiv: 2201.11428 [hep-ex] (cit. on p. 177).

[173] ATLAS Collaboration, *A search for the $Z\gamma$ decay mode of the Higgs boson in pp collisions at $\sqrt{s} = 13$ TeV with the ATLAS detector*, Phys. Lett. B **809** (2020) 135754, arXiv: 2005.05382 [hep-ex] (cit. on p. 177).

[174] ATLAS Collaboration, *Search for invisible Higgs-boson decays in events with vector-boson fusion signatures using 139 fb^{-1} of proton–proton data recorded by the ATLAS experiment*, (2022), arXiv: 2202.07953 [hep-ex] (cit. on p. 177).

[175] ATLAS Collaboration, *Search for associated production of a Z boson with an invisibly decaying Higgs boson or dark matter candidates at $\sqrt{s} = 13$ TeV with the ATLAS detector*, Phys. Lett. B **829** (2021) 137066, arXiv: 2111.08372 [hep-ex] (cit. on p. 177).

[176] ATLAS Collaboration, *Measurement of the Higgs boson mass in the $H \to ZZ^* \to 4\ell$ and $H \to \gamma\gamma$ channels with $\sqrt{s} = 13$ TeV pp collisions using the ATLAS detector*, Phys. Lett. B **784** (2018) 345, arXiv: 1806.00242 [hep-ex] (cit. on pp. 187, 189, 190, 193, 200, 209, 212).